Control of Superconductivity in Cuprate/Manganite Heterostructures

Brian SiewHan Pang

Hughes Hall
University of Cambridge

A dissertation submitted for the degree of Doctor of Philosophy at
University of Cambridge
June 2004

Abstract

Research has shown that the spin alignment in an adjacent ferromagnet is capable of suppressing superconductivity. In this project, devices incorporating cuprate/manganite heterostuctres were successfully fabricated to study the effects of spin transport on the high temperature superconductor, YBCO. Deposition of such oxide ferromagnet/superconductor(F/S) multilayers using the 'eclipse' pulsed laser deposition(PLD) technique was also examined. Reproducible multilayers with ultrathin repeats were deposited, which exhibited superconducting and magnetic properties to minimum thicknesses of 3nm for both YBCO and LSMO.

Using spin injection, via a ferromagnet, to create a spin imbalance in the superconductor, a suppression of superconducting critical current was observed with increasing injection current. However, the exact cause of this suppression could not be solely attributed to spin-induced non-equilibrium effects, as it proved difficult to eliminate the effects of localized heating, current summation and magnetic field. Interfacial studies of the device junction provided evidence of an alternative currnent path at the interface.

The control of superconductivity was also examined using F/S proximity effects, which improves the understanding of how magnetic and superconducting materials coexist. We observed that oxide F/S samples deposited by high O_2 sputtering [1] and 'eclipse' PLD were similar, and that T_c was clearly more suppressed in F/S compared to N(normal metal)/S systems. However, the magnetic moment and exchange coupling, two magnetic properties of significance in ferromagnets, did not, individually, have a major influence on the increased T_c suppression. The Curie temperatures of the multilayers were suppressed with increasing manganite thickness because of structural effects, and also with increasing thickness of the YBCO layer which reduced the coupling between manganite layers.

To study the use of the spin-valve effect as a means to control high temperature superconductors, we fabricated an LSMO/YBCO/LC(0.3)MO pseudo spin-valve structure, which is equivalent to a superconductor sandwiched within a spin valve where both parallel and anti-parallel configurations of the F layers can be achieved within a single magnetic field sweep. Previous research involving a metallic F/S/F/AF structure, showed that the superconductivity was suppressed when the ferromagnets were in the parallel configuration [2].

From the onset of superconductivity, when the normal metallic behaviour of YBCO switches to superconductivity, a magnetoresistance(MR) peak was observed when the F layers were anti-parallel. The MR effect increased with decreasing bias current and temperature, characteristic of a pseudo-spin valve. The result is suggestive of spin transport across the YBCO spacer layer.

Declaration

This dissertation is a result of my own work and includes nothing which is the outcome of work done in collaboration except where specifically indicated in the text. This work has been carried out in the Department of Materials Science and Metallurgy, University of Cambridge, UK since October 2000. No part of this dissertation has been submitted previously at Cambridge or any other University for a degree, diploma or other qualification. This dissertation does not exceed 60 000 words.

Brian SiewHan Pang
June 2004

Publications

$La_xA_{1-x}MnO_3$(A = Sr, Ca)/$YBa_2Cu_3O_{7-d}$ Superlattices Deposited by 'eclipse' Pulsed Laser Deposition Technique.
B.S.H.Pang, R.I.Tomov, M.G.Blamire
Superconductor Science and Technology, 17 (2004) 624-629.

Laser Ablation Deposition of $La_x(Sr,Ca)_{1-x}MnO_3/YBa_2Cu_3O_{7-d}$ Superlattices.
B.Pang, R.I.Tomov, M.G.Blamire
Accepted: Applied Physics A, 24th Febuary 2004.

Effect of Ferromagnetism on Superconductivity in Manganite / Cuprate Heterostructures.
B.S.H.Pang, R.I.Tomov, C.Bell, M.G.Blamire
Submitted to Physica C, 10th March 2004.

Manganite and Superconductor Heterostructures for Active Control of Superconductivity.
B.Pang, R.Tomov, M.G.Blamire
Proceedings of European Conference on Applied Superconductivity, 2003.

Colossal Magnetoresistive Manganite Thin-films for Infrared Detection and Imaging.
M.A. Todd, P.P.Donuhue, P.J. Wright, M.J. Crosbie, P.A. Lane, M.H. Jo, **B.S.H. Pang** and M.G. Blamire.
Annalen der Physik (Leipzig), 13, No. 1-2, 48-51, 2004.

The important thing is not to stop questioning.

Albert Einstein

Acknowledgements

Firstly, I would like to thank my supervisor Dr Mark Blamire for his guidance throughout my PhD. I am glad that amidst all my faffing, there was someone who had the bigger picture of where my PhD was heading. I am also very fortunate to have had the help of various people in the group, who I am sure, by now, are very relieved to hear that I am submitting! 'Please stop hiding from me now!' José Prieto, million thanks for everything, from the many tutorials on magnetics, to captivating an audience with our arguments over free peanuts at the Crown Plaza! Thanks also to Chris Bell, 'the walking encyclopedia', for having an answer to just about everything on this planet, and for the extensive use of his library, to Rumen Tomov for fighting with me over the PLD and for putting up with me during my more stressful times...I'm glad I didn't bet on Bulgaria[1]! To Dennis Leung for admirable patience in face of all my questions. Infinite thanks guys for reading most of this thesis.

I would also like to express my gratitude to the people who have helped me retain some sanity over the years. Thanks to Laura Singh, Ms'M&S', for superseding me as 'black hole', for all the coffee breaks and much-appreciated distractions, and to Dr Debborina Morecroft, P.h.D, M.I.T, F.i.B, A.f.m, for being ever so positive and cheerful, and for unforgettable memories of changing filaments in the...O.A.R! Thanks also to Luis Hueso for clearing my many doubts on physics and manganites, to Karen Yates for plenty of tech/TeX support, to Gavin Burnell for help with Dualscope, and to everyone in DMG who at some point or other pointed me in the right direction. Thanks also to the lunch crew for prying me away from the computer everyday at 1250pm (I still hold the record for lunch at 35pence)!

This thesis would not have been possible if not for the support I have received outside the lab. I would like to express my gratitude to Dad and Mark for their unfailing support, believing in me whatever I get up to. Friends from RI, RJC, and UW whose friendships I have cherished for a long time now, thanks for the words of encouragement which have helped me get through dark endless hours in the lab, and for keeping things in perspective for me.

I wish also to acknowledge Makan Chen and Asea Brown Boveri, Zurich, for funding me through most of my PhD.

BP

[1]For future reference, Sweden 5 Bulgaria 0, Euro 2004!!!

To my mother

Contents

Symbols & Abbreviations

AF	Anti-ferromagnet
AFM	Atomic force microscopy
AMR	Anisotropic magnetoresistance
AP	Anti-parallel
B	Flux density
B_{c1}	Lower critical field
B_{c2}	Upper critical field
BCS	Bardeen, Cooper Schrieffer
CIP	Current in plane
CMR	Colossal magnetoresistance
CPP	Current perpendicular to plane
d	d-spacing, manganite layer thickness in multilayer
d_{crit}	Critical thickness of ferromagnet in multilayers
d_{FM}	Thickness of ferromagnet layer in spin valve structure
d_{NM}	Thickness of normal metal spacer in spin valve structure
d_s	Thickness of perturbed region in superconductor during current injection
d_{spacer}	Thickness of spacer
D	Carrier diffusion constant
D_s	Carrier diffusion constant in superconductor
DBCO	$DyBa_2Cu_3O_7$
e	Electron charge
E	Electric field
E_{ion}	Energy of ion arriving at target
E_{ex}	Exchange interaction
E_k	Energy of an electron with momentum k
EDX	Energy dispersive X-rays
F	Ferromagnet, Lorentz force on vortex
FWHM	Full width half maximum
G	Device gain
GMR	Giant magnetoresistance
h	Planks constant
H	Applied magnetic field
H_{co}	Coercive field
H_{ex}	Mean exchange field
HTS	High-temperature superconductor
I	Insulator
I_{bias}	Bias current
I_c	Superconducting critical current
I_c^+	Upper critical current
I_c^-	Lower critical current
I_{inj}	Injected current
IVC	Inner vacuum chamber

J	Critical current
J_{inj}	Injected current density
k	Momentum
k_B	Boltzmann constant
l_F	Mean free path in ferromagnet
l_{mfp}	Mean free path
l_N	Mean free path in normal metal
L_T	Transfer length
LAO	$LaAlO_3$
LC(x)MO	$La_{1-x}Ca_xMnO_3$
LCO	La_2CuO_4
LNO	$LaNiO_3$
LSMO	$La_{0.67}Sr_{0.33}MnO_3$
M	Magnetization, electron mass
M_s	Saturation magnetization
MH	Magnetization as a function of applied field
MR	Magnetoresistance
MT	Magnetization as a function of temperature
n_{qp}	Quasiparticle density
N	Normal metal
N(0)	Single spin density of states in superconductor
NGO	NdGaO
p	Resistivity of normal metal/majority spin resistivity
P	Parallel
PBCO	$PrBa_2Cu_3O_7$
PLD	Pulsed laser deposition
PR	Photoresist
Q	Activation energy
r_c	Specific contact resistance
rb	Interfacial resistivity
R	Resistance
R_{HF}	Resistance of trilayer in high-field
R_{LF}	Resistance of trilayer in low-field
R_{LCMO}	Resistance of LCMO in trilayer
R_{LSMO}	Resistance of LSMO in trilayer
R_{sq}	Sheet resistance of injector material
R_T	Total resistance of trilayer
R_{YBCO}	Resistance of YBCO in trilayer

S	Superconductor
STO	$SrTiO_3$
t	Number of repeats in multilayer
t_h	Thickness of single crystal
T	Temperature, Transparency
$T(\theta)$	Transmission coefficient at interface for a given angle of quasiparticle trajectory
T_c	Superconducting critical temperature
T_{Curie}	Curie temperature
T_{hm}	Thickness of ferromagnet in spin-valve
T_{hs}	Thickness of superconductor in spin-valve
T_N	Neél Temperature
TEM	Transmission electron microscopy
v	Velocity of flux lines
V_1	Interaction potential of a Cooper pair
V_f	Potential difference between the anode and filament
V_p	Plasma voltage with respect to ground
V_{pa}	Plasma voltage with respect to voltage
V_g	Potential difference between target and source
VSM	Vibrating sample magnetometer
x	YBCO layer thickness
x_{crit}	Critical thickness of superconductor in multilayer
XRD	X-ray diffraction
YBCO	$YBa_2Cu_3O_{7-\delta}$
YSZ	Yittrium-stabilized zirconia

α	$\frac{\rho_\uparrow}{\rho_\downarrow}$, ratio of majority over minority spins
β	Current polarization
δ	Oxygen deficiency in YBCO
δ	Spin diffusion length in manganites
$\delta \mathrm{n}_{qp}$	Excess quasiparticle density
δ_R	Recombination length
δ_s	Spin diffusion length
Δ	Superconducting energy gap
$\Delta \mathrm{E}_{es}$	Exchange splitting energy
ϵ	Error
ε_k	Reservoir energy from which electrons are excited
γ	Proximity effect parameter
γ_b	Transparency factor
$\hbar$	Plancks constant/2π
κ	Ginzburg Landau ratio
λ	Ginzburg Landau penetration depth
λ_w	Wavelength of X-rays
μ	Magnetic moment
$\mu_\circ$	Permeability of free space
μ_B	Bohr magneton
μ_p	Permeability
Φ	Flux quantum
π	Pi
Ψ	Superconducting order parameter
ρ	Resistivity
ρ_F	Resistivity of ferromagnet
ρ_m	Resistivity of manganites
ρ_S	Resistivity of superconductor
$\rho_\uparrow$	Majority spin resistivity
$\rho_\downarrow$	Minority spin resistivity
τ_{eff}	Effective quasiparticle recombination time
τ_R	Recombination time
τ_{sf}	Spin-flip time
τ_{sp}	Effective recombination time due to spin-polarized quasiparticles
θ	Angle between X-ray beam and crystal a-b plane
ν_F	Fermi velocity
ν_{F_N}	Fermi velocity of the normal metal
ξ_{AF}	Anti-ferromagnetic coherence length
ξ_F	Ferromagnetic coherence length
ξ_{GL}	Ginzburg Landau coherence length
ξ_N	Coherence length in normal metal
ξ_S	Superconducting coherence length
χ	Susceptibility

Chapter 1

Introduction

Spin-based electronics, commonly known as spintronics or magnetoelectronics, is an emerging field which fully exploits the quantum nature of electrons. It relies on the electron intrinsic quantity of angular momentum, spin, to perform functions.

In addition to charge, electrons possess an intrinsic magnetic dipole moment and behaves like a miniature bar magnet along its axis of well-defined angular momentums [3]. Spins are either $+\frac{1}{2}$ or $-\frac{1}{2}$, which in a simplistic view, describe their rotation, clockwise or anti-clockwise about their axes with constant frequency [4]. Mainstream charged-based electronics uses ordinary electric currents where electron spins are randomly oriented and play no role in determining the resistance of a circuit. However, the electron spin degree of freedom can be exploited, as the possible spin states naturally represent '1' and '0' in logical operation, to enhance the functionality and speed, and reduce the power consumption [3].

Manifestations of electron spin is most notably found in ferromagnetic metals, where an imbalance of spin populations at the Fermi surface results in a net spin polarization of the charge carriers. Spins, hence, can be injected from a ferromagnetic spin source where the conducting electrons are intrinsically aligned. This spin manipulation is useful for electrical devices. However, an important consideration is to determine how long these electrons remember their spin orientation. If spins relax too quickly, the distance traversed by spin polarized current will be too short for any practical purpose. Research has shown that the spin polarized currents could travel distances comparable to those in modern electronic device structures. The spin diffusion length is 0.1mm in aluminum at 40K [5].

To date, spintronics, in the form of the *giant magnetoresistive effect* has been widely employed in magnetic sensors, in particular by "read-heads" of hard-disk drive. The effective spin injection from a ferromagnet into semiconductors has, however, proven to be difficult due to spin scattering at the interface. LaBella et al have shown that whilst spin injection efficiency, from a single-crystal nickel tip, into gallium arsenide is 92% at the flat terraces, most of the electrons flipped their spins near the steps on the surface [6], emphasizing the sensitivity of spin to interface roughness.

Overview

This project is a more radical approach to spintronics which examines the feasibility of utilising such spin manipulation as a means to control superconductivity, by specifically studying how aligned spins in ferromagnets can directly affect the superconducting state.

This is interesting because the superconductor is a system where the spin balance is rigid. Electron-electron attraction around the Fermi surface in a superconductor, according to the BCS theory of superconductivity, forms Cooper pairs of electrons with anti-parallel spins, thus enforcing an exact balance of spin-up and spin-down carriers in its condensate. This is unlike the parallel-aligned spins in a ferromagnet.

Due to their antagonistic properties, the combination of ferromagnetism and superconductivity has attracted increasing research attention. Spin imbalance, which disrupts the super-

conducting order parameter, can be brought about by spin polarized current injection from a ferromagnet. The project also explores the interplay between ferromagnetic and superconducting oxides in F/S multilayers. Such multilayers can be considered to be artificially structured magnetic superconductors in which the superconductive and magnetic ordering compete. Of particular interest is the capacity to switch a superconductor precisely between states, an important criteria for the employment of superconductors in the field of power electronics.

Materials

The control of superconductivity through magnetic means was studied using cuprate/manganite heterostructures. Compared to metallic films which have been widely studied for F/S proximity effects, oxide F and S films are less explored because of various reasons. Firstly, oxide F and S materials are relatively new discoveries, and the physics of the materials are not as well understood. Also these oxides are more difficult to deposit because of the more complex stoichiometry, and that their properties are usually anisotropic and heavily dependent on epitaxial quality.

However, this project is interesting from an application standpoint because it takes advantage of the recent technological advancements in materials deposition, which has allowed for the effective combination of ferromagnetic and superconducting oxides. Whilst manganites have a high spin polarization and are thus relevant for spin-polarized transport, YBCO is a high temperature superconductor with T_c at 92K and can be maintained at such temperatures using liquid nitrogen instead of the more expensive liquid helium.

Research using cuprate/manganite heterostructures has been focused on spin injection, F/S interaction in bilayers and trilayers, and only very recently, proximity effects in such multilayers.

Outline

An outline of this thesis is as follows:

- Basic aspects of superconductivity and ferromagnetism pertinent to the scope of this research is introduced in Chapter Two. Material properties of $YBa_2Cu_3O_{7-\delta}$ (YBCO) and Lanthanum manganites, is also summarized.

- Chapter Three provides a more detailed insight of the theories of spin injection into superconductors and F/S proximity effects, topics specific to the experimental work. The chapter gives, in relation to the more significant studies performed elsewhere, an overview of the scope of the work done in this thesis.

- Deposition and analysis techniques used are described in Chapter Four.

- Chapter 5 presents the deposition of cuprate and manganite films using the pulsed laser deposition (PLD) systems in the Device Materials Group which was fundamental to this study. The chapter also describes the cleanroom techniques and recipes used for device processing and provides a map of the spin injection device fabrication.

- The effects of spin injection from $La_{0.7}Ca_{0.3}MnO_3$ (LC(0.3)MO) into YBCO was examined in Chapter Six. The chapter also investigates the current behaviour at the device junction interface.

- Chapter Seven examines the feasibility of using cuprate/manganite multilayers for the passive control of superconductivity. Deposition and characterization of these oxide heterostructures by 'eclipse' PLD, together with the variation of the superconducting critical temperature with layer thicknesses in these multilayers is investigated.

- The employment of a ferromagnet/superconductor/ferromagnet spin-valve type structure as a means to control superconductivity is studied in an oxide pseudo-spin valve in Chapter Eight. A summary of the thesis and suggestions for future work is presented in the final chapter.

Chapter 2

Aspects of Superconductivity and Magnetism

2.1 Superconductivity

The definition of a superconductor has been effectively summarized by Poole, C.P [7] as: 'a conductor that has undergone a phase transition to a lower energy state below a transition temperature, T_c, in which conduction electrons form Cooper pairs, which carry electrical current without resistance, and which are responsible for perfect diamagnetism".

2.1.1 Bardeen Cooper and Schrieffer Theory

In 1950, Fröhlich [8] discovered that electron-electron interaction can be transmitted by phonons, and that lattice vibrations were capable of coupling electrons to form the superconducting state.

Cooper [9] followed up by showing that two electrons in the Fermi sea are unstable if there is an attraction, however weak, between them, and will condense into a bound state. These electron pairs are called Cooper pairs. The effective net attraction between the normally repulsive electrons has a pair binding energy in the order of meV, large enough for them to remain paired at low temperatures. The coupling of electrons occur over a range of hundreds of nanometers, three orders of magnitudes larger than the lattice spacing.

The lowest energy or ground state, also known as the condensate, is expected to occur when the total momentum is zero, ie. when all the electrons, having opposite momentum and spin, are coupled together in Cooper pairs. The energy, E_k, required to excite an electron in a Cooper pair to a state k is schematically represented in Figure 2.1, and given by,

$$E_k^2 = \Delta^2 + \varepsilon_k^2 \tag{2.1}$$

where ε_k is the 'reservoir energy' for which electrons are excited. The energy gap, Δ, is the minimum energy required to create an excitation.

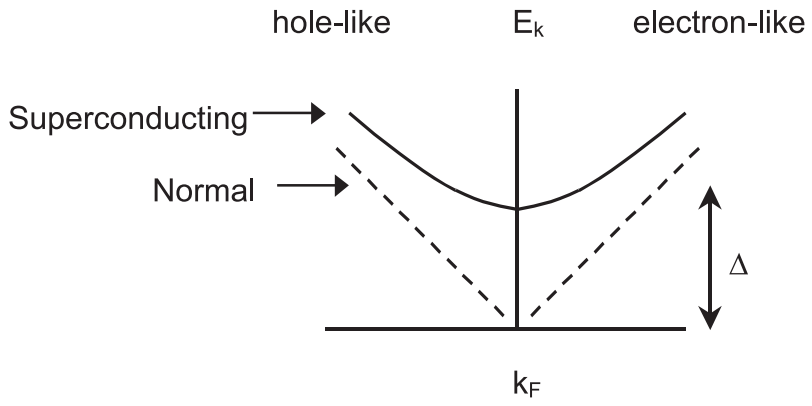

Figure 2.1 Energies of elementary excitations in the normal and superconducting states as a function of k.

Cooper pairs are characterized by the BCS coherence length, ξ_S, a measure of the size of the

pair bound state, which is related to Δ as shown in Equation 2.2. An energy of 2Δ must be supplied to break up a Cooper pair into constituent quasiparticles.

$$\xi_s = \frac{\hbar \nu_F}{\pi \Delta} \tag{2.2}$$

where ν_F is the Fermi velocity.

The BCS approximated equation in which the energy gap caused by thermally modified excited quasiparticles at T>0 is given by:

$$\Delta = V_1 \sum_k \nu_k (1 - \nu_k^2)^{\frac{1}{2}} (1 - 2 f_k) \tag{2.3}$$

where V_1 is the 'negative constant' which represents the interaction potential of a Cooper pair, and $|\nu_k|^2$ and $|u_k|^2$ gives the probability of the momentum pair being full and empty respectively[1]. f_k is the Fermi energy distribution.

At T=0, $\Delta(0)=1.76 k_B T_c$. A good approximation of Δ variation with temperature is such that with increasing temperature, the energy gap remains nearly constant until a significant number of quasiparticles are thermally excited. Δ drops to zero at T_c with a vertical tangent. Close to T_c,

$$\frac{\Delta(T)}{\Delta(0)} \approx 1.74 (1 - \frac{T}{T_c})^{\frac{1}{2}} \tag{2.4}$$

The details of BCS theory apply only to conventional low T_c superconductors. BCS is able to account for properties of low T_c superconductors with respect to the condensation of electron pairs. In high T_c materials, the basic physical mechanism responsible is not yet clear, aside from the fact that two-electron pairing is involved.

Apart from the obvious drop in resistance, superconductors are materials that become perfect diamagnets below their transition temperature, that is, they oppose any existing applied field present, ie. the Meissner effect [10]. They are different from perfect conductors in that perfect conductors will retain their steady state magnetic fields when cooled below their transition temperature, whereas superconductors will exclude their field. The Meissner effect explains why superconductivity is suppressed by a sufficiently large magnetic field, and is thermodynamically reversible in superconductors.

The behavioral exclusion of magnetic fields from the body of a superconductor can be used to classify superconductors into the two fundamental types: Type I and Type II.

2.1.2 Type I and II superconductors

The superconductivity in a Type I superconductor is modeled effectively by the BCS theory. The characteristic parameters which distinguishes Type I superconductors from Type II are the Ginzburg-Landau coherence length, ξ_{GL}, and the penetration depth, λ.

[1] In the ground state, $|u|^2+|\nu|^2=1$

ξ_{GL} is described as the region over which the superconducting wavefunction penetrates the normal region. The London penetration depth, which refers to the exponentially decaying magnetic field (due to the external applied field) at a superconductor surface, is temperature dependent as shown:

$$\lambda = \lambda_\circ / [1 - (T/T_c)^4] \tag{2.5}$$

where $\lambda_\circ$ is the penetration depth at T=0 K.

The ratio of λ / ξ_{GL} is called the Ginzburg - Landau (GL) ratio, κ.

The penetration depth in a Type I superconductor is always smaller than its coherence length, such that $\kappa < \frac{1}{\sqrt{2}}$. A Type I superconductor, when cooled to below its T_c will exhibit zero dc electrical resistance and perfect diamagnetism, if the value of the applied field is less than its critical field (H_c). The superconductivity ceases abruptly above H_c.

However, if the GL ratio exceed 0.70, the total magnetic energy at the surface would be negative. The penetrating flux will tend to break up into the maximum number of flux lines, increasing the normal / superconducting interface area. The minimum flux is a single quantum, $\Phi_\circ$ = h / 2e. This process of subdivision will proceed until the coherence lengths of the flux lines overlap, ie. flux density is limited by the applied field as well as ξ_{GL}.

Each flux line is surrounded by a screening superconducting current which is required to screen the bulk of the superconductor from the flux, hence forming a vortex. The superconducting order parameter goes to zero along the axis of the vortex where the magnetic field is maximum, as illustrated in Figure 2.2. The flux vortices will repel one another, arranging themselves into a triangular array, which has the lowest free energy.

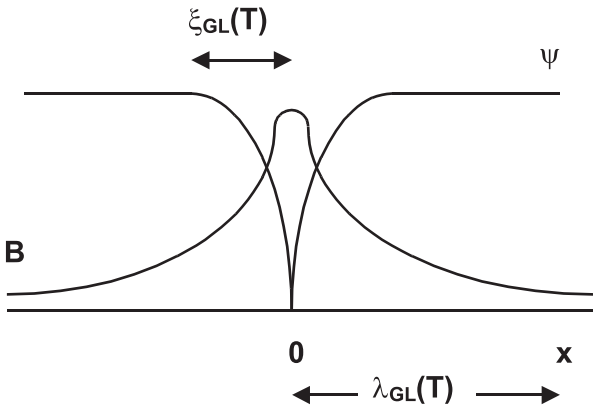

Figure 2.2 Structure of an isolated quantized vortex, showing spatial variation of B and Ψ.

Thus, in a Type II superconductor, there is a gradual penetration of flux at a lower critical field (H_{c1}). This flux reaches B = H at H_{c2}, beyond which the material ceases to superconduct. This region between H_{c1} and H_{c2} is the mixed state of the Type II superconductor, a schematic of which is shown in Figure 2.2. The partial penetration of the magnetic field lowers the dia-

magnetism energy, which holds the field out. Due to this, H_{c2} can be much greater than the thermodynamic critical field, H_c.

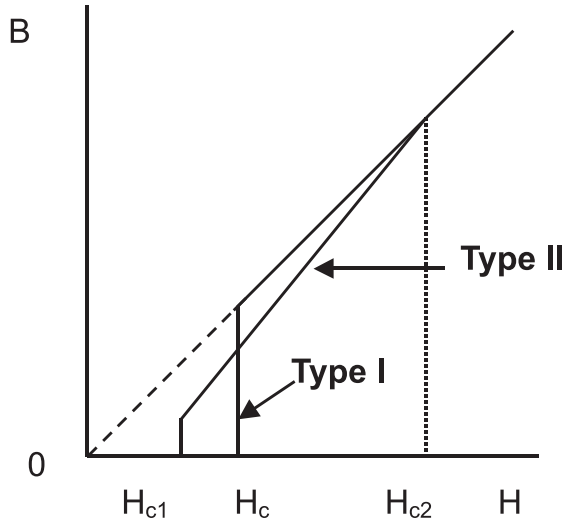

Figure 2.3 Difference in behaviour between Type I and II superconductors to applied magnetic field, H [11].

A summary of the characteristics of Type I and Type II superconductors are shown in Figure 2.3. Type I superconductors usually consist of elements, while alloys and compounds, such as $YBa_2Cu_3O_{7-\delta}$, which we use in our spin injection heterostructure, make up Type II superconductors.

2.1.3 Flux flow and pinning effects

In the presence of a current density, J, in the superconductor, the flux lines experience a Lorentz force, tending to move them in a direction perpendicular to both the magnetic field and the current. The Lorentz force density is:

$$F = J \times B \tag{2.6}$$

where B is the flux density. This flux motion will induce an opposing electric field of magnitude, E = B × v (v being the velocity of the flux lines), in the superconductor which increases the resistance of the superconductor. In an ideal homogeneous superconductor, this flux motion is resisted only by a viscous drag. In the flux flow regime, a resistivity, ρ_f, comparable to ρ_n (the flux flow resistivity of the material in normal state) is observed.

When H is aligned obliquely to the a-b plane in YBCO, a 'kinked' vortex forms.

However, in real materials, some inhomogeneity 'pins' the vortices, so that there is essentially no resistance in the superconductor until a finite current is reached, when the Lorentz force on the flux line exceeds the pinning force. Pinning occurs when there are local variations of ξ, λ

Table 2.1 Summary of the common classification of magnetic materials.

Classification	Susceptibility, χ	Description
Diamagnetic	-10^{-5}	Magnetic response opposes the applied field
Paramagnetic	10^{-3}-10^{-5}	Magnetization is weak but aligned parallel with direction of applied field
Ferromagnetic	50-10 000	Spontaneous magnetization in zero applied field, atomic magnetic moments align parallel to each other
Anti-ferromagnetic	small, positive and temperature-dependent	spontaneous magnetization in zero field, atomic magnetic moments align anti-parallel

or H_c due to impurities, grain boundaries and voids. It is energetically more favorable for the core of the vortex to sit on an impurity or defect which is not superconducting, as opposed to having to drive a superconducting region normal. Inhomogeneity in the scale of ξ or λ have the largest pinning effects [2].

When the magnetic field is reversed, it has been noticed that the vortices remain trapped at the pinning sites until new vortices with the opposite field direction enter the superconductor and the pairs mutually annihilate.

2.2 Ferromagnetism

The response of a magnetic material to an external magnetic field can be represented by two quantities:

- permeability, $\mu_p = \frac{B}{H}$, where B is the flux density in the material and H is the applied field.
- susceptibility, $\chi = \frac{M}{H}$, where M is the magnetization of the material.

Magnetic materials can be classified according to their susceptibility to an external field. A list of the common magnetic classifications of materials is shown in Table 2.1.

As shown in the table, ferromagnetic materials have susceptibility values usually in the range $\sim$ 50 - 10 000. Ferromagnets exhibit spontaneous magnetization. Such materials have magnetic moments in the absence of a magnetic field. Above the transition temperature, also known as the Curie Temperature (T_{Curie}), spontaneous magnetization vanishes. Application of a small field usually produces a magnetization in the material which is many orders of magnitude larger than that produced in a paramagnetic specimen. Magnetization of the entire sample is the sum of all

[2] Inhomogeneity on the atomic scale cause electron scattering instead which reduces the mean free path.

the magnetic moments of all the domains. However, in spite of its spontaneous magnetization, the ferromagnet may exhibit no macroscopic magnetization when the applied field is zero. This is because the moments of the domains cancel as they align to minimize the total magnetostatic energy, as will be discussed. Ferromagnetism can be thought to arise from the asymmetry or splitting of the 3d electron bands, which lead to the presence of net spins and hence a magnetic moment.

There are several models to describe ferromagnetism, which is essentially the alignment of spin moments on adjacent atoms.

Weiss mean field model

Weiss introduced the idea that moments interact with one another in a field, called the 'molecular field' apart from the applied field. This 'molecular field' is very large and always parallel to the magnetization.

Weiss also introduced the concept of magnetic domains into which a ferromagnet is divided into, within which the magnetisation is equal to its saturation value. The magnetization in different domains is in different directions, so that the magnetization of a ferromagnetic specimen can be zero. The saturation magnetization, M_s, of the material can be achieved through the alignment of all the domains in the same direction in the applied field. M_s varies with temperature and reaches zero at the Curie temperature, T_{Curie}. The material does not remain saturated when the applied field is removed.

Heisenberg Model

Heisenberg showed that the 'molecular field' was caused by quantum-mechanical exchange forces. The exchange force is a consequence of the Pauli exclusion principle which states that two electrons can only have the same energy if their spins are opposite.

The exchange interaction is described as the energy between the atomic magnetic moments, which tends to align them parallel (Ferromagnetic) or anti-parallel (Anti-ferromagnetic). The Heisenberg expression for the sum of the exchange energies across a material, is given by,

$$E_{ex} = -2J_{ex}S_iS_jcos\phi \tag{2.7}$$

where J_{ex} is the exchange constant, and ϕ the angle between the two adjacent classical spins. If J_{ex} is positive, E_{ex} is minimum when the spin are parallel (Cos ϕ = 1), and maximum when spins are anti-parallel (Cos ϕ = -1). If J_{ex} is negative, the lowest energy state is thus with anti-parallel spins. Spin quantum numbers at atoms i and j sites are represented by S_i and S_j.

Band theory of ferromagnetism

The previous two models of ferromagnetism are based on local moment. However, for most of the $3d$ ferromagnetic materials, magnetic properties are due principally to the spins of unpaired

electrons which are usually in the outer unfilled shells and are unlikely to be closely bound to the atoms. These itinerant electrons fill up the energy band by occupying the lowest energy levels. In a completely filled energy band, all the electron spins will be paired, and hence does not contribute a magnetic moment. In a partially filled energy band, it is possible to have an imbalance of spins which results in a net magnetic moment per atom.

A normal metal such as copper has equal numbers of electrons with up and down spins at the Fermi surface. There is no net moment, and the current-carrying electrons at the Fermi level are thus unpolarized. In a ferromagnetic metal, the half bands are split as represented by the example of Co in Figure 2.4. This leads to spin imbalance at the Fermi level and can also result in a nonintegral number of magnetic moments per atom. This 'exchange splitting' of the up and down spin states lowers the energy of the system. The moment of Co is proportional to the difference between the occupations of the two spin bands available. Although there are also s and p electrons at the Fermi level, a significant proportion of the carriers are the highly polarized d electrons, which thus produce a partially spin polarized current.

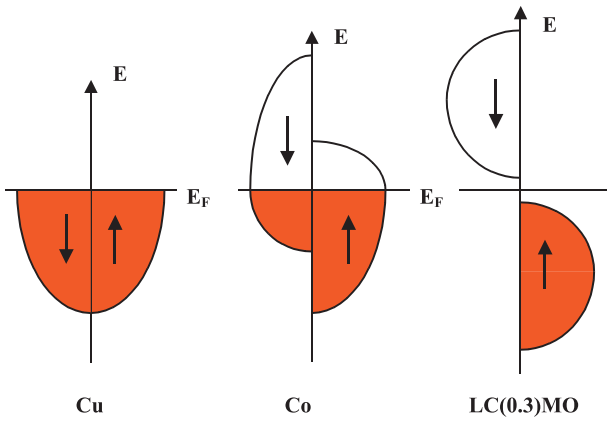

Figure 2.4 Density of states in copper, cobalt and lanthanum calcium manganite.

A larger exchange splitting can lead to a separation between the half bands, as shown by LC(0.3)MO in Figure 2.4. In this case, the spin up band must be filled before electrons can enter the spin down band, and results in an integral number of magnetic moments per atom.

Energy minimization

The total energy of a ferromagnetic material in an applied field is given by the sum of the Zeeman energy, exchange energy (as described in Equation 2.7), anisotropy energies and the magnetostatic energy.

The existence of domains is a consequence of energy minimisation [12]. If the magnetization in a material is homogenous, there would be a high cost of magnetostatic energies due to the formation of free poles at the ends. The magnetostatic energy per unit volume of a dipole of magnetization in a magnetic field is given by,

$$E_{stat} = -\mu_0 \int H.dM \tag{2.8}$$

Domains thus arrange themselves in a way to provide for flux closures, thus minimize the stray field energy, as shown in Figure 2.5. This is provided the decrease in magnetostatic energy is greater than the energy needed to form magnetic domain walls.

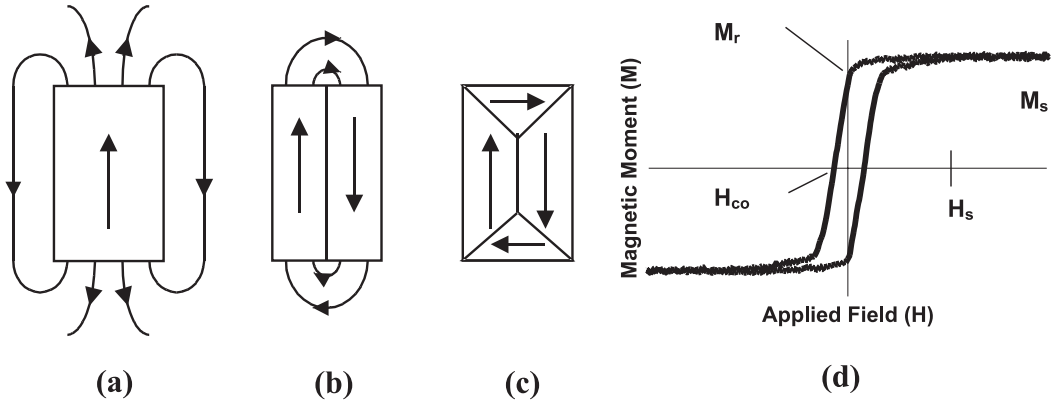

Figure 2.5 Magnetic domains align in such a way as to reduce the magnetostatic energies. (d) shows a typical M(H) loop of a ferromagnet. The saturation magnetization (M_s) is obtained at an applied field (H_s). At M_s, a single domain state is obtained as shown in (a); M_r, remanent magnetization, is obtained when decreasing the field to zero after application of H_s; and the coercive field, H_{co} is the field required to change the sign of M. The corresponding domain state at H_{co} is shown in (c).

The Zeeman energy is due to the interaction between the external field and spin in the ferromagnet and is given by,

$$E_{Zeeman} = -H.M \tag{2.9}$$

The magnetic behaviour of ferromagnets show a dependence on the applied field direction. This anisotropy can significantly affect the shape of the hysteresis loops of the material, and is exploited for commercial applications.

2.2.1 Magnetoresistance

Magneto-resistance refers to the change in resistance of materials when placed in a strong magnetic field. Some materials, particularly the 3d transition metal oxides, exhibit this behaviour which is associated with a paramagnetic-ferromagnetic phase transition. The degree of magnetoresistance in a material is calculated as a percentage as shown:

$$\%MR_H(T) = \frac{R_0(T) - R_H(T)}{R_0(T)} \times 100 \tag{2.10}$$

Where $R_0(T)$ and $R_H(T)$ are the resistances of the material at temperature T, without and with the presence of an applied field respectively.

Magneto-resistance is well known in permalloy, $Ni_{0.8}Fe_{0.2}$. The magneto-resistance effect in permalloy is small, $\sim 2\%$ MR, and anisotropic (AMR). *Anisotropic magnetoresistance* is defined as the resistivity change as a function of the angle between current and magnetization. Low field magnetoresistance data of a high-quality LC(0.3)MO epitaxial film is shown in Figure 2.6. The longitudinal (current parallel to magnetization) resistivity has a maxima while the transverse (current perpendicular to magnetization) resistivity shows a minima at the coercive fields. The %MR associated with AMR is typically a few percent ($\sim 5\%$ at room temperature for a $Ni_{70}Fe_{30}$ alloy.)

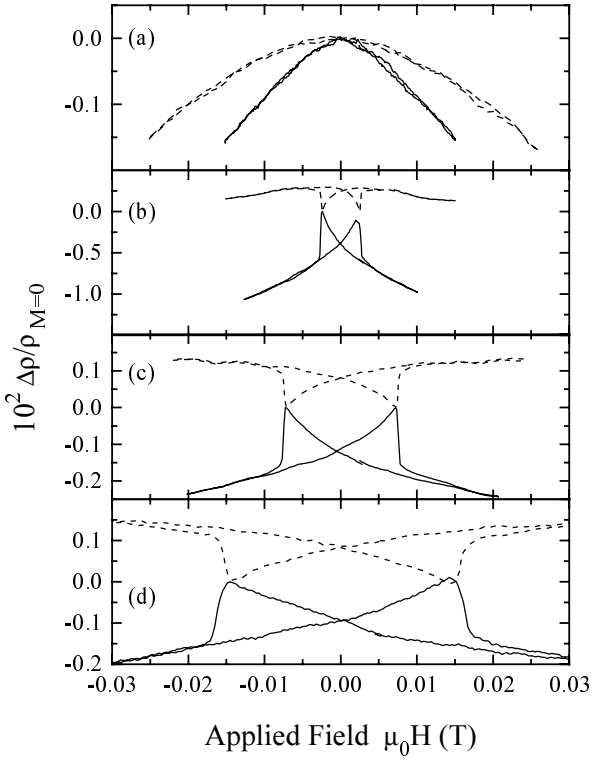

Figure 2.6 AMR observed in $La_{0.7}Ca_{0.3}MnO_3$ films deposited on $SrTiO_3$ substrates. The longitudinal (solid lines) and transverse (dashed lines) magnetoresistance of the sample was measured at (a) 285.3K, (b) 264.1K, (c) 201.3K and (d) 96.1K by Ziese et al [13].

Another type of magnetic-resistance is observed mainly in alternating layers of ferromagnetic (FM) and non-magnetic (NM) films, is *giant magnetoresistance* (GMR) which will be discussed in the following section. GMR can reach 220%MR and increases with the number of layers, up to a maximum.

Colossal magneto-resistance (CMR) effects were discovered in mixed-valence manganites with perovskite structure, $R_{1-x}A_xMnO_3$ where R is a rare earth ion and A is a divalent alkaline. Investigations into this effect, which is also evident in pyrochlores (eg. $Tl_2Mn_2O_7$ and spinel, eg.

$FeCr_2S_4$) compounds, have been mainly conducted around manganese perovskite compounds, $T_{1-x}D_xMnO_3$, where T is a trivalent lanthanide cation (eg. La) and D is a divalent cation (eg. Ca, Sr or Ba). $La_{1-x}Ca_xMnO_3$ is one such compound and is also of particular interest as it is used as our spin injection source. The fundamental physics of the CMR effect is yet to be completely understood. CMR materials possess a uniquely high spin-polarization of conduction electrons, and is important for the study of spin polarized transport. Above T_{Curie}, the resistivity behaves like that of a semiconductor but below T_{Curie}, metallic behaviour is evident.

Giant magnetoresistance

Giant magnetoresistance was discovered by Baibich et al [14] in Fe/Cr multilayers. The %MR in that case was 50% at 4.2K. The GMR effect can be understood by considering the change in electron scattering as the ferromagnetic layers are moved from parallel to anti-parallel alignment, as illustrated in Figure 2.7. The two spin channels are subjected to different degrees of scattering leading to a difference in the resistivities. The magnetic layers thus act as a spin filter. The resistivity of the material is the parallel sum of the two spin channels.

The degree of scattering of a particular electron spin channel is proportional to the density of states of the corresponding spin at the Fermi surface, as given via the Fermi's Golden rule. For homogenous layers, spin scattering is primarily at the interfaces [15]. Hence, the more scattering interfaces an electron interacts with, the stronger the spin filtering effect. However, magnetic defects, such as impurities, within the interior of a film can also contribute to measurable spin scattering.

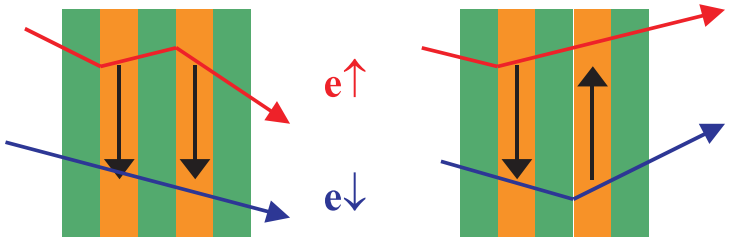

Figure 2.7 Paths of majority and minority spin electrons through a GMR multilayer, with the F layer aligned parallel and antiparallel. In the parallel configuration, the up spin electrons experience more scattering than the down spin electrons. Both spin channels however experience the same spin scattering in the anti-parallel case. The green and orange layers represent spacer and ferromagnetic layers respectively. Red and blue arrows represent the spin up and spin down channels respectively.

It was discovered later that the GMR effect oscillated with spacer thickness as shown in Figure 2.8. The GMR effect can be measured in two configurations: current-in-plane (CIP) where the electric field is applied along the plane of the film, and the current perpendicular to plane (CPP) geometry where the electric field is applied orthogonal to the film. The CPP geometry yields larger effects because there is no shunting of the current through the normal metal spacer layers. All the current must undergo spin scattering at every interface to traverse

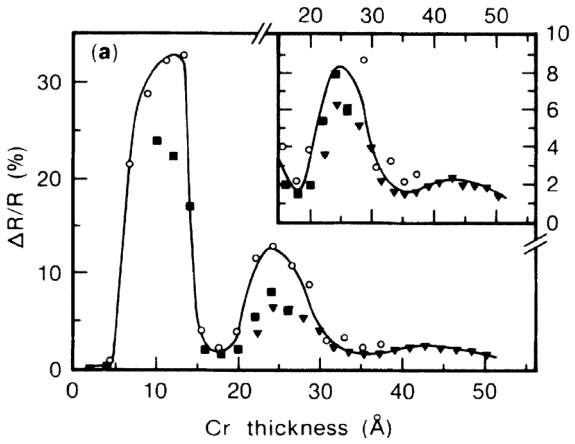

Figure 2.8 Oscillation of the GMR with Cr spacer in a $[Fe_{2nm}/Cr_t]_N$ multilayer with N=20 for open circles and 30 for closed circles [16]. The 1^{st} AF peak, where the alternating F layers couple antiferromagnetically occurs at $\sim$ 1nm spacer thickness, followed by a region of F coupling and a 2^{nd} AF peak at $\sim$ 2nm. The strength of the AF coupling decreases with spacer thickness such that 3^{rd} order AF peaks have only been observed for systems with strong coupling such as Fe/Nb [17].

the layered structure. The GMR effect is widely used in read-heads based on 'spin-valves'.

Spin valves

A simple spin valve consists of two F layers which rotate from anti-parallel to parallel alignment. The AP configuration of the two F layers can be achieved through exchange bias. In this case, an antiferromagnet, when grown adjacent, pins one F layer. The surface spins of the AF layer couple with those of the F layer. This coupling results in a bias field associated with the 'pinned' F layer which allows the F layers to be switched from the parallel to anti-parallel configuration when the external field decreases from saturation field, H_s to -H_{co}. The different H_{co} values of different materials can also be exploited in spin-valves (pseudo-spin valve). The softer F layer aligns with a relatively small field, while the harder material remains unswitched. The higher resistance anti-parallel state can thus be achieved.

In spin valves, the spacer layer is relatively thick to prevent the F layers from coupling, and thus preventing them from switching at the same field. However, when the spacer layer, used in the CIP configuration, is of much lower resistance compared to the F layers, a thicker spacer layer may result in the current being shunted. This will lead to a decrease in %MR.

2.3 Materials

2.3.1 Yttrium Barium Copper Oxide, $YBa_2Cu_3O_{7-\delta}$ (YBCO)

Arguably, the most commonly used HTS, for experimental purposes, is YBCO. YBCO was discovered in 1987 by Wu et al. It has a critical temperature of 93K, higher than that of liquid

nitrogen which occurs when δ is approximately 0.1. YBCO, like all superconductors with a T_c greater than 50K, is a perovskite cuprate. Cuprate superconductors are layered compounds, typically tetragonal or orthorhombic.

2.3.2 Crystal Structure

The basic crystal structure of YBCO is presented in Figure 2.9.

Each unit cell contains three cubic blocks (FCC) on top of each other, in the c direction. If fully oxygenated, ie. $\delta = 0$, the material is orthorhombic and its lattice parameters are as follows: a = 3.83 , b = 3.88 and c = 11.68 (c is approximately 3×a or 3×b).

The copper and oxygen atoms in the planes above and below the yittrium atoms form the copper-oxide planes along the a and b directions. These planes are believed to carry the superconducting Cooper pairs. The charge carriers are localized in the planes, which enhance anisotropy in the structure, with poor conduction in the c direction. However, the copper oxide

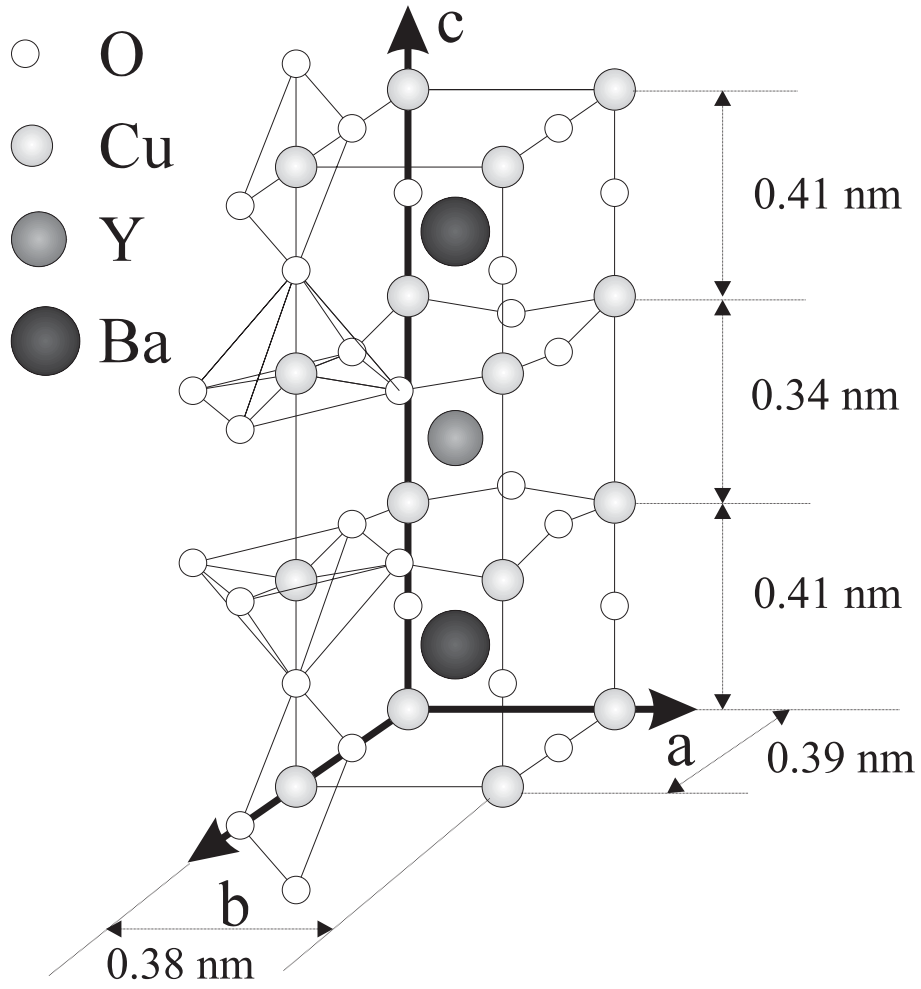

Figure 2.9 Crystal Structure of YBCO [18]

planes are "linked" by copper-oxide chains which act as the binding slab in between the alternate conducting slabs. These chains make YBCO less anisotropic than other HTS because the chains act as hole reservoirs allowing limited electron hopping between copper oxide planes.

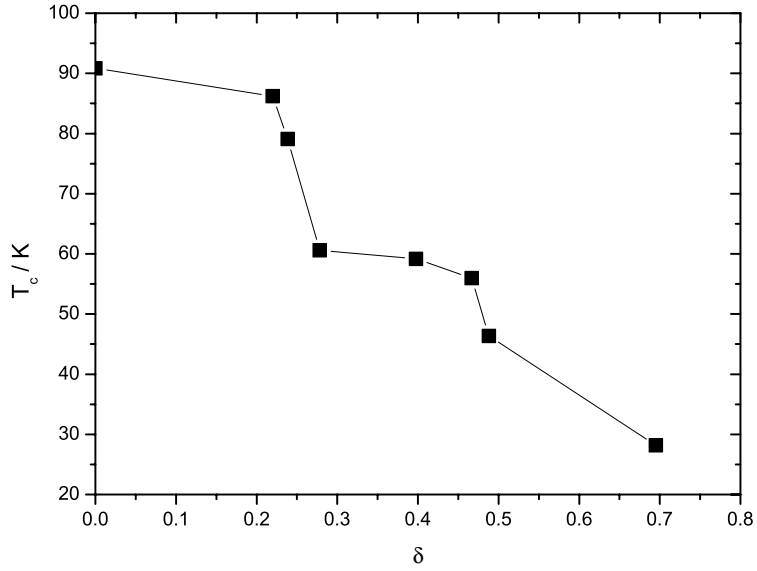

Figure 2.10 T_c vs oxygen deficiency, δ, of $YBa_2Cu_3O_{7-\delta}$ [19]

.

The oxygen content in YBCO directly influences the quality of the material. Figure 2.10 shows the decrease in critical temperature of YBCO with a decrease in oxygen, ie. δ increases. If δ is smaller than 0.7, the crystal structure of YBCO exist in orthorhombic phase, whereas, if d is greater than 0.7, YBCO is more deoxygenated and exists in its non-superconducting tetragonal phase. Hence, growth in low O_2 partial pressures result in the tetragonal system with a = b. Evidently, YBCO, like all cuprates, is very sensitive to carrier doping and is only superconducting for a particular range of doping levels. The phase stability of YBCO is shown in Figure 2.11.

The diffusion of oxygen in YBCO is highly anisotropic. It was found that, at 300°C, the diffusion constant is 2×10^{-12} cm^2/s in the b-axis, 10 times smaller in the a-axis and at 10^4 to 10^6 times smaller in the c-axis [22].

2.3.3 Anisotropy in YBCO

As reflected in their crystal structures, HTS are highly anisotropic. For YBCO, the anisotropy ratio, $\rho_c/\rho_{ab} = 150$ (where ρ_c and ρ_{ab} are the resistivity values in the c and ab directions), which is small compared to that of other HTS, such as $Bi_2Sr_2CaCu_2O_8$ where $\rho_c/\rho_{ab} = 5600$. This

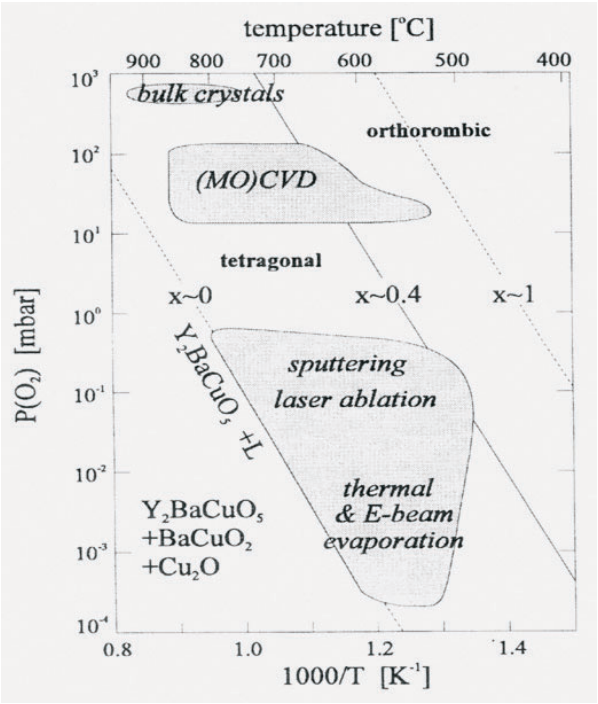

Figure 2.11 Phase stability diagram of $YBa_2Cu_3O_{6+x}$. Also indicated in the diagram are the typical deposition conditions for different common YBCO deposition techniques [20, 21].

lowered anisotropy is due to, as previously mentioned, the Cu-O chains which link the Cu-O planes throughout the YBCO.

This anisotropy extends into other properties as well, such as critical fields, penetration depth, coherence length as summarized in Table 2.2.

Anderson and Zou [23] suggested a mechanism for out-of-plane transport. They propose that the charge carriers for the normal state are hole bosons which are confined to the CuO_2 planes. These hole bosons merge with spin excitations to form physical electrons which tunnel to adjacent planes. Anisotropy is 56-110 at 290K and increases to 120-150 at T_c. The observed resistivity along the a-b and the c- directions are linked by the below equations:

$$\rho_{ab} = A_{ab}/T + B_{ab}T \rho_c = A_c/T + B_cT \tag{2.11}$$

where A and B are constants.

However, Cooper pairs remain as the fundamental carrier in HTS, as proven by Gough et al [24], who showed that flux was quantized in units of h/2e, ie. suggesting that the carriers have the charge of Cooper pairs.

The carrier density in YBCO is relatively low and thus the carriers are less heavily screened than those in normal metals. The interaction between the carriers is low and the penetration depth is high for current flow in the a-b direction. The penetration depth in the a-b plane for YBCO and other HTS also varies in different directions, according to the energy gap. The pair

Table 2.2 Summary of YBCO properties, as taken from Poole et al [25].

Properties	Symbol	Values along the a-b plane	Values along the c direction	General values %
Critical Temperature	T_c			92K
Resistivity at 100K	ρ(100K)	70 - 250 $\mu\Omega$cm	9 - 18 mΩcm	
Resistivity at 290K	ρ(290K)	180 - 550 $\mu\Omega$cm	11 - 21 mΩcm	
Critical density of current at 77K	J_c (77K)			5×10^6 A/cm^2
Critical density of current at 4.2K	J_c (4.2K)			6×10^7 A/cm^2
Penetration Depth	λ	26 - 260 nm	125 - 550 nm	
Coherence Length	ξ_s	1.2 - 4.3 nm	0.2 - 0.8 nm	
Lower Critical Field	B_{c1}	5 - 18 mT	53 - 520 mT	
Upper Critical Field	B_{c2}	110 - 240 T	29 - 40 T	B_{c2}: 120 - 200 T
Energy Gap	$2\Delta_0$			30 meV

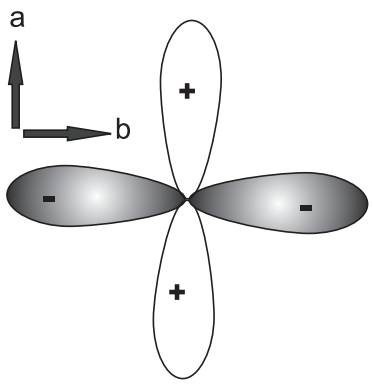

Figure 2.12 Amplitude and phase of the gap parameter with $d_{x^2-y^2}$ symmetry relative to the crystallographic directions a and b.

function in the a-b plane has a $d_{x^2-y^2}$ symmetry [26] which means that the order parameter is zero in some directions of the crystal as illustrated in Figure 2.12. This variation of the energy gap may be an important consideration in spin injection devices as it determines the path of least resistance for the injected quasiparticles.

The low carrier density and the fast relaxation times associated with high temperature superconductors are expected to result in fast devices with high gain [27]. Hence, high temperature superconductors have potential for the realization of superconducting devices with transistor-like characteristics above liquid N_2 temperatures. They are also attractive materials for such transistor devices because of their compatibility with colossal magnetoresistance (CMR) materials.

2.3.4 Lanthanum-based Manganites, LaXMnO$_3$

Crystal Structure

It was discovered in 1994 that around temperatures at which $La_{1-x}A_xMnO_3$ changes from paramagnetic to ferromagnetic, the application of a magnetic field of the order of 6T could produce an MR $> 99.9\%$ [28].

The parent compound of the manganites, $LaMnO_3$ (shown in Figure 2.15), is an antiferromagnetic insulator with Mn having a valence of 3^+ [29]. If between 10-50% of the La^{3+} ions are replaced with divalent ions such as Sr^{2+}, Ca^{2+} or Ba^{2+}, the resistance drops dramatically and the material becomes ferromagnetic, as shown in the phase diagram in Figure 2.13. The Curie temperatures, T_{Curie}, range from 100K to almost 400K, depending on the concentration of the Mn^{4+} ions and the particular element substituted.

In LCMO systems, the Ca^{2+} ions introduced replace the La^{3+} ions. The extra electron present in the Ca outer shell will force the Mn^{3+} ion to loose one. Thus, the number of Mn^{4+} introduced into the system equal the number of Ca^{2+}. Hence, the chemical formula for LCMO can be re-written as $La^{3+}_{1-x}Ca^{2+}_xMn^{3+}_{1-x}Mn^{4+}_xO^{2-}_3$.

Transport

The mechanism relating transport and ferromagnetism within the manganites is double exchange (DE). Double exchange theory, as proposed and developed by Zener [30], describes the hopping of electrons in the e_g orbitals between neighbouring Mn^{3+} and Mn^{4+} sites, with corresponding Hund's coupling by O^{2-} ions in-between.

The Mn^{3+} ion contains four outer electrons, three of which exist within a valence band t_g^2 while the fourth resides in an itinerant band, e_g. This itinerant electron is absent in Mn^{4+}, and the outer electrons are all contained within the t_g^2 orbital. Whenever, an Mn^{3+} and an Mn^{4+} ions are on neighbouring sites linked by an oxygen anion, electrons can hop from the Mn^{3+} onto O^{2-} and from O^{2-} onto Mn^{4+}. This is because the energy level of the oxygen $2p$ orbital and the manganese e_g orbitals are similar [31].

If a 2p electron from the O^{2-} ion jumps into an empty e_g state in the Mn^{4+} ion, an electron of the same spin, hops from an adjacent Mn^{3+} ion into the hole left by the first electron. This process is repeated as the O^{2-} ion moves across the interatomic space to the first Mn^{3+} ion. The Mn^{4+} ion has both e_g states empty, thus allowing the neighbouring oxygen ions to move into its space. The lattice compensates for this by pointing the occupied orbitals towards the Mn^{4+} ions, facilitating the double exchange mechanism. Without violating Hund's law, it is energetically favorable for hopping if the spins on adjacent Mn ions are aligned. Hence, conduction will most easily occur if the material is ferromagnetic, and will tend towards the insulating state if the material is paramagnetic or antiferromagnetic.

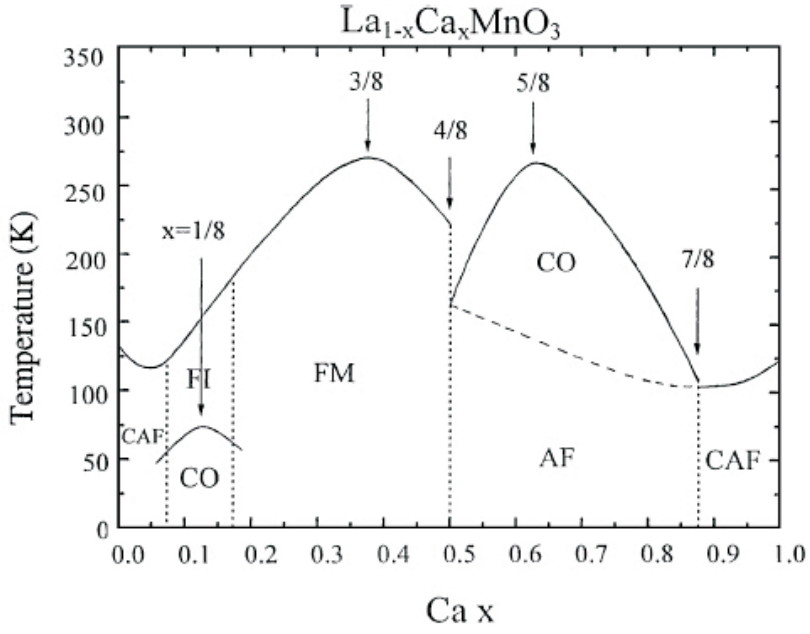

Figure 2.13 Phase Diagram of $La_{1-x}Ca_xMnO_3$ [32]. FM: Ferromagnetic Metal. FI: Ferromagnetic Insulator. AF: Antiferromagnet. CAF: Canted Antiferromagnet. CO: Charged Ordering

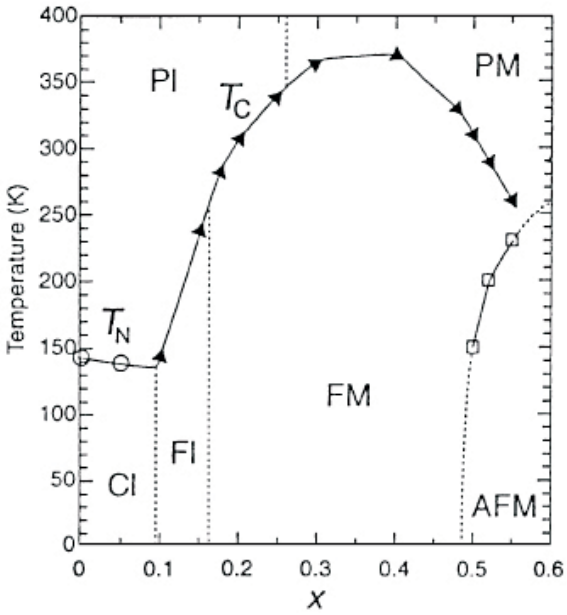

Figure 2.14 Phase Diagram of $La_{1-x}Sr_xMnO_3$ [32]. FM: Ferromagnetic Metal. FI: Ferromagnetic Insulator. AF: Antiferromagnet. PM: Paramagnetic Metal. PI: Paramagnetic Insulator. CI: Spin Canted Insulator. T_c: Curie Temperature. T_N: Neel Temperature.

Double exchange only happens when the doping concentration is large enough (about 0.2). Below this, the concentration of Mn^{4+} is too low and there are insufficient carriers. As more holes are introduced into the parent compound in the form of A^{2+} or oxygen vacancy, there are more charge carriers, the resistivity should decrease until a point where the number of holes exceeds that desirable for transport. The composition reverts to an insulating state when x is above 0.5. Most of the Mn ions are in the d_4 configuration, and double exchange cannot take place. Hence, for each dopant, there is a doping range over which ferromagnetic behaviour occurs. Outside this range, other behaviours such as charged-ordered insulator or anti-ferromagnetism occurs. The optimum doping level for the CMR effect is at x = 0.33. Phase diagrams of LCMO and

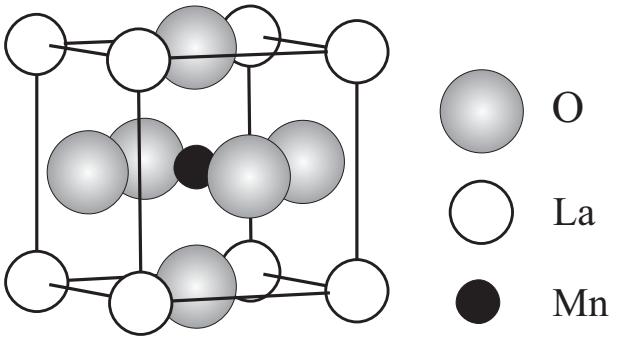

Figure 2.15 Perovskite crystal lattice of $LaMnO_3$

LSMO are shown in Figures 2.13 and 2.14 respectively. In the ferromagnet phase, a magnetic field can be applied to the sample to increase the ferromagnetic transition temperature T_{Curie}, and also the paramagnetic to metallic transition temperature T_p by increasing the conductivity via increased hopping probability of itinerant carriers. However, double exchange theory cannot explain the sharp decrease in resistivity at the ferromagnetic transition.

Chapter 3

Ferromagnet / Superconductor Interaction

3.1 Motivation

The coexistence of superconductivity and ferromagnetism is of relevent interest to the scope of this thesis and will be discussed in this chapter. The chapter gives an overview of spin injection into superconductors by discussing it in terms of non-equilibrium induced in the superconductor through the injection of excess quasiparticles, and how the spin parameter increases this effect on superconductors. The chapter also examines how proximity effects in F/S junctions lead to a decay in the superconducting order parameter, and hence the T_c. Reviews of the significant observations and developments done in these areas are presented and discussed in relation to the work on oxide F/S heterostructures studied here at Cambridge.

3.2 Non-Equilibrium Superconductivity

According to the BCS theory, the superconducting ground state consists of Cooper pairs with equal and opposite momentum and spin. At T>0, thermal energy will break Cooper pairs into quasiparticles with energies greater than the pair binding energy. In the equilibrium state, the rate at which thermal energy breaks up Cooper pairs is balanced exactly by the quasiparticle recombination rate.

Non-equilibrium can be induced by the addition of energy. For instance, the change in the energy distribution of its quasiparticle population can alter the superconducting state [33]. The quasiparticle distribution function described by the Fermi function:

$$f_k(E) = \frac{1}{1 + \exp \frac{E-u^*}{k_B T_e}} \tag{3.1}$$

where T_e is the electronic temperature and u* is the effective chemical potential.

Combining the Fermi function describing the quasiparticle probability distribution with the BCS energy gap (Equation 2.3) [34], it has been shown that the quasiparticle distribution function directly affects the energy gap:

$$\ln(\frac{\Delta(0)}{\Delta}) = \int_0^\infty \frac{N(E,\Delta)f(E,T)}{E} dE \tag{3.2}$$

where N(E,Δ) denotes that the density of states of the superconductor is dependent on the energy and the energy gap.

The excess quasiparticles in superconductors which suppress the energy gap, also reduce the critical current of the film. A sufficiently high density can suppress the order parameter to zero. The exact energy distribution of quasiparticles and phonons, however, is complicated because it depends on several parameters, such as the energy distribution of quasiparticle excitation rates, the phonon-to-quasiparticle and quasiparticle-to-phonon transition rates, phonon lifetimes, and the elastic scattering rates for quasiparticles and phonons.

When the perturbing source is removed from the system, the non-equilibrium state relaxes. Excited quasiparticles can decay through phonon emission into lower energy states. The excess

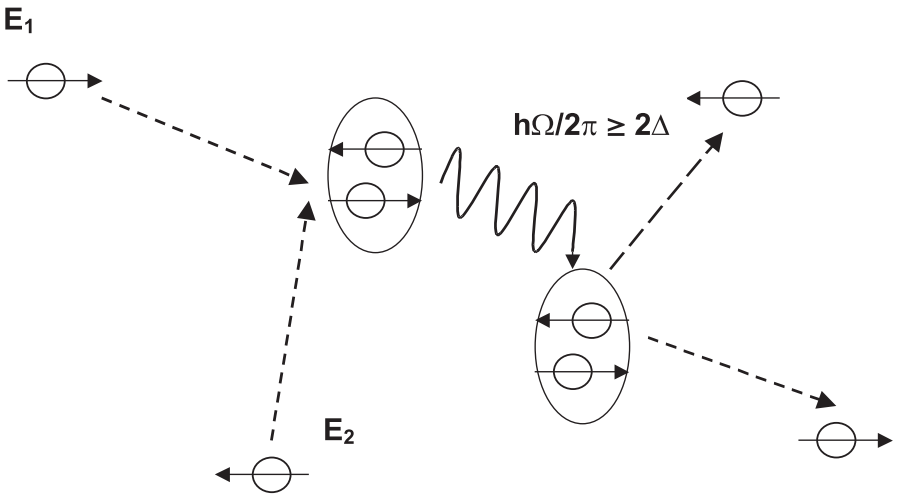

Figure 3.1 Two quasiparticles with energies E_1 and E_2 can form a Cooper pair in its ground state through a phonon emission, $\hbar\Omega = E_1 + E_2$. The minimum phonon energy is 2Δ. These phonons can subsequently be reabsorbed to break up a Cooper pair into two quasiparticles.

quasiparticles will recombine and whilst doing so, emit phonons of energies greater than the 2Δ, which can cause further pair breaking effects, as illustrated in Figure 3.1. These phonons will eventually escape through the surface, such as into the insulator substrate, without reabsorption, or thermalize within the superconductor. Phonons can also be reabsorbed by quasiparticles, but only at high quasiparticle densities, eg. at $T \sim T_c$.

The introduction of the non-equilibrium state in superconductors is a central part of investigations involving quasiparticle injection into superconductors. The injector can be a superconductor or a normal metal in the case of ordinary particle injection, while spin injection involves the use of a magnetic injector. The following sections examine current injection into superconducting thin films devices.

3.2.1 Ordinary Particle Injection

This section discusses, from a different perspective, non-equilibrium induced in the superconductor specific to current injection and excess quasiparticles. Although the equations used here to explain the effects of quasiparticle injection [27] were derived and applied for conventional s-wave superconductors, they serve to provide a better understanding of the d-wave HTS spin injection device behaviour[1].

Consider current injection into a normal metal/superconductor (N/S) junction. Excess quasiparticle density (number of quasiparticles (N) per volume) is proportional to the injected current in the equation,

[1]However, it should be noted that in addition to the nodes in the gap function of a d-wave superconductor, HTS also have a finite quasiparticle density at low temperatures.

$$\delta n_{qp} = \frac{J_{inj}\tau_{eff}}{ed_s} \tag{3.3}$$

where δn_{qp} represents the excess quasiparticle density, J_{inj} is the injected current density, I_{inj} / A where A is the N / S contact area, and assuming uniform injection over the contact, τ_{eff} is the effective quasiparticle recombination time, e represent the electron charge, and d_s is the thickness of the perturbed region.

The excess quasiparticles can cause uniform perturbation of equilibrium superconductivity if the film is sufficiently thin, i.e. if the film is thinner than the quasiparticle recombination length in a superconductor, which is defined by,

$$\delta_R \sim \sqrt{D_s\tau_{eff}} \tag{3.4}$$

where D_s is the carrier diffusion constant.

For a thick film, the superconductivity is only perturbed near the injection source to a depth of δ_R.

As shown in the previous section, the superconducting order parameter decreases monotonically with increasing quasiparticle density, n_{qp}, in an S/N junction for example, as illustrated by the equation below [35]:

$$\frac{\Delta(n_{qp})}{\Delta(0)} \cong 1 - \frac{2n_{qp}}{4N(0)\Delta(0)} \tag{3.5}$$

where $\Delta(n_{nq})$ is the perturbed energy gap, and N(0) is the single-spin density of states in the superconductor.

Equations 3.3 and 3.5 combine to give the following equation [27], which shows that the superconducting energy gap in a thin film decreases with increasing injection current.

$$\frac{d\Delta}{dJ_{inj}} \cong -(\frac{\tau_{eff}}{2eN(0)d_s}) \tag{3.6}$$

where d_s is the thickness of the superconducting film.

Equations 3.3 and 3.6 show that both the excess quasiparticle density and the gap suppression vary linearly with τ_{eff}, which is temperature dependent as shown in equation 3.7. In the case of ordinary quasiparticle injection, $\tau_{eff} \approx \tau_R$.

$$\tau_R \cong \tau_0(\frac{\Delta(T)}{kT})^{\frac{1}{2}} \exp\frac{\Delta(T)}{kT} \tag{3.7}$$

where τ_0 is a characteristic spin relaxation time associated to electron-phonon coupling strength. From 3.7, τ_R, which is the recombination time, is material and temperature dependent.

The above equation holds true because τ_{eff} increases exponentially at lower temperatures due to the exponential decrease in the number of available thermal quasiparticles with which to recombine [36]. At low temperatures, τ_{eff} is long, the rate of suppression of Δ with I_{inj} increases. This is indicative that the gain of injection devices increases with decreasing temperature [37].

τ_{eff} is also expected to increase slightly as T_c is approached but these effects are small [38].

According to the Ginzburg-Landau theory, the superconducting critical current is monotonically related to the order parameter, $J_c \propto \Delta^3$. This facilitates the use of critical current as a measure of the order parameter.

3.2.2 Spin-polarized quasiparticle injection

τ_{eff} and thus non-equilibrium effects in superconductors can be further enhanced with the injection of spin-polarized electrons. This is because the spin balance in a superconductor is rigid. According to the BCS model, singlet Cooper pairs require the exact balance of spin-up and spin-down carriers. Hence, during spin injection, quasiparticle recombination in the superconductor must be preceded by spin-flip, τ_{sf}. Hence, with the addition of the spin degree of freedom, $\tau_{eff} \approx \tau_{sf} + \tau_R$, which is represented by τ_{sp} (the effective recombination time due to spin-polarized injection).

Spin injection is achieved by passing a current from a ferromagnet into a superconductor. Electrons are spin polarized in the ferromagnet due to the splitting of the density of states. This polarization decays monotonically with distance away from the interface. Spins can relax through exchange coupling with other electrons in the vicinity of magnetic atoms or via spin-orbit coupling to impurity atoms or defects. In the absence of these influences, the orientation of the carriers' spins may be very long-lived, although carriers may undergo numerous scattering events [39].

The superconducting order parameter, which is perturbed near the interface, regains its bulk value over the quasiparticle spin diffusion length,

$$\delta_s = (D_s \tau_{sp})^{\frac{1}{2}} \tag{3.8}$$

In the equilibrium state, the polarized current is constantly adding net spin to the perturbed region, while relaxation, which occurs at a rate of $1/\tau_{sf}$, prevents spin accumulation. The non-equilibrium that results is a imbalance between the source and sink processes [40].

In summary, spin-polarized current injection causes pair breaking in superconductors via 2 mechanisms, through raising the effective, non-equilibrium temperature (present also in ordinary quasiparticle injection) which weakens the quasiparticle pairing interaction, and through exchange interaction between itinerant spin polarized quasiparticles with quasiparticles present in the superconductor, which results in spin-flip scattering [41].

Temperature Dependence of τ_{sp}

Near T_c, an injected carrier should recombine rapidly regardless of its spin due to the higher thermal background. τ_{sp} should not differ very much from τ_R. At low temperatures, however, the thermal quasiparticle density becomes negligible in s-wave and very small in d-wave materials, represented by the following [38].

$$n_{qp}(T) \cong 4N(0)\Delta(0)(\frac{\pi}{2}\frac{\Delta(T)k_BT}{\Delta(0)^2})^{\frac{1}{2}} \exp -\frac{\Delta(T)}{k_BT} \tag{3.9}$$

Thus, well below T_c, there is a larger perturbation of the superconducting order parameter due to spin-polarized injection compared to ordinary quasiparticle injection. Hence, in line with equation 3.7, the amount of suppression of the order parameter due to spin-induced non-equilibrium effects is dependent on temperature.

It is important to note that although it is true that τ_{sf} increases at low temperature, hence causing a larger suppression of the order parameter, the superconducting energy gap also increases with decreasing temperature, as explained in Section 2.1.1. The stronger order parameter at lower temperatures is thus in direct competition with the increasing spin-induced non-equilibrium. Hence, taking advantage of the lower energy gap at close to T_c, most investigations into HTS (shown in the Table A.1) have been performed at higher temperatures (ie. $\sim$50-90K).

3.2.3 Transport across F/S interface

We have based our F/S interface model on the presumption that the transport in oxide systems is similar to that in metals. The complications, on the micro-scale, associated with electron site-hopping in these perovskites were not addressed.

On the microscopic level, the transport across the F/S interface can occur through 2 main channels: a) Andreev reflection, which is dominant for transport below the superconductor energy gap, and b) spin diffusion whereby aligned electrons with energy greater than the energy gap cross into the S layer.

Andreev reflection is a phenomenon which occurs at the N/S interface. An incident electrons with less energy than the gap is retro-reflected as a hole while a Cooper pair carries the current into the superconductor. This is the process whereby normal current is 'converted' to supercurrent at the N/S interface.

Andreev reflection should be sensitive to the polarization of the conduction electrons in the F layer, since not every electron from the 'up' spin can find a 'down' spin electron with which to pair. Such electrons will thus not be able to enter the superconductor [42]. At a perfect manganite/YBCO interface at 0 K, Andreev reflection cannot occur because of the 100% spin polarization of manganites. The reverse is also true, ie. a Cooper pair experiences no pair breaking effect at the F/S interface because a hole of the minority spin will not exist within F. Hence, the perfect interface at 0 K will have no transparency. At $T > 0$, spin-aligned electrons with energy larger than the superconducting energy gap can diffuse into the superconductor, thus causing a reduction in the order parameter. The pair breaking effects extend over the spin diffusion length, $\delta_s = (l_{mfp}\nu_F\tau_{sf})^{0.5}$. where l_{mfp} is the electron mean free path and τ_{sf} is the spin-flip time of the quasiparticle [10]. The length scales associated with spin diffusion is thus larger than that of Andreev reflection because the spin diffusion time of the spin-aligned quasiparticles is an added dimension. We expect spin diffusion to be the predominant cause of

pair breaking effects at the F/S interface.

3.3 Spin Injection Devices

As discussed 3.2.1, the I_c is typically investigated in spin injection devices incorporating high temperature superconductors. From the current-voltage (IV) characteristics of the superconductor as shown, for instance in Figure 6.5, we can obtain the I_c using equation 3.10. The value of the I_c obtained in this equation excludes any current offsets caused by current summation effects as will be discussed in Section 3.14.

$$I_c = \frac{I_c^+ - I_c^-}{2} \tag{3.10}$$

where I_c^+ and I_c^- are the maximum and the minimum biased current, I_b, at zero voltage.

The gain, G, of the device is a measure of its response to injected current.

$$G \equiv -\frac{dI_c}{dI_{inj}} \tag{3.11}$$

the minus sign is included to make the device gain a positive value.

We expect the gain to be proportional to the quasiparticle recombination time. Hence, the gain increases in magnitude with decreasing temperatures.

In the following sections, we discuss several important parameters essential for the experimental design of spin injection devices [27].

3.3.1 Current Polarization

The efficiency of spin injection devices depends on the extent of polarization of I_{inj}. This is, in turn, directly dependent on,

1. The intrinsic polarization of the magnetic material. Permalloy has a maximum polarization of $\sim 40\%$. Half-metallic ferromagnets, LSMO and CrO_2, have been ideal choices of injector materials for YBCO because they carry 100% spin polarized current, and are also more compatible for deposition and processing with YBCO. Point-contact experiments [43] have shown that the LSMO, below 9K, has a polarization of $78\pm40\%$, while interestingly, that of CrO_2 is $90\pm3.6\%$.

2. The amount of depolarization across the boundary. A reduction in the spin polarization as a result of spin glass formation due to the interdiffusion or oxygen vacancies can occur at the F/S interface. In the case when spin injection is injected from the F to the S layer across a barrier layer, spin-flip events can also occur at defects in the barrier layer. Hence, a thinner barrier would introduce less spin scattering.

As discussed in Section 3.2, direct quasiparticle injection also causes suppression of the superconducting order parameter. This has been demonstrated by Schneider et al [44], who

showed a device gain of up to 15 at 81K and estimated it to be 20 at 77K in YBCO/STO/Au current injection devices. Hence, it is necessary to isolate the polarization effects as the cause of I_c suppression observed in spin injection devices.

3.3.2 Length Scales

The *transfer length*, L_T, is the finite length at the device injector junction (N/S or F/S) over which current is injected into the supeconductor.

$$L_T = (\frac{r_c}{R_{sq}})^{\frac{1}{2}} \tag{3.12}$$

where r_c is the specific contact resistance (Ωm^2), and R_{sq} is the sheet resistance of the injector material. $R_{sq} = \rho/\text{thickness}$. A more resistive interface, represented by a larger r_c will lead to a longer L_T.

Hence, CMR/HTS junctions have small transfer lengths because a) the junctions have low barrier resistances due to the small lattice mismatch of the materials, and b) CMR materials have relatively high resistivity. Junctions with shorter transfer lengths would have a higher local excess quasiparticle density, and hence a larger effect due to current injection.

The *diffusion length* as mentioned in Section 3.2.1, is directly related to the diffusion constant of a material. The a-b plane carrier diffusion constant, D, in YBCO, can be determined from its resistivity.

$$\rho = \frac{1}{2e^2 N(0) D} \tag{3.13}$$

where N(0) is the single spin density of states, and D is the carrier diffusion constant.

Using values as suggested by Gim et al [27], $2N(0) = 3 \times 10^{22}$ eV^{-2} cm^3 and $\rho = 100\mu\Omega$ [45], D is esimated to be $2cm^2/s$. This means that when τ is 1ns, the diffusion length is $1\mu m$. The spin diffusion length, δ_s (see section 3.2.2), which also takes into account the spin flip time (τ_{sf}), has been estimated to be approximately 0.5 μm in silver [46], and $1.2\mu m$ in gold [47]. These length scales are important considerations for spin injection device fabrication.

For spin-polarized current injection, we also have to consider the *magnetic domain size*. If the recombination length is larger than a single domain, opposite spins from adjacent domains may average out and recombine, hence reducing the effects of spin injection [2].

3.3.3 Device Geometry and Current Summation Effects

The most common investigations on spin injection into superconductors have been performed on thin film devices. In these devices, current is injected via a ferromagnet into a superconductor whilst the I-V characteristics of the superconductor is measured. All devices incorporating

[2] As a rough estimate, the magnetic domains in an $La_{0.77}Sr_{0.23}MnO_3$ film grown on $SrTiO_3$ substrate are several tens of microns [48].

perovskite manganite/cuprate heterostructures performed thus far employ the use of in-situ film deposition.

In-situ deposition of films is particularly crucial in metallic systems because most metals oxidize and form an insulating oxide layer when exposed to the atmosphere. In perovskite systems, this deposition process would also correspond to good quality interfaces between individual layers as there is a much lower probability of introducing a foreign element between layers. Poor interfaces can result to undesirable spin scattering which in turn reduces the efficiency of spin polarized current injection. However, the main limitations of in-situ deposition are that the devices cannot be patterned and processed using microelectronic techniques into smaller dimensions essential for spin injection studies (which will be elaborated further in the following sections), and that there is less versatility in device design to facilitate current injection from various direction.

Due to these limitations associated with in-situ deposition, investigators have employed the following device geometries in the study of spin injection into superconductors. The device geometries are studied with respect current summation in the *absence* of non-equilibrium effects caused by the introduction of spin-polarized electrons. To improve clarity of the figures, a colour scheme for the following device illustrations is shown in the Figure 3.2.

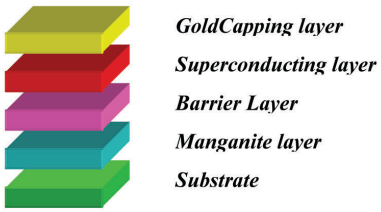

Figure 3.2 Legend for the following schematics of various device geometries used in spin injection device investigations.

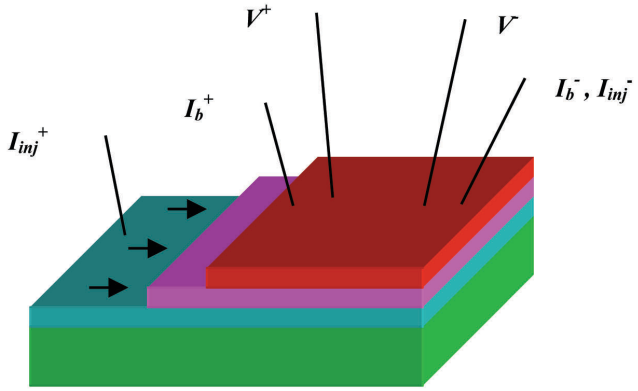

Figure 3.3 3-Terminal "inline" Device Geometry

Illustrated in Figure 3.3 is the 3-Terminal (3T) inline device geometry where current is injected (I^+_{inj}) through a bottom manganite electrode into the superconductor. Current is injected near one end of the superconductor and exits, together with the bias current (I_b), from the opposite end of the superconductor electrode.

The transfer length, L_T, varies depending on the materials' properties. Assuming that L_T is shorter than the distance of I^+_b from the edge of the superconducting film, the current in the superconductor, I_s is:

$$I_s = I_b + I_{inj} \tag{3.14}$$

Using this geometry, assuming no current losses to heat and, more importantly, no non-equilibrium effects, the critical current of the superconductor can be predicted by equations 3.15 and 3.16. Using ac measurement currents, I^+_c and I^-_c values are determined by the smaller current values, in either current direction, at which critical current is reached.

$$I^+_c = I^0_c - I_{inj} \tag{3.15}$$

$$I^-_c = -I^0_c - I_{inj} \tag{3.16}$$

where I^0_c is the critical current of the device without current injection.

Hence, using equation 3.11, we can expect the gain of such devices to be 0 in the absence of non-equilibrium effects.

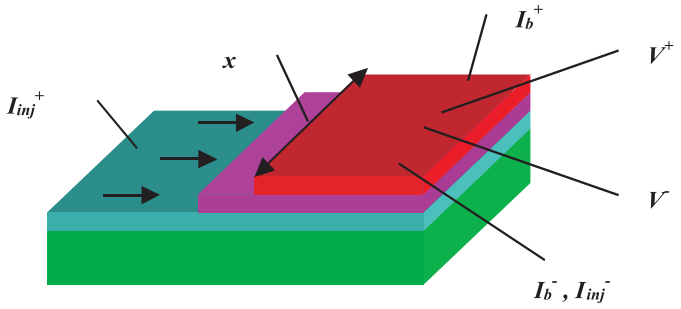

Figure 3.4 3-Terminal "side" Device Geometry

The current injection as shown in Figure 3.4 is spatially non-uniform, that is, the amount of current injected into the superconductor layer varies with the distance away from the edge of the superconductor. $I_s = I_s(x)$ where x is the position along the length of the superconductor.

Assuming uniform current injection along the entire length, L, of the superconductor, and that the superconducting strip is sufficiently narrow that the injected current at any point x along its length flows across its cross-section,

$$I_s = I_b + I_{inj}(\frac{x}{L}) \tag{3.17}$$

Hence, similar to equations 3.15 and 3.16,
At the common electrode,

$$I_c^+ = I_c^0 - I_{inj}; I_c^- = -I_c^0 - I_{inj} \tag{3.18}$$

At the other electrode,

$$I_c^+ = I_c^0; I_c^- = -I_c^0 \tag{3.19}$$

Following equation 3.10, I_c of the device, using the smaller I_cs in either current direction, is:

$$I_c = \frac{I_c^+ - I_c^-}{2} = \frac{2I_c^0 - I_{inj}}{2} = I_c^0 - \frac{I_{inj}}{2} \tag{3.20}$$

Hence, the gain of 3-Terminal "side" injection devices is 0.5 without any non-equilibrium effects.

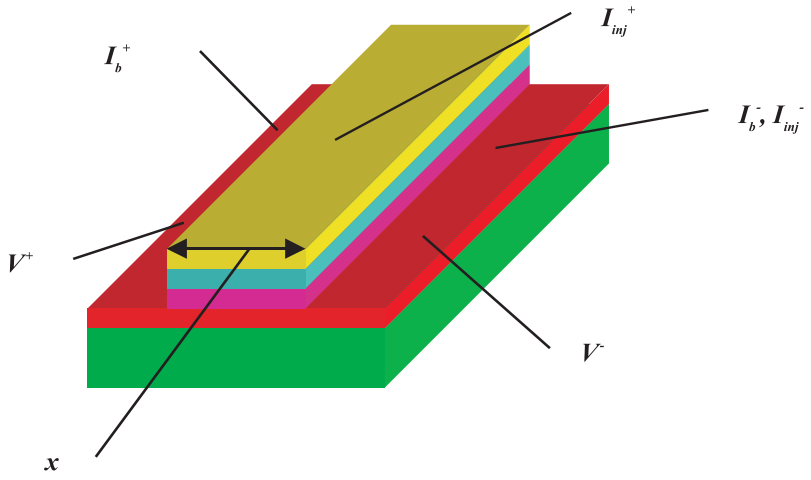

Figure 3.5 3-Terminal "top" Device Geometry

The 3-Terminal "top" device geometry shown in Figure 3.5 is similar to the 3-Terminal "side" geometry in that current injection into the superconductor is spatially non-uniform. The current at a particular point, x, in the superconductor under the manganite varies linearly with its distance along the width of the manganite strip, similar to that represented in equation 3.17. The gold capping layer is a low resistance material used to distribute the injected current uniformly throughout the width of the ferromagnetic track.

A significant advantage of the 3-Terminal "top" geometry over the "side" geometry is that it is easier to obtain superconducting films of thicknesses in the nanometer scale than it is to pattern a top superconducting film layer into a track nanometers wide. As the spin diffusion lengths in high-temperature superconductors is estimated to be shorter than 1 micron, the "top"

injection geometry would be more useful. It is more likely that the entire cross-section of the superconductor at the point of current injection is perturbed in the "top" geometry case.

The gain in the 3-Terminal device geometry is 0.5 without non-equilibrium effects.

The final device geometry is the 4-Terminal device geometry as shown in Figure 3.6.

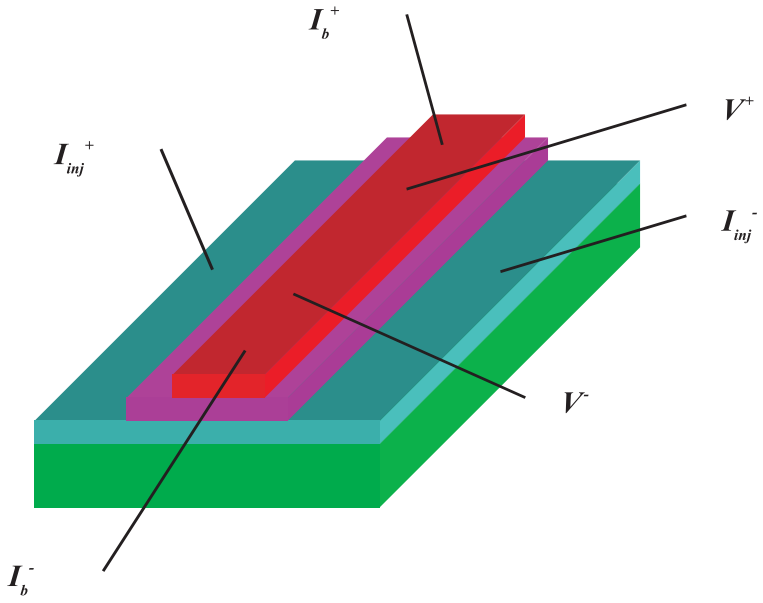

Figure 3.6 4-Terminal Device Geometry

For measurements on devices which use the 4-Terminal geometry, there is no shift in the IV curve. Due to the preferred c-axis growth of YBCO, it is impossible to inject current along the a-b plane of the superconductor for samples with films deposited in-situ. In addition, for such geometries, an external voltage cannot be applied across the F/S junction, and hence, according to our definition in Section 3.2, current injection is not possible.

As I_{inj} is perpendicular to I_b, it is possible that when $I_{inj} > I_c$, the flux vortices in the superconducting track experience a net Lorentz force directing them along the length of the track, between the voltage contacts. Hence, a finite voltage is sensed. This happens even if I_b is small.

It is essential, thus, to take into account the different device geometries used by various investigators when reviewing spin injection experiments. Up until current summation effects of differing device geometries were highlighted by Gim et al [27], device gains were mostly attributed to spin injection or localized heating. A knowledge of the device geometries and their corresponding current summation effects has enabled the effective comparison of the very different investigations performed in various research groups, and the reliability of the results obtained.

3.3.4 Spin Injection through Barrier layers

In many of the device geometries of the investigations performed on high temperature superconductors thus far, barrier layers are deposited in between the ferromagnetic and the superconducting films. Barrier layers are used to inhibit cation diffusion between layers, hence chemically protecting the superconductor. The barrier layer also aids in the distribution of current more uniformly throughout the interface. An insulating layer would be more effective for current distribution. As suppression of superconductivity occurs at weak links, an insulating barrier layer will ensure that the injected current will reach the weak links and not be completely shorted through the better quality regions. Metallic barrier films, such as gold, have been used to prevent the formation of spin glass phase at the interface which will lead to spin scattering at the interfaces [49]. According to Lee et al [50], a minimum of 10nm of Au was required in between YBCO and Co in order to avoid YBCO degradation.

Current injection through the F/S junction can occur through tunnelling, capacitive coupling or defects such as pinholes or grain boundaries [51]. Capacitive coupling is a charge-based current transfer across the interface. As no current actually flows through the junction during capacitive coupling, the spin is not preserved through the interface. Hence, spin injection occurs in various degrees via tunnelling and defects across the F/S junctions. The degree of tunnelling at the junction depends on the thickness and transport properties of the interface barrier material.

3.3.5 Local Heating

Localized heating at the device junctions is a major issue in most spin injection experiments performed thus far. Heating occurs when current is injected through the device circuitry, the amount of which is related to the energy equation, $E = I^2Rt$. When examining the spin injection devices, the superconducting tracks will be superconducting but the resistances of the ferromagnetic and barrier layers are still relatively high as the films are usually only tens of nanometers thick.

An increase in temperature of a superconductor suppresses its superconductivity. As localized heating during current injection in devices is almost impossible to detect, it is difficult to attribute any measured effects during current injection solely to non-equilibrium effects induced by excess spin polarized quasiparticles.

Investigators have used a number of approaches to eliminate localized heating as the cause of the observed I_c suppression:

- The most common experimental design is to compare current injection from a ferromagnetic and a non-magnetic injector layer of similar structural and thermal properties [50, 52, 53]. In all these experiments, the I_c suppression observed in the superconducting layer is greater with the ferromagnetic injector layers. Although this method is a reasonable control to exclude heating effects, the choice of control samples have introduced other discrepancies.

The relative quality of the interfaces between the oxide superconductors or barrier layers with the different injector layers has always been a source of concern. It has proven to be very difficult to compare two devices, F/S and N/S, to isolate spin injection effects due to the different resistivities associated with different materials. Even very similar devices like those of Dong et al [52] have questionable comparisons because the resistivity of LNO is about three times lower than that of NSMO. This difference resulted in a difference of 19% (of sample length) in the transfer lengths of both samples.

- Devices with varying barrier thickness have also been studied. Devices with thicker insulating barrier layers were found to have smaller gains [53, 52], despite an increase in resistance and, hence, heating effects. The decreased I_c suppression effects here have been attributed to increased spin scattering through the thicker barrier layer.

- Pulsed injection current has also been used to reduce the effects of heating. Gains have been observed for current pulsed lengths of 200μs. Such pulse periods yielded a negligible temperature rise of <10mK. During the pulsed period, the temperature of the sample is raised, reaching a maximum value at the end of the pulse, and dropping quickly at the end of the pulse to the initial value [54]. Mikheenko et al argued that above 100ms, the suppression of I_c is dominated by heating. Pulses shorter than 100ms show only a weak effect on the superconducting state.

- To reduce direct heating, investigators can also opt for smaller injector microbridge widths. A smaller I_{inj}, and hence input power, is required to produce the same current density in the device junction.

3.4 A Review of Spin Injection into HTS

The use of perovskite manganites and high-temperature cuprate superconductors for spin injection studies has gained popularity for various reasons: a) technology has enabled the deposition of manganite/cuprate with little reaction at the interface, which leads to enhanced spin transfer across these interfaces, b) the potential of high temperature superconductors for various device applications at temperatures above that of liquid nitrogen, c) the short superconducting coherence length of HTS allows the material to sustain superconductivity down to very small thicknesses, and d) the full spin polarization of manganites. Table A.1 provides a brief summary of the more significant spin injection into HTS studies performed by various research groups thus far.

Vas'ko et al [55] published the first evidence of spin injection in HTS. Current was injected from LS(0.3)MO into a 300μm wide $DyBa_2Cu_3O_7$ track, with a gain of 1. Control samples which substituted Au for LSMO showed minimal I_c reduction compared to the former F/S structure. However, the device did not show a temperature dependent I_c suppression with I_{inj}. The I-V characteristics of current injected into the superconductor were also magnetic field independent

(from 10^{-3} to 0.05 T). The control sample used to pinpoint spin injection effects were also very different from the spin injection device.

Better control samples were used by Dong et al [52]. The spin injection experiments were an improvement compared to that by Vas'ko et al [55] because of the smaller device dimension and the inline geometry which allowed the current path to be better defined. The device gain of 5 at 74K was larger than that observed in the control samples. The authors claim that power input of 2W/cm^2 was much lower than the 100 - 1000 W/cm^2 needed to raise the temperature of YBCO by several K to see change in the I_c. Dong argued that heating was not the cause of the I_c suppression because devices with thicker insulating barrier layers were observed to have lower gains (as opposed to larger gains due to increased heating effects). The experiment provided strong evidence of non-equilibrium effects. There were, however, some ambiguity over the difference in the transfer lengths associated with the sample and the control.

Another significant study was performed by Yeh et al [53]. In this investigation, it was argued that the pulsed currents used eliminated the dc joule heating. The pulse width chosen ($\sim$ 200 μs) showed a negligible temperature rise (<10mK) in the YBCO under the maximum I_{inj} of $\sim$ 300mA. The results showed that the Gain of $\sim$ 1 decreased slightly with decreasing temperature close to T_c. Apart from that, the I_c suppression with I_{inj} showed little temperature dependence. Again, the gain was not observed in the controlled sample. The YBCO track had a width of 200μm, which is still very large compared to the transfer length of $\sim$2μm, as estimated by Gim et al [27] for the LSMO/STO/YBCO sample at 4.2K. The transfer length is expected to decrease with increasing sheet resistance and increasing temperatures. Yeh et al estimated the δ_s to be $\sim$80nm close to T_c (at [1-$\frac{T}{T_c}$]$\sim$0.01) and $\sim$10nm as T$\longrightarrow$0.

The turning point of the research of spin injection into HTS was the detailed analysis by Gim et al [27]. The study proved conclusively that all the spin-injection experiments performed till then had been hampered by device geometry effects and inadequate control samples. Unlike localized heating, these were issues which were not widely addressed previously. The study analysed the various device geometries employed and the minimum gain expected due only to simple current summation effects. Based on these models, most of the I_c vs I_{inj} measurements acquired previously failed to show any evidence of non-equilibrium effects. The study also stressed that current gain should increase with decreasing temperature and increasing magnetization.

Negative results were also obtained by Gim et al [27] using LCMO/STO(2nm)/YBCO devices. This was due mainly to geometry effects as the YBCO tracks used were too wide (50μm) compared to their estimated device transfer length of 1μm, meaning that only the edges of the films were perturbed, if at all. The transfer length of a more resistive interface, LCMO/STO(10nm)/YBCO was estimated to be 40μm at 10K. The study, however, provided some insight with respect to heating as a cause of I_c suppression. At 90K, The temperature of YBCO rose by roughly 0.2K for an I_{inj} value of 5mA, and 0.8K for an I_{inj} of 10mA. They noted that the power dissipation with I_{bias} of 5mA was <10W/cm^2, which was very small as thermal effects generally occur at power levels on the order of kW/cm^2, hence concluded that the localized heating was unlikely to be the major problem in most spin injection into HTS

measurements, even with d.c. current injection.

Heating was, however, attributed as one of the two factors of I_c suppression observed with current injection into YBCO grain boundary junctions, as observed by Ireland et al [56] in YBCO/STO/LC(0.3)MO trilayers. The group investigated the effects of current injection from LC(0.3)MO into the region of grain boundary junction, ensuring that the transfer length of 6μm was significant over the device junction widths of 6μm and 10μm. They concluded that the I_c suppression was due to a combination of heating and self-field effects.

Spin injection quasiparticle non-equilibrium in cuprate/manganite heterostructures was observed by Wei et al [41] using cryogenic scanning tunnelling spectroscopy. A spin-diffusion depth of ~20nm along the c-axis and a spin relaxation time, τ_s of ~40ns was estimated.

In the spin injection experiments performed at the Device Materials Group at Cambridge, efforts were made to isolate spin injection effects from other I_c suppression effects, such as localized heating, flux, current summation and ordinary particle injection. In our devices, the maximum YBCO tracks measured was 8μm, significantly smaller than the other geometries previously used. The devices were fabricated through cleanroom processing techniques as discussed in Chapter 5. Unlike all work prior, our devices were fabricated to facilitate current injection into the a-b plane. This is because YBCO is anisotropic and conduction is predominantly along the Cu-O planes. We explored also the dependence of I_c suppression with applied magnetic field, hence using the applied magnetic field to modulate the spin polarization of the injected quasiparticles to induce non-equilibrium in the superconductor.

3.5 Proximity Effects

When the superconductor is in contact with a non-superconducting material, such that the interfacial resistance is low, Cooper pairs will 'leak' into the non-superconducting material. This reduces the number of Cooper pairs in the superconductor near the boundary, as shown in Figure 3.7.

For proximity effects at the S/N interface, the mean free path of the electrons in the normal metal, l_N, determines the form of the coherence length in the normal metal, ξ_N. In the clean limit when the impurity level is low, where $l_N > \xi_N$, the exponential decay in the number of Cooper pairs over the ξ_N, given by,

$$\xi_N = \frac{\hbar \nu_{F_N}}{2\pi k_B T} \tag{3.21}$$

where ν_{F_N} is the Fermi velocity in the normal metal, k_B is the Boltzman constant and T is temperature.

In the dirty limit, where $l_N < \xi_N$, the coherence length becomes a function of the l_N, as shown,

$$\xi_N = \sqrt{\frac{\hbar \nu_F l_N}{6\pi k_B T}} \tag{3.22}$$

The superconductor coherence length, ξ_S is shown in Equation 2.2.

The suppression of the superconducting order parameter in the S layer near the boundary leads to a reduction of the T_c. Hauser et al [57] showed that ferromagnetic films grown in contact with superconducting samples suppress the transition temperature to a much greater extent compared to interfacial contact with a normal metal.

3.6 Superconductivity and Ferromagnetism in F/S Multilayers

To date, there has been extensive research into F/S interaction in metallic multilayer systems. However, there has recently been increasing motivation in studying the interaction in oxide systems. This is due to the interest in the effects of spin quasiparticle injection into cuprate high-temperature superconductors and their potential applications in spin electronics, and also to understand the F/S interaction in layered intrinsic superlattices.

The fundamental difference is that in metallic systems, the short-range spin diffusion length of several nm will confine the interaction effects to regions close to the interface. However, the interaction length in oxides are estimated to be longer [58].

3.6.1 F/S co-existence in intrinsic superlattices

Superconductivity and ferromagnetism can co-exist within some intermetallic compounds, regarded as intrinsic superlattices [59]. For instance, long range antiferromagnetic order has been observed to co-exist with superconductivity in rare earth molybdenum selenides (RMo_6Se_8, where R is Gd, Tb, Er) and in rare earth rhodium borides (RRh_4B_4, R is Nd, Sm, Tm). Also, a re-entrant normal state was observed to be due to long range ferromagnetic ordering discovered in $ErRh_4B_4$ and $HoMo_6S_8$. $RuSr_2GdCu_2O_8$, a ferromagnetic superconductor, has a T_{Curie} of 130 - 140K and a T_c of 20 - 50K. It is thought that superconductivity occurs in the CuO_2-Gd-CuO_2 layers while Ru^{5+} ions contribute to the magnetic properties in $RuSr_2GdCu_2O_8$ [60, 61, 62].

The interplay of magnetic and superconducting properties of such layered compounds has been similarly modelled and studied in superlattices of alternating F/S layers. The F/S close proximity interaction can be studied more effectively in such heterostructures through varying the individual layer properties and thicknesses.

3.6.2 Proximity Effects in F/S structures

In layered F/S systems, the coexistence of superconductivity and ferromagnetism can be studied in a controlled manner, for instance, changing the layer thickness changes the relative strengths of the two competing order parameters, and also, the two antagonistic phenomena within these multilayer structures are separated in space.

We expect the superconducting order parameter in F/S multilayer to be suppressed near the F/S interfaces due to pair breaking effects caused by interactions between the aligned spins in the ferromagnet and the singlet Cooper pairs in the superconductor. Mattheias et al [63] investigated the interaction between the superconducting electrons and the magnetic moments known similar to the exchange interaction between spins in the ferromagnet. The exchange field will tend to align spins of the electrons in Cooper pairs in the same direction. This magnetic ordering is possible in impurites in the presence of superconductivity. The uniform exchange field due to the aligned spins will interact with the superconducting electrons. This interaction will cause a Zeeman splitting of the electron levels. If the Zeeman energy is larger than the superconducting energy gap, superconductivity will be quenched.

This theory suggests that the co-existence of ferromagnetism and superconductivity can occur for weak ferromagnets with a T_{Curie} below the superconducting T_c. The Clogston limit is the point when the field induced by the F layer completely suppresses the superconductivity of the system, and occurs at:

$$H_{ex} = \frac{\sqrt{2}\Delta}{g\mu_B} \tag{3.23}$$

where H_{ex} is the mean exchange field, μ_B the Bohr magneton and g the Landé factor.

This theory may be evident in the re-entrant normal state observed in LC(0.33)MO / YBCO superlattices at the onset of saturation magnetization at T=30K [64].

Anderson and Suhl, however, have shown that ferromagnetic ordering is less likely in proximity to superconducting phases compared to normal ones. The superconducting state causes a negative long-range interaction with a spatial extent of the order of the ferromagnetic coherence length, ξ_F. Hence, modulation of the magnetization is evident to several tens of nanometers [23].

Specific to F/S multilayers, the pair breaking events are localized within the superconducting coherence length, ξ_S, and the ferromagnetic coherence length, ξ_F. Hence, within the Cooper limit (as described in the following sections) the superconductivity in multilayers depends directly on the thicknesses of the individual layers, as described below:

1. In the S layers, pair breaking events occur within the superconducting coherence length, ξ_s, of the F/S interface, which is given by $(\hbar D/k_B T_c)^{0.5}$ where D is the electron diffusion coefficient of the superconductor. The amount of suppression in ξ_s of the S layer is inversely proportional to ξ_F and thus the magnetic properties of the F layer, as linked by the below equations.

$$\xi_F = \frac{\hbar \upsilon_F}{\Delta E_{es}} \tag{3.24}$$

where υ_F is the Fermi velocity and ΔE_{es} is the exchange splitting.

$$\Delta E_{es} = I_{eff}\mu \tag{3.25}$$

where I_{eff} is some effective integral which includes exchange coupling.

ξ_F is smaller for ferromagnets with larger magnetic moments, μ, or exchange interaction, ΔE_{ex}. Comparing two F/S interfaces of the same interface quality, we expect the superconducting order parameter in the S layer to be more suppressed at the interface with a stronger magnetic material, as illustrated in Figure 3.7.

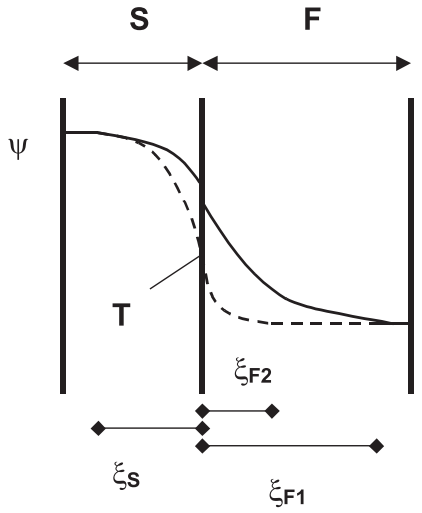

Figure 3.7 Schematic of the superconducting order parameter at the F/S interface. It represents an illustration of the spatial probability of finding a Cooper pair at the F/S interface. The solid line shows the decrease of order parameter in the ξ_S and ξ_F. The dash line indicates the increased suppression at the F/S interface with F2 having a higher magnetic moment. The diagram shows that F2 has a shorter ξ_F and a lower transparency T at the F/S interface.

Therefore, in multilayers with S thickness, d_S, smaller than $\sim 2\xi_S$, the superconducting order parameter in all parts of the S layer will be suppressed. The critical thickness of S, x_{crit}, refers to the S thickness larger than which the superconducting order parameter will not be suppressed.

2. For an F/S interface with the thickness of F, $d_F < \xi_F$, the amount of suppression of the superconductivity in S also depends on the thickness of the d_F.

3. The superconducting order parameter in the F layers exists in ξ_F. Within $d_F < \sim 2\xi_F$, the superconducting order parameters of the two S layers on both sides of the sandwiched F layer overlap. This coupling between the S layers enhances the superconductivity within the multilayers. Thus, with increasing F thickness in the multilayers, the coupling amongst the S layers decreases, resulting in more suppression of the superconductivity. When $d_F > \sim 2\xi_F$, the S layers are decoupled. Beyond this critical thickness, which we refer to

as d_{crit}, the thicknesses of the F layer do not directly affect the superconducting order parameter in the multilayers.

In summary, the superconductivity in a multilayer is suppressed when the S layers are thinner than x_{crit}, and also when the F layers are thicker than d_{crit}. The length scale is defined as the Cooper limit.

3.6.3 Dependence of Proximity Effects on Interface Transparency

At the F/S interface, the order parameter within ξ_S, is affected by interactions at the interface which can be studied with the following parameters.

- The proximity effect parameter, which is a measure of the strength of the proximity effect between F and S is given by,

$$\gamma = \frac{\rho_S \xi_S}{\rho_F \xi_F} \tag{3.26}$$

  where ρ_F and ρ_S are the resistivities of F and S respectively.

- The transparency factor, which describes the effect of boundary transparency is represented by the equation,

$$\gamma_b = (2/3)(l_F/\xi_F)\langle\frac{1-T(\theta)}{T(\theta)}\rangle \tag{3.27}$$

  where $T(\theta)$ denotes the transmission coefficient through the interface for a given angle θ between the quasiparticle trajectory and interface and $< >$ denotes the angle averaging over the Fermi surface. A perfectly transparent interface is represented by $\gamma_b = 0$.

Transparency, T, is related to γ_b [65] in:

$$T \sim \frac{1}{(1+\gamma_b)} \tag{3.28}$$

As mentioned earlier, a more magnetic material with a smaller ξ_F implies that the contribution due to proximity effects at the interface is greater for the system, ie. assuming a constant interface transparency, a smaller ξ_F leads to increased pair breaking effects in the S layer. However, as the probability of Cooper pairs in a more magnetic material is lower, a more magnetic material leads to a lower interface transparency. This in turn reduces the pair breaking effects in ξ_S. These 2 contradicting effects in S which result from a more magnetic adjacent layer are in competition in the F/S multilayers. The effect of ξ_F on the suppression of superconducting order parameter is thus dependent on the dominance of the interface transparency as illustrated in Figure 3.8.

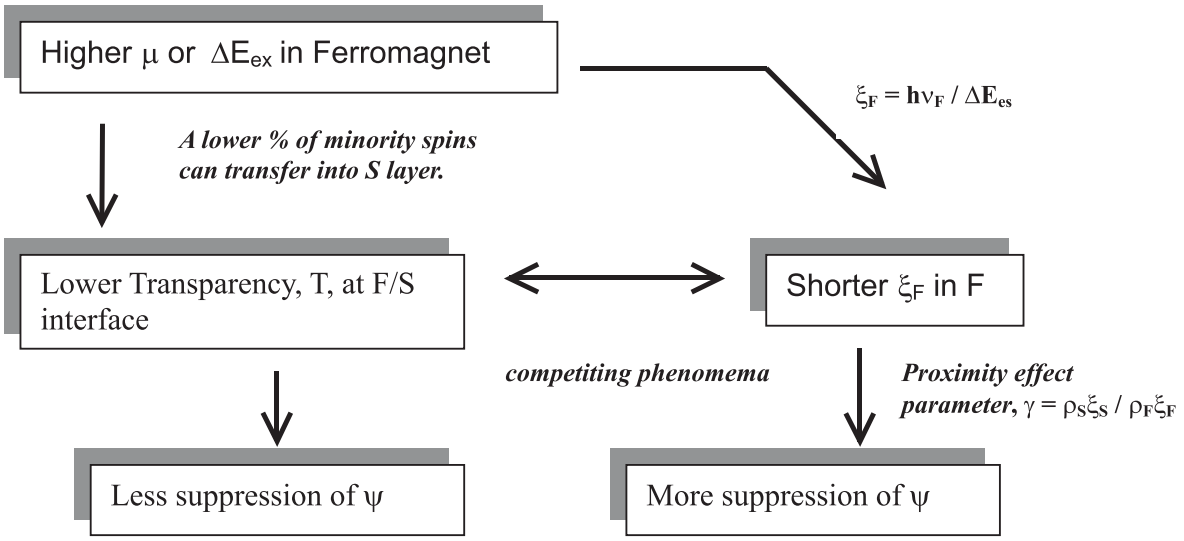

Figure 3.8 Dependency of proximity effects on interface transparency.

3.6.4 Review of F/S metallic structures

As mentioned before, most of the investigations of competing order parameters in F/S multilayers have been done on metallic systems. This is due to several reasons:

- Metallic multilayers with high quality interfaces are in general easier to deposit and reproduce.
- The conventional low temperature superconductors in metallic systems have longer coherence lengths, compared to high temperature oxide systems. The longer length scales allow for enhanced coupling between the S layers, thus resembling more closely the F/S interaction in the intrinsic superlattices. The ferromagnetic effects in the S layers of the multilayers can be observed over a larger range of thicknesses.

Whilst the behaviour of these metallic heterostructures are reasonably well established, the study of multilayer cuprate/manganite F/S behaviour is still in an early stage. A summary of some of the significant proximity studies and results on metallic systems have been tabulated (Table B.1) in order to improve the understanding of F/S behaviour in similar oxide heterostructures covered in this thesis.

Figure 3.9 shows the first evidence of F/S proximity effects from Hauser et al [57]. It plots the superconducting T_c vs S layer thickness, d_s, of an F/S Fe/Pb multilayer, showing the trend of T_c decreasing with d_s. The curve-fits on the plot suggest the accelerated suppression of superconductivity when in proximity with a ferromagnet.

The investigations into T_c suppression with F layer thicknesses in F/S heterostructures, however, have been more complicated due to the contrasting results obtained by various groups. Buzdin et al and Radivic et al have suggested that the superconductivity in S/F multilayers is

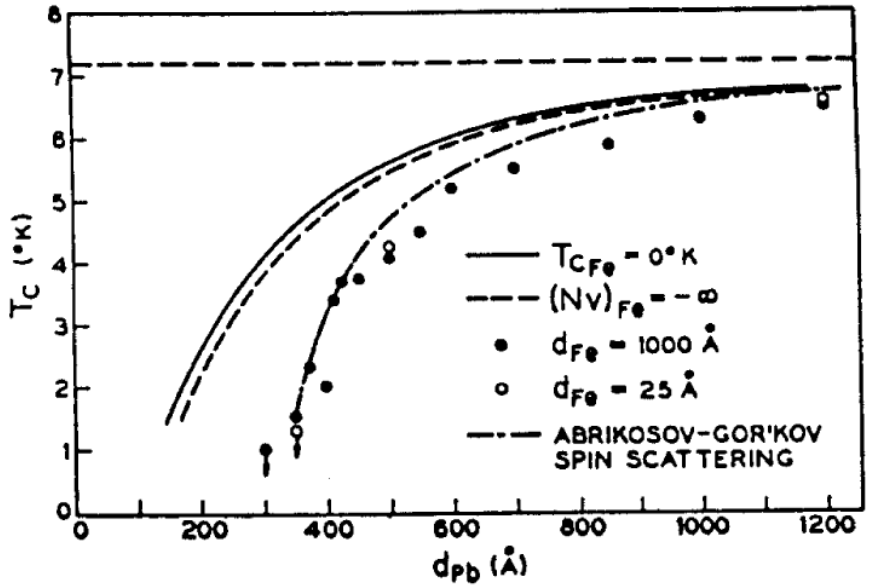

Figure 3.9 T_c suppression with superconductor thickness. Solid line is the fit assuming that the Fe spacer layer behaves like a non-ferromagnetic metal. Dashed line is the fit assuming that the electron-electron interaction between Pb and Fe is repulsive. The data fitted best with the Abrikosov-G'orkov theory [57].

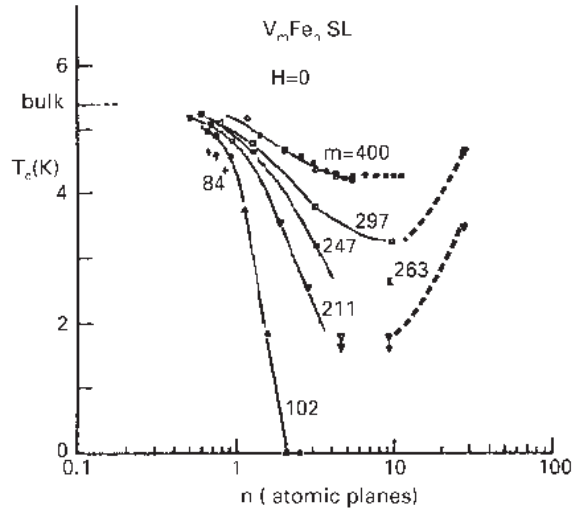

Figure 3.10 First T_c oscillatory behaviour observed in F/S multilayers. Superlattices of V_mFe_n deposited by Wong et al [66].

suppressed because of the large conduction-band exchange splitting in FM layers which extends into the superconductor via proximity effects. At the same time, Cooper pairs which leak into the F layer acquire a spatially dependent phase.

Theoretical work by Radovic et al [67] attributed the pecularities observed before by Wong et al [66] (as shown in Figure 3.10) to Josephson π-coupling between two superconducting layers separated by a ferromagnetic layer. In such systems, at certain ferromagnetic thicknesses, the superconducting order parameter on both sides of the F layer has opposite phases. Such π coupling in F/S systems can result in higher T_cs. Radovic's theory, however, assumes that the F/S system in question has perfect interface transparency.

Radovic's theory triggered further F/S proximity effect studies which produced contrasting results.

1. Strunk et al observed a step-like behaviour in T_c with d_F, similar to those observed by Muhge et al [68] with their Nb/Fe bilayers, and Verbanck et al [69], as shown in Figure 3.11.

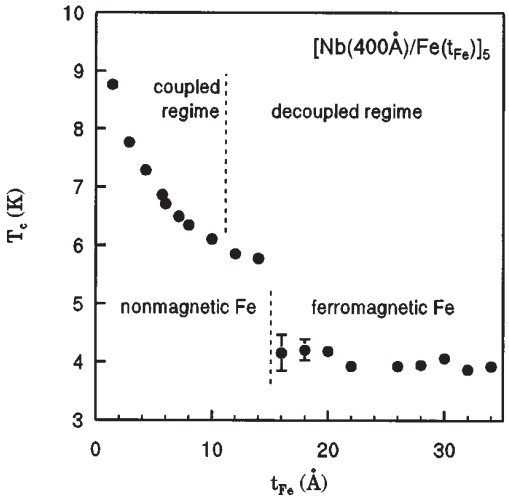

Figure 3.11 Nb/Fe multilayers MBE-deposited by Verbanck et al [69] show a step-like behaviour.

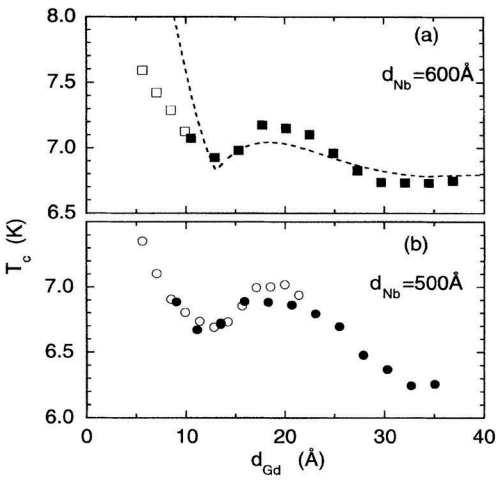

Figure 3.12 Jiang et al [70] observed oscillatory T_c behaviour in Fe/Nb/Fe multilayers.

2. Oscillatory T_c behaviour, such as in Figure 3.12 was, however, observed by Jiang et al [70] and Muhge et al [71] with Fe/Nb/Fe films.

   Further inspection revealed that the films with step-like T_c behaviour were deposited by molecular beam epitaxy (MBE) whereas those showing oscillatory T_c behaviour were deposited via sputtering. Hence, the logical conclusion drawn from these studies was that the pecularities observed was due to the existence of an intermediate layer at the interface whose thickness varied with preparation methods and conditions.

3.6.5 Review of S/F Oxide multilayered Heterostructures

The study of F/S interaction in multilayer cuprate/manganite systems is relatively new. The recent interest is due largely to the demonstration of compatibility of the two classes of materials,

the 100% polarization associated with manganites, and the potential of device application above liquid nitrogen temperatures.

Due to the short ξ_s associated with HTS, the criteria for studying F/S interaction in cuprate/manganite multilayers is the deposition of such heterostructures with very thin repeats. Thin oxide cuprate and manganites have not been widely studied because of the complexities of such systems compared to similar metallic ones, such as dependence of the transport properties of these materials on its crystal structure, implying that the layers have to be epitaxially grown.

Multilayer deposition

Most of the recent work (see Table C.1) [1, 64, 72, 73] have shown conclusively that epitaxial cuprate/manganite multilayers can be deposited by high O_2 pressure sputtering. Superconductivity in the YBCO spacer layers in these multilayers have been observed down to thicknesses of 3-4nm. TEM and XRD scans have been used to confirm the continuity and epitaxial quality of the individual layers. Some of the important results, with respect to the work done at Cambridge, are summarized.

Habermeier et al [64] investigated the interaction of magnetism and superconductivity in these superlattices. Most interestingly, they observed a re-entrant normal state at 30K (T_c=52K), at the onset of saturation magnetization in $[YBCO_{7.5}/LC(0.3)MO_5]_{t=20}$ multilayers. In further work with Holden et al [74], an YBCO d_{crit} of $\sim$20nm in the multilayers was estimated using ellipsometry measurements. It was observed that the free carrier response was suppressed in the YBCO/LC(0.3)MO superlattices compared with pure YBCO, LC(0.3)MO films and YBCO/LNO multilayers.

Systematic studies on the effect of cuprate and manganite thickness on the multilayer properties [1] showed that increasing manganite thickness led to an increase in M_s and a suppression of T_c in these multilayers. Hence, there was a corresponding decrease of T_c with increasing M_s in the multilayers. Decreasing superconductor thickness also led to T_c suppression. This rate of T_c suppression was faster in an F/S compared to an N/S multilayer, concluding thus that proximity to magnetic layers led to a suppression of superconductivity in YBCO.

Przyslupski et al have studied the magnetic properties of cuprate/manganite incorporating NSMO and LSMO. From magnetic characterization of the LSMO/YBCO multilayers, it was observed that the T_c is higher than the diamagnetic temperature, T_{cd}. Observed exchange bias effect in the superlattices was evident of the formation of an AF interlayer at the interface due to hole-charge exchange (which changes the Sr doping in LSMO to > 0.48, AF phase).

Research on cuprate/manganite multilayers at Cambridge investigated the feasibility of depositing such heterostructures using the PLD technique. PLD, which is expected to produce rougher films (compared to high pressure sputtering) due to droplet contamination, is effective for the deposition of oxide compounds. We studied the effects of individual layer thickness on the superconductivity in these multilayers, and hence the corresponding proximity effects observed in the multilayers. Specifically, we examined how the exchange coupling and magnetic moment

of the manganite layers suppress T_c. This study was aimed at understanding the effective ways of using magnetism as a means to control the superconductivity.

3.7 Trilayer Devices

A variation of the employing the use of magnetism to control superconductivity is to sandwich a thin S layer in between two F layers of different coercive fields, H_{co}s, such that they behave like a spin valve. Tagirov et al [75] proposed a four-layer AF/F/S/F metallic thin film device structure where one F layer can be pinned by the adjacent AF layer whilst the direction of magnetization of the other FM layer can be rotated by a weak external field. Assuming dirty limit conditions, they were able to demonstrate mathematically that a wide window exist where the superconductivity is completely destroyed for the parallel F alignment but only weakly suppressed for the antiparallel case, hence that superconducting current flowing along the superconducting layer can be switched on and off through the rotation of free F layer. In this device, when the F layers are parallel aligned, the spin-polarized perturbations of the pairing function from both layers are of the same sign and enhance each other, thus quenching superconductivity. In the anti-parallel configuration, the pair-breaking polarization in the S layer cancel each other. As the coercive fields for elemental ferromagnets is small, for example $\mu_\circ B \sim 3.5$mT for 22 thick Fe layer on top of Nb [76], such a superconducting spin switch device can work on very low fields which by themselves are insufficient to destroy superconductivity.

Gu et al [2] reported the first experimental evidence of the variation of T_c in an F/S/F sandwich structure with respect to the magnetic orientation of the ferromagnets. This experiment was done using the structure, Py/CuNi/Nb/CuNi/Py/FeMn. The antiferromagnetic FeMn pins the adjacent Py/CuNi layer via exchange bias such that it remains fixed in the weak magnetic fields which can be used to orientate the other Py/CuNi bilayer. This allows the ferromagnets on both sides of the superconductor to be parallel (P) or anti-parallel (AP).

Spin-polarized electrons extending from the ferromagnet into the superconductor cause the breakup of Cooper pairs. In an AP configuration, the pair-breaking effects on both sides of the superconductor cancel each other out. In the P configuration, this effect is stronger, thus suppressing the superconductivity.

The investigators observed that $T_c^{AP} > T_c^P$. However, the difference in T_c values, ΔT_c, is small. The largest difference in resistance at the transition temperatures of the two configurations is 0.6 ohm. When this system has been optimized, larger ΔT_c values may be achieved.

We investigated the use of this novel spin valve sandwich to actively control the superconducting state of a LSMO/YBCO/LC(0.3)MO trilayer device. In the process, we fabricated an oxide pseudo spin valve, with a thin YBCO spacer (10nm) which allowed for increased exchange coupling between the F layers on either side. Ideally, we can switch a superconductor between its superconducting and normal states through the use of a small magnetic field, just large enough to change the configuration of the spin valve structure.

Chapter 4

Deposition and Analysis Techniques

4.1 Motivation

The more important equipment and techniques used in our study will be described in this chapter. This will provide a better understanding of the processing methods and procedures used for film growth and device fabrication processes described in the next few chapters.

Pulsed laser deposition was the deposition technique used for our deposition of cuprates, manganites and similar multilayered heterostructures in this thesis. Another deposition technique used, mostly for the deposition thin metallic film (such as gold and permalloy) was Argon ion sputtering. One such system was the 'New OAR' (NOAR), which was used also for the dry etching of our device through ion milling.

The chapter includes also various materials characterization and device analysis techniques used in the course of this study. They include X-ray diffraction (XRD), atomic force microscopy (AFM) and dip probes used for transport measurements of our films and devices.

4.2 Pulsed Laser Deposition

The PLD system consists of a target holder, a substrate stage / heater housed in a vacuum chamber. A high powered laser is used as an external energy source to vaporize materials (from the targets) which will be deposited as thin films. The KrF Excimer laser beam is focused onto the target using a system of optics producing a rectangular beam spot homogeneous in intensity.

4.2.1 PLD film growth - Processing parameters

The PLD of oxide films is usually carried out in a reactive environment containing gas or gas mixtures with or without plasma excitation. There are several important parameters to consider with PLD deposition:

Laser

The most commonly used range of laser wavelength for thin film growth by PLD lies in the UV region (195 to 508nm) between 200 to 400 nm. Most materials used for deposition exhibit strong absorption in this spectral region. Below 200nm, strong absorption by molecular oxygen can make working in the spectrum difficult. In addition, the optics for shorter wavelengths are more difficult to handle. Bulk damage due to color center formation occurs much more easily at shorter ultra violet laser wavelengths.

The absorption co-efficients of materials tend to increase at the shorter wavelength end of this range, and thus the penetration depths into the target materials are reduced. This may be favourable, however, as thinner layers of the targets are ablated with use of shorter wavelength lasers. For deposition sources, most of the work has been done using Nd^{3+}:YAG and excimer lasers.

Table 4.1 Excimer Laser Operating Wavelengths [77].

Excimer	Wavelength (nm)
F_2	157
ArF	193
KrCl	222
KrF	248
XeCl	308
XeF	351

An excimer laser is a gas laser which emits radiation directly in the UV range. Table 4.1 shows the excimer laser operating wavelengths. Excimer molecules are formed in the gaseous mixture of their component gases. Energy is pumped into the gas mixture through electric discharge excitation. The pumping creates ions and electronically excited species that react chemically and produce excimer molecules. The chemical reactions leading to the formation of the KrF Excimer molecules can be briefly shown in the equations below:

$$Kr + e^- \longrightarrow Kr^+, Kr^*, Kr^{2+}$$

$$F_2 + e^- \longrightarrow F + F^-$$

$$Kr^+ + F^- + X \longrightarrow KrF^* + X$$

$$Kr^{2+} + F^- \longrightarrow KrF^* + Kr$$

$$Kr^* + F_2 \longrightarrow KrF^* + F$$

* denotes the electronically excited species and X represents a third body (He, Ne).

Once, the excimer molecule is formed, it will decay via spontaneous emission and collisional deactivation, giving the molecule a lifetime of about 2.5ns. Thus, in order for lasing action to occur, the formation rate of the ionic and excited precursors must be fast enough to produce excimers at a rate of several 10^{23} / $cm^3 s^{-1}$.

For a chosen material and a fixed laser wavelength, the laser fluence on the target has the most significant effect on the film stoichiometry, particulate size and density. The laser fluence affects the instantaneous deposition rate and the degree of supersaturation of vapour, and can be varied by varying the laser power or the laser spot size.

In general, there exists a threshold laser fluence below which the particulates are barely

observable. Below the threshold, deposition is in the thermal regime, similar to evaporation. Above this threshold laser fluence, the particulate number density increases rapidly with increasing fluence.

Laser Beam

A homogeneous, uniform beam is essential for good quality deposition. Poor beam quality can result in non-stoichiometric films as well as undesirable droplet formation.

Target

Successful depositions can be made from pressed powders, sintered pellets, cast material, single crystals, and metal foils. Porous and inhomogeneous targets yield poor quality films. High density and smooth target surfaces are desirable features of a target material in order to avoid splashing due to defoliation of the surface. To achieve uniform target erosion and consumption, the target is usually rotated during deposition. Also, the target should be flat to provide for uniform ablation.

When the laser ablation is absorbed on the target surface, electro-magnetic energy is converted first into electronic excitation and then into thermal, chemical and even mechanical energy to allow evaporation, ablation, excitation, plasma formation and exfoliation.

Targets are usually mounted on a carousel containing several other targets. This is advantageous as it allows for fabrication of in-situ multilayer structures.

Plume

Evaporants from the ablated target form a plume, which consists of a mixture of energetic species including atoms, molecules, electrons, ions, clusters, micron-sized solid particulates, and molten globules. The plume is always perpendicular to the target regardless of the angle of the incident laser beam.

Due to the increased collisions between the laser produced plume and the background gas, the plume expansion decreases when as the background gas pressure increases. The substrate to be coated should be placed at a distance on the edge but just within the visible part of the laser plume. The plume is usually elongated, hence, one of the disadvantages of PLD is that film deposition only takes place uniformly over a small area.

Ambient Gas Pressure

The use of an ambient gas during pulsed laser ablation deposition can be characterized as either passive or active. The passive use of an ambient gas is mainly to compensate for some loss of a constituent element such as oxygen or nitrogen in ceramics. Active use refers to the introduction of inert or reactive gas to deliberately form particulates with a desired size or composition.

The gas pressure in the deposition chamber also reduces the vapour flux. The gas molecules provide a high flux of background gas particles bombarding surface during deposition.

Heater/substrate holder

As the evaporants from the target are ejected as a highly forward-directed plume of material along the target normal, the substrate has to be held directly opposite the target. The target-substrate distance varies according to the energy delivered to the target. This distance affects the film stoichiometry and the deposition rate. When the target-substrate distance is much smaller than the plume length, there is no marked difference in particulate size and density. As the distance increases, the proportion of smaller particulates decreases, and a few larger particulates appear indicating a merge during flight. If the substrate is located far beyond the plume, the adhesion of the deposited film to the substrate is poor. Thus, the location and orientation of the substrate relative to the target are important. Frequently, the substrate must be heated to produce good adhesion and/or epitaxy.

The temperature of the substrate is important in preserving the stoichiometry of the films. There exists a critical substrate temperature, below which the structure of the film is not monocrystalline. The rate of crystallization also depends on the substrate temperature. A lower substrate temperature results in a faster cooling rate, which in turn leads to a lower velocity of crystallization as the adatom diffusion distance is short. Temperature uniformity becomes critical when the formation energy of the desired compound, or the need for epitaxy, forces the deposition temperature into a narrow band. For instance, in the case of YBCO, high substrate temperature favors the growth of c-axis oriented films. As the need for temperature uniformity increases, so does the complexity of the heater and its material.

Smoother films can be deposited at a lower substrate temperature, but this improved morphology is at the expense of the film structure as the smoother films are typically a mixture of a and c axis oriented material as opposed to being exclusively c-axis oriented.

Pulse Frequency

The laser pulse rate is especially important when the deposition is performed at elevated temperatures, and the diffusion time constants of the material atoms are comparable to the laser frequency.

If the period of pulsing is much larger than the time constants for all other relevant diffusion, agglomeration, and dissociation phenomena, the pulsing is not expected to have any effect on the final microstructure.

4.2.2 YBCO deposition using PLD

PLD has proven to be the simplest technique to produce YBCO films with a T_c of above 85K [78]. Here are several important parameters of consideration for the PLD deposition of YBCO:

Table 4.2 Relationship between processing parameters and the microstructure development in thin films deposition by PLD [7].

Category	Parameters	Effect on Process	Possible Effects on Microstructure %
Primary	Laser Wavelength	Thermal or non-thermal evaporation	Retention of target stoichiometry
	Laser Repetition Rate	Ratio of neutral to ionic species in plasma	Formation of metastable structures
		Kinetic energy of the ejected species	Particulates
Secondary	Substrate Temperature	Surface mobility of ablated species	Formulation of metastable microstructures
	Oxygen Partial Pressure	Oxygen content of film	Establishment of epitaxy
			Control of crystal structure (orthorhombic - tetragonal)
Tertiary	Substrate - Pellet distance	Film thickness	Not known

O_2 Partial Pressures

With regards to the growth of YBCO, there are two distinct regimes. At low O_2 concentration, the metal species are quite mobile at low temperatures (630 to 700°C). At higher O_2 concentrations, the metal species are less mobile as the majority is in the oxidized state. Higher substrate temperature would thus be required for the formation of the required phase. The latter conditions, which are typical of laser ablation and high pressure sputtering, allow for the formation of a structure with a higher oxygen content (ie. $YBCO_{7-\delta} > YBCO_{6.3}$).

Deposition Temperature

Thin film growth depends on diffusion, which can be characterized by the diffusion coefficient, D,

$$D = D_o e^{\frac{-Q}{k_B T}} \tag{4.1}$$

where D_o is usually in the range of 0.01 to 1 $cm^2 s^{-1}$ [78], and Q is the activation energy.

YBCO films tend to be smoother at lower deposition temperatures because mobilities of Y

and Ba are low. The film would hence take the shape of substrate surface features. However, outgrowths are commonly observed in YBCO films. These form due to the nucleation of a-axis material on an otherwise uniformly growing c-axis film, and is due to the surface diffusion in the Cu-O (a-b) planes being more rapid than diffusion in the c-axis[1] At higher temperatures (T>740°C in a O_2 rich environment, island growth occurs on the substrate. The highest quality films in terms of rocking curve widths and narrowness of superconducting transition widths are all produced at higher temperatures and O_2 pressures. However, temperatures greater than 750°C were not suitable for manganite/cuprate heterostructure growths due to the interdiffusion of cations across the interface which leads to poorer interface quality and contamination of the individual layers.

4.2.3 Optimized Manganite Deposition in MK10

Pulsed laser deposition (PLD) is the also system of choice for $La_{1-x}Ca_xMnO_3$ thin film deposition because it allows for the ease of depositing oxide films consisting of several elements. Our LCMO films were deposited using an on-axis PLD system, MK10, consisting of a Lambda Physik Excimer Laser COMPex laser source, a Fecralloy heater strip connected to a Lambda LLS-9000 power source. Picture of the MK10 is shown in Figure 4.1

Heater Construction

The side view of the heater is shown in Figure 4.2. The heater consisted of a Fecralloy^R strip connected between 2 copper contacts attached to the power source.

Fecralloy^R dimensions used:	Length	60mm
	Width	13mm
	Thickness	0.1mm

The heater was curved around the ends, and fitted between the cleaned copper contacts of the heater flange. The edges along the length of the heater were bent upwards slightly to prevent the substrates from falling off during deposition. The heater was then passivated using the recipe shown below.

Passivation of newly constructed heater

Passivation of the new heater strip was required to remove contaminants from the alloy surface and to create an inert oxide layer, preventing further reaction of the alloy.
Passivation recipe (from Dr. Neil Mathur)

1. Load and level heater strip

[1]This does not prove that the diffusion is faster in the a-b plane. It demonstrates that the growth sites are easily accessible for an atom moving on a plane which contains the c-axis.

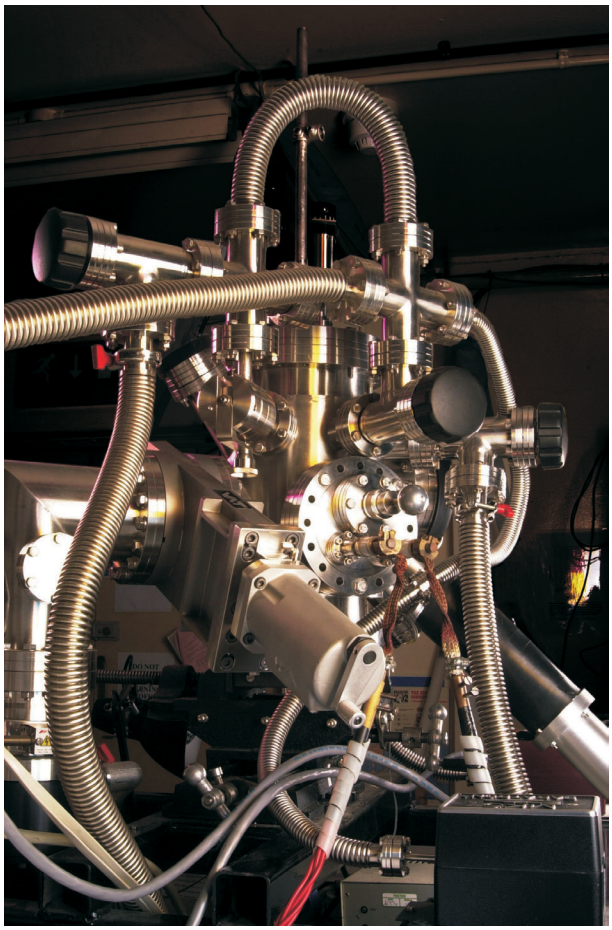

Figure 4.1 Photograph of the MK10 PLD system. Courtesy of Dr M.Blamire.

2. Pump chamber down to 2×10^{-6} mbar
3. Let in 1 atm O_2,
4. Ramp up and anneal heater at 200W for 1hr
5. Pump chamber down at 200W for 1hr
6. Turn heater off, and completely cool
7. Ramp up heater at 200W for 4hrs
8. Turn heater off, cool for 1 hr
9. Anneal heater at 200W for 4hrs
10. Cool for 1 hr

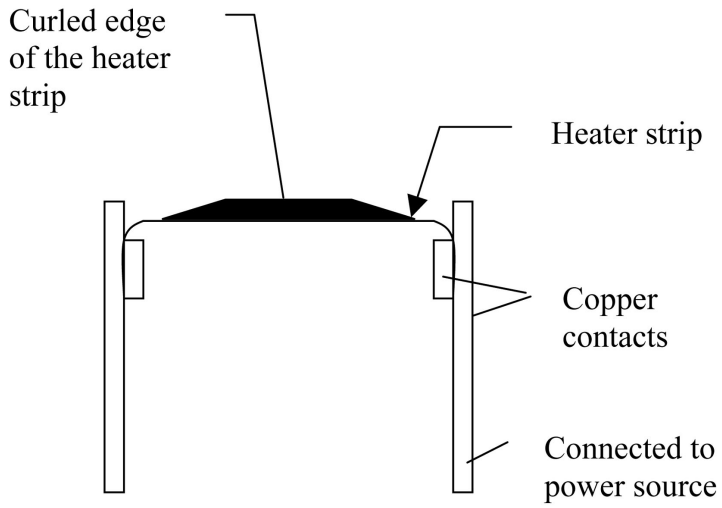

Figure 4.2 Side view of the Fecralloy^R heater used in the MK10

4.2.4 Deposition in the MK9

'Eclipse' PLD

One disadvantage of using pulsed laser deposition over other deposition techniques such as sputtering or evaporation is droplet contamination. This occurs when relatively large particulates are dislodged from the target surface, and usually occurs when target surface is rough. There are a variety of procedures which can help to reduce this problem, such as polishing the target between deposition runs (which was practised), defocussing the laser spot in an optimal way [78], or mechanically chopping part of the plume.

One method to obtain PLD thin films of lower rms roughness is to insert a mask directly between the ceramic target and the substrate/heater used in a conventional PLD deposition system. This technique is known as 'eclipse' PLD, and is illustrated in Figure 4.3. The droplets and larger ablated particles from the target have a smaller angle of dispersion than the smaller, ligher species. The mask thus acts as a shield to prevent these larger and heavier particulates and droplets from falling directly from the ceramic target onto the substrate surface. As a result, the film in the 'eclipse' technique is 'made up' of smaller target particles from the plume which create a smoother, more homogenous film. This technique is essential for using laser ablation for depositing multilayers which will be described further in Section 7.2.

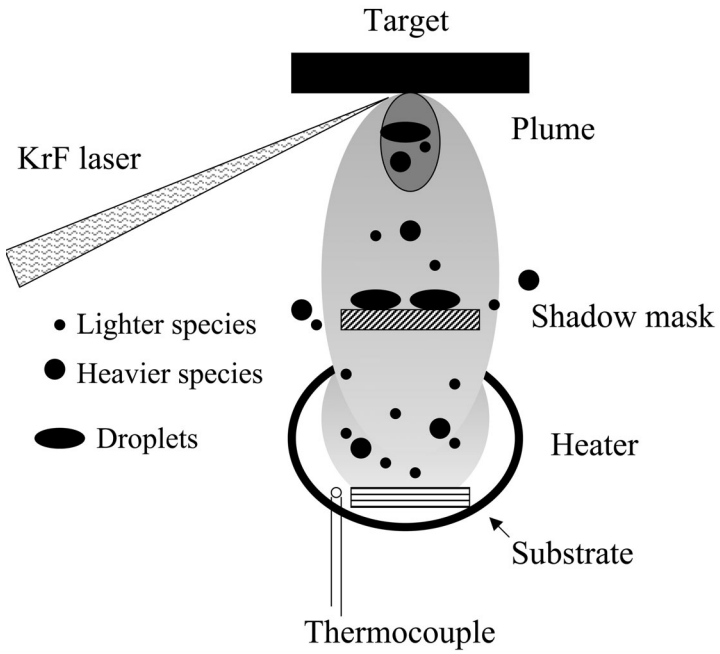

Figure 4.3 Schematic of 'eclipsed PLD technique'

4.3 Ion Milling and Sputtering

4.3.1 Sputtering

Another deposition technique used in this study was sputtering, which is one of the main methods of metal film deposition in microelectronics fabrication. In sputtering, a plasma is initiated by applying a large voltage across a gap containing a low pressure gas. Once a plasma is formed, the ions in the plasma are accelerated towards the negatively charged cathode. Sputtering of the cathode results due to the steady stream of ion bombardment.

The 'NOAR' is used specifically for the deposition of gold on our devices. The sputtering technique used in the 'NOAR' is magnetron sputtering, whereby a magnetic field is applied which cause the electrons spiral around in the direction of the magnetic field lines. This increases the probability that the electrons will collide with neutral species within the plasma, resulting in higher ion densities, and hence increasing the rate of ion bombardment on the cathode. The use of magnetron sputtering allows the formation of plasma at lower chamber pressures, typically 10^{-3} mbar. It also increases the sputtering rate and improves the purity and microstructure of the sputtered material.

The 'NOAR' has the capabilities for ion milling and sputtering. Such a feature is useful in device fabrication because it allows in-situ milling and sputtering. This process removes microscopic impurities on the surface of the film due to contact with the atmosphere (for instance, undesirable oxides or other compounds which form when the film is exposed to air). This improves the interfaces between materials, and reduces contact resistance during gold deposition.

4.3.2 Ion Milling

Ion milling is a mechanical process which makes use of noble gases, most commonly, argon. Unlike chemical etching, it involves no chemical reactions with the etch species. Our films were ion-milled in the 'NOAR'. The ion beam was generated by a Kaufmann ion source.

Kaufmann source

The Kaufmann source [79] contains an electron filament. Electrons boil off the filament and accelerate towards the anode (held above the filament potential). This potential difference must be large enough so that the accelerated electrons impact the neutral gas atoms with sufficient energy to ionize them. The Ar^+ ions were accelerated towards the target. Ions arrive at the target surface with energy:

$$E_{ion} = e|V_p - V_g| = e|V_f + V_{pa} - V_g| \tag{4.2}$$

where V_p is the plasma voltage with respect to ground, V_g is the potential difference between the target and the source, V_f is the potential difference between the anode and the filament, V_{pa} is the plasma voltage with respect to the anode, and e represents the electron charge.

Milling in the 'NOAR'

The ion beam sputtered away the surface of the film at a rate which varies with material on the surface. The rate of surface particle loss depends on the momentum transfer, which depends also on the mass of the surface particle in relation to that of Ar^+, and the bonding energy of the surface particles. In this way, the carbon-based photoresist milled away at a slower rate than the thin film.

The milling chamber is pumped down to below 4×10^{-6} mbar before introducing a small amount of Ar/O_2 gas. During the milling process, the chamber is kept at a pressure of 10^{-3} mbar. The good vacuum will minimize collisions between the Ar^+ ions and the residual gas molecules, allowing the ejected ions to travel in straight lines towards the target electrode with maximum energies. The higher vacuum also reduces possible reactions between the film surface and gaseous impurities during the milling process.

Use of Ion Milling

Ion milling is used for our device fabrication because it has several significant advantages over chemical etching: Ions in the beam, are accelerated by a strongly vertical electric field, and with a low chamber pressure, impinge almost completely vertically on the film surface. Hence, ensuring that the etched pattern has sharp, vertical sides. It can also be used to pattern a wide variety of materials, including ternary and quaternary compounds, such as YBCO and LCMO.

However, below are several technical problems which may be encountered when using Ar^+ ion milling:

- A taper in the photoresist mask will be transferred to the film. This will cause the resultant pattern (which has been etched onto film) to be broadened.
- Eroded material is not volatile, and can be redeposited on the surface of the film, leading to uneven etching.
- Trenching can occur. This happens when the mask erosion, or a slight taper in the mask causes the sidewalls to be tapered at a steep angle. Low angle incident ions will reflect off the tapered surface towards the film, causing trenches.

To resolve some of these processing issues, the 'NOAR' has a fully rotating stage, which allows the samples to be rotated with respect to the incident beam during milling. The rotation results in more uniform milling throughout the device surface and minimizes some of the above mentioned effects.

In-situ MagnetoResistance Measurement Rig

An in-situ magnetoresistance rig has been designed and built into the 'NOAR'. It consists of a aluminium sample carrier with copper contact pads and field coils which are connected to external electrical set-up.

In our device processing, we measured the in-situ resistance of the films during milling, so as to detect the end point and hence prevent over-milling. The detrimental effects of overmilling will be discussed in Section 5.7.1.

The procedure for in-situ resistance measurements is described as follows:

1. The sample was mounted with silver paint on the sample carrier, and wirebonded in the four-point configuration to the carrier contact pads.
2. The sample carrier was attached to the rotational sample stage using vacuum grease.
3. The current and voltage pins on the sample holder were connected to corresponding pins which facilitated resistance measurements to be performed externally.

4.4 Atomic Force Microscopy

The AFM is an essential tool for imaging surfaces and for probing the nanomechanical as well as other fundamental properties of sample surfaces, including their adhesive and elastic properties.

The AFM makes use of a cantilever, which is a silicon/silicon nitride probe. Mounted at the end of the cantilever is a tip that is used to sense a force between the sample and the tip. For normal topographical imaging, the probe is brought into continuous or intermittent contact with the sample. Scanning the lever over the surface and measuring the deflection of the cantilever, a piezoelectric scanner which translates in 3 directions, the x, y, and z, can generate topographical images by plotting the local sample height versus the horizontal probe tip position.

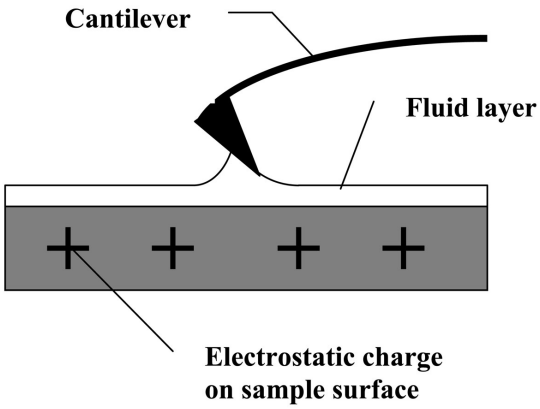

Figure 4.4 In contact AFM mode, electrostatic and surface tension forces from the adsorbed layer pull the scanning tip towards the sample surface.

In the conventional Contact Mode of the AFM, the cantilever is dragged across the surface. This dragging motion, combined with the adhesive forces between the tip and the surface can cause substantial damage to both sample and probe. In addition, as shown in Figure 4.4, capillary action, due to adsorbed gases (eg. condensed water vapour) can cause a meniscus to form. This vertical force, coupled with possible trapped electrostatic charge on the tip and sample creates adhesive and shear forces between the tip and the sample which may distort data or damage the sample.

To avoid this problem, we use the Tapping Mode for imaging in the AFM. The Tapping Mode makes use of an oscillating cantilever assembly at or near the cantilever resonant frequency using a piezoelectric crystal. In this mode, the tip is placed in contact with the surface to provide high resolution, and then lifted off the surface to avoid dragging the tip. The piezomotion causes the cantilever to oscillate at a high amplitude ("free air" amplitude, typically greater than 20nm) when the tip is not in contact with the surface. The oscillating tip is lowered until it lightly 'taps' the surface. During scanning, the vertically oscillating tip alternately contacts the surface at a frequency of 50 to 500 kHz.

As the oscillating tip contacts the surface, the oscillation is necessarily reduced due to the energy loss caused by the tip contacting the surface. Thus, the amplitude is reduced when the tip passes over a bump, and increases when it passes over a depression. This change in the oscillation amplitude is used to identify and measure surface features. The amplitude is measured by the detector, and the digital feedback loop then adjusts the tip-sample separation to maintain a constant amplitude and force on the sample.

In this way, high resolution imaging can be performed on films that are easily damaged or loosely adhered to their substrates. The Tapping Mode overcomes problems associated with friction, adhesion, electrostatic forces. We are thus able to use AFM to study the roughness and

to profile the tracks of $YBa_2Cu_3O_{7-\delta}$ and manganite films.

The Digital Instruments Atomic Force Microscope was used to obtain scans of our films' surfaces. From each scan, a root-mean-square (rms) roughness value can be calculated. The rms roughness value is only representative of a localized area of film, and may not be indicative of the film as a whole. Such scans should also be taken of areas which are free of uncharacteristically large defects. An investigation of the film roughness can give an estimate of the interfacial roughness. This is especially useful in multilayer heterostructures. The AFM surface scan can also indicate the film's growth mechanism, i.e. step-flow growth indicated by terraces or island growth.

4.5 X-ray Diffraction

Another major technique for epitaxial film characterization is X-ray diffraction, XRD. This techniques provides information about the texture and crystallinity of the films. XRD is a fast, non-destructive technique which provides information both at an atomic scale and from co-relations over thousands of angstroms.

4.5.1 Phase Identification

A diffraction peak only occurs when the Bragg's condition, as shown below, is met:

$$n\lambda_w = 2dsin\theta \tag{4.3}$$

where λ_w is the wavelength of the X-rays, d is the separation of the lattice planes, and θ is the angle between the incident x-ray beam and the crystal plane.

When this condition is met, such that n is an integer, the diffracted beams interfere constructively, producing a peak in the spectrum. At directions outside this criteria, there will be some degree of destructive interference of the diffracted beams. Our samples were scanned over a range of angles, producing an X-ray spectrum which is characteristic of the material/compound.

The peaks in an X-ray $2\theta/\theta$ scan have increased intensity when the planes are textured. Broadened peaks occur because of several factors, three obvious ones are:

- The X-ray beam incident on the sample is spread out, ie. when large source collimation slits are used.
- Localized stress and strain in the films, due for instance to the impurities, can result in a larger distribution of lattice spacings.
- For single crystal films, broadened peaks also correspond to fewer interferences of diffracted X-rays brought about by thinner films, as represented by the Scherrer formula. This is further explained in the next section.

4.5.2 Film Thickness

X-ray diffraction can be used to investigate the film/repeat thickness of high quality epitaxial films / multilayers. One such method is through the use of the Scherrer formula.

As described in the eariler section, destructive interference is as much a consequence in the periodity of the atoms as the constructive interference. For example, if the path difference between rays scattered by the first 2 planes in a sample differ only slightly from an integral number of wavelengths, then the plane scattering a ray exactly out of phase with the ray from the first plane will lie deep within the crystal. If the crystal is so small that this 'lower' plane does not exist, there will not be complete cancellation of all the scattered rays. There is a connection between the amount of "out-of-phaseness" that can be tolerated and the size of the crystal. Hence, for small crystals, diffraction angles close to, but not equal to, the exact Bragg angle cause broadening of the diffracted beam. The width of the diffracted curve increases as the thickness of the crystal decreases, and can be linked by the Scherrer formula:

$$t_h = \frac{0.9\lambda_w}{B_{2\theta} cos\theta} \tag{4.4}$$

where t_h is the thickness of the crystal, λ_w the wavelength of the diffracted X-ray radiation, $B_{2\theta}$ the full width half maximum (FWHM) of the 2θ peak, and θ is the angle of the incident ray on the reflecting surface.

As the films we are investigating in this study are single crystal and epitaxially grown, we can assume t to be the thickness of the film. Hence, for these same reason, unless the film quality is sound, the Scherrer formula should not be used as the only means of film thickness determination, but as a method of film thickness confirmation.

Other methods of determining repeat thicknesses in multilayers, by X-ray diffraction, is (1) by low-angle reflectivity and (2) from the spacings between fringes/satelite peaks on either side of the Bragg peaks in the 2θ scan [80].

4.5.3 Mosaic Spread

All crystals possess, in various degrees, mosaic structures, in which the crystal lattice is broken up into a number of tiny blocks, each slightly disoriented from one another. In single crystal thin films, this misorientation of layers occur due to dislocations present in the film.

A rocking curve can be performed on a sample at a defined peak/angle to check the degree of disorientation of the 'tiny blocks' in the c-axis, ie. the degree of misalignment of its atomic planes at that particular angle. This is done with an Omega scan, in which the sample is rocked back and forth slightly at a particular 2θ value. The width of the peak directly indicates the mosaic spread of the planes at the particular value of d-spacing.

Analysis of the mosaic spread of the films provides an indication of the epitaxial quality of the films, and directly affects the transport in the oxide films studied here. This is because transport in YBCO occurs along the Cu-O planes perpendicular to the c-axis, and double-exchange in the

manganites occur in the a-b directions. In our heterostructures, where each layer of film serves as a building block onto which another film is grown, the degree of mosaic spread directly affects the quality of the subsequent layers, and hence the heterostructure as a whole.

4.6 Transport Measurements

Electrical measurements of our films and devices were performed using several cryogenic probes in the Device Materials Main Lab. In brief, the films / devices were loaded into the probes by wire-bonding onto a designated sample holder, or connected by pogo pins. The probes, which were immersed in liquid nitrogen (77K) or into a dewar of liquid helium (4.2K), were connected to electronics which are computer-controlled using a National Instruments Labview software. The 'Dualscope' program which was designed by Dr Gavin Burnell was used for data acquisition and processing.

4.6.1 Cryogenic Probes

Several cryogenic dip probes were used during the course of this study, depending on the requirements of the transport measurements. A summary of the probes used, and some of their specifications, are listed in Table 4.3. The Heliox, used extensively for the spin injection measurements, will be described in the following section.

Table 4.3 Summary of the cryogenic probes used for various transport measurements in the Device Materials Lab.

Name of Probe	Maximum magnetic field(T) @ Minimum measurement temperature(K)
CMR Probe	0.34 @ 77
J_c Rig	8 @ 4.2
Heliox	2 @ 0.3
Phil's / Wilf's Probe	0.07 in x-y plane @ 4.2 0.03 in z-plane @ 4.2
T_c Probe	No field but min. T=4.2

4.6.2 Heliox

The Oxford Instruments Heliox was designed as a low-cost ^{3}He cryostat. Measurements using the Heliox can be performed down to 0.3K, and with a 2T applied magnetic field.

The Heliox insert fits into any dewar, which is sufficiently long and has a neck diameter $\sim$ 50mm. The Heliox operates on the principle of a sorption pumped ^{3}He insert. It contains a sealed reservoir of ^{3}He gas and a charcoal sorption pump.

The device was mounted onto the copper block of the sample carrier using silver paint, which increases the thermal contact between the sample and the thermocouple, and wirebonded onto

a sample holder and attached at the bottom of the 1K pot, in the inner vacuum chamber (IVC). The IVC, which is sealed, is pumped with a diffusion pump to 10^{-4}mbar in order to remove any reactive gaseous molecules such as water vapour, and then filled with approximately 10-12cm^3 of He^{4+} exchange gas, which increases the rate of heat transfer between the sample and the Heliox shell.

The IVC is cooled by immersing it in liquid N_2 to approximately 150K and then transferred into a dewar of liquid He. Liquid helium is also pumped, by a rotary pump, through the 1K pot thermally connected to the sample, which increases the rate of cooling down to about 1.2-1.4K. The sample can be further cooled to 0.3K using the enclosed ^{3}He cooling system.

The insert also consists of a superconducting magnet mounted at the end, as shown in Figure 4.5. The magnet consists of a number of concentric solenoid sections wound from superconducting wire, niobium titanium (T_c = 10K) filaments. The magnet is connected in parallel to a superconducting switch, which is essentially a superconducting wire wound non-inductively with an electric heater. The 'switch heater' allows the superconducting magnet to be run in the pesistent mode.

The devices were cooled and maintained at temperatures close to their respective T_cs by setting the heater temperature and adjusting the rate of flow of helium in the 1K pot.

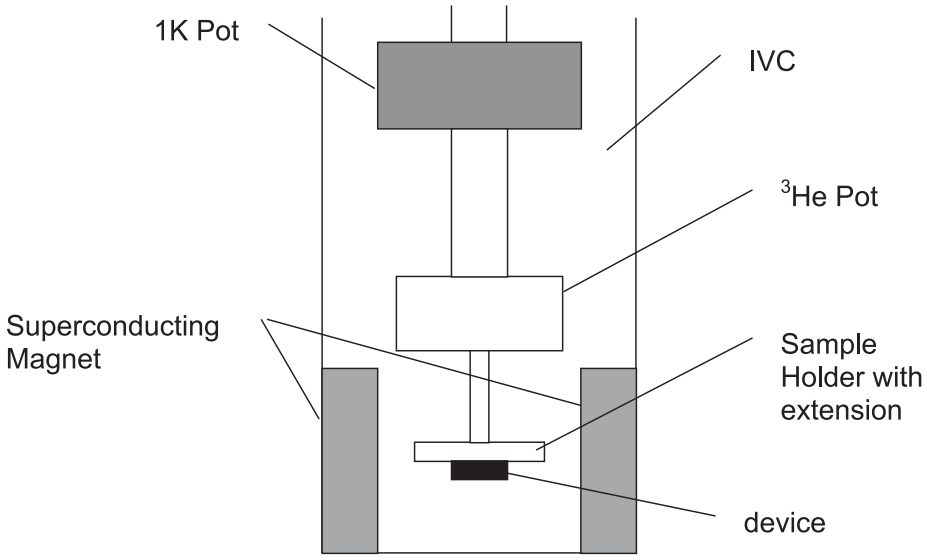

Figure 4.5 Cross-section of the IVC illustrating the sample position with respect to the superconducting solenoid magnet in the Heliox.

High temperature measurements using the Heliox

The Heliox was particularly useful for our measurements because of its large magnetic field at below 77K. In order for the superconducting magnet to function, it had to be immersed in liquid helium. Our spin injection measurements were, however, performed at temperatures close to

the devices T_cs, approximately between 50 to 70K. Such sample temperature in the Heliox can be obtained using a thermal gradient achieved by the heat exchange between the heater fitted close to the sample carrier, and the cooling of the 1K pot.

This large temperature gradient within a space of 1cm (between the sample and the magnetic solenoid) posed some difficulties as it caused an undesirably large helium boil-off, which is potentially very dangerous due to the quick build-up of pressure in the dewar. The quickly decreasing level of liquid helium in the dewar also caused a continuous non-equilibrium thermal state. The sample carrier was 2cm long from base (at 1K pot) to sample. Therefore, although the sample is thermally connected to the thermocouple, there is a time lag between the changes in the sample temperature and the thermocouple/heater. This temperature instability in the dewar made constant-temperature measurements extremely difficult.

Adapting Heliox for high temperature measurements

A much-improved sample temperature stability within the insert was achieved by removing the ^{4}He exchange gas in the IVC, and maintained in vacuum without the small amount of ^{4}He exchange gas. This removed convection as a means of heat transfer and the sample is cooled mainly by conduction achieved by pumping liquid helium from the dewar, via capillaries, through the 1K pot. The rate of cooling is very slow (time>36hrs). The sample could, hence, be maintained in the temperature range 50 - 70K using the combination of the heater and 1K pot, whilst that of the superconducting magnet was kept at 4.2K.

The rate of cooling was significantly increased by allowing the IVC to cool to approximately 110K in liquid N_2 before transferring it to liquid helium. This is because more of the gaseous molecules present in the IVC which contribute to heat transfer between the sample and the IVC walls in contact with liquid helium is cryogenically pumped when the insert was dipped in liquid N_2. This insulation is, however, very useful for constant-temperature measurements, as discussed earlier in the section.

4.7 Magnetic characterization

The study of magnetic properties was done using a vibrating sample magnetometer (VSM) which measured the magnetic response of the sample to an external field. The VSM is a common technique used to characterize magnetic samples and has a sensitivity in the μemu range.

In the VSM, the sample to be measured was placed in between a pair of stationary pick-up coils and vibrated in a uniform field. A lock-in amplifier was used to tuned in to this vibration frequency. The moving sample induced electro motive force (emf) in the pickup coils, due to Faraday's Law. Prior calibration of the VSM with a 'calibration sample' of known magnetization allowed absolute values of the magnetic moments in the sample to be obtained.

Chapter 5

Spin injection 1: Film growth and device fabrication

5.1 Motivation

This chapter describes the experimental work which was necessary for the successful combination of cuprate/manganite heterostructures, as well as the experimental procedures used for the fabrication of 3T devices used for spin injection measurements. The chapter is divided into three main parts: Firstly, a discussion of thin film deposition of YBCO and manganites and a study of the deposition of LC(0.3)MO on YBCO by PLD. Secondly, an outline of the various cleanroom techniques and procedures used is presented, as well as the design of the device mask, photolithography recipes and the fabrication of ramp junctions, all of which pertained directly to the fabrication of the spin injection devices. In the last part of this chapter, we described, in detail, the fabrication of the spin injection device, D4.

Although trilayer devices were also fabricated and studied, as discussed in Chapter 8, the processing of spin injection devices was more complicated. A more detailed description of the spin injection device processing techniques were thus presented.

5.2 Manganite/Cuprate Heterostructures

The deposition of cuprate/manganite heterostructures was first performed by Toshiyuki et al [81]. They concluded that YBCO could be fabricated on antiferromagnetic $La_{0.3}Ca_{0.7}MnO_3$ with little reaction at the interface. Goldman et al [82] have also observed that the $DyBa_2Cu_3O_7$/ $La_{0.67}Ba_{0.33}MnO_3$ interface is free of secondary phases and that the crystallinity of the materials at the interface is very similar to that in the bulk.

Due to the compatibility of these two classes of perovskites, manganite/cuprate heterostructures have been deposited for investigating proximity effects of the antagonistic natures of these materials. Table 5.1 shows the lattice parameters of several cuprates, manganites and single crystal substrates which have been combined in recent studies.

Manganite/cuprate heterostructures have also been deposited by sputtering [83, 1], by pulsed laser ablation [52, 51] or by ozone-assisted molecular beam epitaxy (MBE) [55]. Of these three techniques used, MBE offers the most control over film composition [82]. Sputtering is, however, the most common deposition method for such heterostructures because it is a relatively efficient deposition process. Most sputtering systems have the capability for depositing, within a single run, several samples, with different layer thicknesses. Films deposited by PLD tend to be rougher due to contamination with droplets and particulates ejected from the ceramic targets during ablation [78].

5.3 Deposition of manganite/cuprate bilayers

The deposition of manganite/cuprate heterostructures was performed using two different PLD systems in the Device Materials Lab, namely the MK9 and MK10. A comparison of the two systems is shown in Table 5.2. In brief, the MK9 system has been used mainly for the deposition

Table 5.1 Lattice parameters of various cuprates, manganite and substrate compounds commonly combined in studies involving cuprate/manganite heterostructures. The manganites are effectively cubic [82].

Materials Class	Compound	lattice parameters (Å)
Cuprates	$DyBa_2Cu_3O_7$	a = 3.847, b = 3.903, c = 11.738
	$YBa_2Cu_3O_7$	a = 3.823, b = 3.886, c = 11.681
Manganites	$La_{0.67}Ca_{0.33}MnO_3$	c/2 = 3.85
	$La_{0.67}Sr_{0.33}MnO_3$	c/2 = 3.87
	$La_{0.67}Ba_{0.33}MnO_3$	c/2 = 3.92
	$Nd_{0.67}Ca_{0.33}MnO_3$	c/2 = 3.82
Substrates	NdGaO	c = 3.864
	$SrTiO_3$	c = 3.905
	$LaAlO_3$	c = 3.778

Table 5.2 Characteristics of two PLD systems used in the Device Materials Lab. Thin film growth was performed in both systems.

Parameter	MK9	MK10
Target-substrate distance (cm)	5	7
Laser spot size for lense used (mm^2)	3.6	12.7

of YBCO films together with various buffer layers for coated conductor applications, while the MK10 has been optimized for manganite growth.

5.3.1 YBCO deposition in the MK9 PLD system

YBCO thin films were deposited using a 248nm wavelength KrF excimer laser at $3J/cm^3$ and 5Hz in 15 Pa flowing oxygen at 730 - 760°C. After deposition, the samples were cooled to 480°C at 10°C/min and annealled at 1 bar O_2 for 30 min. A typical YBCO film on STO substrate film deposited in the MK9 is shown in the AFM image in Figure 7.3. The film had a T_c of 90K.

5.3.2 Manganite deposition in the MK10 PLD system

The MK10 PLD system has been optimized for the deposition of mangnites. The recipe, similar to that used for YBCO deposition in the MK9 is as follows [84]:

1. The substrates were loaded onto the heater, together with a thickness monitor, such that they sit at the visible tail end of the plume. This position was determined from previous records of substrates and plume positions observed through the windows of the PLD chamber.

2. The ceramic target surface was polished using various grades of emery paper before each deposition to reduce droplets on the surface of the grown film.

3. The chamber was vacuum pumped to the order of 10^{-6} mbar, as verified by the VG ARGA mass spectrometer.

4. Pre-anneal: the heater temperature was raised to 850°C in vacuum.

5. Deposition: the film was deposited at 1Hz, 15Pa flowing O_2, at 850°C and a laser fluence of $2J/cm^2$.

6. Post-anneal: the film was post annealled at 850°C, 60kPa O_2 for 1hr.

The characterization of a typical 60nm LC(0.3)MO film deposited on an STO substrate is shown in Figures 5.1 and 5.2.

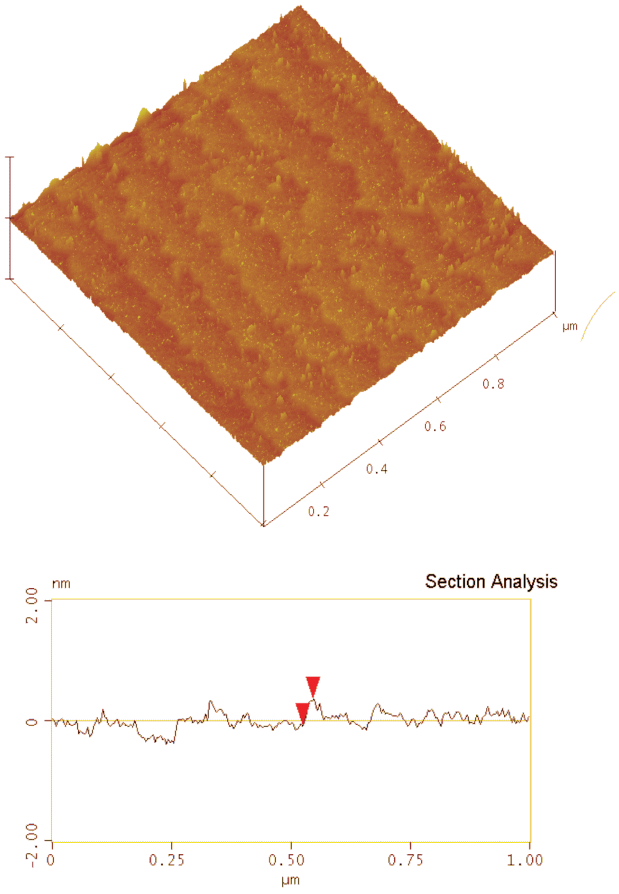

Figure 5.1 AFM image of a single film of LCMO deposited epitaxially on STO substrate using optimized growth conditions in the MK10 PLD system. A 1μm section profile of the film was taken corresponding to the scale shown on the surface view.

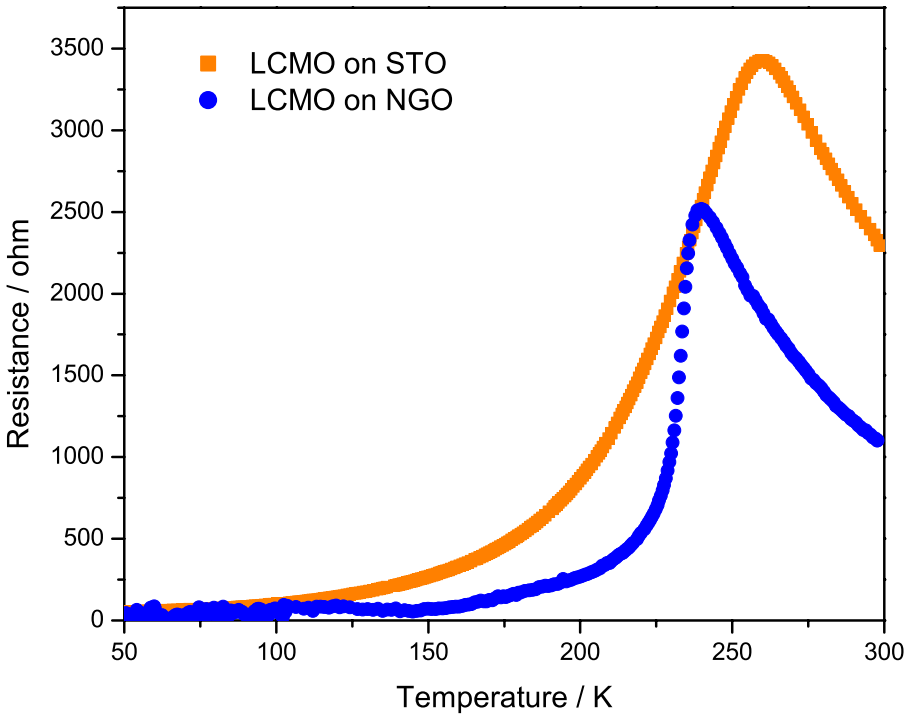

Figure 5.2 RT plots of continuous films LC(0.3)MO deposited on NGO and STO single crystal substrates in the MK10 PLD system.

The terraces, shown in Figure 5.1, are indicative of the step-flow growth during deposition. In step-flow growth, the adatoms start by collecting initially at the corners of the steps on the substrate surface, and then growing outwards towards the edge of the step. This results in layer by layer growth and hence, an even distribution of the deposited film. The height of each step, between the two red arrows shown in the section analysis, is 0.475nm, approximately the height of one unit cell.

Figure 5.2 shows the RT of LC(0.3)MO films deposited on STO and NGO substrates using the same conditions in the MK10. The different RT characteristics of both films is due to the lattice mismatch between LC(0.3)MO and the different substrates as discussed in the following sections. Calculated from Table 5.1, the lattice mismatch between LC(0.3)MO with STO and NGO is -1.41% and -0.36% respectively.

5.3.3 Influence of lattice mismatch on LC(0.3)MO transport properties

A small substrate-film lattice mismatch was crucial for the quality of the heterostructures fabricated and used in this thesis. We examined the effect of lattice mismatch on the RT behaviour of LC(0.3)MO films. For good spin transport from a manganite film into a superconductor, a high T_{Curie}, together with a sharp transition at the film's T_{Curie} is favorable because it is indicative of the homogeneity of the film. A poorly epitaxial film with higher density of defects and T <

T_{Curie} would result in a lower polarization of the current injected from the ferromagnet into the superconductor[1]. It was observed, from Figure 5.2, that the film grown on STO has a T_{Curie} of 260K while that grown on NGO has a T_{Curie} of 240K. The LC(0.3)MO lattice being smaller will stretch in alignment with the sides of each substrate a-b unit cell.

In the case of NGO, with its small lattice mismatch with LC(0.3)MO, the small tension in the film can reduce the film roughness. However, the T_{Curie} of the strained film is lower than that of the bulk, $\sim$ 270K. This is because, with its lattice in tension, it is more difficult for ferromagnetic ordering via double exchange mechanism to take place. The T_{Curie} of the film can be improved, but at the expense of its smoothness.

The film deposited on STO will be more strained due to the larger lattice mismatch. At some point during film growth, interfacial dislocations are likely to occur when the thickness of the growing film reaches a critical thickness [78]. Here, the unit cells of the LC(0.3)MO film are also in tension, but the film is expected have a shorter critical thickness, due to the added strain, beyond which relaxation through defect formation and columnar growth occurs. The relaxed upper portion of the LCMO film hence accounts for the film's higher T_{Curie}. The higher T_{Curie} observed is thus related to this increased strain at the STO-LCMO interface.

Evident also in Figure 5.2 is the wider transition range of the LC(0.3)MO grown on STO, due to the bigger range of strained states present in the LC(0.3)MO/STO film, as discussed above. The sharper paramagnet to ferromagnet transition observed in the LC(0.3)MO/NGO plot indicates that the film is more homogenous and has a higher degree of epitaxy.

Whilst we were mainly interested in LC(0.3)MO films with high T_{Curie} and sharp paramagnetic to ferromagnetic transitions, we had to ensure the smoothness of our films as that indicated the film's integrity down to its interface with the substrate.

5.3.4 Cuprate / Manganite Bilayer Deposition

The effective deposition of LC(0.3)MO on YBCO is vital for the success of fabricating our devices. Although their close lattice match allows for these two class of materials to be grown epitaxially, there are, however, several issues when depositing such heterostructures, such as:

1. The surface roughness of YBCO is high due to its tendency for spiral growth, thus the subsequent LC(0.3)MO film deposited tends to be rough. This roughness propagates throughout the layers, and promotes the defect formation in the subsequent layers, thus increasing the total film surface roughness with each additional layer.

2. As noted by Schoop et al [86], a spin glass phase develops at the YBCO/LC(0.3)MO interface, even for high quality interfaces. The formation of this phase is due to several reasons,

[1] In good quality LCMO films, the transition, from paramagnetic to metallic, temperature (indicated by a peak, T_p in RT measurements) has been observed to be the same as the T_{Curie} (measured by MT plots) [85]. These values might differ by 1-2K depending on the film quality. For ease of measurements in this thesis, T_p was assumed to be T_{Curie}.

such as interfacial strain, inter-diffusion of atoms at the interface and the deoxygenation of the films.

3. The high temperatures required for deposition of epitaxial LC(0.3)MO ($\sim 850°C$) results in the deoxygenation of the previously deposited layers. Deoxygenation is especially detrimental to the T_c of YBCO as discussed in Section 2.3.3. The high temperatures also increases the mobility of atoms and may cause the increased interdiffusion of atoms between adjacent layers.

We investigated and optimized the deposition conditions for the growth of such heterostructures using the systems available in the Device Materials Lab. This study of the manganite/cuprate thin film deposition, with respect to as many of the above mentioned issues, was essential for the fabrication of our devices.

LC(0.3)MO on YBCO deposition parameters

In order to deposit high-quality LC(0.3)MO films whilst reducing degradation of the YBCO film, the substrate temperature and the O_2 partial pressure were fine-tuned.

As can be seen from the YBCO phase diagram in Figure 2.11, the pre-anneal step used in the deposition of LC(0.3)MO which subjects the samples to 850°C in a vacuum of 10^{-7} Pa, would destabilize YBCO, causing it to break down into Y_2BaCuO_5 + $BaCuO_2$ + Cu_2O. This partial decomposition of YBCO into its constituent compounds would lead to a suppression of T_c.

The pre-anneal and deposition conditions would also lead to a structural change in YBCO due to deoxygenation. This occurs through the out-diffusion of oxygen atoms from the Cu-O chains, leaving a tetragonal[2] structure. This instability of orthorhombic YBCO at high temperatures and low O_2 partial pressures is evident in the phase diagram. For instance, for YBCO to retain its orthorhombic structure at 700°C, the O_2 partial pressure has to be above 5kPa. At a slightly higher temperature of 730°C, the O_2 partial pressure required is 100kPa.

Hence, as expected, the high temperatures optimum for the deposition of LC(0.3)MO is unfavorable for YBCO. The length of exposure time of YBCO to these deposition conditions should be kept to a minimum. After deposition, the bilayer should be post-annealled in excess O_2 partial pressures, at lower temperatures and for a longer duration. The post annealling parameters are important for oxygenating YBCO and thus restoring its T_c.

The following procedure was used for the deposition of LC(0.3)MO on YBCO:

1. The YBCO film was heated to 730°C in 100kPa O_2 at a rate of 25°C/min.

2. The O_2 in the chamber was vacuum-pumped, a flowing O_2 partial pressure of 15Pa was introduced, as per optimized LC(0.3)MO deposition procedure.

[2]It must be noted that the a-b lattice parameters of tetragonal YBCO is 3.87, compared to a = 3.82 and b = 3.88 of the orthorhombic structure. Hence, as the a-b lattice parameters of these two YBCO phases are not significantly different, the LC(0.3)MO films were still able to grow epitaxially on the tetragonal YBCO.

3. LC(0.3)MO was deposited at 730°C, and 15 Pa O_2 partial pressures, using a pulsed laser frequency of 1 Hz, and a laser fluence of $2J/cm^2$.

4. After the LC(0.3)MO deposition, the films were post-annealled for 1hr in 100kPa O_2 at 500°C, as per standard YBCO post-annealling procedure used in the MK9 PLD system.

An LC(0.3)MO deposition, using these LC(0.3)MO deposition parameters, on patterned YBCO tracks grown on single crystal STO substrate show that the YBCO retained a T_c of 88K for both the 8μm and the 4μm wide YBCO tracks. The T_p of the 8μm track was $\sim$ 250K. This proved that the above procedure worked sufficient well to be used for the device fabrication.

5.4 Device Fabrication

The following sections provide an overview of the processes involved in device fabrication. A schematic of the junction profile is shown in Figure 5.3.

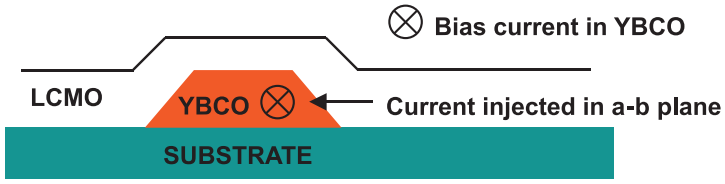

Figure 5.3 Current injection through the a-b plane in ramp junctions of our spin injection devices

5.5 Mask Design

Mask patterns, used in the lithography to produce the YBCO and LC(0.3)MO tracks for our spin injection devices, were designed to facilitate our study of the length scales associated with spin effects. These mask designs are shown in Figures 5.4 and 5.5.

The mask pattern for the bottom YBCO track in our spin injection device is represented in green in Figures 5.4 and 5.5. Taking into account the estimated transfer lengths associated with LC(0.3)MO/YBCO junctions in our devices, we designed the device tracks with widths of <10μm. Devices of such widths were also suggested by Gim et al [27]. The main YBCO track varied in width from 8 μm, to 6 μm and to 2 μm at its narrowest.

The pattern was designed such that the LC(0.3)MO tracks will bridge, orthogonally, the center of the YBCO tracks at these three different widths, ie. there will be three different devices on each superconducting track. The pattern was also designed such that the transport measurements will be taken of each device at its narrowest region, ie. where the LC(0.3)MO bridges the YBCO.

Patterns were also designed with the YBCO track angled at 45° to the a or b axes, so as to take advantage of the nodes of the d-wave superconductor. The energy gap in YBCO is

Figure 5.4 Mask design of 90° spin device. Green represents mask for YBCO tracks while pink represents mask for LC(0.3)MO tracks. At the largest YBCO/LC(0.3)MO track junction, the YBCO track width is 8μm.

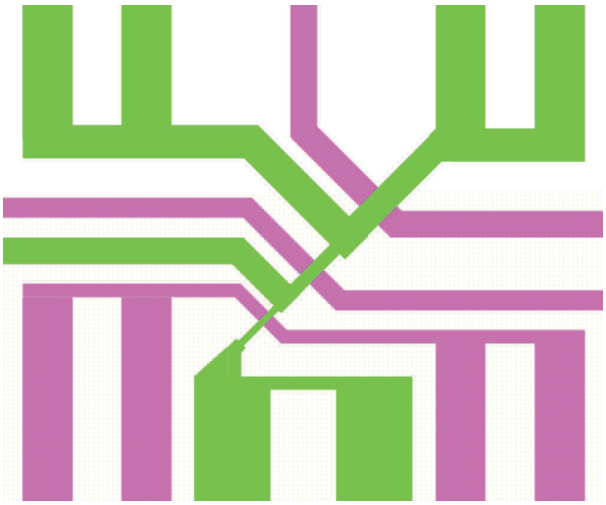

Figure 5.5 Mask design of 45° spin device. Green represents mask for YBCO tracks while pink represents mask for LC(0.3)MO tracks. At the largest YBCO/LC(0.3)MO track junction, the YBCO track width is 8μm.

zero in the nodes, presumably allowing the maximum injection of spin-polarized quasiparticles from the ferromagnet. Enhanced effects observed in this set of devices would prove that these effects are due to the injection of spin-polarized quasiparticles, and not to resistive heating. The complementary mask patterns for the topmost LC(0.3)MO tracks is represented in pink in Figures 5.4 and 5.5.

As the conduction through YBCO occurs predominantly in the a-b plane, as shown in Table

2.2, we expect to observe more pronounced effects in the a-b direction (ie. along the Cu-O planes). Hence the devices were fabricated such that current was injected parallel to the a-b direction.

5.6 Photolithography

Photolithography was performed in a Karl Suss mask aligner. It can be performed before or after film deposition to produce tracks during device fabrication.

For our spin injection devices, the following lithography steps were performed on 100nm YBCO film grown on a LAO[3] substrate:

1. The film and substrates were soaked in an acetone bath and ultrasound to remove traces of grease and dust which might be on the surface.

2. The surface of the film was further cleaned by spray drying with propanol using an airbrush.

3. The chip was then transferred to the resist spinner onto which four drops of Shipley AZ5214 positive photoresist was pipetted.

4. The chip was spun at 4000 rpm for 30 seconds, leaving a uniform thin layer of resist approximately 1.4μm thick in the middle.

5. The chip was then transferred to the Karl Suss for photoresist edge-bead removal.

6. The edge bead was removed using the edge-bead mask. Exposing the levees of photoresist on the chip edge to UV for 30 seconds.

7. The chip was then developed using 4:1 developer:water solution to remove the edge-bead, cleaned with de-ionised water, and then examined under the optical microscope to ensure the higher photoresist on the edges of the film have been completely removed.

8. Mask patterns of the YBCO and LC(0.3)MO tracks were transferred from the designed masks onto the photoresist using UV light in the Karl Suss.

9. The photoresist was developed in 3:2 developer:water solution to allow the finer features of the track patterns to be developed more slowly and carefully.

10. Gold deposition for contact pads was performed using a negative mask. For gold deposition, the photoresist, after exposure, was soaked for two min in chlorobenzene to harden the upper surface of the photoresist, which develops at a slower rate compared to the rest of the photoresist. This allows for 'ledges' in the photoresist profile to develop. These 'undercut' edges promote the easier removal of gold from undesired regions of the chip during lift-off after deposition in the NOAR.

[3]LAO has a similar lattice mismatch to YBCO as NGO, See Table 5.1

5.7 Ramp Type Junctions

Ramp junctions have been developed for the fabrication of HTS oxide Josephson junctions. The ramp geometry allows materials to be coupled in the preferred crystallographic directions, which can be particularly important for strongly anisotropic materials. Ramp junctions also allow for the possibility of fabricating smaller junctions with area well below 1 μm^2.

For YBCO where $\xi_{ab} > \xi_c$, ramp junctions allow for the combination of the perovskite type oxides in the a-b direction. However, the ramp angle affects the orientation of LCMO deposited. For ramp junctions with slopes steeper than 40°, the [100] orientation grows, leading to the formation of two grain boundaries in the top YBCO layer. If the slope is below 40°, the [001] orientation grows preferentially. Hence, a high quality epitaxial junction is dependent on a smooth ramp surface with no variation in slope or protruding outgrowths [86].

There have been several methods used to fabricate ramp junctions [87]. In the shadow mask method [88, 89], the ramp is formed during the deposition, and hence contamination is reduced a minimum. Ex-situ methods require the deposition of a photoresist mask after deposition of the first electrode. After the mask deposition, the ramp can be formed by wet chemical etching [90] or ion milling [91, 92, 93]. Although ex-situ processes result in contamination at the ramp interface due to exposure to the atmosphere, and also chemicals used for etching or the photolithography techniques, it was the best method for creating ramp-junctions on the micron-scale tracks used in our experiments.

The use of ion milling remains the most established way to fabricate ramp junctions. However, during the ion milling process of YBCO ramp junction fabrication, the crystal structure of the ramp is affected and a thin amorphous surface layer may be formed [93]. The amorphous film is caused by the combination of ion bombardment and contamination due to the ex-situ process. Damage to YBCO surfaces can be minimized by reducing the momentum of ions perpendicular to the ramp surfaces.

Smooth ramp junctions are also difficult to fabricate because outgrowths form at the bottom of the ramp during annealing [86]. A plausible explanation for the roughness is the recrystallization of the amorphous YBCO surface. As heating is required for the deposition of the adjacent films, the outgrowths which form even on the smoothest ramp surfaces may reduce the epitaxial quality of the film at the interface.

5.7.1 Fabrication of ramp junction

The fabrication procedure for ramp junctions is similar to that of the fabrication of a track using photolithography, as described in Section 5.6. There are two significant additions to the procedure: resist reflow and off-axis milling. At least one of these can be used for ramp junctions fabrication.

Ramp junctions of 30° could be obtained by resist reflow [94]. This step includes annealing the photoresist mask on a hotplate after patterning and developing of the photoresist. The

annealing step will cause the resist to flow due to the surface tension. The resulting ramp angle is typically 14-30° smaller than the initial resist profile [86].

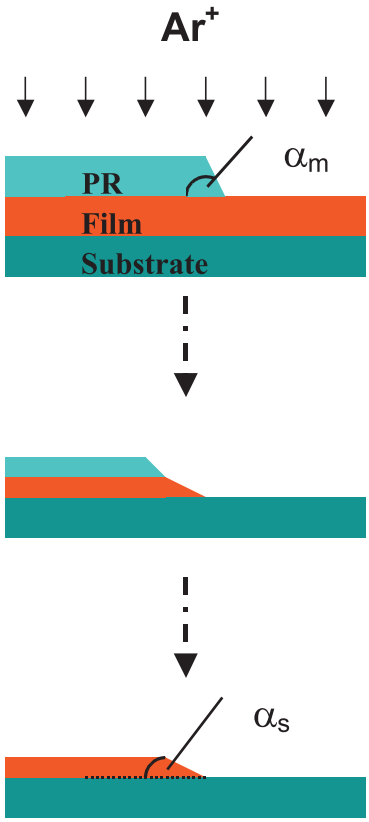

Figure 5.6 Schematic of ramp junction fabrication with direct ion bombardment.

The use of resist reflow alone, with ions at normal incidence to the substrate surface, for ramp junction fabrication is shown in the schematic in Figure 5.6. Two important parameters in this method [95] are the ratio of ion milling rates between the mask material and the film, v_m/v_s, and the mask profile. A higher ratio of v_m/v_s will yield a gentler slope [95].

A disadvantage of resist reflow is that the exact angle of the resist slope is not reproducible as very little is known about the influencing factors such as photoresist aging and viscosity and post-bake parameters. Due to the differential etching rates of the photoresist and the films, the slope of the photoresist facilitates the formation of ramp junctions.

During ion milling, the sample is also installed such that the incident beam is at a 30° angle to the substrate perpendicular. Rotation of the sample allows for the etching of redeposited material, and hence improving the quality of the ramp surfaces. An advantage to this off-axis ion milling is that the amount of direct perpendicular ion bombardment on the ramp surface, and hence ramp surface damage, is reduced.

Overmilling of narrow ramp-edged tracks can reduce the widths of the tracks significantly. In the worst case, the track may have a triangular cross-section, which is also detrimental for

further epitaxial growth of films on top. It is thus necessary for controlled milling during ramp fabrication.

5.7.2 Procedure used for ramp edge fabrication

In our investigation ramp type junctions were necessary for the epitaxial growth of LC(0.3)MO films onto YBCO tracks, preserving the homogeneity of the LC(0.3)MO track, as described earlier. This was done by annealing the photoresist, after patterning and developing the YBCO tracks, in a 120°C heater for 1.5 min. This annealing 'relaxes' the sides of the resist, forming a sloped profile. The chip was then milled on the rotating stage at a 45° angle to the bombarding ion beam in the NOAR. The track profile was then examined under the AFM. The sides of the tracks were consistently angled at 12-16°, allowing further processing. It is expected that homogeneity of the film would be preserved if the junction angle is below 40° [18].

5.8 Overview of device fabrication procedure

In this section, we map the fabrication procedure of our spin injection devices. The procedure can be briefly summarized in the following steps:

1. The surface of the 100nm YBCO film was cleaned by soaking in acetone and propanol in turn in an ultrasound bath to remove surface contaminants such as grease or dust.

2. We used contact photolithography to pattern the films in the Karl Suss mask aligner. This procedure was described in Section 5.6.

3. The YBCO film was then ion-etched into tracks of varying widths using the NOAR. The film was milled at an angle to the argon ion beam to fabricate ramp edges.

4. After milling, the chip was cleaned in acetone and propanol to remove the photoresist.

5. The chip was milled again very quickly in the NOAR to remove contaminants such as residual photoresist or acetone. This step is necessary because some of the photoresist may be hard-baked during the previous ion-etching step. Hard baked photoresist is almost impossible to remove with acetone. This short (3-5min) etching step was done to improve the interface of our YBCO/LC(0.3)MO ramp junctions.

6. Immediately after milling, the chip was removed, placed into the MK10 PLD chamber for LC(0.3)MO deposition. Unfortunately, the YBCO surface had to be exposed to atmosphere during the transfer from the NOAR to the PLD. Exposure of oxide films to the atmosphere was less detrimental compared to metallic films which tend to form an insulating oxide passivation layer at the surface.

7. 100nm of LC(0.3)MO was grown on the entire top surface of the chip using pre-determined optimized growth conditions.

8. The LC(0.3)MO film was patterned using contact photolithography into the corresponding tracks as shown in Figures 5.4 and 5.5.

9. Photolithography was subsequently performed with the 'gold negative mask' for gold contact deposition.

10. Gold deposition was performed by first pre-milling the film surface to remove impurites, and then sputtering in-situ in the NOAR. The pre-millin step improves the quality of the Au/oxide interface

11. The final processing step of our spin injection device is gold lift-off.

The fabrication of the chip, D4, is mapped below.

5.8.1 Fabrication of chip D4

Prior to processing, the YBCO film was examined using XRD for its epitaxial quality and phase homogeniety. Figure 5.7 shows that there are no additional phases or orientations present in the YBCO film. This scan also serves as a comparison, at later stages of the fabrication process, for checking that the quality of the YBCO had not deteriorated with processing (eg. annealling) and for the presence of additional phases after LC(0.3)MO deposition. The FWHM of the YBCO acquired in a rocking curve was 0.54°Omega. The root-mean-square (RMS) roughness of the YBCO film was 7-8nm.

The YBCO was patterned, using contact photolithography as discussed in Section 5.6, and then milled in the NOAR into tracks with ramp edges. For better control of the milling process, we measured the resistance of the top surface of the chip (ie. YBCO film) during milling . This in-situ resistance measurement, as shown in Figure 5.8, allows for endpoint detection and hence prevents over-milling.

As discussed earlier, overmilling of the YBCO ramp-edged tracks can result in a change in track profile, which is detrimental for the further epitaxial deposition of films. For our devices, the profile of the ramp edge can be studied using the AFM, as shown in Figure 5.9.

Photographs of the two devices, 90° and 45°, are shown in Figure 5.10 and 5.11.

The YBCO tracks were milled quickly to remove surface impurities. 100nm of LC(0.3)MO was grown epitaxially on the substrate and over the YBCO tracks. The quality of the LC(0.3)MO film was investigated again using XRD and AFM. In Figure 5.7, we see that the LCMO (001) and (002) peaks at 22.9° and 47.0° respectively coincide with the (003) and (006) peaks of YBCO at 22.8° and 46.6°. The figure also confirms that no additional phases due to ion diffusion developed during the high-temperature deposition of the LC(0.3)MO.

We also performed transport measurements on the LC(0.3)MO film to investigate the paramagnetic to ferromagnetic transition behaviour of the LC(0.3)MO film. This four-point measurement was done using pogo pin-contacts on the edge of the chip to prevent damage to the devices. Figure 5.12 shows a comparison of the transport properties of two LC(0.3)MO films deposited in

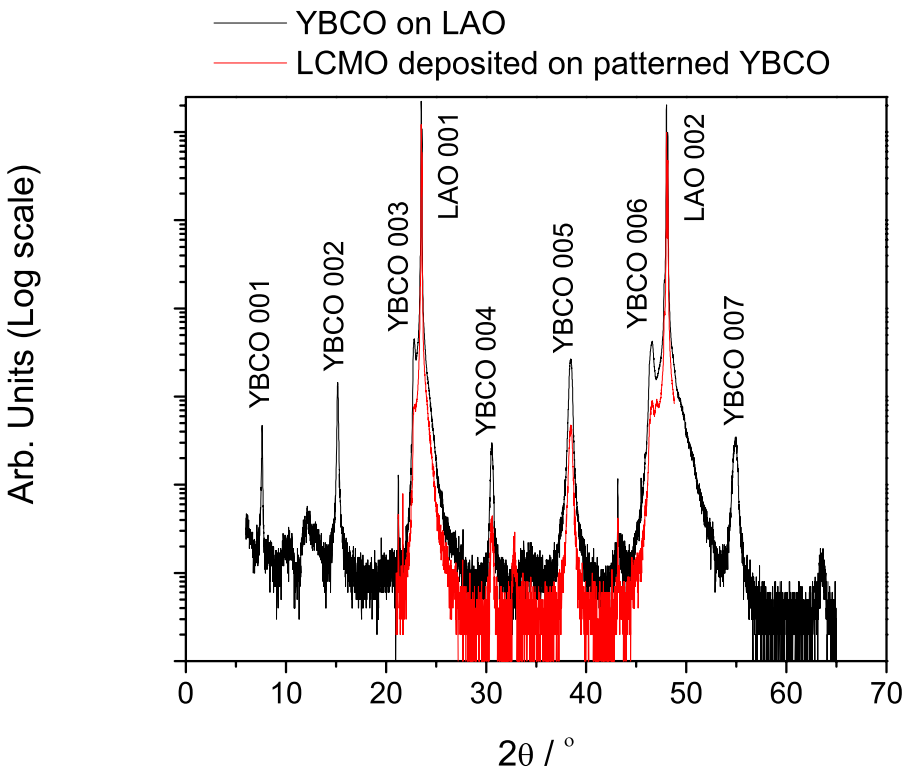

Figure 5.7 XRD scans of the YBCO and LCMO films during fabrication process.

the same run: one on a cleaned LAO substrate and the other on the chip with patterned YBCO tracks. The transition temperature for the LC(0.3)MO film on LAO was 260K, while that of the film deposited on D4 was 265K. The drop in resistance with decreasing temperatures in both samples were similar, indicating that the two films are of comparable quality.

The resistance-temperature (RT) plot also showed a drop in resistance due to a superconducting transition at 87K. RT of the LC(0.3)MO/D4 is lower because a fraction of the bias current is shunted by the lower resistivity YBCO. Hence, this behaviour can be attributed mainly to the YBCO film. This high YBCO T_c confirms that the YBCO had not deoxygenated during the PLD of LC(0.3)MO. These transport measurements confirmed that the quality of the LC(0.3)MO and YBCO at this stage in the fabrication process.

We also the measured the magnetic properties of the LC(0.3)MO film on the chip, as shown in Figures 5.13 and 5.14. The magnetic plots confirmed that the LC(0.3)MO film deposited on YBCO tracks was ferromagnetic. These measurements also provided the saturation field values for our films, which in this case is approximately 250mT at 120K. The film has a H_{co} of 9mT and 16mT at 200K and 120K respectively. Figure 5.14 shows that the magnetic properties of the chip was dominated by the diamagnetism of the YBCO. The plot shows a complex interaction between the Meissner currents in YBCO with the ferromagnetism in LC(0.3)MO, similar to that observed by Przyslupski et al who studied the magnetic properties of LSMO/YBCO superlattices

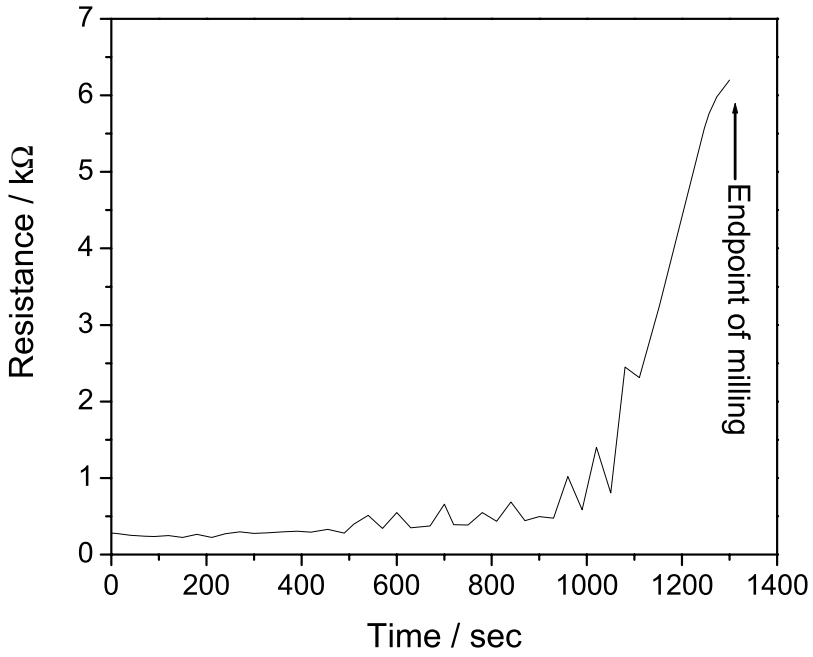

Figure 5.8 In-situ two-point resistance measurements of YBCO film during milling in the NOAR. The endpoint of the milling was reached when the resistance of the film increases exponentially by over an order of magnitude.

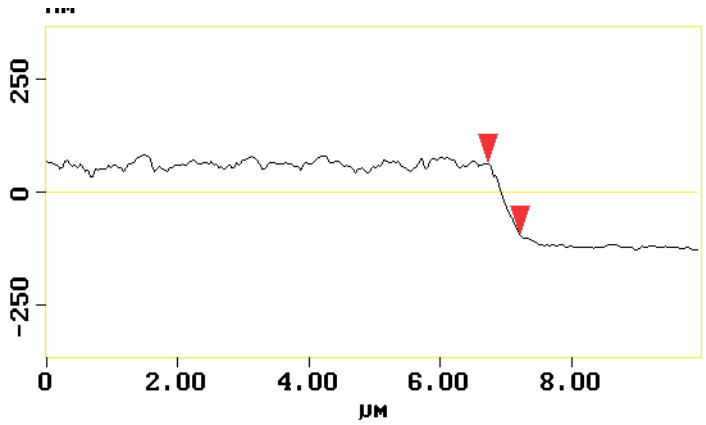

Figure 5.9 AFM profile of a YBCO ramp-edged track. The angle of the ramp is 17.9°

[96].

The MH characteristics of the plain LC(0.3)MO/LAO is shown in Figures 5.15 and 5.16.

Most importantly, the LC(0.3)MO/YBCO sample showed similar H_{co} value to plain LC(0.3)MO samples, as this was evident that the films were of similar epitaxial quality. The LC(0.3)MO

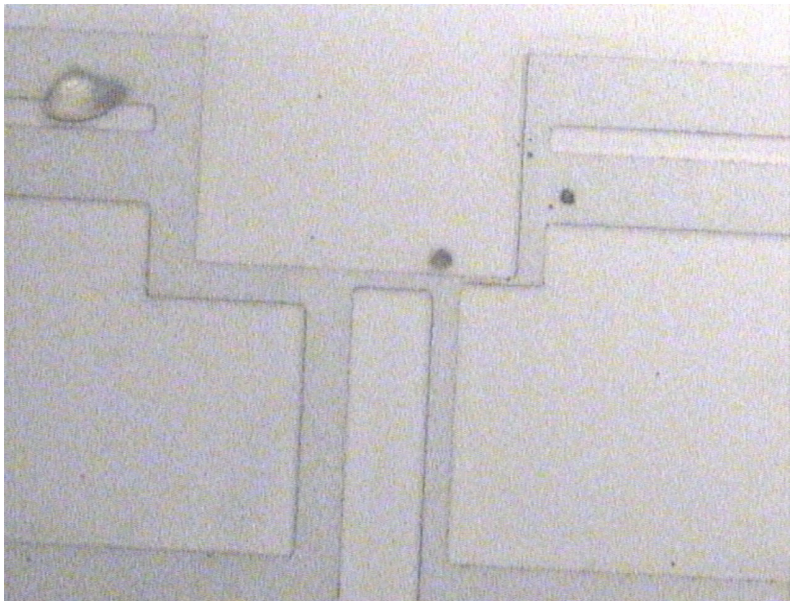

Figure 5.10 Photograph of patterned YBCO film, 90° device, D90°. Magnification: 400×.

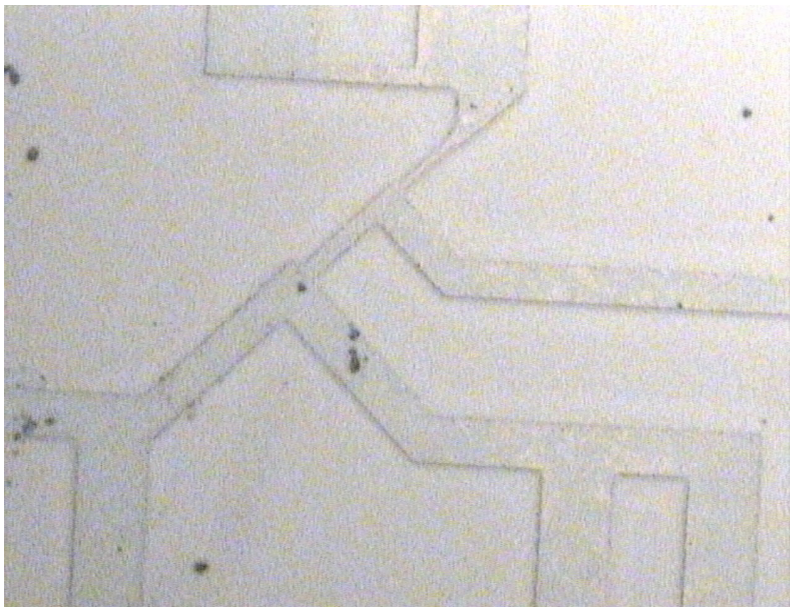

Figure 5.11 Photograph of patterned YBCO film, 45° device, D45°. Magnification: 400×.

film on D4 was subsequently patterned and milled into tracks which bridge the YBCO tracks.

RT plots of the some of the final devices are shown in the following figures, and a picture of the final 90° device is shown in Figure 5.20.

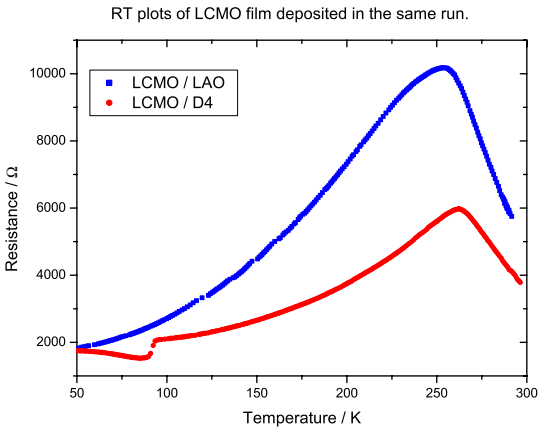

Figure 5.12 RT plot of LC(0.3)MO films deposited on cleaned a LAO substrate, and a chip with patterned YBCO tracks

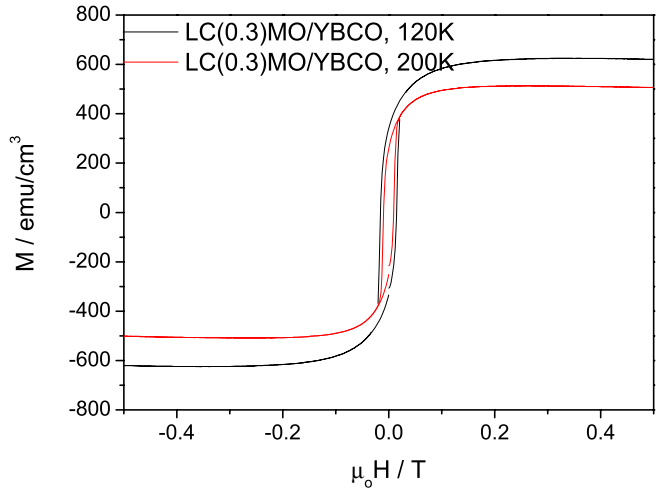

Figure 5.13 MH characteristics of LC(0.3)MO film deposited on patterned YBCO tracks in D4.

5.9 Conclusions

We have successfully used various deposition techniques (namely PLD and Ar^+ ion sputtering) and cleanroom processing techniques to fabricate micro-devices with cross junctions of LC(0.3)MO over YBCO. These devices, which consist of ramp-edge junctions, were to used for 3-terminal measurements of spin injection from colossal magnetoresistive material into high temperature superconductors.

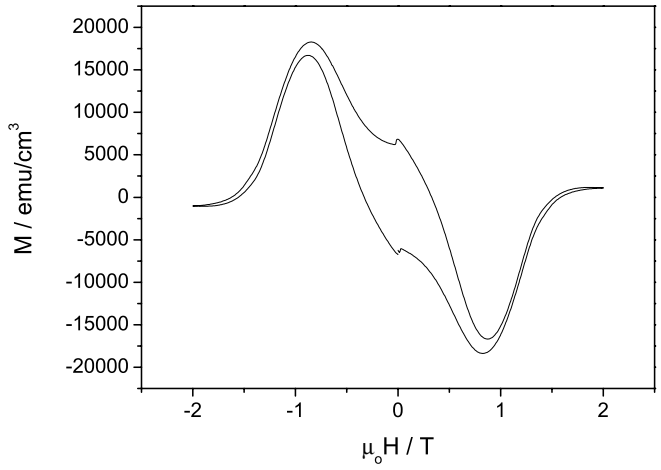

Figure 5.14 MH characteristic at 50K of D4 after LC(0.3)MO deposition. The diamagnetic characteristics of YBCO dominate the magnetic properties.

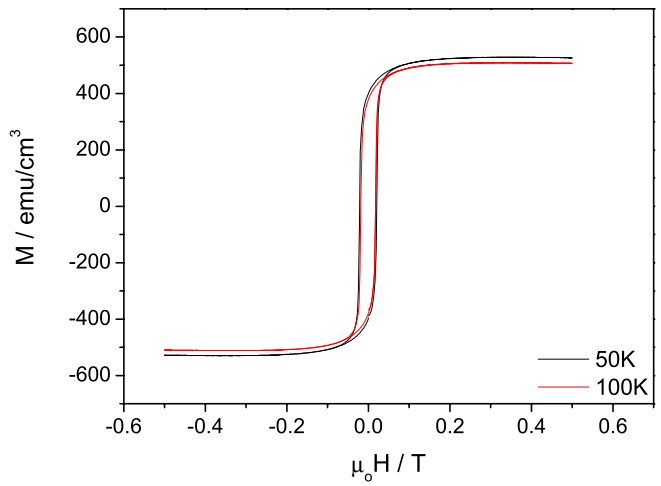

Figure 5.15 MH of LC(0.3)MO on LAO sample grown in the same deposition run as D4.

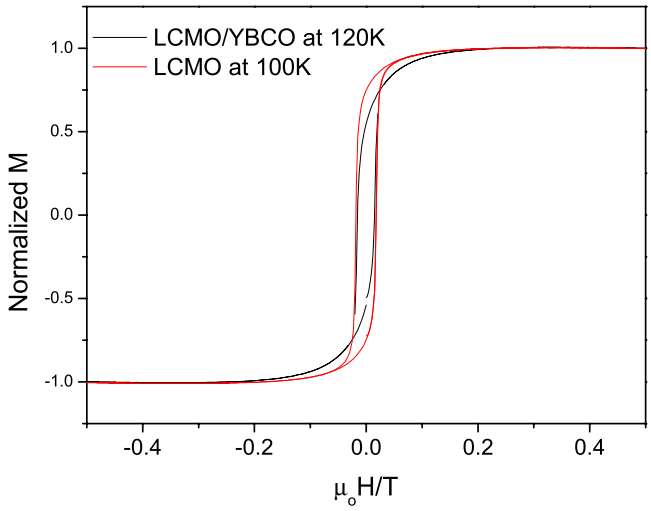

Figure 5.16 A comparison of the MH properties of LC(0.3)MO on LAO with that of LC(0.3)MO on YBCO/LAO at similar temperatures.

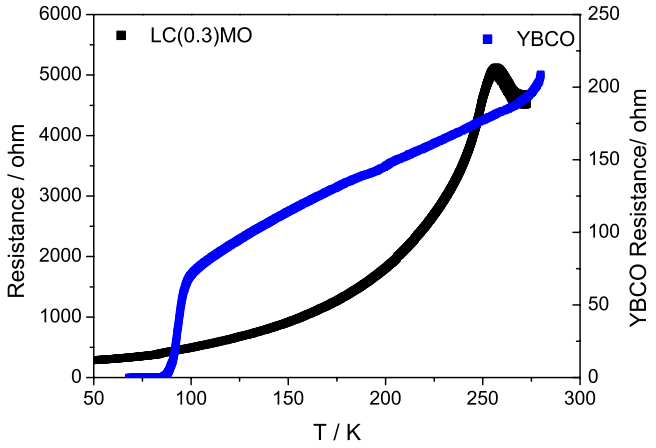

Figure 5.17 RT plots of the 8μm YBCO and LC(0.3)MO tracks in the 45° device. The device was superconducting at 85K.

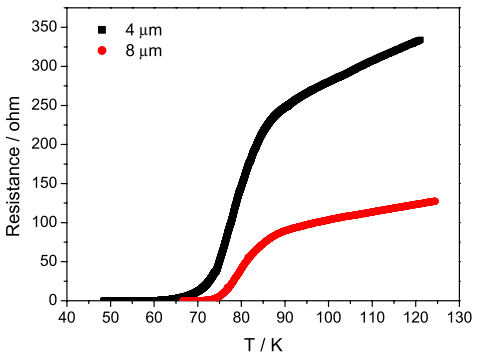

Figure 5.18 RT plot of 4μm and 8μm YBCO tracks in the 90° device. The devices have T_c values of 63K and 73K respectively.

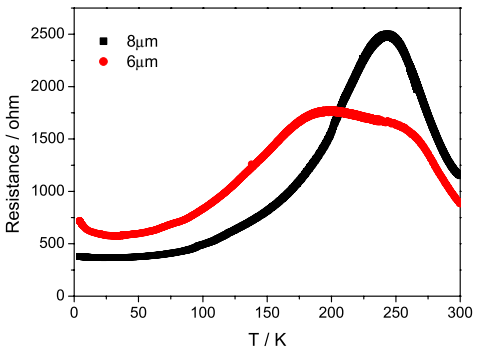

Figure 5.19 RT plots of 6μm and 8μm LC(0.3)MO tracks in the 90° device.

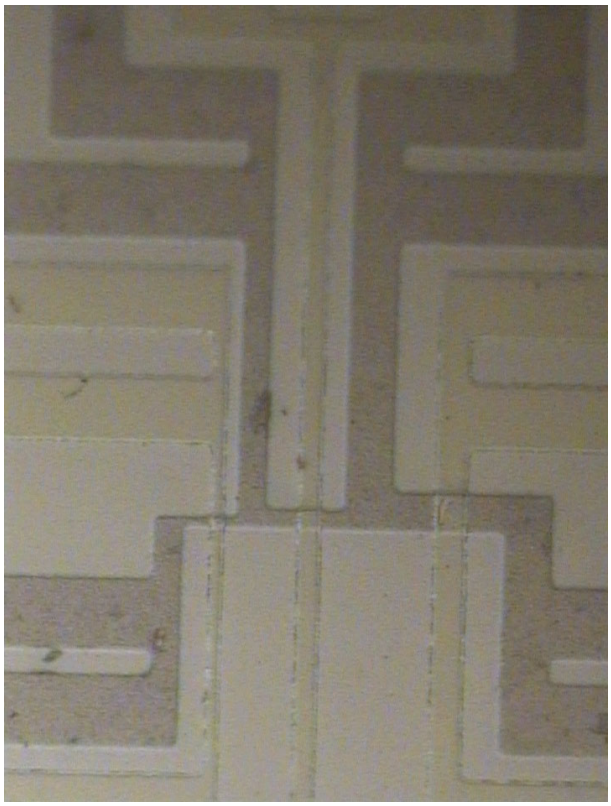

Figure 5.20 Photograph of final D90° device. Magnification: 400×.

Chapter 6

Spin Injection 2: Critical current studies

6.1 Motivation

As discussed in Chapter 2, spin polarized current is expected to induce further non-equilibrium in YBCO compared to ordinary particle injection. This is due to the additional spin flip time required for the injected spin-polarized particles to relax and recombine into part of the superconducting condensate.

This chapter investigates the feasibility of using polarized injection current as a means to control superconductivity. We examined the effects of injection current I_{inj} on the critical currents, I_c, in YBCO, and how the degree of current polarization affects the I_c suppression in our devices. Unlike other groups, our devices were designed inject spin polarized current into the YBCO a-b plane. These effects were studied in our devices with tracks aligned both 90° (D90°) and 45° (D45°) to the a and b axis of the single crystal materials.

As mentioned earlier, there are several other issues which obscure the results observed in similar spin injection into superconductor experiments performed elsewhere. Current summation effects due to the device geometry, local heating effects due to the injected current and flux effects due to the presence of the external field were the main problems in such experiments, and were described in detail in Sections 3.14 and 3.3.5. Our measurement procedures were designed to isolate and eliminate such effects in order to pinpoint effects caused solely by spin injection into YBCO.

In this chapter, we analyse the device used, describe and discuss the spin injection measurements performed. There is also an analysis of the current path at the injector/YBCO junction.

6.2 Measurement Setup

Current injection measurements were performed using the following setup. The quasi-dc I_{bias} current, which was controlled by the computer, was passed into the sample in the measurement probe. The resulting voltage signal was sent via a voltage amplifier back to the computer.

These measurements were performed using the Heliox, described in Section 4.6.2, because it was able to provide a large (relative to the other dip probes) magnetic field with its superconducting coil, which had to be immersed in liquid helium and operated in its superconducting state. The samples thus did not heat up as a consequence of the increased current supplied to achieve a greater magnetic field, as was observed with the other cryogenic dip probes used. The sample was cooled using a flow of liquid He from 1K pot and maintained, in combination with a heater, at a temperature below the device T_c. As the Heliox was mainly used for low temperature measurements, maintaining a stable temperature at a higher temperature was more complicated. The procedure we found most effective was described in detail in Section 4.6.2. The devices, when measured, were placed in the middle of these coils so as to maximize the applied fields to the samples.

There are two kinds of electric sources which can be used in our measurements setup shown in Figure 6.1. For our measurements, it is essential that a current source instead of a power

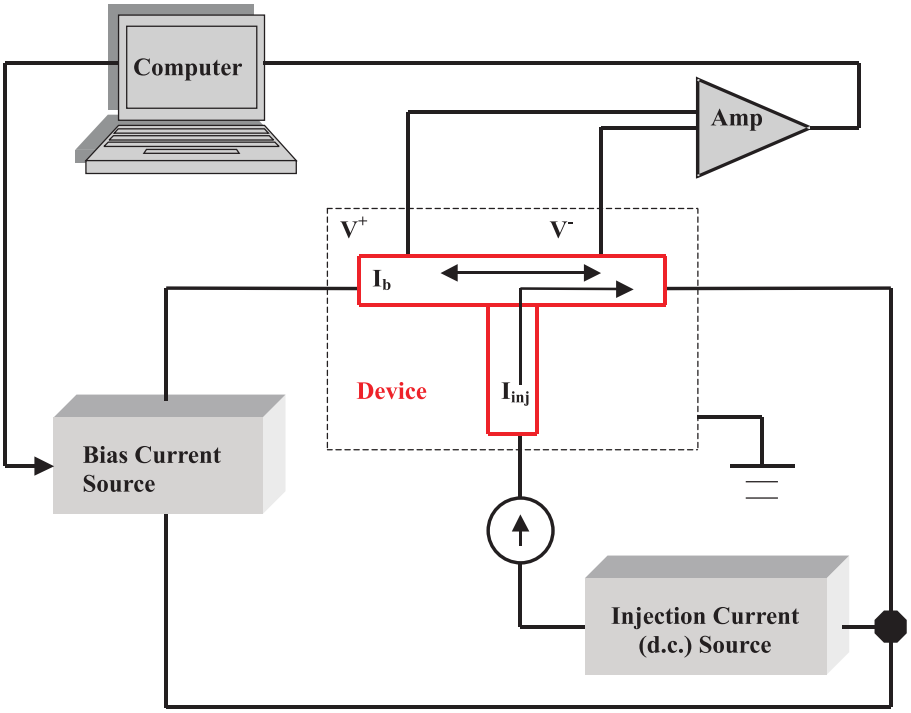

Figure 6.1 Experimental set-up used for spin injection measurements. The Heliox was the main cryogenic probe used for the measurements.

source was used to supply the injected current.

Using the current source, the current in the circuit will remain constant through fluctuating resistance, as the power required compensated with a corresponding voltage. The current in the circuit when using a voltage source, however, fluctuates with changing resistance, which may occur due to temperature drift or localized heating for example.

6.3 Device characterization

Before conducting spin injection measurements, it was necessary to characterize the devices in order to better interpret the observations.

6.3.1 Transfer Length

As mentioned in the previous chapter, the devices were designed such that the YBCO tracks were narrower than those previously measured by other groups. The transfer length is thus significant compared to the track widths.

The transfer length for our LC(0.3)MO/YBCO devices was calculated using Equation 3.12.

For a 100nm thick LC(0.3)MO, the sheet resistance, ρ/thickness, is shown in Figure 6.2.

Using specific contact resistance values of 10^{-4} and 10^{-6} Ωcm^2, an approximation range for cuprate/manganite interfaces [27], the transfer length of the spin injection device at 50K was

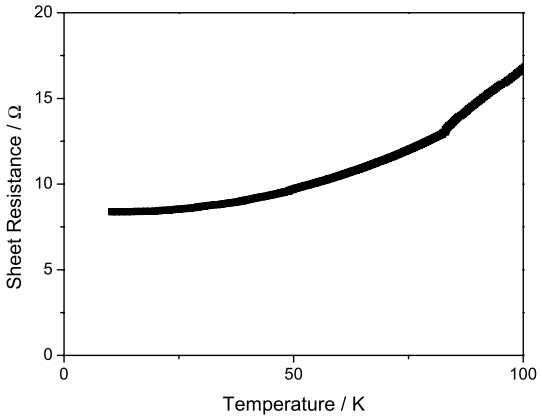

Figure 6.2 Sheet resistance versus temperature in D45°.

estimated to be 32μm and 3.2μm respectively. Current in the devices was thus injected into a significant part of the 8μm wide YBCO track used for the spin injection measurements.

6.3.2 Device Geometry Effects

As described in Section 3.14, the 3-terminal side geometry employed in our devices has characteristic current summation effects. These current summation effects were largely unaccounted for by many groups investigating the spin injection into superconductors before 2001. However, it is very important to isolate these current summation effects due to the device geometry in order to effectively examine for effects due to spin polarized current injection. Current summation, with respect to our device geometry as shown in Figure 6.3, is discussed below. In this discussion, as I_{bias} was quasi-dc, current in the direction 'A' was assumed as the positive direction. I_c^+ and I_c^- represent the maximum and minimum zero-voltage currents.

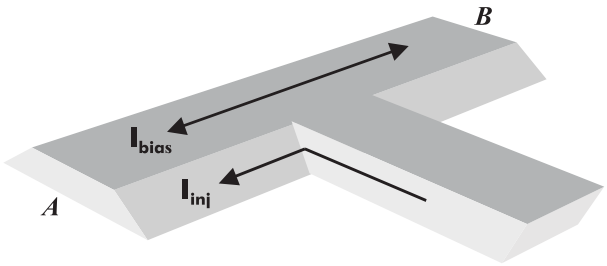

Figure 6.3 Schematic of the 3T side geometry used in the device. The geometry is different from those employed by other groups because it was designed for current injection into the a-b plane, over a narrow width of 4-8μm.

Consider a point at end 'A',

The I_c, when I_{bias} is in the positive direction, is given by,

$$I_c^+ = I_c^0 - I_{inj} \tag{6.1}$$

where I_c^0 is the I_c at I_{inj}=0.

When I_{bias} is in the negative direction, I_c is given by,

$$I_c^- = -I_c^0 - I_{inj} \tag{6.2}$$

At end 'B',

When I_{bias} is in the positive direction,

$$I_c^+ = I_c^0 \tag{6.3}$$

When I_{bias} is in the negative direction,

$$I_c^- = -I_c^0 \tag{6.4}$$

For I_{bias} in either direction, the $I_c^{\pm}$ values measured by the voltage leads are dominated by the region of the track (A or B in Diagram 6.3) where the $|I_c^{\pm}|$ value is greater. Hence, Equations 6.1 and 6.4 will characterize the behaviour, due to current summation effects, of a perfect 3-terminal device of geometry shown in Figure 6.3. I_c^+ varies with I_{inj}, while I_c^- is independent of I_{inj}, as illustrated by Figure 6.4.

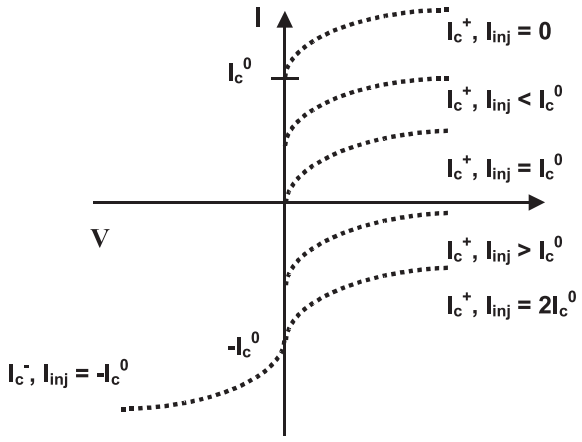

Figure 6.4 Expected I_c suppression observed in device IV measurements due solely to current summation effects, excluding any non-equilibrium effects. I_c^- remains constant, but I_c^+ varies with I_{inj}. I_c° represents the I_c at I_{inj}=0. We notice that superconductivity is completely suppressed in the device when I_{inj}=2I_c°.

The mid-point of the I-V curves were shifted by -I_{inj}/2. This information is a useful tool to assess the current path in the device. It is apparent from the Figure 6.4 that the spin injection measurements in the 3T geometry can be measured up to $I_{inj} = 2I_c^0$.

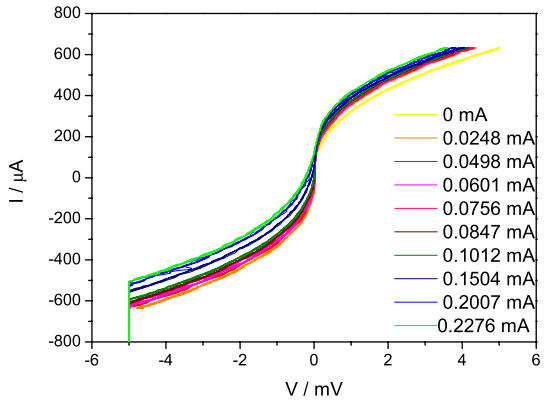

Figure 6.5 IV curves as a function of I_{inj} used in D90°. I_{inj} anti-// I_{bias}.

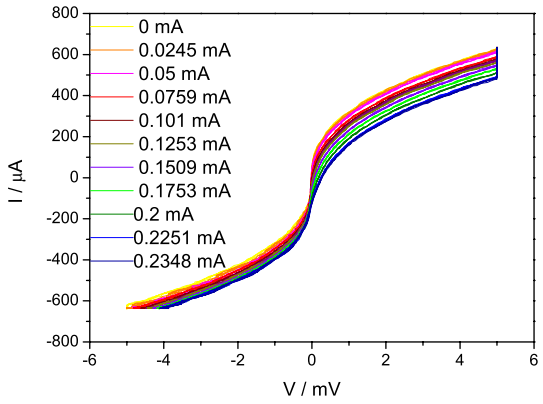

Figure 6.6 IV curves as a function of I_{inj} used in D90°. I_{inj} // to I_{bias}.

6.4 Spin Injection Measurements

This section describes the experiments performed for the investigation of spin injection into superconductors, and presents some of the results observed. There were three different approaches to detect for spin injection effects in our devices:

1. I_c vs I_{inj} measurements in the absence of an external field. Effects observed were thus due to the injected current only.

2. Measurements were also performed using an external applied magnetic field, H. These measurements taken in a field sweep but at the same I_{inj} values eliminate heating effects. The applied magnetic field was employed to increase the alignment of domains in the LC(0.3)MO, which hence increases the net polarization of the injected current into YBCO in our devices. Increased spin polarization of I_{inj} was expected to enhance non-equilibrium effects in the superconductor, thus suppressing its order parameter.

   Field measurements, however, have a drawback due to the introduction of flux vortices in YBCO which can also suppress the I_c of the superconductor. The B_{c2} value along the YBCO c-direction is in the order of 30-40 T while that in the a-b plane has been estimated as 100-200T (see Table 2.2). The magnetic field applied was hence insufficient in completely suppressing the superconductivity in YBCO.

   The external field, however, can suppress superconductivity by introducing flux vortices which reduce the superconducting order parameter. But with the field applied along the a-b plane of the device, longitudinally with the current, I_c suppression due to flux flow in the a-b plane was kept to a minimum (although a flux density of magnitude larger than 5-18mT (See Section 2.2) would introduce flux vortices in YBCO along the a-b plane which

increases the flux density). Within the scope of experimental error[1], we expect 'kinked' vortices to form. In this case, regions of the flux lines along the c-direction would induce an electric field when moving perpendicular to I_{bias} and H.

As the effects due to localized heating at the same value of I_{inj} is the same, any changes in I_c suppression observed would thus be due to the effects of the external field. Comparing measurements at constant I_{inj} values would also eliminate I_c suppression due to the self-field effects of the injected current, as was observed by Ireland et al with grain boundary junctions [56].

3. In order to eliminate effects due to local heating, current summation and increased B due to external magnetic field, I-V measurements of the device was performed at zero-moment and remanent states.

   This was an effective measurement because the I_c values were evaluated at two different states of the ferromagnetic current injector. The spins in the ferromagnet were more aligned in its remanent state compared to its random state initially at zero field. In this measurement, current summation and localized heating effects can be differentiated because the IV curves taken at the same I_{inj} values were compared. Very importantly, effects due to the external magnetic field were eliminated due to the absence of H at the time of the IV acquisition. This investigation examined how the degree of current polarization directly affects the superconducting I_c.

6.4.1 Transport measurements as a function of injected current

The I_c of the device as a function of the I_{inj} were investigated in D90° and D45°. These measurements were done without an applied magnetic field.

D90° measurements

Figures 6.5 and 6.6 each show a series of I-V curves acquired as a function of the injection current for the 8 μm wide track. In Figure 6.5, the injected current was varied from 0mA to 0.235mA. The polarity of the injected current was then reversed. Subsequently, 0mA to 0.227mA current was injected into the superconducting track (illustrated in Figure 6.6).

The I_c^0 was $\sim \pm 100\mu$A. As the amount of I_{inj} increased from 0mA, to beyond the I_c^0, the superconductivity was increasingly suppressed (I_c decrease with increasing I_{inj}). This I_c suppression characteristic was also observed by other groups [51, 52, 55] who attributed it as evidence of spin injection effects.

The figures show that I_c suppression was more evident in one direction of I_{bias}. This behaviour was consistent when the I_{inj} direction was reversed. A significantly smaller suppression of I_c^- in Figure 6.5 and I_c^+ in Figure 6.6 was also observed. A series resistance in the I-V curves when I_{inj}

[1] It is unlikely that the angle between I_{bias} and H is exactly zero

$> I_c$ which was indicative that part of the device was normal while other parts still exhibited superconductivity.

D45° measurements

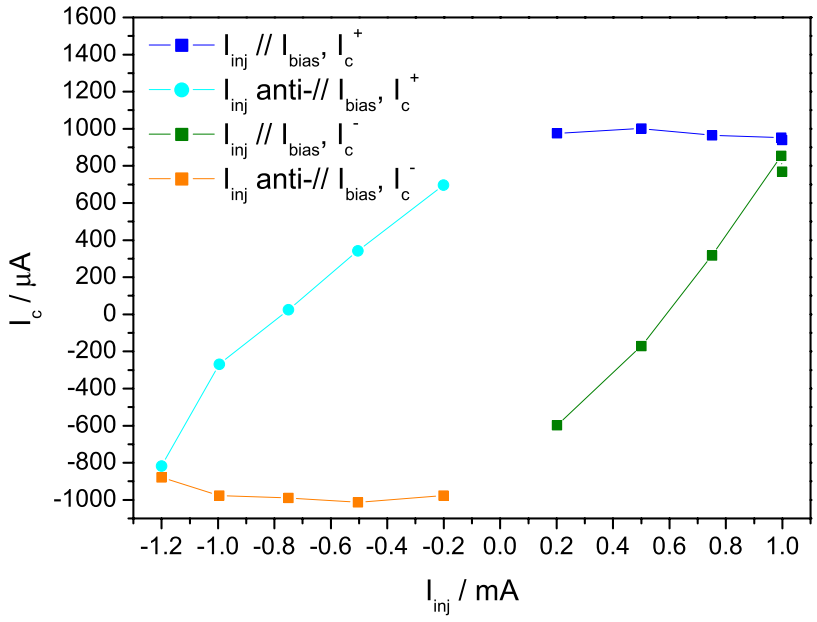

Figure 6.7 Variation of I_cs with I_{inj} in D45°.

The asymmetric suppression of superconductivity in our devices due to the 3-Terminal geometry was also clearly evident in D45° as illustrated in Figure 6.7. The I_c^+ and I_c^- values were extracted from the I-Vs acquired at various I_{inj} using a voltage criteria. To remove any current offsets present in the measurement, the I_c values of the measurements were obtained using Equation 3.10, shown in Figure 6.8

The I_c^0 in the device was ±1mA. It was observed that the I_c^+ and I_c^- extracted in each I_{inj} current direction converged when $I_{inj} = I_c^0$, thus superconductivity in our 45° device was completely suppressed at that point.

From Figure 6.8 we observed the parabolic decrease of I_c with I_{inj} for both I_{inj} directions. This parabolic decrease of I_c with I_{inj} is similar to all the spin injection into superconductor measurements performed by other groups in Table A.1. These rates of I_c suppression were greater than 0.5, indicating that the suppression was due to heating or non-equilibrium effects, on top of current summation effects, as discussed earlier (See Section 3.14).

These results were promising because they implied that, current summation effects aside, non-equilibrium effects were induced in the superconductor in D45° due to I_{inj}. However, spin

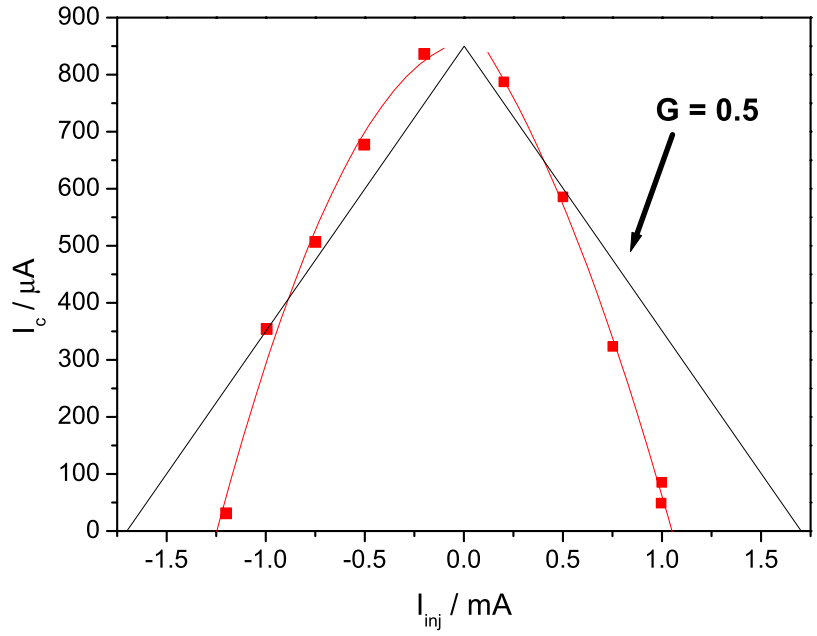

Figure 6.8 I_c vs I_{inj} plots of D45° at 78K. The black line indicates the gain due to current summation effects only (G=0.5).

injection effects were not a definitive cause of I_c suppression in these current injection measurements as the effects of localized heating could not entirely be eliminated. The increased I_{inj} in the device may result in increased local heating at the LC(0.3)MO/YBCO interface, which would also reduce the I_c of the superconductor.

D45° temperature studies

As discussed in Section 3.2.2, I_c suppression due to the spin polarized injection is expected to be greater at lower temperatures. This is because of τ_{sf} being longer due to fewer thermal scattering events at lower temperatures.

This behaviour was, however, not observed in Figure 6.9 which shows little variation in I_c suppression of D45° with temperature,as there was no systematic trend in the curvature of the parabolic fits of the data with temperature.

6.4.2 Measurements in Magnetic field sweep

In these measurements, I-V curves were acquired with constant I_{inj} at various points in a field sweep at 70K, $\frac{T}{T_c} = 0.97$. Sample were demagnetized using gradually decreasing minor loops prior to the measurements being acquired for each field sweep at each pre-set I_{inj} value.

However, from a comparison of the sets of I-V curves obtained. We were able to rule out both

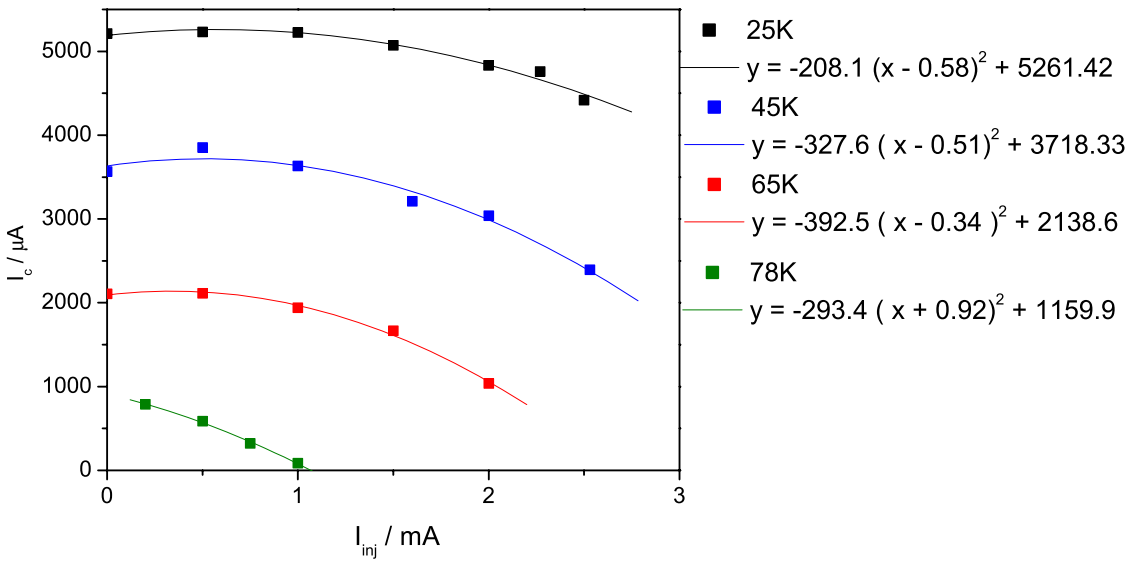

Figure 6.9 I_c vs I_{inj} of D45° at various temperature below T_c = 87K.

thermal and various magnetic effects as possible causes of increased I_c suppression by examining if the magnetic field affects the suppression caused by I_{inj}. This was done by first investigating the rate of I_c suppression due to an applied external field at I_{inj}=0, and subsequently comparing that at various constant I_{inj} values, as will be illustrated by the following I-V data which best represents the measurements taken in a field sweep.

Figure 6.10 presents sets of I-V curves of the 8μm 90° device for I_{inj} = 0 in a field sweep corresponding to a flux density of 0 to 440mT to -440mT to 0. The I-V curves were grouped and presented in sets of threes according to their sequence within the field sweep. This was done to improve the clarity of results observed due to the external magnetic field sweep as the effects observed were very small.

The figure indicated a small I_c suppression with μ_oH in both H directions as the green I-V (which represents μ_oH = 0) was consistently the largest, and the black I-V was the smallest. This effect was magnified in Figure 6.11. As μ_oH was greater than B_{c1}, the cause of this suppression is the increase in B.

Figures 6.11, 6.12 and 6.13 show sets of three I-V curves from 0 to 440mT taken at I_{inj}=0, 0.15mA and 0.23mA. From the figures, the current summation effects are apparent with the increasing asymmetry of the I-V curves with injected current. Suppression was greater in one I_{bias} direction compared to the other. The figures also show that with increasing H, the rate of I_c suppression with I_{inj} also increased. This was suggestive of spin injection effects as will be discussed later.

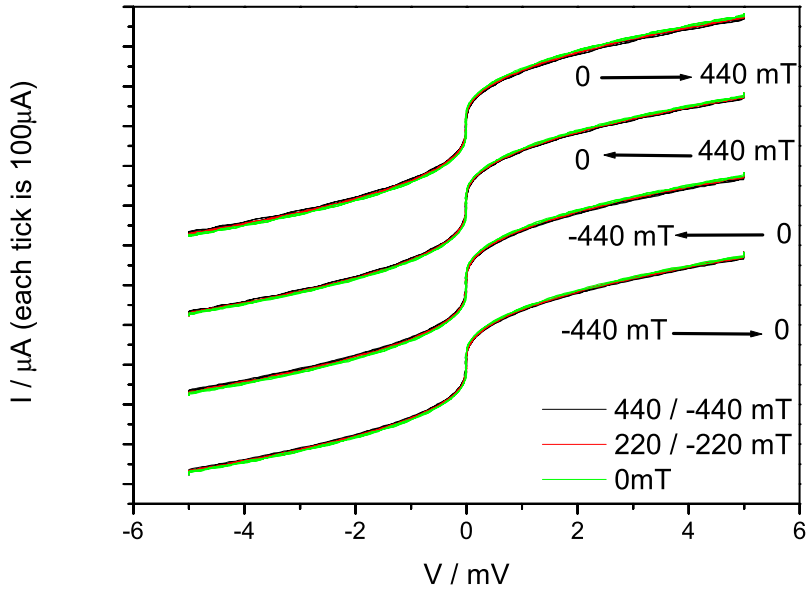

Figure 6.10 IV curves acquired in as a function of H ranging from μH=0 to 440mT in 90° device.

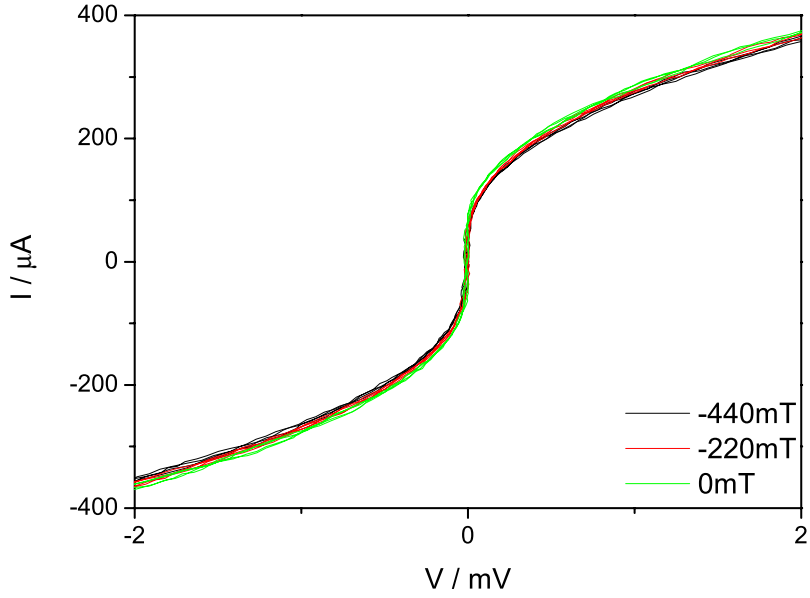

Figure 6.11 D90° 8μm at I_{inj} = 0. Sequence of $\mu_\circ$H= 0, 220mT and 440mT.

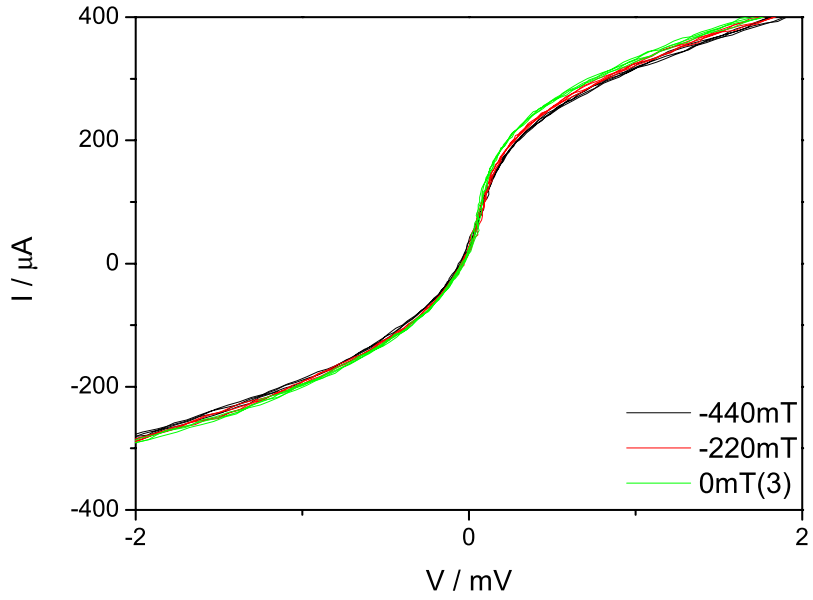

Figure 6.12 D90° 8μm at I_{inj} = 0.15mA. Sequence of $\mu_\circ$H = 0, 220mT and 440mT.

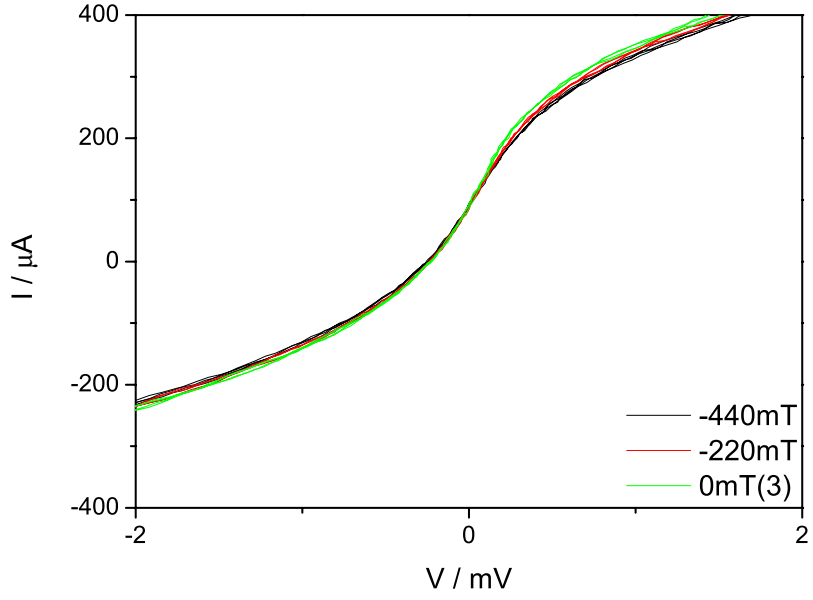

Figure 6.13 D90° 8μm at I_{inj} = 0.23mA. Sequence of $\mu_\circ$H = 0, 220mT and 440mT.

45° device

A similar measurement as a function of a smaller field sweep was performed using D45°. D45° was measured at μ_oH = 0, 20mT, 80mT and remanent field. Figure 6.14 shows no observable variation in I_c suppression in D45° at all μ_oH values.

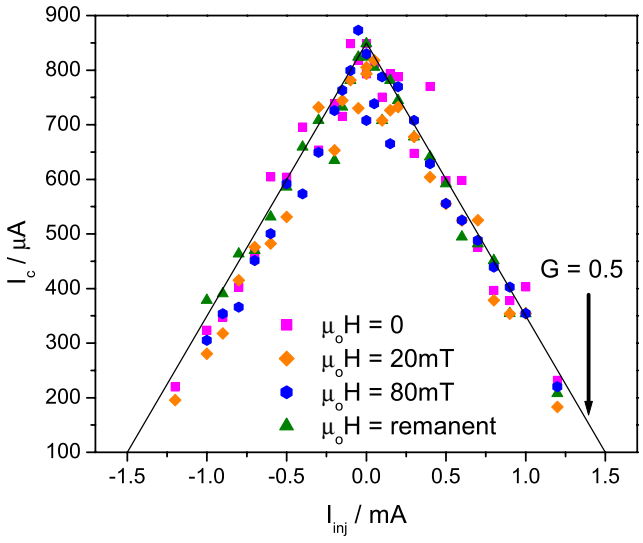

Figure 6.14 Plots of I_c vs I_{inj} at different applied fields in D45° at 78K.

6.4.3 Comparison of measurements at zero with remanent magnetization

In this experiment, the device was initially demagnetized using gradually decreasing minor loops. I-V data was acquired at various I_{inj} values. An external magnetic field greater than the saturation field of the device was applied, and subsequently reduced to zero. This leaves the F layer of the device in its remanent state. I-V curves were again acquired at these two states in the same I_{inj} values. The rate of I_c suppression of the device in the random and remanent state were compared.

Figures 6.15 and 6.16 show the suppression of I_c with I_{inj}, varying the terminals of the injected current in the device, as shown in the inset. The purpose of varying the direction of the I_{inj} in the device was to ensure that the effects observed in the device was not due to inhomogeneity in the YBCO track. The measurements were taken at 58K, $\frac{T}{T_c} = 0.8$.

The figures show a characteristic I_c suppression with increasing I_{inj}, with current injected up to I_c^0. The I_c^0 values of this device was $\pm 260\mu$A. This I_c suppression showed a parabolic behaviour in the I_c suppression with I_{inj}. As suppression effects due to current summation effects are linear, as indicated in Equation 3.20, there were additional causes of suppression in this case. We attributed these to heating effects induced by the injected current, as heating

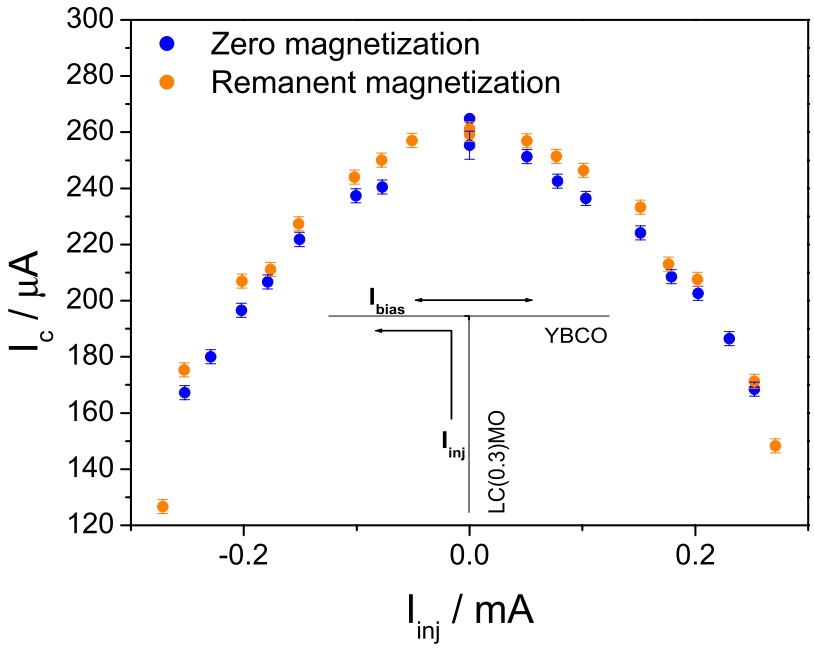

Figure 6.15 I_c vs I_{inj} plots for 8μm D90° at 58K. The plots compare the I_c suppression in zero fields and remanent magnetization. Inset shows the I_{inj} with respect to I_{bias}.

effects vary with I_{inj}^2.

We observed from the figures no distinct difference in the rate of I_c suppression with I_{inj} when the LC(0.3)MO was in its remanent state compared to its random zero-field state. In Figure 6.15, the rate of suppression of I_c with I_{inj} is smaller than the rate expected from current summation effects alone.

6.5 Spin injection Discussion

The spin injection results observed were consistent with varying current direction and with different parts of the 3T device geometry. There was evidence of the various I_c suppression effects discussed earlier, which obscure the effects due to spin polarized particles.

Current summation effects were evident in the asymmetry of all the IV curves. These effects cause I_c to vary linearly with I_{inj} with an expected device gain of 0.5. The I_c suppression we observed was, however, parabolic. Some of the I_c vs I_{inj} measurements in zero applied field also showed a device gain > 0.5 (Figures 6.8). This was evidence of additional I_c suppression effects caused by the injected current. This suppression may be due to non-equilibrium effects caused by local heating or spin injection.

We attribute the parabolic I_c suppression with I_{inj} behaviour to *localized heating* caused by

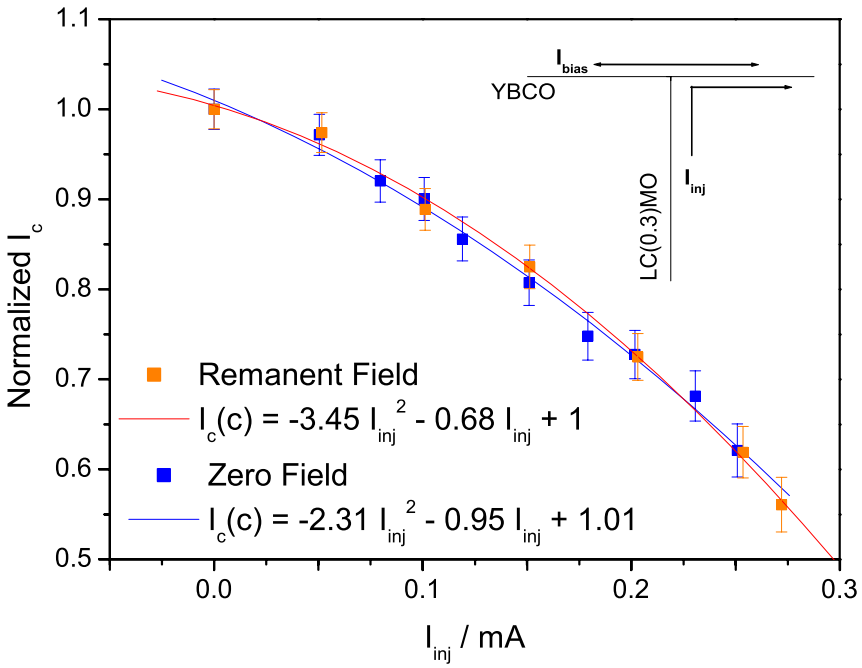

Figure 6.16 Normalized I_c vs I_{inj} plots for 8μm D90° at 58K, with I_{inj} grounded in the opposite terminal in the 3-Terminal device. Plot compares I_c suppression with I_{inj} at zero and remanent magnetization. Inset shows I_{inj} direction with respect to I_{bias}.

the injected current, as heating effects vary with I_{inj}^2 Section 3.3.5. The *increase in flux density* in YBCO, caused by an increase in the external magnetic field, also led to an I_c suppression. This was evident in the Figure 6.10. These I_c suppression effects occurred in conjunction with one another, making it difficult to isolate the effects due solely to spin injection.

6.5.1 Evidence of Spin Injection Effects

The only evidence of spin injection observed in our devices is shown in measurements performed at constant I_{inj} in an external field sweep. These results indicated that the I_c suppression varied with the external magnetic field sweep and I_{inj}. These two causes were first considered separately to analyse the I_c suppression effects. If suppression effects were solely due to increasing B in YBCO, the rate of I_c suppression at different I_{inj} values should be the same. If the I_c suppression were due solely to local heating cause by the injection current, the rate of suppression should not vary with applied magnetic field as seen Figures 6.11 because the I_{inj}=0.

In a more complicated scenario where I_c suppression in our devices were due to a combination of increasing B in YBCO and I_{inj}, the absolute I_c values in Figures 6.12 and 6.13, compared to I_{inj}=0 and $\mu_\circ$H=0, would be smaller for I_{inj}=0.15mA and even smaller for I_{inj}=0.23mA.

However, the rate of I_c suppression with H should remain the same in all three I_{inj} values. This is because increased B and heating were independent causes of I_c suppression, as it was unlikely that an injection current would cause more localized heating in the presence of a higher external magnetic field.

However, there was a relationship between H and I_{inj} in the I_c suppression of the device. The rate of I_c suppression with increasing H increased with I_{inj}, which implied that H was directly affecting the amount of suppression caused by a particular I_{inj}. I_c suppression observed in the device was, hence, due to factors in addition to localized heating and H. This I_c suppression with increased flux density and increased injection current was attributed to two possible causes.

- Spin induced non-equilibrium in the superconducting track. There was a relationship between the polarization of the injected current(due to domain alignment in the ferromagnet with a magnetic field) with I_c suppression. An increase in I_{inj} polarization led to increased I_c suppression effects. These effects, however, were very small.

- Flux flow with injected current. Flux vortices were induced in the YBCO track ($H>H_{c1}$) due to the external field. The flux density increases with increasing applied field in the field sweep. There was also increased flux flow at higher I_{inj} values. Suppression of the I_c was thus enhanced with increasing I_{inj} and H.

The most effective measurements for studying spin injection effects were the I-V measurements in zero and remanent magnetization.

The results shown in 6.15 and Figures 6.16 indicated that there was very little difference between I_c suppression in the zero and remanent magnetizations. The rate of suppression in both states are similar. This may be because the difference in spin polarization of the LC(0.3)MO in the zero and remanent magnetization states was small. Subjected to partial spin scattering at the interface, the spin-induced effects became negligible compared to the other I_c suppression effects.

In Figure 6.9, we observed that the I_c suppression in the D45° device increased with increasing temperature. This was opposite to what was expected if the I_c suppression effects were caused by spin polarized particles. With decreasing temperature, τ_{sf} of the particles is longer. Hence, we can expect the spin-induced non-equilibrium effects in the devices to be more evident at lower temperatures.

We have also performed spin injection experiments on D90° at various temperatures. Measurements shown in Figure 6.10 were performed at 70K while those shown in Figures 6.15 and 6.16 were performed at 58K. All measurements however showed no clear evidence of spin injection effects.

6.6 Investigation of interfacial resistance

The quality of the F/S junction interface was very important for the transport measurements. Although this fact is well-known, as the amount of spin polarization in the injected current in

YBCO is dependent on the quality of the interface at the injector junction, the interfaces of spin injection devices performed elsewhere have not been directly addressed. The assumption was that the good lattice match between LC(0.3)MO and YBCO allows for a high-quality epitaxial interface (often proven structurally by TEM) capable of transmitting spin from the F layer into the S layer with little spin scattering.

In this section, the interfacial resistance in the spin injection devices was probed using a 4-point measurement as shown in Figure 6.17. This information is important for the understanding of spin injection junctions.

Apart from examining the interface resistance, current behaviour at the interface was investigated. This was done primarily because, unlike other spin injection experiments, we examined the effects of spin injection into the YBCO a-b plane, where the resistivity is approximately three orders of magnitude lower compared than that along the c-direction. Due to this anisotropy in conductivity, a higher proportion of the injection current in our devices was expected to flow along the a-b planes in YBCO. Also, other groups [97] have reported alternate current paths in their spin injection devices.

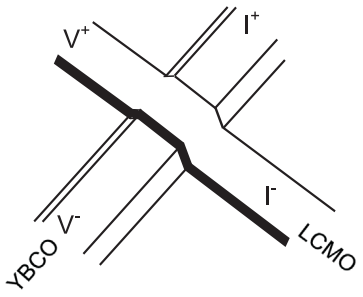

Figure 6.17 Schematic of junction interface resistance measurement. Current was passed from the F track into the S track. Voltage signals were tapped on the opposite corner of the injected current.

To study the interface current behaviour, two different devices were fabricated as described in the following. RT measurements of the interface of these devices were studied for current behaviour at the interfaces.

- A normal device, D6, which consisted of YBCO tracks overlapped with LC(0.3)MO tracks.
- A device, D7, processed in a similar way, except for the deposition of a 40nm thick STO buffer layer on top of the bottom YBCO layer. During the processing of the ramp junction, this STO buffer layer on the ramp edges was milled away, thus leaving STO only on the top portion of the YBCO track. LC(0.3)MO was subsequently deposited on top. In this device, current was forcibly injected through the ramp junction in a-b direction. This device design was not used in our spin injection experiments because the discontinuity of the LC(0.3)MO bridging the YBCO track did not allow for an analysis of the LC(0.3)MO film quality at the device junction.

6.7 Results of interfacial studies

6.7.1 Variation of resistance with temperature

The product of resistance and overlap area of the tracks in D6 is plotted against temperature as illustrated in Figure 6.18. This enabled all three curves to be plotted on a similar scale. Most significantly, the resistance passed through the x-axis for all three devices, suggesting that the current path at the device interface varied with temperature.

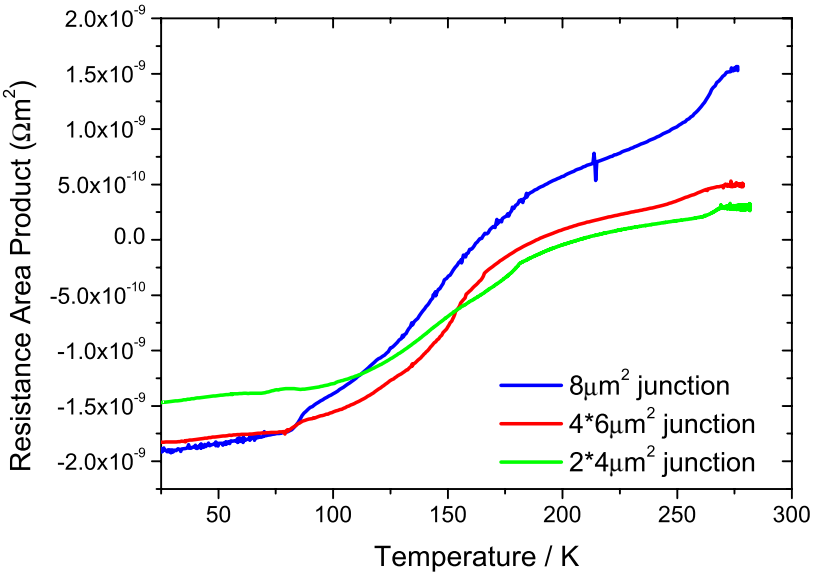

Figure 6.18 Resistance behaviour of LC(0.3)MO/YBCO device interfaces as a function of temperature in D6.

6.7.2 Consistency in RT junction behaviour

Similar resistance vs temperature interface measurements of the $2\mu m^2$ wide YBCO and $4\times6\mu m^2$ wide LC(0.3)MO junction is illustrated in Figure 6.19. In this measurement, the current and voltage leads were permutated through four different combinations at the junction. These measurements investigated the reproducibility of the current behaviour at the interface through varying the source and ground of the current (at both opposite corners of the junction).

The plot was symmetric about the x-axis, and the resistance switched from positive to negative at the same temperature for all current paths. A set of I-V data of the device as shown in Figure 6.20 confirmed that the voltage detected was gradually shifting in orientation, and that the I-V was ohmic throughout this change of sign. This behavior was unlike the observation in Figure 6.18 where the device with lower resistivity passed through the x-axis at a higher

temperature. This confirms that the change in current direction was an interfacial effect caused by variation of interfacial resistivity with temperature.

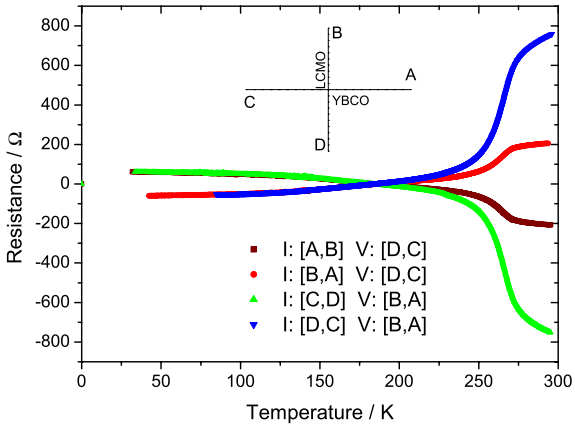

Figure 6.19 RT plot of D6 $2\times4\mu m^2$ interface. The voltage and current leads were permutated through 4 different combinations. The current path was reversed at opposite corners.

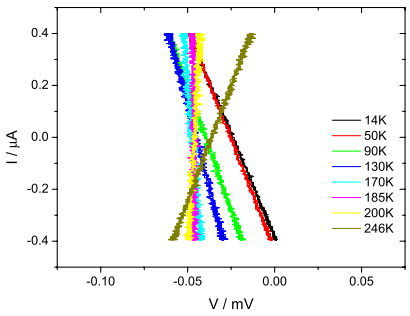

Figure 6.20 A typical set of IV data measured as a function of temperature, acquired during an RT measurement shown in Figure 6.19. The IVs show a change in gradient from positive to negative with decreasing temperature, accounting for the 'negative' resistance values observed.

6.7.3 Comparison of current behaviour with D7

Figure 6.21, which illustrates the similar measurement performed on the $8\mu m^2$ junction on D7, indicated a trend of decreasing resistance with temperature at the interface. However, the interface appeared to be insulating below $\sim$ 117K. Unlike in D6, there was no indication of an alternate current path.

A study of resistance in different parts of the track in the device, D7, was shown in Figure 6.22. The junction measurements were illustrated more clearly in Figure 6.23. The results show that:

1. A two-point measurement of the LC(0.3)MO track near its contacts, measured through contact 1 and 2, show a typical LC(0.3)MO RT characteristic with a paramagnetic to metallic transition at 248K. This confirmed the quality of the LC(0.3)MO film.

2. The transition peak was also evident in four-point measurements for half (I path: 1 and 4, V contacts: 2 and 5), and whole (I path: 1 and 3, V contacts: 2 and 3) of the LC(0.3)MO track in D7. The tracks, however, showed an insulating behaviour below T $\sim$ 236K, suggesting a series resistance associated with the LC(0.3)MO track measurements.

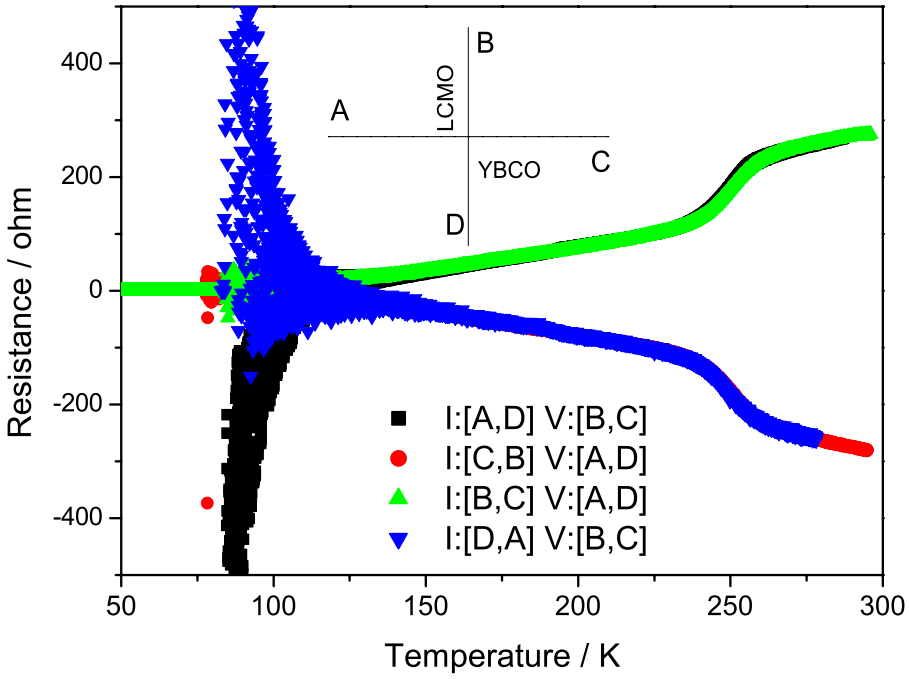

Figure 6.21 RT plot of D7 $8\times8\mu m^2$ interface. The voltage and current leads were permutated through 4 different combinations. The current path was reversed at opposite corners.

3. As observed from the schematic in Figure 6.23, both the RT measurements of the half and the full LC(0.3)MO track in this device include one and both ramp interface resistance in series, respectively (as the STO on top of the YBCO track was insulating). These series of plots hence reveal that the ramp-edge interface was resistive. The resistance of the track was thus dominated by that of the LC(0.3)MO track at T> 236K. At T<236K, the resistance of the interface dominated.

6.8 Discussion of interfacial studies

6.8.1 Current flow at interface

The experiments on D7 show that the interfacial resistance was insulating. We see that the resistance measured of the interface reaches zero with decreasing temperature. Current was passed through the ramp junction at high temperatures, but at lower temperatures, the ramp interface was insulating to current flow.

However, a comparison with RT plots of D6 interface indicated that at the normal spin injection device interface, there was an alternate current path at the interface below $T<T_{R=0}$. This change is illustrated in Figure 6.24B and C.

The figure also provides an explanation for the 'negative' resistance measured in such a geometry. It also helps to explain the similar effect observed by Lian et al [97]. To explain the

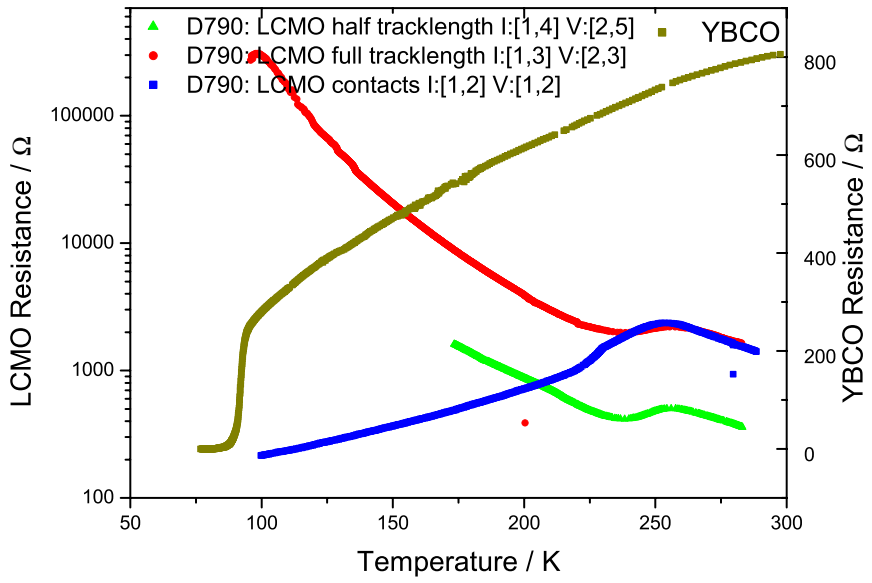

Figure 6.22 RT plots of the 4μm wide YBCO track, and various sections of the 6μm wide LC(0.3)MO track. The current and voltage leads used as indicated correspond to those illustrated in Figure 6.23. The T_c of YBCO was 85K, and the T_{Curie} of the LC(0.3)MO track was 248K.

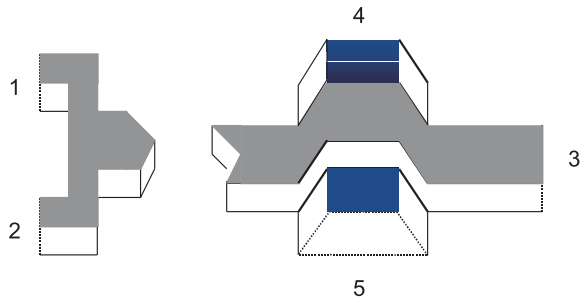

Figure 6.23 Schematic of the spin injection junction, not drawn to scale.

change in sign in resistance, we consider two scenarios: T= room temperature and T<T_c.

Basically, the junction cannot be considered as a point, and therefore the behaviour of potential lines has to be considered. From Figure 6.24, the current takes the least resistive path close at the nearest corner across the junction, whilst V_a and V_b measure the voltage in the YBCO and at the 'opposite' LC(0.3)MO track respectively. Note the V_b measures through an interface which can become insulating at lower temperatures.

At T= room temperature, current passes through the ramp junction, as was evident in the RT measurements of D7. In this case, $V_b < V_a$ because there is a potential drop across the interface between V_a and V_b ($V^+ > V_a > V_b$). Voltage measured, V_T=V_a-V_b=positive.

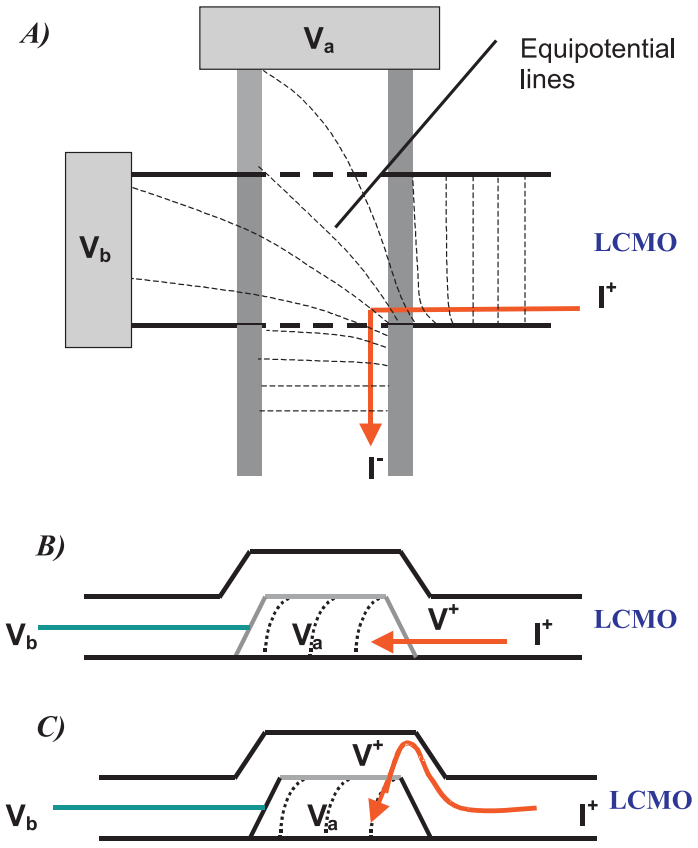

Figure 6.24 Schematic of interface measurement during current injection at the YBCO/LC(0.3)MO junction. A) shows the plan view of the junction with current injection into the YBCO track with voltage leads probing equipotentials at some point in the junction. B) shows current injection into the YBCO track at high temperatures. C) shows that the current path into the YBCO is through the c-axis at low temperatures.

At T<T_c, YBCO is superconducting. V_a is ground voltage. The current in this case also passes into the S layer through the c-axis because the resistance of the ramp interface is too high (evident in Figure 6.21). Here, V_a measures ground voltage. $V_b \sim V^+$ assuming zero current through the voltage leads. As $V^+ > V_a$, thus, $V_b > V_a$. V_T=V_a-V_b=negative.

Therefore, the resistance of the track changes sign with temperature. The change in sign occurs because of the increasing resistance of the ramp junction to a point when it becomes insulating to current flow. At this point, the current finds an alternate path through in the c-axis, and voltage is tapped at different parts of the interface junction. This current behaviour also explains the following characteristics of the interface resistance measured:

- R=0 is the point where V_a=V_b, and occurs when current is injected through both the ramp and the top junction at T>T_c.
- In the range T>∼150K, the decreasing resistance with temperatures corresponds with the decrease in YBCO resistance. V_a decreases faster than V_b.

- At T<T_c, V_a is constant with temperature while V_b is small (most of the current is shorted through the YBCO). Thus, the change in R with temperature at T<T_c is very small.
- The peak in the RT corresponds to the T_{Curie} of LC(0.3)MO. This suggests that even at high temperatures, the ramp junction was sufficiently insulating that some of the current was injected through the top interface.

6.8.2 Quality of the cuprate/manganite interface

The difference in resistance behaviour at the interface between the ramp and top edges of the YBCO track may be due to the fact that the ramp edge was Ar^+ milled for a longer period of time. Defects, due to ion milling and the ex-situ device fabrication process, at the interface can cause spin scattering and hinder transport across the interface. However, it was observed that although ion-milling at the top edge of the track was minimal (1 min maximum to remove residual photoresist, compared to ∼20 min to fabricate ramp junction), the edge was less resistive than the ramp junction only at T<117K in D6. At high temperatures, the resistance of the ramp junction was lower than that on top of the YBCO track.

Transport across the YBCO/LCMO interface was thus a lot more complex than previously assumed. The transport behaviour, and not just its structural integrity, require further examination. Perhaps, as speculated by Przyslupski et al [96], an anti-ferromagnetic interlayer forms at the LSMO/YBCO interface.

6.9 Conclusions

Probing for spin injection effects in F/S devices has been proven to be complicated as evident in the review in Section 3.4. The spin injection in superconductor measurements performed were an improvement on previous similar investigations elsewhere in several ways. The device junctions were smaller than any of the devices measured previously. The transfer length was at least the same order of magnitude as the junction width. The measurements took into account all the I_c suppression factors which obscured previous measurements.

The measurements were evidence that I_c suppression effects were due to the combination of various causes induced by I_{inj} and the applied magnetic field. These factors were difficult to separate because the spin injection effects, if present, were very small in comparison. Hence, like the other groups prior, clear evidence of direct spin injection on I_c suppression in devices was not observed.

Spin injection along the a-b plane did not occur as initially intended. At measurement temperatures T<T_c, current was injected more favorably along the c-axis in the device junctions, resembling the geometries studied by other groups. Although XRD and TEM studies elsewhere have indicated that cuprate/manganite superlattices have well defined superlattice structure, it was evident, however, that spin transport and current behaviour across the F/S interface, which essential for inducing I_c suppression, requires further characterization.

Thus, as spin injection effects in manganite/cuprate systems are very small, and transport mechanism across such interfaces are not well defined, direct spin injection in superconductors has proven to be an ineffective means, experimentally, to actively control superconductivity. Other methods, such as using F/S proximity effects for passive control of superconductivity were thus explored.

Chapter 7

Proximity effects in F/S multilayers

7.1 Motivation

There has been considerable interest recently in using oxide manganite/cuprate F/S multilayers for proximity effect investigations. There are several reasons that justify this interest. Firstly, as explained previously, it is possible to deposit YBCO on manganite films with little reaction at the interface. The growth of superlattices with high quality interfaces reduces spin scattering at the interfaces. Secondly, the higher T_c and the low carrier density of YBCO, and the fully polarized conduction bands of the manganites [98], allows the potential for highly sensitive applications above liquid N_2 temperatures. Finally, the short coherence lengths associated with high-temperature superconductors (HTS) also allows the material to sustain superconductivity down to very small thicknesses.

This chapter describes the deposition using 'eclipse' PLD, and the characterization of cuprate/manganite superlattices of ultrathin layers. We examine the F/S proximity effects in these heterostructures. This interaction results in a suppression of the superconducting order parameter in the S layers and hence the T_c of the heterostructure. The interaction between the layers is affected by several factors, including interface transparency, and the properties of the magnetic layer such as the moment and exchange energy.

7.2 Deposition of F/S oxide multilayers

The deposition of F/S multilayers was performed in the MK9 PLD system. As described earlier in Section 5.3.1, the MK9 has been set up and optimized for YBCO deposition, although most YBCO films grown in the system were relatively thick, ∼500nm, compared to our requirements. As YBCO T_c was very sensitive to the oxygen content in the films, it was hence the safer option to optimize the deposition of manganites in the MK9 system.

Due to the ultrathin repeats in the multilayers required for the investigation of proximity effects in manganite/cuprate multilayers, we employed the use of the 'eclipse' PLD technique. The deposition was carried out by introducing a Cu hard mask between the target and the substrate in a conventional PLD configuration in the MK9 PLD system. The target-mask and mask-substrate distances were chosen to be 35 mm and 15 mm, respectively. We used pure a Cu mask 5 mm wide such that the STO and NGO substrates 5×10 mm in dimension were shadowed completely by the mask. A study of 'eclipse' PLD film deposition in the MK9 will be covered in the following sections.

7.2.1 Study of single layer films using 'eclipse' PLD

In 'eclipse' PLD, as per conventional PLD, sintered stoichiometric $YBa_2Cu_3O_{7-\delta}$, LSMO and LC(0.3)MO targets were ablated using a KrF excimer laser (of wavelength 248nm). The repetition rate and the pulse energy were set at 4Hz and 90 mJ/pulse respectively. The films were deposited in-situ at 720°C, in a flowing O_2 environment of 112.5 mTorr.

In the MK9 PLD system, a tube-type Fecralloy resistive heater was utilized unlike the flat heater used in the MK10. This curved heater ensures more uniform heating of the substrates as well as more reliable temperature control. The reported substrate temperature (T_s) was measured by two thermocouples situated in close proximity to the substrate. After the deposition, the chamber was filled to 750 Torr with pure oxygen, whilst slow-cooling (<10°C/min). The samples were then annealled for one hour at 460°C.

In 'eclipse' PLD, the ablated particles are scattered by the background gas and transported through diffusion onto the substrate surface. The introduction of a mask shadowing the substrate from the direct impact with ablated species is expected to lead to several positive and negative effects:

- Positive Effects

    1. The obvious result is the elimination of droplets contamination. Due to their heavy mass, the droplets and loose particles of target material scatter at smaller angles from the target surface and are collected by the mask.
    2. The improvement in homogeneity of the deposited film is another positive effect related to diffusion type transport of the ablated species, thus avoiding the sharp angular dependence of the laser generated plasma plume.

- Negative Effects

    1. A compositional problem might appear as a result of the bombardment of the mask by the energetic plasma plume causing sputtering of Cu particles and consequent Cu enrichment at the substrate surface. To check that our films deposited by 'eclipse' PLD were not contaminated by the mask, we performed EDX (energy dispersive x-ray) analyses of LSMO and LC(0.3)MO films deposited on STO substrates by 'eclipse' PLD. This EDX was performed using the using a JEOL 5800 LV scanning electron microscope. The resulting spectra is shown in Figure 7.1. The spectra of both films shows that the expected elements are present in our films and reveals no evidence of CuO formation in both cases.
    2. The most important negative effect is the possible deviation from the target stoichiometry due to the different volatility and distribution of the growing species. Trajanovic at al [99] found that although Ba and Cu distributions are largely unaffected by the processing pressure and target-shadow distances, the Yttrium distribution is unstable and can be strongly influenced by both factors. To verify that our films are of the right stoichiometry, we performed X-ray diffraction to check for the presence of undesirable phases / orientations in our epitaxial film.

Typical high-angle XRD patterns of 200 nm thick YBCO films deposited on (100) STO substrates by 'conventional' and 'eclipse' PLD at the same conditions are shown in Figure 7.2

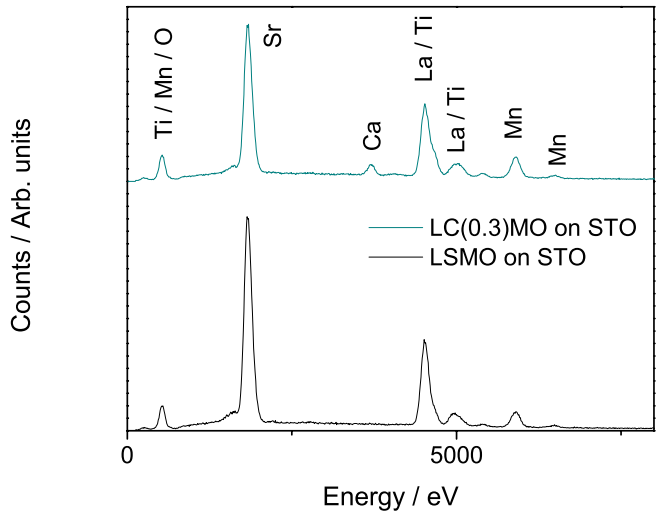

Figure 7.1 EDX scan of single layer LSMO and LC(0.3)MO thin films deposited on STO substrates.

(samples A and B respectively). Only (00l) reflections from YBCO were observed revealing that both films are well c-axis oriented. FWHM values of the (005) peak rocking curves are comparable (FWHM = 0.11 - 0.12°) confirming the good epitaxial quality of both films. For both films, no other reflections than that of YBCO [00l] have been recorded over the whole scanned region (6-75°). This confirms that the absence of other phases or orientations of the film.

The AFM pictures of samples A and B shown in Figure 7.3 and Figure 7.4, clearly demonstrated the improvement of surface quality by using the 'eclipse' technique. Measured RMS values for samples deposited by 'conventional' and 'eclipse' methods are 21.7 and 3.7 nm respectively.

Transport measurements were used to check the transition temperatures and electrical properties of the films, as deviations in the film composition result in a change in the electrical properties of the materials. The RT plot of single layer 20nm YBCO grown by 'eclipse' PLD is shown in Figure 7.5. The superconducting properties of a 20 nm thick single YBCO layer (D) show an onset temperature at 90 K and transition width of 5 K, which does not suggest significant deviation from the bulk stoichiometry or oxygen deficiency. These growth conditions also yielded single layer 100nm LSMO and LC(0.3)MO films of T_{Curie} of 360K and 250K respectively. These results show an improvement the roughness in single layer film using the 'eclipse' PLD technique without degrading T_{Curie}.

7.2.2 Multilayer deposition by 'eclipse' PLD

We compared the quality of single layered films deposited by 'conventional' and 'eclipse' PLD in the MK9 system. As described below, after verifying that these single layer films are of better

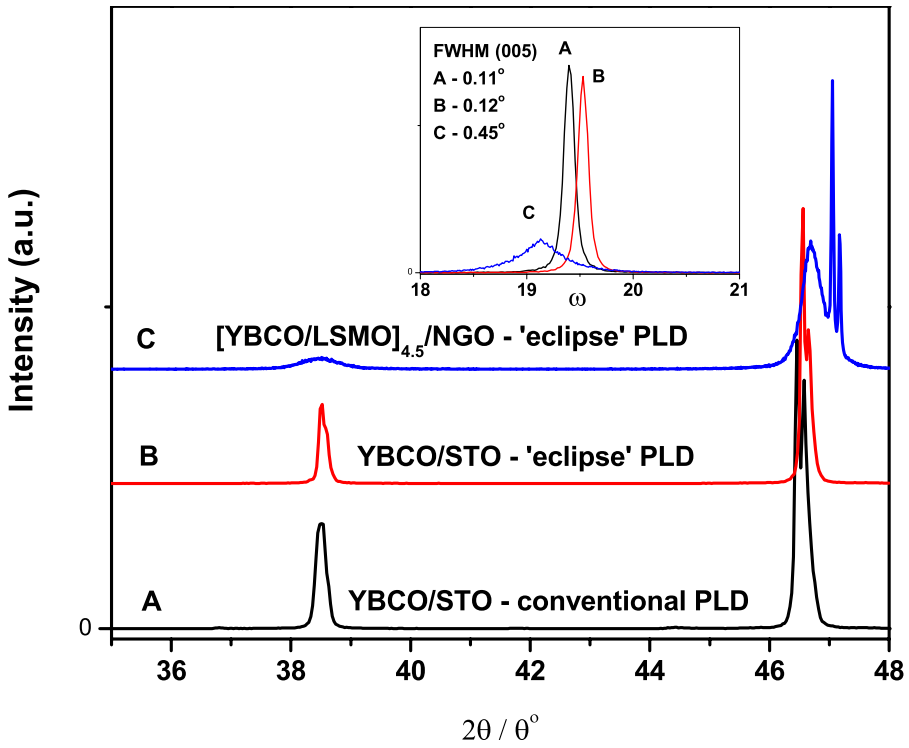

Figure 7.2 XRD $2\theta/\theta$ scan of YBCO on STO films deposited by conventional and 'eclipse' PLD in the MK9 PLD system. Sample C is the multilayer $[\text{LSMO/YBCO}]_{t=4.5}$ on NGO. The inset shows the FWHM of the (005) YBCO peak.

quality, we proceeded with multilayer deposition. Below are two specific issues we addressed pertaining to the multilayer deposition:

1. Choice of manganite material: LC(0.3)MO vs LSMO

   Both ferromagnetic manganites have very similar lattice parameters, but different properties. Although both manganites were essential for our multilayer investigations, this section summarizes the pros and cons of using each of the two materials.

   A major motivation in the study of F/S superlattices is to understand the F/S interaction in intrinsic superlattices. Habermeier et al [59] observed a re-entrant normal state at the onset of saturation magnetization in the $[\text{LC(0.3)MO}_5/\text{YBCO}_{7.5}]$[1] superlattices, as shown in Figure 9.2. In order to reproduce and investigate this effect which required a multilayer with a low T_{Curie}, LC(0.3)MO would be the preferred manganite.

   However, from an experimental viewpoint, LSMO was the easier of the two materials to

[1]In this thesis, $[\text{LC(0.3)MO}_d/\text{YBCO}_x]_t$ would refer to a multilayer of d nm thick LC(0.3)MO and x nm thick YBCO with t number of repeats. Instead of layer thicknesses, each layer was represented in terms of unit cells (u.c.) if this demonination was used by the various authors whose multilayers we discuss. Also instead of t, total thickness of the multilayer may be used instead when the total thickness was intended as a constant for a series of multilayers deposited.

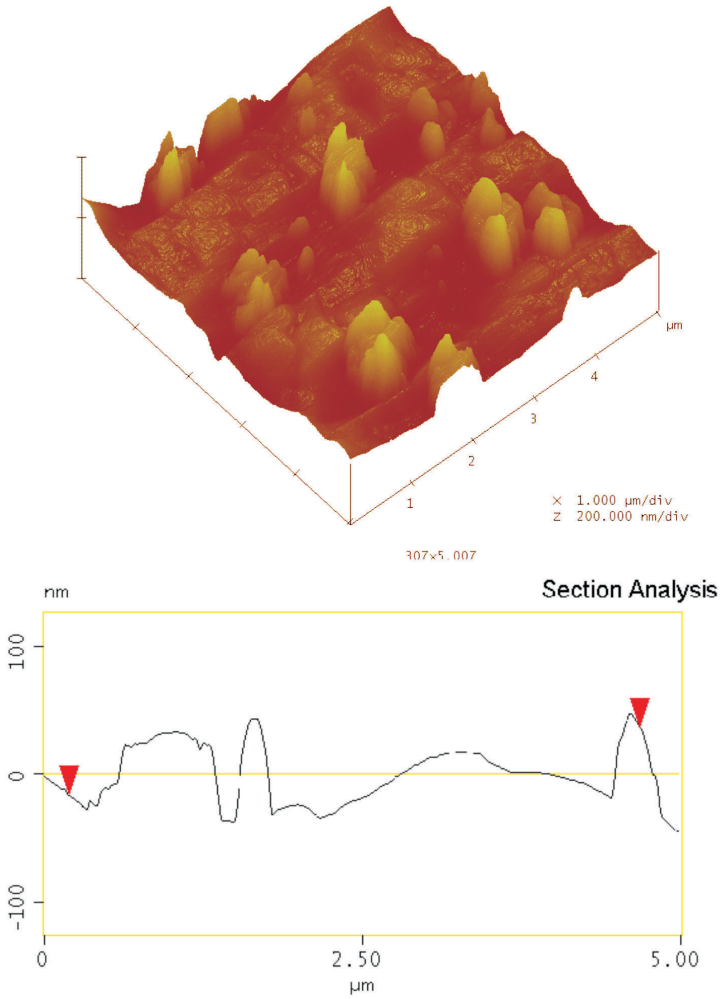

Figure 7.3 Surface profile of 200nm thick YBCO on STO deposited by conventional PLD, Sample A. Section profile taken along the scale shown in surface view.

optimize in the MK9. This is because LC(0.3)MO is structurally more distorted (Jahn Teller distortion) compared to LS(0.33)MO. LC(0.3)MO has a smaller tolerance factor, t_F, of 91.7% than LSMO (t_F = 93.5%) where t_F = 100% represents a perfect cubic structure [100].

We also investigated the compatibility of Ca^{2+} ions and Sr^{2+} ions with YBCO. Figure 7.5 shows the RT plots of two tri-layers of LSMO (30nm)/YBCO (20nm)/LSMO (30nm) (Sample E) and LC(0.3)MO (30nm)/YBCO (20nm)/LSMO (30nm) (Sample F). The degree of suppression of the superconductivity in the samples E (T_c onset = 86 K) and F (T_c onset = 77 K) differs substantially by about 10K. Although the T_c suppression in both samples indicates the interaction between superconductivity and magnetism, factors like interface disorder, strain or interdiffusion, should also be taken into account. We believe

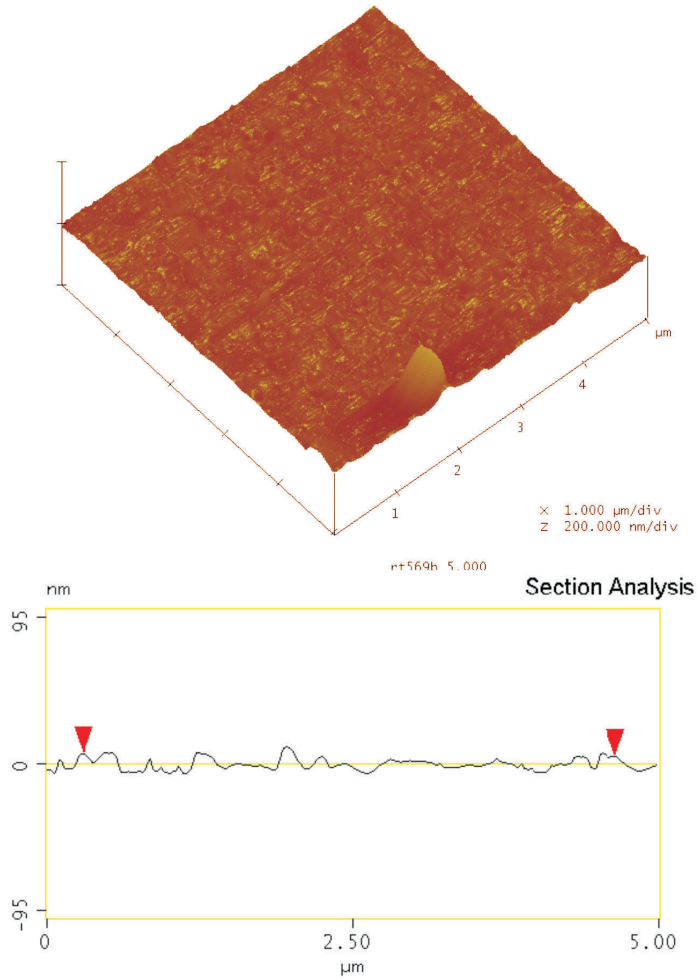

Figure 7.4 Surface profile of 200nm thick YBCO on STO deposited by 'eclipse' PLD, Sample B. Section profile taken along scale shown in surface view.

the large difference in the suppression for samples E and D maybe due in part to the Ca doping as a result of an interdiffusion between YBCO and LC(0.3)MO sub-layers. This interdiffusion is undesirable for proximity effect studies in such multilayers with ultrathin YBCO layers (<10nm).

Subsequently, multilayers with total thicknesses of approximately 180nm (but with varying LSMO and YBCO thickness) were examined for trends of T_c variation vs individual layer thicknesses. The required individual film layer thicknesses were achieved through prior calibration of the deposition rate of each material at the same conditions.

2. Multilayer film characterization.

   These multilayers were analysed for film quality and accuracy in thickness calibration. As the repeats are very thin, the thickness of the individual layers is also indicative of the

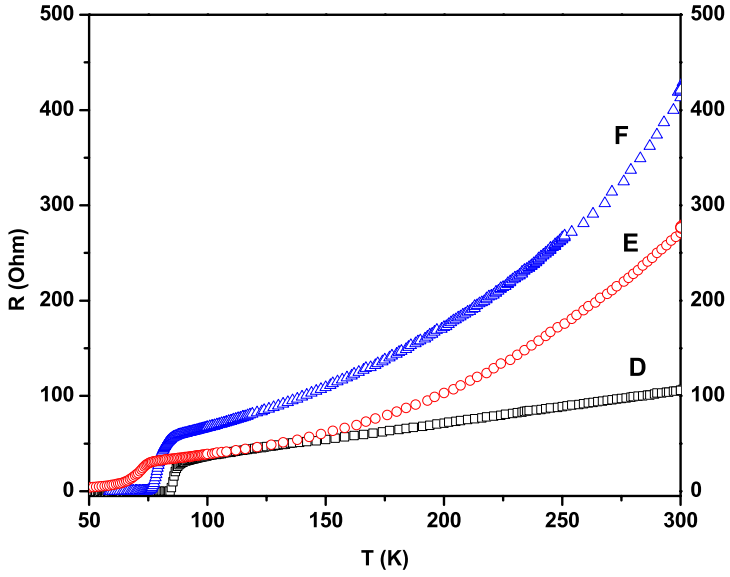

Figure 7.5 Resistance vs temperature curves for 20nm thick YBCO layer (Sample D); LSMO(30nm)/YBCO(20nm)/LSMO(30nm) (Sample E) and LC(0.3)MO(30nm)/YBCO(20nm)/LSMO(30nm) (Sample F). All films were deposited by 'eclipse' PLD on (100) STO substrates.

smoothness of the layer interfaces and the homogeneity of the layer thicknesses.

To study the quality of the multilayer structures, we used various X-ray diffraction (XRD) analysis techniques. XRD was an effective characterization technique for the quality of multilayers because it provides a quantitative analysis. Unlike TEM images, the analysis area is large. For instance, the YBCO (005) peaks analysed in Figure 7.10 were over an area of approximately $10\times0.8\text{mm}^2$.

2θ XRD scans were performed using Cu Kα wavelength in the Philips Xpert system. The layer thicknesses and interfaces were further studied with the Philips PW3050/65 high-resolution diffractometer.

Sample C in Figure 7.2 represents 180 nm thick $[\text{YBCO}_{20nm}/\text{LSMO}_{20nm}]_{t=4.5}$ multilayer deposited on (100) NGO substrate where t is the number of the YBCO/LSMO repeats. As expected LSMO peak is completely screened by the substrate. The rocking curve of (005) YBCO peak is weaker and broader (FWHM = 0.45°Omega). Pole figures were performed on YBCO [102] plane. The 4-fold symmetry observed in Figure 7.6 confirms the good in-plane epitaxy of YBCO, and consequently LSMO in Sample C, with an YBCO in-plane FWHM of 1.0°Phi. In Figure 7.6b, we can observe that the in-plane epitaxy in multilayers deposited by this method is highly reproducible even with much thinner repeats. The in-plane FWHM of multilayer $[\text{YBCO}_{8nm}/\text{LSMO}_{4nm}]_{t=14.5}$ as shown in Figure 7.6b is 1.3°Phi. The rocking curve FWHM of (005) YBCO peak in this sample is 0.41°Omega.

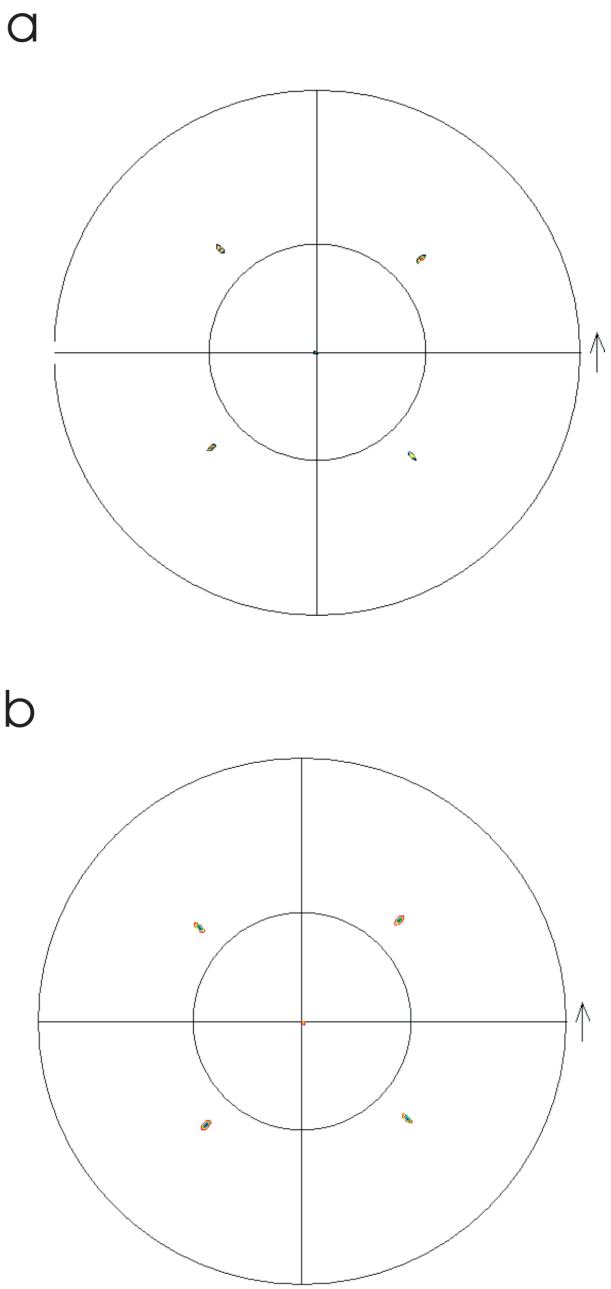

Figure 7.6 Pole figures of the [102] plane in LSMO/YBCO multilayers. (a) YBCO peak in Sample C, $[YBCO_{20nm}/LSMO_{20nm}]_{t=4.5}$. (b) YBCO peak in $[YBCO_{8nm}/LSMO_{4nm}]_{t=14.5}$.

Figures 7.7 and 7.8 show the (002) superlattice peak of the $[YBCO_{8nm}/\ LSMO_{4nm}]_{180nm}$ measured at $2\theta = 47.13°$. The superlattice peak and the corresponding fringes observed are very similar to those obtained by Przyslupski et al [96] for $[LSMO_{16u.c.}/\ YBCO_{1-8u.c.}]_{t=16}$. They obtained superlattice peaks with 1-3 satellite/fringe peaks.

The spacing between fringe peaks, as indicated in the Figure 7.7 confirm a superlattice thickness of 11.6 ± 0.3 nm, very close to our estimated thickness of 12nm, while that in

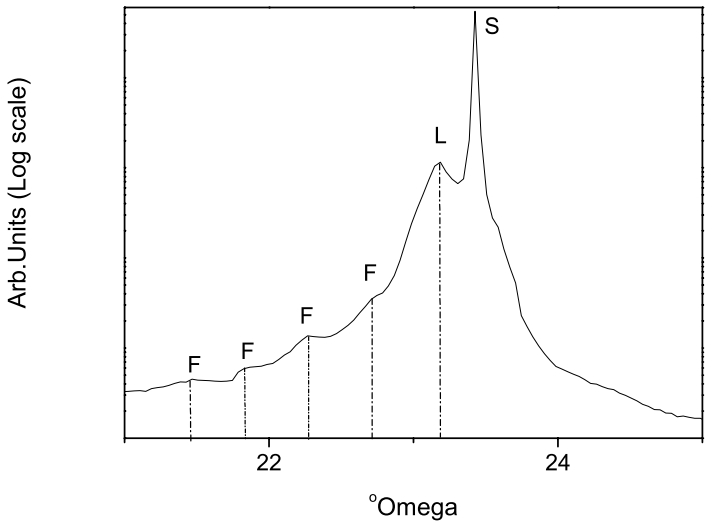

Figure 7.7 XRD scan of (002) YBCO peak in $[YBCO_{8nm}/LSMO_{4nm}]_{t=14.5}$. The spacing between fringes confirms that the thicknesses of each (YBCO+LSMO) repeat is ∼11.6 ± 0.3nm. S, L and F indicate the substrate, superlattice and fringe peaks respectively.

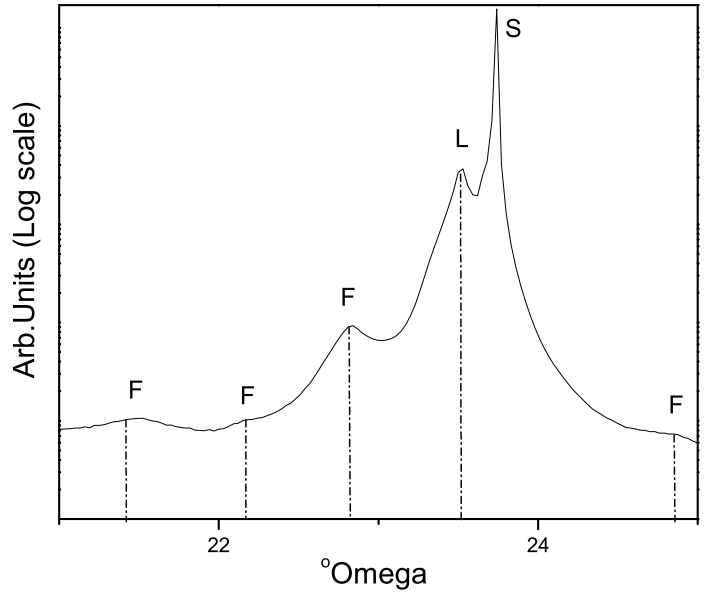

Figure 7.8 XRD scan of (002) YBCO peak in $[YBCO_{4nm}/LSMO_{4nm}]_{t=22.5}$. The spacing between fringes confirms that the thicknesses of each (YBCO+LSMO) repeat is ∼7nm ± 0.3nm. S, L and F indicate the substrate, superlattice and fringe peaks respectively.

Figure 7.8 indicate a thickness of 7nm. The reproducibility of our films was further confirmed by low angle reflectivity data obtained for the latter multilayer [$LSMO_4/YBCO_4$], as shown in Figure 7.9. The simulated scan fitted to the reflectivity data determined a superlattice period of 7.6nm while that calculated from our deposition rate was 8nm.

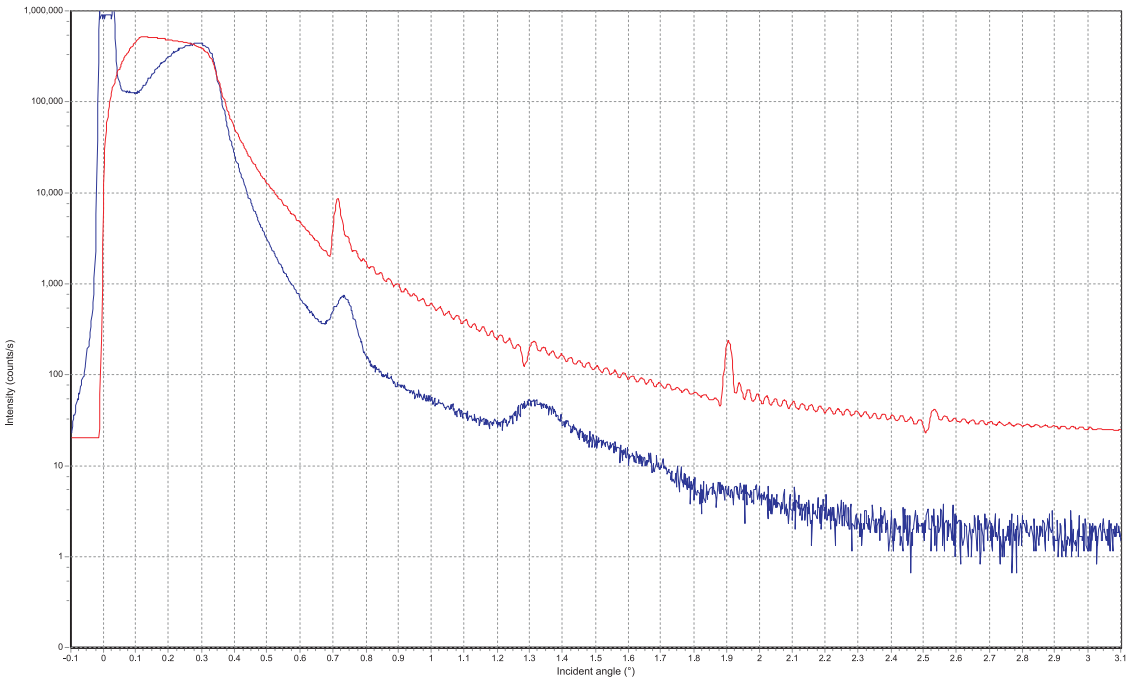

Figure 7.9 Low angle X-ray reflectivity scan of $[LSMO_4/YBCO_4]_{22.5}$ (blue), compared with a simulated scan which assumed a perfectly smooth interface (red).

Figure 7.10 shows a series of $2\theta/\theta$ scans of $[LSMO_4/YBCO_h]_{180nm}$ with LSMO thickness fixed to 4 nm and a variation of YBCO sub-layer thickness x. The plot reveals the widening of the (005) YBCO peaks with decreasing x. This relation can be explained using the Scherrer formula, $t_h = \frac{0.9\lambda_w}{B_{2\theta}cos\theta}$, where t_h is the film thickness, the wavelength of the X-rays used, $\lambda_w = 0.15405$nm Cu K_α); $B_{2\theta}$ is the FWHM of the 2θ film peak and θ is the angle.

In the inset, the FWHM values of the YBCO (005) peaks obtained experimentally in our multilayers with varying YBCO thicknesses were plotted against the relationship between YBCO (005) FWHM values and film thicknesses obtained from the Scherrer formula. The experimental values based on previously calibrated 'eclipse' PLD deposition rates fitted well with the Scherrer formula, hence, verifying again that the presented individual layer

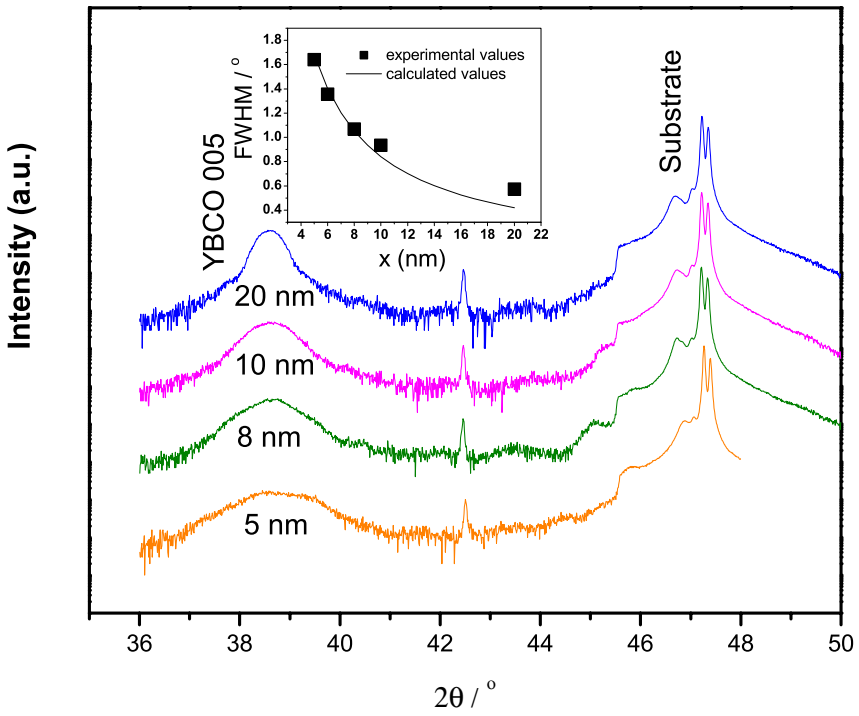

Figure 7.10 XRD scans of $[LSMO_{4nm}/YBCO_x]_{180nm}$ multilayers where the YBCO thickness x varies between 5 and 20nm; the inset represents the experimental and theoretical values (obtained from the Scherrer formula) of FWHM of YBCO (005) peak versus layer thickness.

thicknesses are accurate and reproducible.

The multilayers were studied for the properties of each component layer as a function of their layer thickness.

7.3 Effect of individual layer thickness on T_{Curie}

The effect of individual layer thicknesses on multilayer T_{Curie} was investigated. Magnetic measurements of the multilayers were performed using the VSM. At these measurement temperatures, the YBCO was in the normal state, and hence behaved like a normal metal. A direct MT plot was not useful due to the paramagnetic characteristic of the NGO substrate used. In these measurements, the moment vs temperature (MT) characteristic of each multilayer was acquired through the individual extraction, of the saturation magnetization, M_s, from each MH hysteresis loop taken at a series of temperatures.

Figure 7.11 shows the variation of LSMO T_{Curie} with LSMO layer thickness within the multilayer. The figure indicated that the T_{Curie} of the multilayer decreased with decreasing

manganite thickness. However, the multilayer remained magnetic ($T_{Curie} \sim 225K$) down to an individual LSMO layer thickness of 4nm. Multilayers with 3nm thick LSMO layer did not show any magnetic properties down to T=10K. Sefrioui et al [1], however, observed a moment in the [LC(0.3)MO/$YBCO_{5u.c.}$] films down to approximately 1.2nm. This difference is again attributed to the strong paramagnetic signal from our NGO substrates which masked the smaller magnetic signals from the films with thinner LSMO. Figure 7.11 also indicated that the M_s values of the multilayers appear to decrease for thinner manganite layers.

In the corresponding measurements of magnetization versus temperature variation with YBCO thickness, an increase in the T_{Curie} of the multilayers was observed with decreasing YBCO thickness, as illustrated in Figure 7.12.

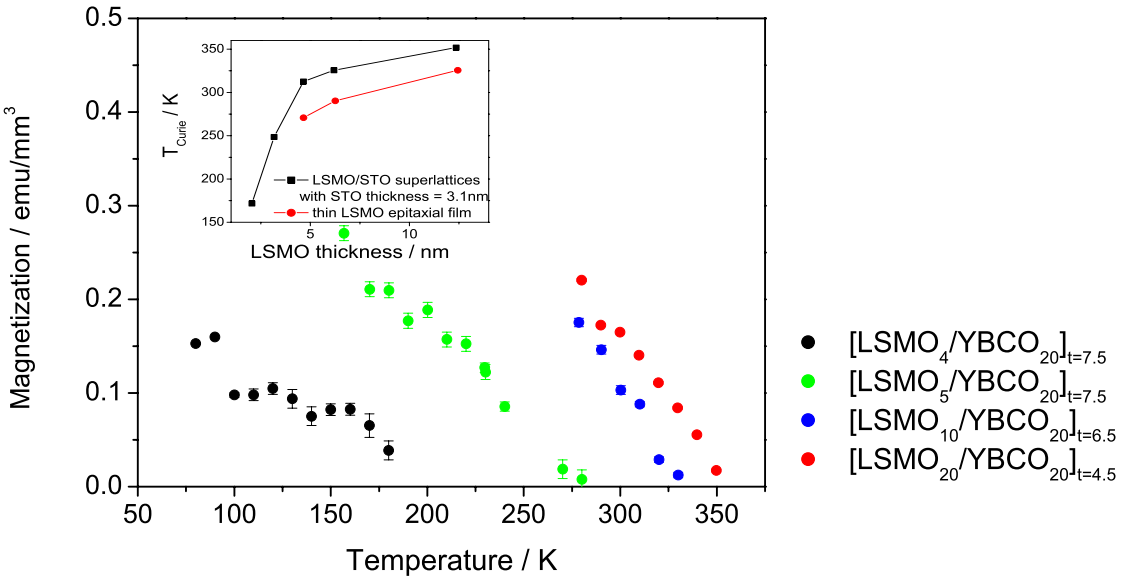

Figure 7.11 Plot of magnetization of multilayer with temperature for LSMO/YBCO superlattices with varying LSMO layer thickness. Inset shows the the decrease in T_{Curie} values obtained for LSMO/STO and single epitaxial LSMO films with decreasing LSMO layer thickness studied by Dubourdieu et al [101]. Magnetization of the multilayers were calculated using the total volume of the manganite layers.

Discussion

The decreasing T_{Curie} observed with decreasing LSMO thickness in Figure 7.11 can be accounted for by several explanations.

An increase in T_{Curie} of a ferromagnetic film can be caused by an increase in the exchange interaction, $\Delta E_{ex} \sim (k_B T_{Curie})$, between moments in the magnetic layer. A structural change in the film, such as an increase in the distance or a change in the angle between between coupling moments, directly affects ΔE_{ex}. This argument is strongly suggestive of increasing strain (with

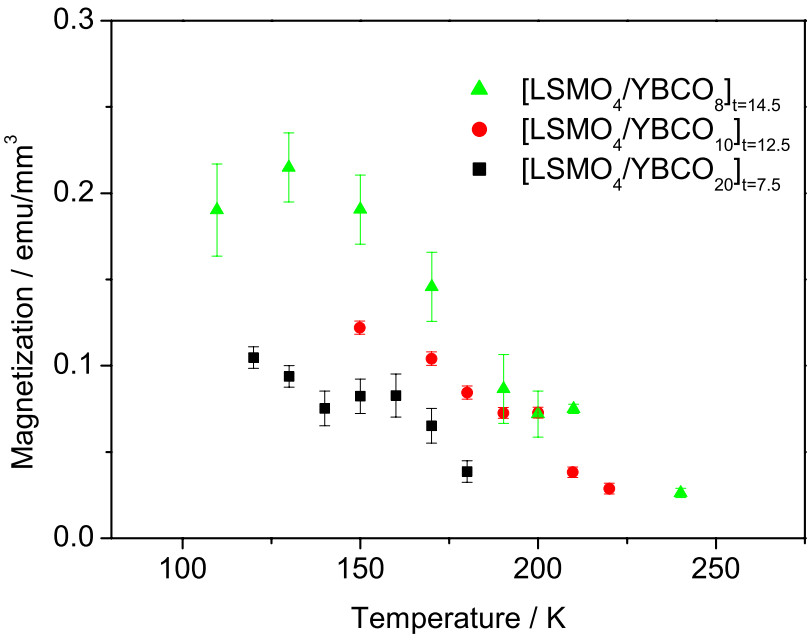

Figure 7.12 Plot of magnetization of multilayer with YBCO layer thickness.

decreasing LSMO thickness) as the dominant cause of the decreasing T_{Curie} in the multilayers. Unfortunately, it was not possible to verify this using XRD because of the presence of strong NGO peaks, as well as the YBCO peaks, very close to all LSMO (0 0 k) peaks. The decrease in T_{Curie} values was very similar to that observed by Dubourdieu et al [101] in LSMO/STO superlattices, as shown in the inset.

An increase in the surface area/volume ratio in particulate manganites leads to a decrease in the magnetization per unit volume [102]. This is because the surface of the manganites is in a different magnetic state caused by oxygen vacancies and other faults in the crystal structure which lead to a magnetically disordered state. Multilayers with thinner manganite layers have a larger interface area/volume ratio and hence higher percentage of magnetically disordered states, which can result in a lower saturation magnetization values as suggested in Figure 7.11.

It is also apparent that the M_s values of the multilayers with thinner manganite thicknesses are lower. The calculated M_s value for the multilayers at T=0K is 0.59 emu/mm^3 which is of the same order of magnitude as that obtained by extrapolating the MT data in Figure 7.11. The cause of this M_s suppression is likely to be the increasing strain in the LSMO with decreasing layer thicknesses, and the increasing interface/volume ratio, which were discussed.

The T_{Curie} and the M_s of the multilayers also decreased with increasing YBCO layer thicknesses. This is because coupling between the manganite layers is suppressed with increasing spacer thicknesses, as the manganite layer thickness, and hence the layer properties should be

the same in all cases shown in Figure 7.12. The figure is thus evidence of magnetic coupling between manganite layers across the YBCO spacers in the cuprate/manganite multilayers.

7.4 T_c suppression in F/S multilayers

In this study we investigate F/S interaction in manganite/YBCO multilayers and examine the suppression of superconductivity and its associated causes with respect to the properties of the ferromagnetic layers. We deposited three sets of multilayers comprising YBCO with three different magnetic materials, LC(0.3)MO and LSMO which are ferromagnetic with different T_{Curie}, and $La_{0.45}Ca_{0.55}MnO_3$ (LC(0.55)MO) which is antiferromagnetic. All three manganites have very similar lattice parameters and are structural and chemically compatible with YBCO. Specifically, we compared T_c suppression in the [LC(0.3)MO/YBCO] and [LSMO/YBCO] samples, which contain F layers with different exchange interaction, and that in [LC(0.3)MO/YBCO] and [LC(0.55)MO/YBCO] samples to examine the effect of stray field from the F layers in the multilayers. By varying the F and S layer thicknesses individually, the length scales associated with F/S interaction in these heterostructures were investigated.

Proximity effects in our F/S oxide multilayers were investigated using the T_c of the samples. The behaviour of the superconductor T_c is representative of that of the superconducting order parameter. The change in T_c of the multilayers is a measure of the suppression of superconducting order parameter in the S layer.

7.4.1 Results

In Figure 7.13, we plot T_c of the various multilayers against the YBCO layer thicknesses, x. The figure also compares our results with that observed by other groups. Note that T_c suppression in our [LC(0.3)MO/YBCO] films is similar to the results obtained by Sefrioui et al [1], which confirms the reproducibility of these multilayers.

We observe in Figure 7.13 that the T_c suppression is greater in all magnetic manganite/YBCO multilayers, including the antiferromagnetic, AF, manganite spacers, compared to the multilayer incorporating non-magnetic $PrBa_2Cu_3O_7$ (PBCO) spacers [103]. Note also that the T_c in the manganite/YBCO samples deviates from PBCO/YBCO samples at x $\sim$ 20nm. This corresponds to the minimum thickness of YBCO beyond which the T_c is not affected by the F layer. We will refer to this as the critical thickness of YBCO, x_{crit}. Figure 7.13 also shows that the rate of T_c suppression is comparable in both F/S [LC(0.3)MO/YBCO] and AF/S [LC(0.55)MO/YBCO] samples. As both the F and AF layers have almost the same structural and chemical compatibility to YBCO, the possibility that the T_c suppression in the F/S multilayers is dominated by the stray field from the F layers can be ruled out.

Figure 7.14 shows a plot of the T_c against the thickness of the manganite layer, d, along with data from [LC(0.3)MO/YBCO] samples from Sefrioui et al [1]. We observed that the T_c of the multilayers decreased with increasing d. Figure 7.14 also indicated an increase in T_c suppression

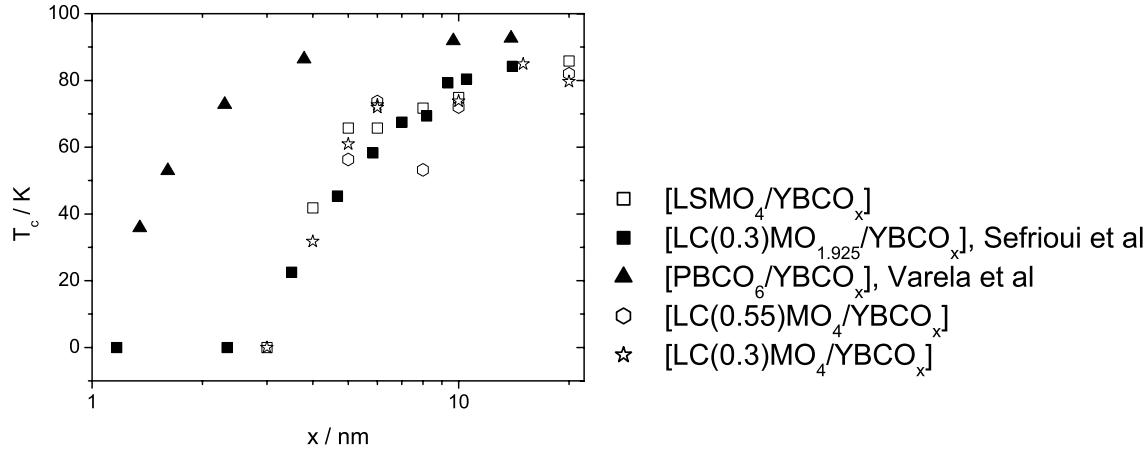

Figure 7.13 Plot of multilayer T_c with YBCO layer thickness, x, compared with values obtained from literature. As indicated in the figure, $[LC(0.3)MO_{1.925}/YBCO_x]$ and $[PBCO_6/YBCO_x]$ multilayer data were acquired from Sefrioui et al [1] and Varela et al [103] respectively.

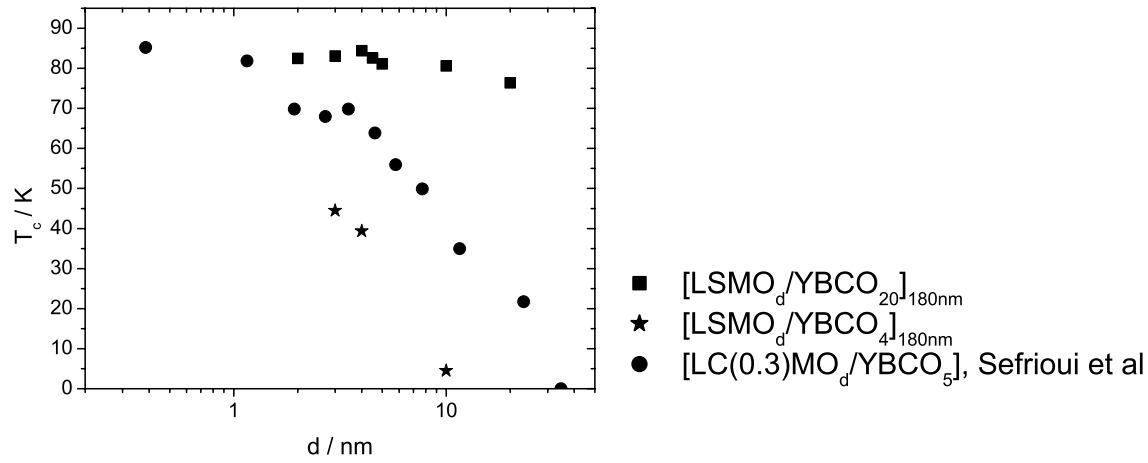

Figure 7.14 Plot of multilayer T_c with manganite layer thickness, d, compared with literature values.

when x decreases from 20nm to 5nm and further to 4nm. T_c suppression begins to level off for the multilayers with x = 20nm. Beyond this thickness, the superconductivity in the multilayers is unaffected by the F layer thickness. Therefore, we can estimate that $x_{crit} \sim 20$nm, similar to the value estimated from Figure 7.13.

Table 7.1 Lattice mismatch between PBCO, LSMO and LC(0.3)MO, with YBCO.

Material	Lattice Mismatch with YBCO, %	
	a-axis	b-axis
PBCO	-0.7	-1.1
LSMO	-1.2	0.4
LC(0.3)MO	-0.7	0.9

7.4.2 Discussion

PBCO and manganites have very similar lattice parameters which match those of YBCO, hence eliminating strain as a possible cause of the difference in suppression effects. The lattice mismatch between PBCO and the manganite spacers with YBCO are very similar as shown in Table 7.1. Hence, the difference in the rates of T_c suppression between the PBCO/YBCO and manganite/YBCO multilayers was attributed to F/S interaction.

The interplay within F/S multilayers is studied with respect to two significant length scales: ξ_S, the superconducting coherence length and ξ_F, the ferromagnet coherence length. ξ_F is directly related to the strength of the ferromagnet through, (in the clean limit)

$$\xi_F = \hbar\nu_F/\Delta E_{es} \tag{7.1}$$

where ν_F is the Fermi velocity and ΔE_{es} is the change in exchange splitting in the ferromagnet. We can write $\Delta E_{es} = I_{eff}\mu$ [65] where μ is the magnetic moment and I_{eff} is some effective exchange coupling energy.

Interface Transparency

The F/S interface properties are important in determining the degree of suppression of the order parameter in the S layer. The proximity effect can be characterized with the following parameters [65]:

a) The proximity effect parameter, which is a measure of the strength of the proximity effect between F and S, is given by

$$\gamma = (\rho_S\xi_S)/(\rho_F\xi_F) \tag{7.2}$$

where ρ_F and ρ_S are the resistivities of F and S respectively.

b) The transparency of the boundary is represented by the equation, $T \sim 1/(1+\gamma_b)$ where γ_b, the transparency parameter, is proportional to (l_F/ξ_F). A perfectly transparent interface is represented by $\gamma_b = 0$.

Hence, a larger E_{ex} gives a smaller ξ_F due to more pair breaking in the S layer. However, it may also lead to a lower transparency for carriers at the F/S interface and a weaker contribution from proximity effects. These two effects are in competition, as discussed by Aarts et al [65].

Assuming constant transparency and thickness, multilayers containing magnetic spacers with higher magnetic moment and/or exchange energy will have shorter ξ_F and consequently a lower T_c. This is illustrated in Figure 3.8

As we expect the interface quality in all our samples to be the same, we can investigate the variation in T_c with respect to the individual layer thicknesses and the properties of the magnetic layers. From Figure 7.13, we investigate the T_c suppressing effects of the magnetic layers by considering the two significant contributions to ξ_F, μ and exchange interaction ΔE_{ex}.

Effect of Magnetic Moment, μ

From the point of view of the magnetic moment μ, the samples [$LSMO_4$ / $YBCO_x$] and [$LC(0.3)MO_4$ / $YBCO_x$] have similar moment per unit cell ($3.67\mu_B$ and $3.7\mu_B$ respectively) and perhaps only a small difference in the suppression could be expected. However, we can compare our results with those obtained by Przyslupski et al using [$(Nd_{0.67}Sr_{0.33}MnO_3)_{3.91}$/ $(YBa_2Cu_3O_7)_x$] [73] ($Nd_{0.67}Sr_{0.33}MnO_3$ has a bulk T_{Curie} of 280K [104]) and [$(Nd_{0.81}Sr_{0.19}MnO_3)_{3.91}$/ $(YBa_2Cu_3O_7)_x$] [105] where the Nd contributes to a stronger moment of $6.10\mu_B$ and $6.74\mu_B$ respectively.

The calculations of the magnetic moment of a unit cell of $(Nd_{0.81}Sr_{0.19}MnO_3)_{3.91}$ are shown in the box. Surprisingly, despite the large difference in magnetic moment between NSMO compared to LSMO and LC(0.3)MO, the rate of suppression of T_c is similar for both sets of multilayers. In this case, it would seem that the magnetic moment is not a crucial parameter in the suppression of superconductivity in manganite/YBCO multilayers.

Effect of exchange interaction, ΔE_{ex}

From the point of view of the influence of the exchange interaction ΔE_{ex}, we can consider the different Curie temperatures of the materials (if we consider $E_{ex} \sim (k_B T_{Curie})$). Hence, since LSMO and LC(0.3)MO have $T_{Curie} = 370K$ and 260K respectively, one would expect a difference in the T_c suppression. This difference is not observed to within experimental error, although manganites might not be ideal for such studies on exchange interaction influence because of their relatively similar Curie temperatures. Common metallic ferromagnets have a big range of T_{Curie}s: gadolinium, iron and cobalt have T_{Curie}s of 293K, 1043K and 1403K respectively [12].

There are 2 separate contributions to the total magnetic moment in $(Nd_{0.81}Sr_{0.19}MnO_3)_{3.91}$, Nd^{3+} ions, and Mn^{3+} and Mn^{4+} ions.

- Magnetic moment contribution from Mn^{3+} and Mn^{4+} ions,

$$\begin{aligned} \mu_{Mn} &= 2 \times (0.81[\mu_{Mn^{3+}}] + 0.19[\mu_{Mn^{4+}}]) \\ &= 2 \times (0.81(2) + 0.19(3/2)) \\ &= 3.81\mu_B \end{aligned} \tag{7.3}$$

- Magnetic moment contribution from Nd^{3+} ions is illustrated in the following equations,

  Total angular moment,

$$J = \frac{9}{2} \tag{7.4}$$

  Gyromagnetic factor,

$$\begin{aligned} g &= 1 + [\frac{J(J+1) + S(S+1) - L(L+1)}{2J(J+1)}] \\ &= 1 + [\frac{\frac{9}{2}(\frac{11}{2}) + \frac{3}{2}(\frac{5}{2}) - 6(7)}{\frac{18}{2}(\frac{11}{2})}] \\ &= \frac{8}{11} \\ &= 0.727 \end{aligned} \tag{7.5}$$

  Effective magnetic moment,

$$\begin{aligned} p &= g\sqrt{J(J+1)} \\ &= 3.62\mu_B \end{aligned} \tag{7.6}$$

Total magnetic moment = sum of magnetic contributions = [0.81 × 3.62] + 3.81 = 6.74 μ_B

Effect of anti-ferromagnetism on superconductivity

We studied the T_c suppression effects in similar AF/S multilayers. For this investigation, we used LC(0.55)MO which has very similar lattice parameters to the ferromagnetic manganites, LC(0.3)MO and LSMO, used in this study. The AF layer has a zero net moment as shown in Figure 7.15, but exchange energy similar to that in the F manganites.

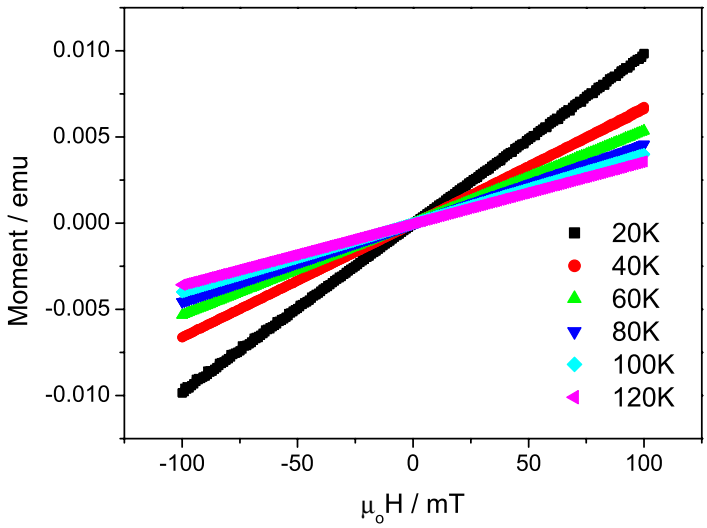

Figure 7.15 MH characteristics of [LC(0.55)MO_4/$YBCO_8$] AF/S multilayers at various temperatures confirm that the AF layers have zero net magnetic moment.

As mentioned in the previous section, we also observe a strong suppression of superconductivity in the multilayer with an antiferromagnetic manganite LC(0.55)MO, very similar to that observed in the F/S manganite/YBCO samples. Due to the nature of the AF material, this result indicates that the T_c suppression in our multilayers cannot be based on stray induction due to net magnetic moment in the F layer. The similar rate of suppression of T_c in F/S and AF/S samples, compared to the non-magnetic PBCO measurements, implies that the suppression observed in the AF/S samples is based also on its magnetic properties. This is consistent with experimental [106, 107] observations elsewhere and theoretical work by Krivoruchko [108] considering band antiferromagnets. The coherence length in a band AF (in the dirty limit) is given by,

$$\xi_{AF} = [2\hbar D/\Delta E_{ex}]^{0.5} \tag{7.7}$$

where D is the diffusion constant and $\Delta E_{ex} \sim k_B T_N$, where T_N is the Néel temperature. Using the ξ_F and ξ_{AF} length scale equations for LC(0.3)MO and LC(0.55)MO (as $T_N \sim 160$K), we note that ξ_F and ξ_{AF} are very similar. This may help to explain the observed comparable

suppression of superconductivity.

Effect of layer thickness on T_c suppression

The effect of S layer thickness on the suppression of T_c was also investigated. T_c in multilayers is also directly affected by ξ_S, and thus the thickness of the superconducting layer, as $x_{crit} \sim 2\xi_S$. x_{crit} in YBCO as observed in both Figures 7.13 and 7.14 is approximately 20nm, almost two orders of magnitude larger than expected. Our result supports that of Holden et al [74] who observed a suppression of free-carriers in LC(0.3)MO/YBCO superlattices for YBCO spacers thinner than approximately 20nm. The large length scales observed may be due to the structural compatibility between manganites and YBCO. The high-quality epitaxial interfaces associated with such heterostructures result in greater pair breaking effects in the S layer. A thicker S layer, and hence a larger x_{crit}, is required to saturate the multilayer T_c.

7.5 Conclusions

In summary, the effects of individual layer thickness on the multilayer T_c and T_{Curie} were investigated. This chapter described the successful deposition of reproducible oxide F/S multilayers of ultra thin repeats using the 'eclipse' PLD technique. With the YBCO superconducting down to a thickness of 4nm, these multilayers facilitated our investigation into the different causes of T_c suppression.

Coupling between manganite layers across the YBCO spacers was evident in the multilayers, with T_{Curie} values decreasing with increasing YBCO spacer thicknesses in the multilayers. The decrease in T_{Curie} with manganite layer thicknesses, however, is likely to be structural in origin.

The suppression of superconductivity in manganite/YBCO multilayers due to interaction of S layers with the F spacers was also evident. Contrary to what was initially expected, the different magnetic nature of the manganite layers, did not seem to have a major influence on T_c suppression. Suppression, however, was stronger with F spacers than NM ones. We observe, also, that the magnetic length scales in AF/S and F/S multilayers are comparable. These length scales were larger than that expected based on the coherence lengths associated with cuprates, as predicted previously by other groups [41, 74].

We have also estimated the critical thickness, x_{crit}, for ferromagnetic [LAMO(A=Ca, Sr)/ YBCO] multilayers to be $\sim$ 20nm. This value is similar to the experimental value obtained by Holden et al [74]. This result suggests that length scales associated with proximity effects in oxide multilayers are much longer than expected.

Chapter 8

Trilayer Devices

8.1 Motivation

As reported in the last chapter, the in-situ deposition of cuprate and manganite layers in the MK9 is reliable, and the competition between ferromagnetism and superconductivity in these heterostructures exhibit superconducting critical current suppression. We aim to investigate these effects further, as a means to fabricate devices which we can use to actively control the states of a superconductor, suitable for power switching applications. One potential way to achieve this is by fabricating alternate layers of LSMO / YBCO / LC(0.3)MO. Since the coercive fields of LCMO and LSMO are different, we can switch the multilayer structure, like a spin-valve, from a parallel to its anti-parallel state. A similar metallic device was first investigated by Gu et al [2] using Nb as the superconducting spacer, and CuNi/Permalloy(Py) as the ferromagnetic layers, one of which was pinned by an adjacent FeMn layer. Gu et al observed that the superconductivity was suppressed when the F layers were aligned in parallel. Here, the similarly polarized carriers from the ferromagnets are expected to suppress the formation of Cooper pairs in the S layer, and hence its superconductivity.

Our aim in this chapter is to investigate the effects of the suppression of superconductivity in such oxide pseudo spin-valve heterostructures which incorporate high-temperature superconductors. This chapter describes the initial characterization of the trilayers and details the device measurements performed and the results obtained as a function of the external field used to change the configuration of the F layers. We discuss the pseudo spin valve effects observed in the device.

8.2 Trilayer Devices

8.2.1 Double Coercivity

The fundamental parallel (P) to anti-parallel (AP) switching of our proposed 'spin-valve' oxide trilayer device relies on the ability to switch only one of the two F layers. A larger window of difference in coercive fields, H_{co}, of the two F layers is desirable as this allows the effects due to the orientations of the two magnetic states to be more easily distinguishable. The effects can thus be measureable over a larger window. The difference in H_{co} of the manganite layers used in our oxide heterostructures is shown in Figure 8.1. With different coercive fields ($\mu_\circ$H = 4.5 mT and 16 mT for LSMO and LC(0.3)MO respectively), they can potentially be aligned in an antiparallel configuration, hence resembling a spin valve. The coercive fields of these ferromagnetic layers may also be 'altered' by varying F layer thicknesses.

An LSMO/YBCO/LC(0.3)MO trilayer of thicknesses 15nm, 10nm and 15nm respectively was deposited on an STO substrate. Figure 8.2 shows that the sample has two T_{Curie}s, at 165K and 265K which corresponds to that of LC(0.3)MO and LSMO respectively. The two different T_{Curie}s are indicative of the presence of the two separate manganite layers in the trilayer. However, the T_{Curie} values are smaller than the bulk values of 260K and 360K for LC(0.3)MO

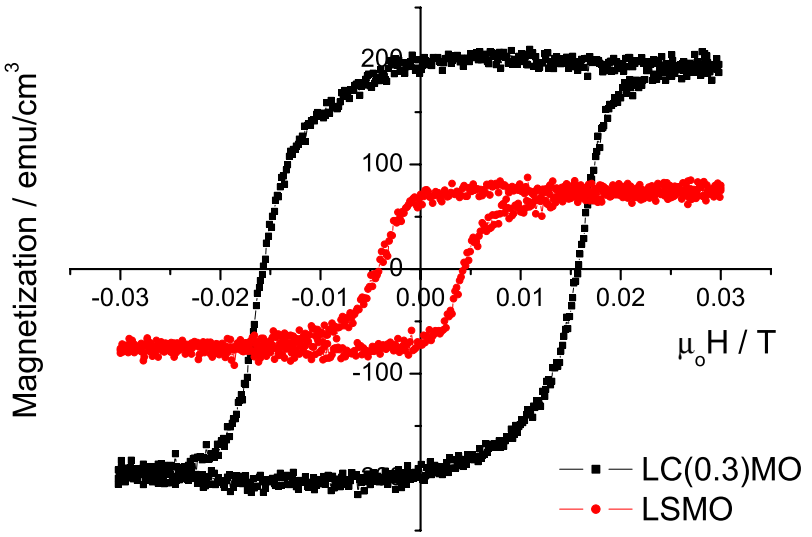

Figure 8.1 MH plots of LC(0.3)MO and LSMO films at 100K. θ refers to the angle between the long axis of the chip and the magnetic field, H

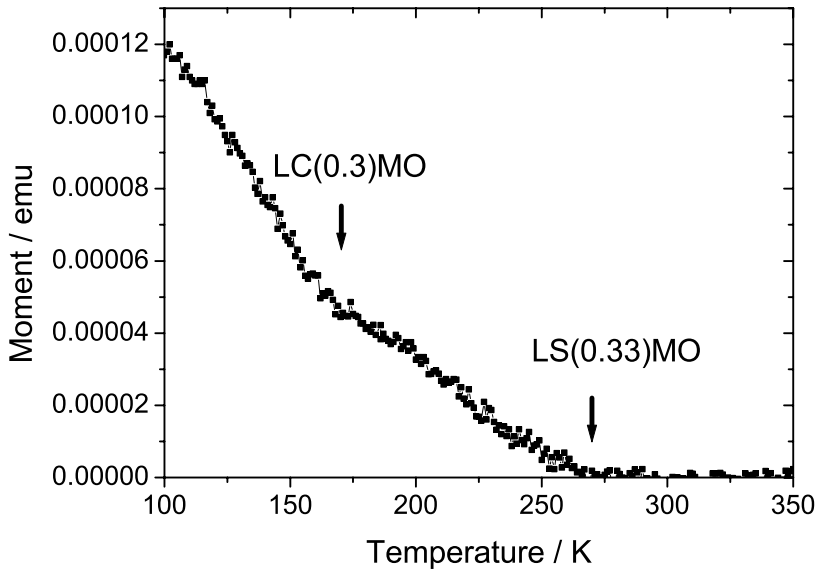

Figure 8.2 Magnetic moment of LSMO/YBCO/LC(0.3)MO trilayer with temperature. The kinks in the plot are indicative of the T_{Curie} values in the two manganite layers.

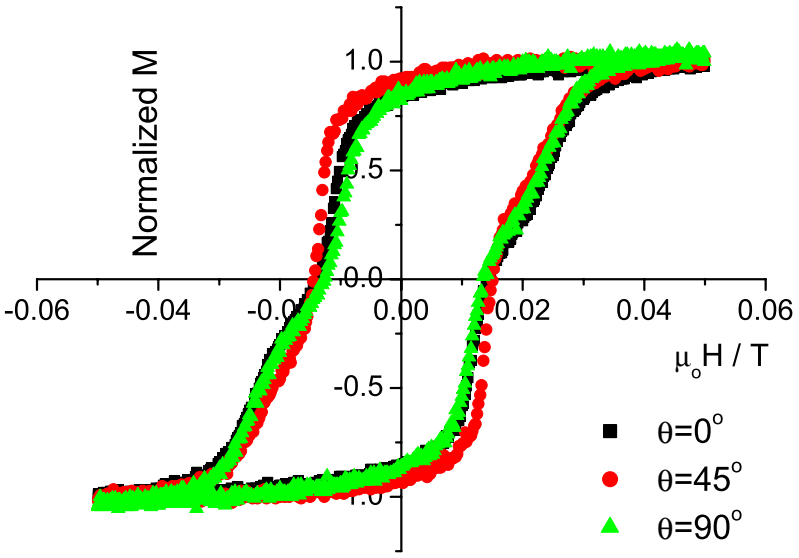

Figure 8.3 MH plot of M9, LSMO/YBCO/Lc(0.3)MO trilayer at 100K. The film demonstrates a double coercivity characteristic. θ is the angle between the long edge of the film sample and the applied field.

and LSMO respectively. This could be due to epitaxial strain in the thin films.

In the LSMO/YBCO/LC(0.3)MO trilayer above its T_c, we observed a double coercivity due to the different manganite films, as shown in Figure 8.3, a magnetic measurement of the trilayer M9. The coercive fields correspond to $\mu_\circ H$ = 12 mT and 22 mT for LSMO and LC(0.3)MO respectively.

Softening of LSMO using Permalloy

The observed double coercivity in the trilayer was a preliminary indication of the feasibility of fabricating our proposed oxide devices. We investigated the possibility of expanding this 'anti-parallel' window through the softening of the top LSMO layer with a deposition of an adjacent softer ferromagnet, Py. Py has a typical coercive field in the range of $\mu_\circ H$ = 0.1-1 mT.

We deposited 30nm of LSMO in the MK9 on an STO substrate. The film was diced into 2.5 × 2.5mm squares, which were loaded into the MKIII sputtering system for Py deposition. We deposited 20nm, 40nm and 80nm of Py on the LSMO films, and measured the magnetic properties of the bilayers using the VSM.

From Figure 8.4, we observed that the field required to saturate the bilayers, H_s, was not sufficiently changed by the addition of Py on top of LSMO. The sample with 80nm of Py showed a distinct double coercivity characteristic, due to the very different H_{co}s of the Py and LSMO layers. However, H_{co} value of this bilayer was not smaller compared to the plain LSMO.

The saturation magnetization, M_s, of the samples increased with increasing Py thickness as

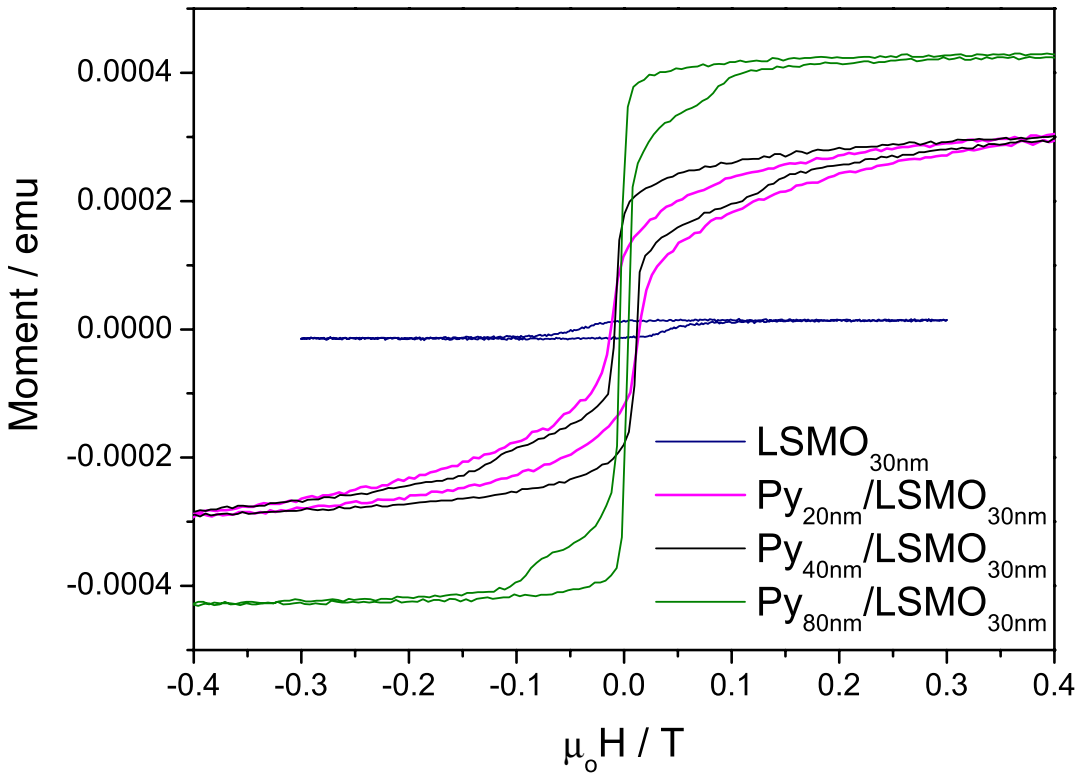

Figure 8.4 MH loops of 30nm LSMO films with 0, 20nm, 40nm and 80nm Py deposited on top. The M_s values of the samples increased with increasing Py thickness as expected. The plots were normalized for easier comparison of the features with respect to the changes in coercive fields.

expected. However, we observed that the samples with 20nm and 40nm Py have very similar M_s values. An explanation for this is the error in the dimensions of the two films. The sample with 40nm Py was smaller than that with 20nm Py as one of the edges of the square samples was not at 90° to the adjacent sides. The slight difference in film dimension accounted for the noticeable error in M_s values because the film samples were small.

This series of films indicated that Py did not soften the magnetization process of LSMO and both materials switched independently. An alternative method to increasing the applied field range of the AP window would be to decrease the thickness of the LCMO to increase its coercive field. The F layers in our devices were kept at constant thicknesses, however, so as to achieve a zero net moment in the anti-parallel configuration.

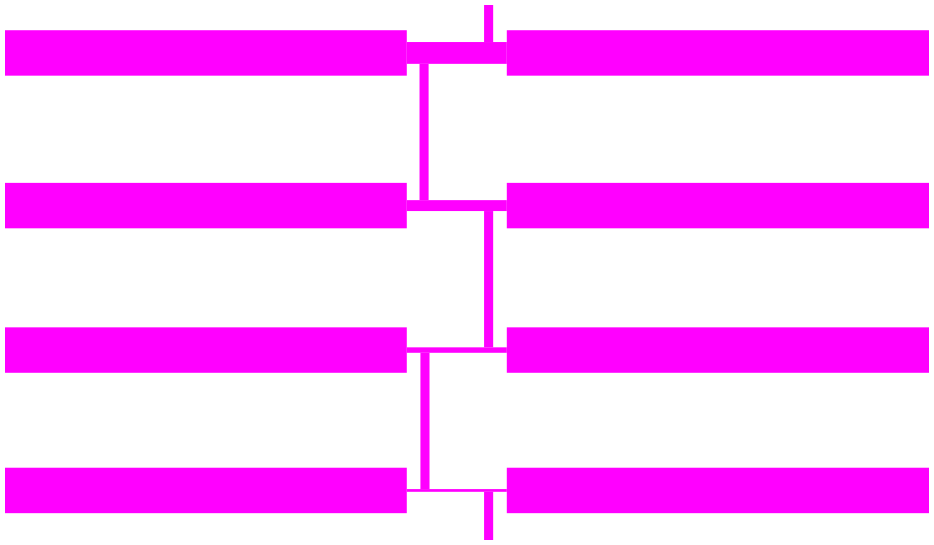

Figure 8.5 Mask pattern used for the fabrication of trilayer devices. The pattern was designed for 4-point measurements on tracks of 3μm, 6μm, 12μm and 24μm widths, as seen here as the horizontal tracks. Voltage contacts are along the tracks.

8.3 Device results

To investigate the effects of AP and P configurations of the F layers in the trilayer M9, on the its superconductivity, we processed the film into a device, using the pattern as shown in Figure 8.5. The pattern was designed for 4-point transport measurements of a series of parallel tracks of widths 3μm, 6μm, 12μm and 24μm.

Device fabrication was performed in the Device Materials Clean Room using similar processing procedures are that described in Section 5.8.1. The M9D devices were wired onto a sample holder and measured using the 'CMR rig'. The chip was cooled and maintained in liquid N_2 at 77K for the duration of the transport measurements to reduce effects due to localized heating on the chip. We observed that at 77K, the sample is in the pseudo-superconducting region, above its T_c ($T_c \Rightarrow$ T when R > noise level in RT plot). The MR plots of 6μm, 12μm and 24μm tracks are shown in the following figures.

We observed a field dependence in the track resistance. The resistance of the trilayer tracks increases to a maximum at H = $\pm$0.02T, within the window of the coercive fields of the two different manganites. The trilayer resistance is thus highest when the manganite magnetic moments are oppositely aligned.

These effects of anti-parallel aligned F layers on the sandwiched superconducting layer was further investigated using the "J_c Rig".

8.3.1 Device Measurements in "J_c Rig"

Due to limitations associated with the CMR rig, subsequent more detailed transport measurements were performed in the "J_c Rig" in the Device Materials Main Lab. The "J_c Rig" was more

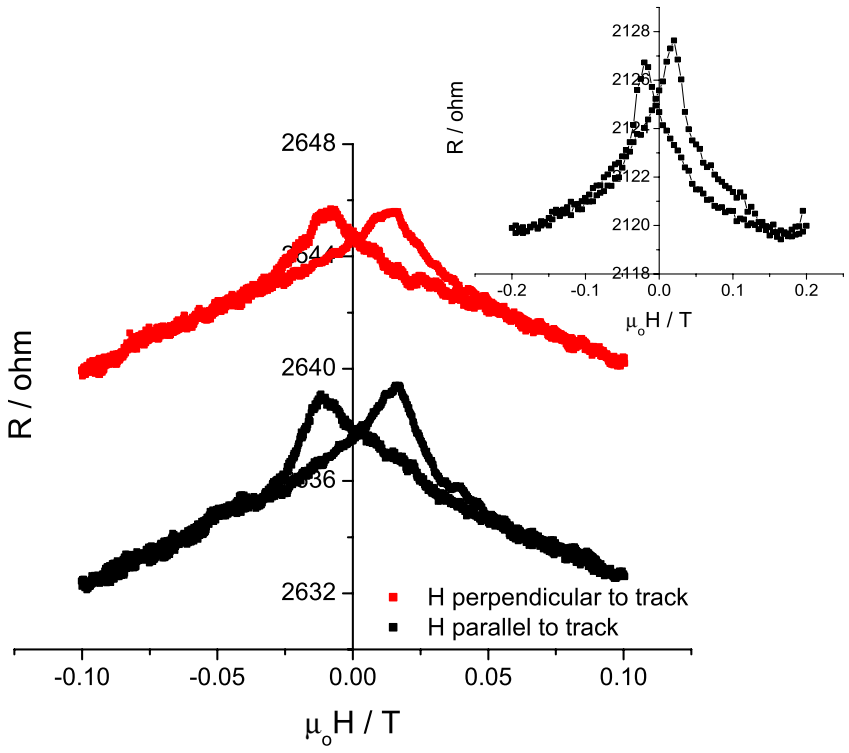

Figure 8.6 M9D: MR plot of 6μm track measured at 77K in the "CMR" rig immersed in liquid nitrogen. Inset shows the same measurement performed at 77K in the "J_c Rig" with H parallel to I_{bias}

suitable for our intended measurements because of the following reasons.

- We could perform MR measurements at stabilized temperatures below 77K by using a combination of heating and cooling with flowing helium gas which allowed for more accurate sample temperature control.
- The superconducting magnet in the "J_c Rig" could easily generate and maintain a field of 200mT required for our measurements without affecting the sample temperature. This is because the superconducting magnet can be kept at 4.2K in liquid helium, in thermally isolated chambers.

From Figure 8.9, we observe that the 6μm and 24μm tracks in our devices become superconducting at T_cs of 44.5K and 70.5K. Within the resolution of the measurement rig, we observed no change in the RT behaviour of our devices for both the parallel and anti-parallel configurations, as the RT plots in both configurations overlapped each other. The devices were measured for MR characteristics within the pseudo-superconducting region.

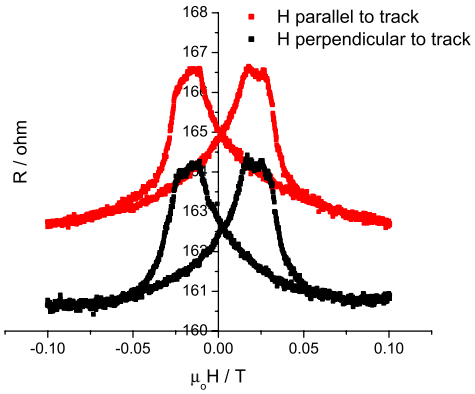

Figure 8.7 M9D: MR plot of 12μm track measured at 77K.

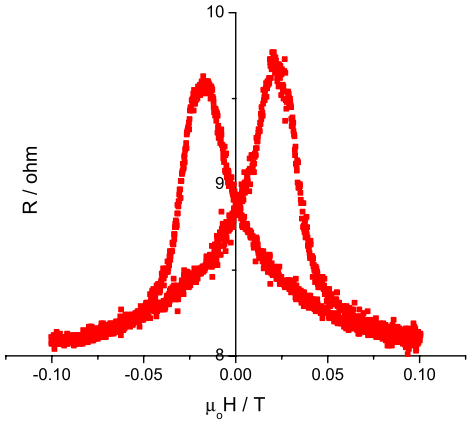

Figure 8.8 M9D: MR plot of 24μm track measured at 77K.

H-dependence of track resistance

The reproducibility of the peak in MR characteristic was illustrated in Figure 8.6 which shows that MR of the 6μm track measured in both measurement rigs are similar. Both measurements were performed using 10μA current, and we observe a small difference in the track resistance. This occurred because the actual sample temperature in both systems, although pre-set to 77K in both cases, were different. The samples were in different thermal environments in different measurement rigs.

%MR variation with temperature

Figures 8.10 and 8.11 show the MR plots of a 6μm and a 24μm wide track at different temperatures. To facilitate easier comparison of MR characteristics of the same track at different temperatures, only a single direction of the MR sweep is plotted. The plots in both directions of H sweep were, however, symmetric to each other about the y-axis. The sweeps were also normalized for R at H=200mT.

Below the onset of superconductivity, T within the T_c transition range

We can observe that the resistance peak, and hence the MR, at $\mu_\circ$H $\sim$ 20mT increases significantly at lower temperatures. However, the MR plots at lower temperatures were also noisier because of the lower tracks resistances at the given current. We have included, in both figures, MR sweeps at the minimum temperatures at which a peak is decernible above the noise level. Thus, whilst using the same I_{bias} at T=67K and T=68K for the 6μm and the 24μm wide tracks respectively, the peak at $\mu_\circ$H $\sim$ 20mT disappears below the noise level. The instrumental limitations were reached.

The plots also show that the %MR decreases as the superconducting track tends towards

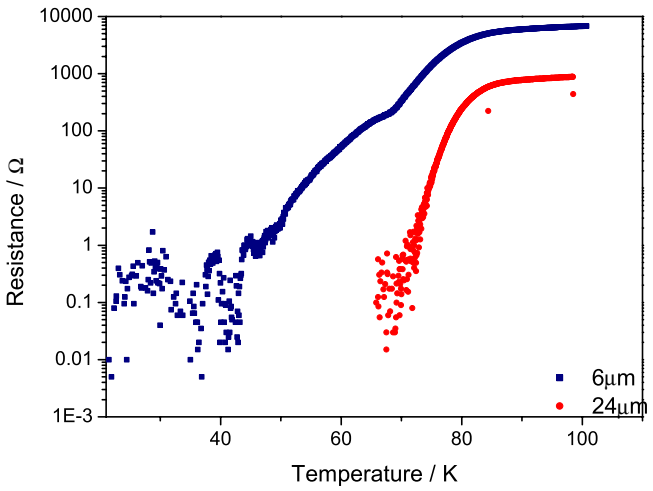

Figure 8.9 RT plot of 6μm and 24μm device. The T_c values of the devices was defined as the temperature below which the resistance was not decernible above the noise. The RT plots for the device in its P and AP configurations were the same.

its normal state. Hence, the peak in MR was largest at $T \sim T_c$ when $I_{bias} \sim I_c$. At temperatures higher than T_c but within the superconducting transition, the %MR decreased. Further measurements showed that no MR peak was observed in the 24μm track at 82K and above, the onset of superconductivity for the device.

From Figures 8.10 and 8.11, we notice that, at lower temperatures, the MR peak was centered at a larger value of H. This small shift, in applied field, at which the peak occurred is due to the corresponding increase in coercive fields of any ferromagnetic material with decreasing temperature.

%MR variation with bias current

The effects of I_{bias} on the %MR characteristics of the F/S/F trilayer were investigated using the 24μm wide track. We measured a series of MR plots at various I_{bias} at constant temperatures. This was done over a range of temperatures from 44K, through the pseudo-superconducting region (T=68K, 72K and 78K) and into the normal state (T=82K and 88K). Sets of MR measurements with varying I_{bias}, taken at the first four measurement temperatures, are shown in the following figures. We observed no MR characteristic when the device entered the normal state.

The %MR was measured over different I_{bias} for each temperature. The peak in MR characteristic was most evident when $I_{bias} \sim I_c$. At each constant temperature, this characteristic was larger with a lower I_{bias}, thus demonstrating a similar trend to its variation with temperature (at constant I_{bias}) as described in the previous section. For example, in Figure 8.13, it is apparent

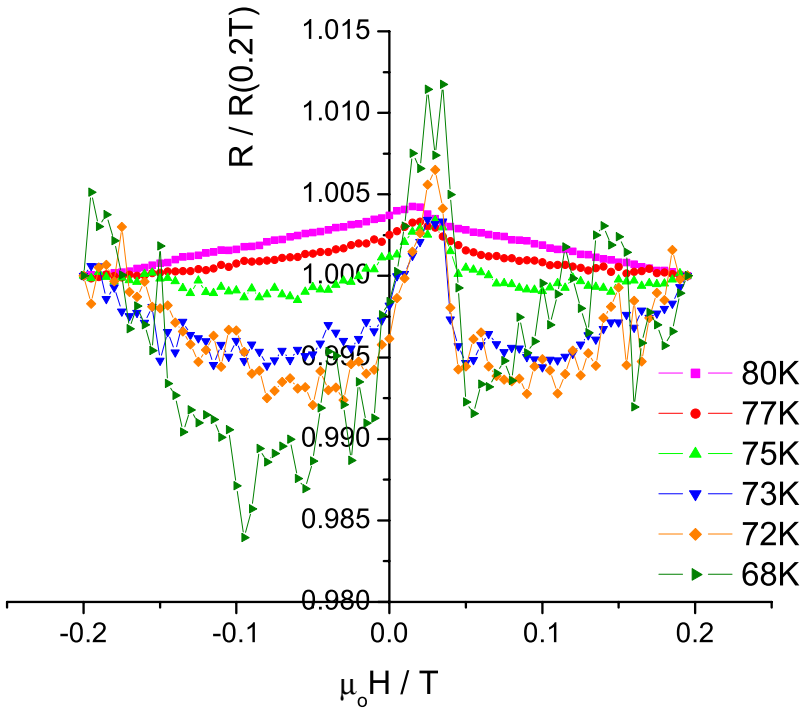

Figure 8.10 Normalized MR plot of the 6μm wide track with H applied perpendicular to I. I=10μA in all cases.

that at T=68K, just below the device T_c, MR increases with decreasing I_{bias}. This trend was observed at T$\ll$T$_c$, as shown in Figure 8.12, at I $\sim$ I$_c$.

The relationship between the MR characteristic with I_{bias} within the T_c transition range is summarized in Figure 8.16. It is clear that the %MR increases with decreasing I_{bias} and T. We observe that the %MR at temperatures above the T_c of 70.5K tends towards a value associated with the device resistance at very small I_{bias}, (MR= $\frac{\Delta R}{R_T}$). Therefore, at such low I_{bias}, the %MR just below T_c can be potentially very high, if measurable above the noise level associated with the electronics[1]. This is because the MR varies directly with the track resistance which, in those circumstances, is close to zero.

Magnetoresistance peak at 44K

As observed in Figure 8.12, the trend of decreasing %MR with increasing I_{bias} was also observed when I_{bias} was just above I_c at 44K. The observed peak at 44K, however, has a smaller MR than that at 68K. This observation was in line with the trend of decreasing %MR with increasing

[1]The standard deviation for T=68K for I_{bias} is very large because the resistance of the device is very low. The mean resistance, measured at values of H where both layers are parallel, is $8\times10^{-3}\Omega$. At those conditions, the YBCO spacer thus shunts a very high percentage of the current through the CIP device.

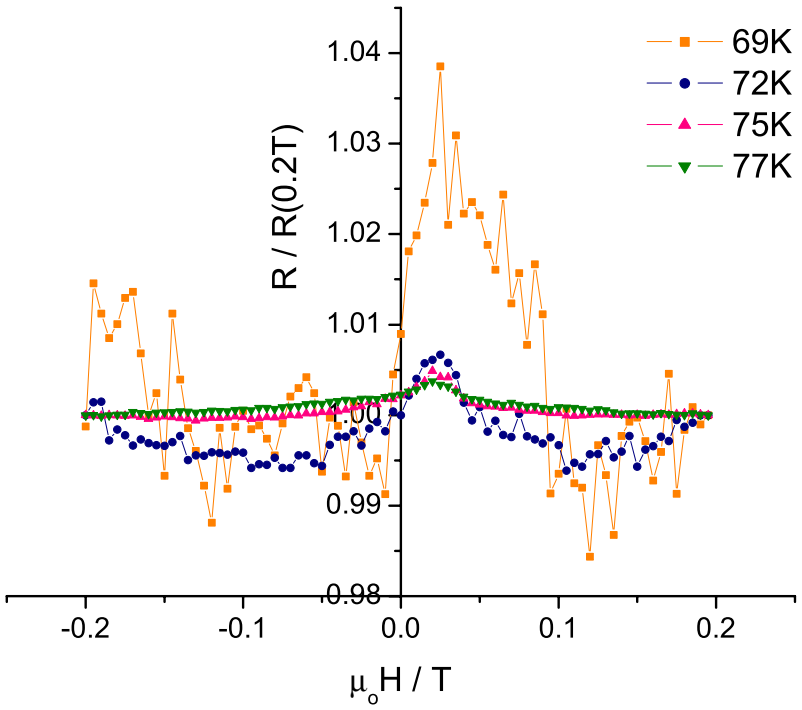

Figure 8.11 Normalized MR plot of 24μm wide track with B applied parallel to I. I=500μA in all cases.

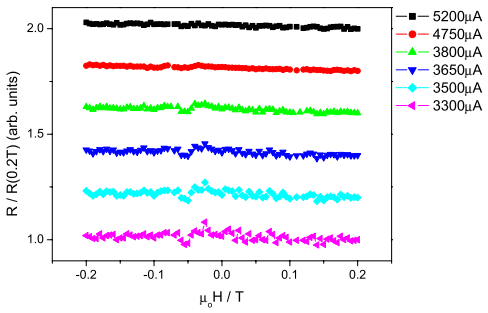

Figure 8.12 M9D: MR plots of 24μm wide track at 44K at various I_{bias}. For clarity, only half of the MR scans were plotted, and displaced.

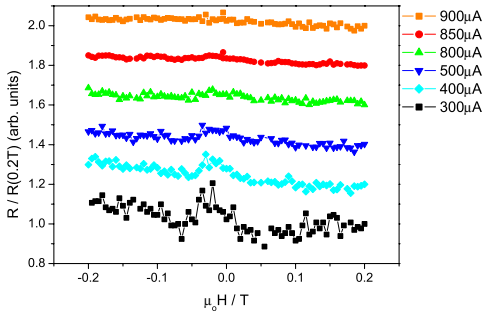

Figure 8.13 M9D: MR plots of 24μm wide track at 68K at various I_{bias}. For clarity, only half of the MR scans were plotted, and displaced.

I_{bias}. At 44K, the I_{bias} required for MR observation, i.e $I_{bias} \sim I_c$, was 3mA. This value of I_{bias} if applied to the device at 68K, would show no evidence of the MR peak. Hence, for a given I_{bias}, the %MR increases with decreasing T, as indicated earlier in Figures 8.10 and 8.11.

Figure 8.17, which illustrates this trend for the 24μm wide device at $T \sim T_c$ and $T \ll T_c$,

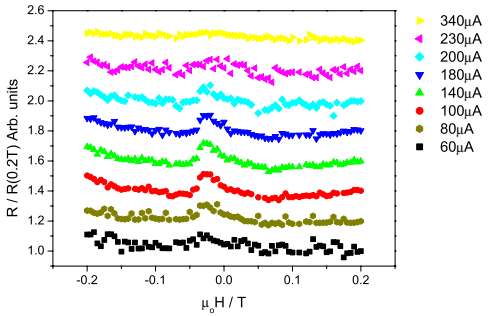

Figure 8.14 M9D: MR plots of 24μm wide track at 72K at various I_{bias}. For clarity, only half of the MR scans were plotted, and displaced.

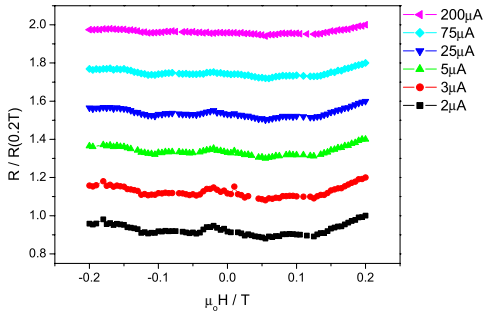

Figure 8.15 M9D: MR plots of 24μm wide track at 78K at various I_{bias}. For clarity, only half of the MR scans were plotted, and displaced.

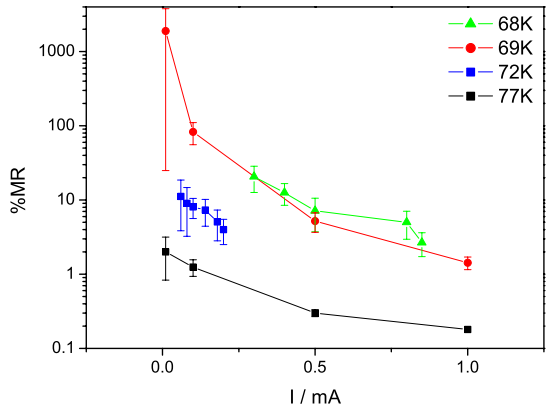

Figure 8.16 Variation of %MR with I_{bias} parallel to B at various temperatures in 24μm wide track. The plots at T=69K and T=77K were acquired as MR sweep at a particular set I_{bias}. For plots at T=68K and T=72K, IV curves were acquired in a field sweep. The %MR values were subsequently derived from these IV curves using an I_{bias} criterion. These two sets of data at 68K and 72K were noiser, as indicated by the larger error bars. This is because more derivation steps were required to present it in the form shown in the figure. The plots acquired by both means are similar, evident in the data sets T=68K and T=69K.

provides a comparison of the %MR with device resistance, measured at μ_oH = 0.2T. We can assume that the superconductor was in the same state within its transition from superconducting to normal (or vice versa) if the track has the same total resistance. The above figure shows that the %MR rises exponentially with decreasing total track resistance. The %MR at a particular resistance is higher at 68K than at 44K. A possible explanation for this observation is that I_{bias} at 44K $\gg$ I_{bias} at 68K.

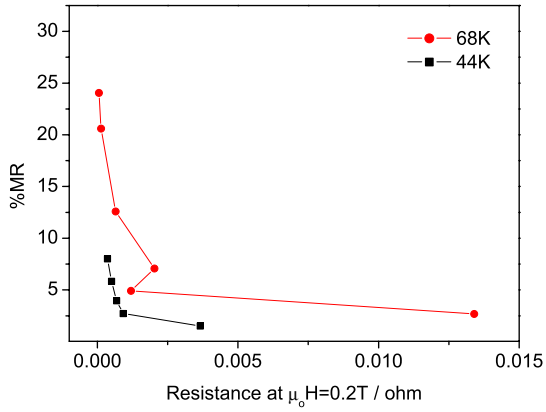

Figure 8.17 Comparison of the %MR with the resistance in the 24μm wide track with H applied parallel to I. A comparison of these two plots at T < T_c=70.5K shows that the %MR is higher at a higher temperature. The I_{bias} values applied at 44K was greater than that at 68K.

8.4 Discussion

The MR observed is puzzling because it was contrary to those observed elsewhere in the similar metallic systems [2]. As discussed in Section 3.7, in the case where the orientation of the F layers can be switched with respect to each other, the superconductivity in the spacer is affected by the alignment of the F layers: When the F layers are saturated and a majority of the spins are aligned, proximity of Cooper pairs, which consist of coupled electrons of oppositely aligned spins, to the adjacent F layers will lead to their break-up into quasiparticles. The parallel-aligned F layers thus suppresses superconductivity in the sandwiched S layer due to proximity effects. When the F layers are aligned anti-parallel, the opposite spins in the 2 F layers are more favorable for the formation of Cooper pairs leading to I_c enhancement. These effects at the anti-parallel configuration, as suggested by Tagirov et al [75], were however opposite to our observations in oxide F/S/F system.

The results obtained were not completely understood. However, in this section, we explore the various possibilities which may contribute towards the MR characteristic observed.

8.4.1 Multidomain?

As observed, the MR peak in the devices occurred at H_{co}s of the F layers. This magnetic state also corresponded to the multidomain state of the F layers, as opposed to the single domain state above M_s in the saturation state. The multidomain state in F layers have accounted for several effects on superconductivity. For instance, Kinsey et al [109] observed an increase in I_c near the H_{co}s of the S/F bilayers. Similar effects were observed by Rusanov et al [110] in CuNi/Nb/CuNi trilayers. This effect was attributed to the minimizing of ferromagnetic exchange interaction in the S layers beneath the domain walls separating antiparallel domains.

Thus, in order to distinguish the effects due to the anti-parallel configuration of the F layers from those due to the multidomain states of the F layers, we investigated the behaviour of the track resistance in a field sweep, with respect to degree of alignment of the F layers.

In this experiment, we measured the resistance of the same trilayer, after demagnetizing, at 68K and various I_{bias}, using smaller field-sweeps, 1, 5, 10 and 20mT, not exceeding saturation fields of either manganite material. Subjecting the device to a small field, not larger than saturation field of any of the 2 F layers will prevent the device from acting like a spin-valve. We will thus not 'lock' the orientation of one layer with respect to the other, thus preventing the anti-parallel configuration. However, we would still be able to qualitatively compare the resistance of the device with respect to the number and size of domains in the F layers, a more magnetized F layer will have fewer and larger domains. A comparison with similar measurements using a field of 200mT, where the moment of both layers are saturated, can reveal if the anti-parallel configuration of the F layers was essential for the observation of the MR peak.

We found that the resistance of the device did not change with field for all 1mT, 5mT, 10mT and 20mT field sweeps, unlike those with sweeps to 200mT. This was indicative that, the MR characteristic depends on at least one of the F layers being saturated in either H direction. We can conclude that the peak in MR in LSMO/YBCO/LC(0.3)MO trilayers occurred only when the F layers are in the anti-parallel configuration, and not just in the multidomain state.

8.4.2 Anisotropic Magneto-Resistance (AMR)

A similar MR peak was observed by Rusanov et al [110] in a CuNi/Nb/CuNi trilayer which they attributed to the AMR effect. Although AMR is present in all ferromagnets [13], we believe that the MR measured in our devices is not due to AMR effects in the F layers due to the following reasons:

- The MR plots in Figures 8.6 and 8.7 indicate that the change in resistance is in the same direction when H is parallel and perpendicular to I.
- Figure 8.18 which illustrates the increase in %MR with decreasing temperature for the 6μm wide track with H applied parallel and perpendicular to I_{bias}, also shows that there is no significant difference in %MR for both B parallel and perpendicular to I.
- The MR was also not observed at temperatures higher than the onset of superconductivity.

In addition, the inset in Figure 8.18 shows that the change in resistance, ΔR, is similar for the temperature range. Hence, it is the rapid decrease in track resistance at lower temperatures which accounts for the significant increase in %MR. This trend is interesting because, within the superconducting transition temperature range, the device resistance drops rapidly to 0, implying that the %MR observed is potentially very high at T$\sim$T$_c$ and at I$\sim$I$_c$. However, this decrease in track resistance also results in increased noise levels which gradually drowns the MR measurements.

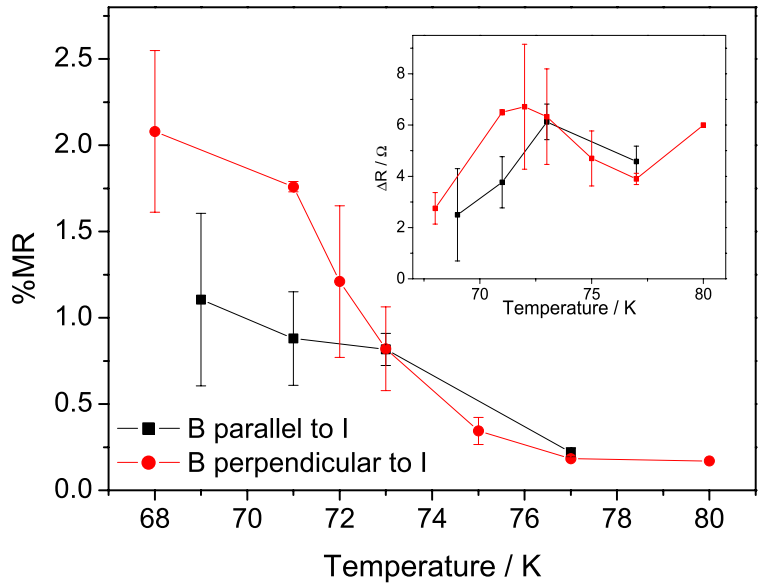

Figure 8.18 Comparison of the MR in 6μm wide track with H applied parallel and perpendicular to I=10μA. The inset shows that the change in resistance, ΔR, is similar within the temperature range.

8.4.3 Parallel Current flow through Trilayer

The MR characteristic is present in all ferromagnetic manganite films. One possibility of the MR observed in the trilayers is the combination of the MR which is characteristic of both manganite layers if I_{bias} flows in all 3 parallel layers separately. To study this possibility that the MR observed is solely due to the individual F layers in a field sweep, we model the extreme case when I_{bias} flows separately and is isolated in all 3 layers, as shown in Figure 8.19.

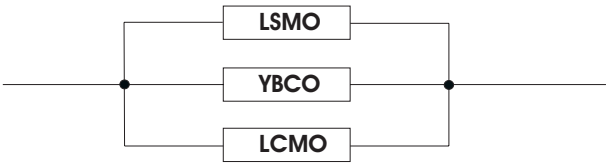

Figure 8.19 Circuit diagram of trilayer device assuming that the current passed separately through each layer.

This model of current flow would apply to the circumstance when the mean free path is short compared to the layer thickness. The electric current in each layer would be independent as the electrons do not propagate across the layers.
The total resistance in the trilayer, R_T, can be represented as:

$$\frac{1}{R_T} = \frac{1}{R_{LCMO}} + \frac{1}{R_{YBCO}} + \frac{1}{R_{LSMO}} \tag{8.1}$$

The total MR, MR_T, of the trilayer is

$$MR_T = \frac{\Delta R_T}{R_T} \tag{8.2}$$

Considering that MR is a measure of the change in resistance with respect to field, we differentiate equation 8.1 with respect to H. We have also excluded the $\frac{1}{R_{YBCO}}$ term because YBCO does not show an MR behaviour. This was shown experimentally as we have observed no change in the T_c or the I_c of the trilayer at the two fields, $\mu_\circ$H=0.02mT and 0.2mT.

$$\frac{d}{dH}(\frac{1}{R_T}) = \frac{d}{dH}(\frac{1}{R_{LCMO}}) + \frac{d}{dH}(\frac{1}{R_{LCMO}}) \tag{8.3}$$

$$\frac{1}{R_T^2}\Delta R_T = \frac{1}{R_{LCMO}^2}\Delta R_{LCMO} + \frac{1}{R_{LSMO}^2}\Delta R_{LSMO} \tag{8.4}$$

$$\Delta R_T = (\frac{R_T}{R_{LCMO}})^2 \Delta R_{LCMO} + (\frac{R_T}{R_{LSMO}})^2 \Delta R_{LSMO} \tag{8.5}$$

$$MR_T = \frac{R_T}{R_{LCMO}^2}\Delta R_{LCMO} + \frac{R_T}{R_{LSMO}^2}\Delta R_{LSMO} \tag{8.6}$$

which can also be represented as

$$MR_T = \frac{R_T}{R_{LCMO}} MR_{LCMO} + \frac{R_T}{R_{LSMO}} MR_{LSMO} \tag{8.7}$$

As T decreases, we can expect all the resistance values in Equation 8.7 to decrease while the MR values of the manganites increase accordingly (due to the increase in carrier mean free path within the manganites). In the superconducting transition temperature range, $R_{YBCO} \longrightarrow 0$ with decreasing T. Assuming that the rate of decrease in R_T (due mostly to the rapid drop in R_{YBCO} in the transition range) was much higher than the increase in %MR of each manganite layer with decreasing temperature, we expect that as $R_T \longrightarrow 0$, $MR_T \longrightarrow 0$.

This trend modelled here, however, is opposite to that observed in Figure 8.16, where the $\%MR$ increased with decreasing T within the superconducting transition range. We can thus exclude the possibility that this current path throught the parallel 'resistors' might be the source of the MR observed.

8.4.4 Flux Flow

Resistance increase in a Type II superconductor in the transition from the superconducting to normal state is attributed to the Lorentz force on the flux lines becoming large enough to overcome the pinning energy and thus inducing an electric field by moving perpendicular to both

the I_{bias} and H. Therefore, although there was experimental evidence that the peak observed in the MR was due to the anti-parallel configuration, and that the %MR observed did not vary with the inplane orientation of H with I_{bias} see Figure 8.18, a comprehensive study of the flux flow in the devices was essential before excluding its effects as a possible cause of the MR observations.

We observed in the MR measurements that the resistance peak occurs at the coercive fields of the manganites, which corresponds to the multidomain state of the manganite, as opposed to the single domain state beyond the saturation field of the material. At the coercive fields of the manganites, there are smaller domains of about 1-6μm^2 [111], and thus a higher density of domains than at saturation field (where a single domain is expected).

We examined how the different domain states of the F layers affected the flux density and flow, and hence causes a change in the resistance in the S layer. An analysis of the various potential causes of MR, due only to the effects of the domain states of adjacent F layers on flux behaviour, is summarized Table 8.1. The table provides a comparison of the flux density, B, in the high field (applied magnetic field) and low field states, and the consequent change in device resistances and MR behaviour of the device. This is a simplified model based on several assumptions:

- The F layers are single-domain in high field and multidomain in low field.
- The low applied field was assumed to be the point of inflexion in Figure 8.3, in between the H_{co}s of the two manganite layers.
- Each phenomenon occurred independently of the others. Hence, the resultant MR behaviour, due to the occurance of several causes of flux behaviour, at any instance is the summation of their independent effects.

The domains in both manganite layers can couple magneto-statically across the spacer layer when the YBCO thickness is smaller than the penetration depth (λ_{YBCO} = 12nm, Table 2.2) along the c-direction. Table 8.1 shows that in parallel-alignment of the F layers at high field (low field), B in YBCO is higher (lower) as a result of increased (decreased) magnetostatic coupling across the YBCO spacer as well as the increased (decreased) stray field due to less (more) flux compensation by domains. This results in a dip in the MR behaviour, unlike what we observed. Even if we consider the scenario where there is a higher flux density in the YBCO in the anti-parallel configuration, an increase in I_{bias} in the YBCO will lead to an increase in Lorentz Force experienced by the perpendicular vortices, as represented by the equation, Lorentz Force density, $F=J_c \times B$, where J_c is the critical flux density. This will result in an increase in resistance, and hence a higher %MR, with increasing I_{bias}. The opposite is observed in our system.

Table 8.1 This table lists the possible causes and effects of flux vortices present in YBCO in the the LSMO/YBCO/LC(0.3)MO trilayer device, and compares the resultant device MR behaviour due to flux density and flux flow with respect to an applied magnetic field. The effects of each phenomenon was studied individually and assumed to be independent of the others listed. Abbreviations in table: ↑ and ↓ represent an increasing and decreasing trend respectively, R_{HF} and R_{LF} represent the total device resistance at high field and low field respectively.

Source of Flux Vortices	High Field, HF (Single Domain)	Low Field, LF (Multidomain)	MR behaviour, MR=$\frac{R_{LF}-R_{HF}}{R_{HF}}$
External Field applied in a-b plane only	B: High R_{HF} ↑ with ↑ I	B: Low R_{LF} ↑ with ↑ I.	$R_{LF} < R_{HF}$ → dip in MR
Magnetostatic coupling between F layers Across YBCO spacer (in c-direction) only	B: 0 R_{HF} constant	B: High R_{LF} ↑ with ↑ I	$R_{LF} > R_{HF}$ → peak in MR MR ↑ with I ↑
Self field due to I flow parallel to a-b plane only	B ↑ with ↑ I	B ↑ with ↑ I	MR = 0
Stray field due to configuration of the F layers only	B ↑ in // state	B ↓ in anti-// state	$R_{LF} < R_{HF}$ → dip in MR
Pinning sites at domain walls only	fewer pinning sites $R_{HF} > R_{LF}$, More pinning of flux lines at LF	more pinning sites	dip in MR characteristic

This analysis proved that we can exclude flux flow as the primary cause of the MR characteristic observed in our trilayers.

8.4.5 Pseudo Spin Valve

The peak in the MR characteristic associated with the anti-parallel configuration of the F layers on either side of the superconducting spacer is similar to the giant magnetoresistance effect observed in a normal spin valve, which consist of two F metals sandwiching a metallic spacer. In such systems, one of the F layers is pinned to an AF material while the other F layer 'switches' its orientation more easily with an externally applied field. There is an increase in magnetic scattering when the F layers are oppositely aligned compared to when they are parallel. This results in an increase in resistance in the AP configuration when $l_{mfp} \sim d_{spacer}$, where l_{mfp} and d_{spacer} represent the electron mean free path and the thickness of the spacer layer respectively.

In our devices, the spin diffusion depth, δ_s, in the c-axis of the YBCO spacer at $T \sim T_c$ has been estimated to be as large as 90nm [112] and 80nm [53]. Wei et al [113] has estimated it to be about 20nm. Using these spin diffusion length scales, and assuming that the spacer behaves like a normal conductor, we can expect spin information to be transferred across the YBCO, from one F layer to the other, hence allowing the device to function like a spin valve. Using this assumption, we can explain the following characteristics of the GMR effect observed in the trilayer device.

- Temperature dependence. The increase in %MR with decreasing temperature (observed within the T_c temperature range of the device) is characteristic of a spin valve. A decrease in device temperature results in an increase in the l_{mfp}, and hence the %MR.
- Current dependence. As observed from Figure 8.9, the device does not behave ohmically in the T_c transition temperature range. This suggests that an increase bias current in the device leads to an increase in the percentage of scattering events, reducing the l_{mfp} and δ_s of the YBCO. The %MR of the device thus decreases with increasing current.

Simple Resistor Model

The variation of %MR is comparable to a simple resistor model used to explain the origin of current-in-plane GMR [114]. According to the resistor model, each layer in the spin valve is treated as an independent resistor.

The resistors are added in parallel or in series depending on the relationship between l_{mfp} and the layer thickness. If $l_{mfp} <$ layer thickness, d, each layer will conduct the electric current independently and the resistors will be added in parallel, just like in Figure 8.19. The resistance of the parallel and anti-parallel configurations are the same. The GMR in this case is thus zero. If the ratio $l_{mfp}/d > 1$, electrons can propagate across the spacer layer freely, sensing the magnetizations of the two F layers. The probability of spin scattering within the multilayer is thus the sum of all the scattering with each layer and interface. Hence, the total resistance equals

the addition of resistors in series. Our LSMO/YBCO/LC(0.3)MO trilayer device is similar to the latter scenario.

In this model, which omits the ferromagnet-spacer interface resistance, the MR is given by:

$$MR = \frac{(\alpha - 1)^2}{4(\alpha + pd_{NM}/d_{FM})(1 + pd_{NM}/d_{FM})} \tag{8.8}$$

where d_{NM} and d_{FM} represents the non-magnetic spacer and ferromagnet thicknesses, $\alpha = \rho_\downarrow/\rho_\uparrow$, and $p = \rho_{NM}/\rho_\uparrow$. $\rho_\uparrow$ and $\rho_\downarrow$ represent the majority and minority spin resistivities respectively.

The model indicated that for fixed α and thickness values, the %MR observed in CIP spin valve structures varies inversely with ρ_{NM}, the resistivity of the spacer layer. The variation of %MR with spacer resistivity (ρ_{NM} in this case) is thus very similar to the MR vs R device behaviour illustrated in Figure 8.17. Although a direct comparison of the model with our experimental data was not appropriate due to the simplification of the model (which assumed zero interface resistance, spin diffusion length and spin-flip time), the similarity in MR behaviour with the spacer resistivity observed provides evidence of GMR characteristics in the device. This is suggestive of spin transport through the spacer.

8.5 Conclusions: spin transport through YBCO?

Having analysed the obvious possibilities of the MR characteristic observed, it is apparent that the trilayer device exhibited giant magnetoresistive properties. This behaviour can be effectly explained by assuming YBCO has characteristics of a normal conductor within its T_c transition temperature range:

- The δ_s of the quasiparticles present in YBCO at any temperature $T > 0$, is larger than d_{YBCO}. The spin information from each F/S interface can hence be transported, by the quasiparticles, across the YBCO spacer, as suggested by Maekawa et al [115].

- The orientation of the F layers with respect to each other can be sensed by the quasiparticles. Hence, the amount of quasiparticle spin scattering at the F/S interfaces is increased when the trilayer is in the AP compared to the P configuration.

- The MR observed is *temperature-dependent*. τ_{sf} and l_{mfp} increases with decreasing temperature due to fewer scattering events. As $\delta_s = (l_{mfp}\ \nu_F\ \tau_{sf})^{0.5}$ [53], δ_s also increases with decreasing temperature, which results in a higher %MR in the AP configuration.

- An explanation for the *current-dependence* of the MR is that the device was in the non-ohmic state. An increase in I_{bias} results in an increase in the number of excitations from which to scatter [27], which consequently leads to smaller l_{mfp} and τ_{sf} values. Increasing I_{bias} in this case sees a drop in the %MR.

- The GMR characteristic of the device disappeared when the resistance of the device was very low. This is because most, if not all, of the I_{bias} was short-circuited by the YBCO spacer layer, thus nulling the effects of spin configuration of the outside F layers.

- The MR peak was, therefore, only observed when the device was not completely short-circuited by the YBCO spacer. I_{bias} through the F layers were essential for the exchange of spin information at the F/S interface, and thus the pseudo spin valve to function.

- A small MR peak was also observed at $I > I_c$ at $T \ll T_c$. An explanation for a smaller %MR at 44K compared to 68K is that I_{bias} required to achieve the $> I_c$ state at 44K was approximately an order of magnitude larger.

These observations in the trilayers were unexpected due to the presence of superconductivity in the YBCO spacer at the measurement temperatures. Conventionally, the transfer of spin information across a superconductor is unlikely due to the symmetry of singlet Cooper pairs. The MR observed when I_{bias} exceeded the YBCO I_c also suggested that the increasing voltage observed in the S transition state was not solely due to the movement of vortices in the superconductor. These measurements, hence, raised questions about the mode of spin/charge transport in the superconducting transition region, ie. when $I_{bias} \sim I_c$, $T \sim T_c$.

However, assuming that the spin and charge degrees of freedom of electrons in superconductors are carried separately by quasi-particles and Cooper pairs respectively [115], these measurements provide some evidence that quasiparticle behaviour in YBCO in its transition region resembles that of electrons in a normal conductor.

8.6 Summary

LSMO / YBCO / LC(0.3)MO heterostructural devices with a double coercivity characteristic have been fabricated. An unexpected result was that the I_c of the superconductor remained unchanged, within our measurement limits, in the AP and P device configurations. As mentioned earlier, this observation was contrary to some results obtained by two other groups [2, 110] using similar metallic systems. Any observation of the suppression of superconductivity due to proximity effects, observed in other systems, should be observable in YBCO because of the nodes in its d-wave order parameter. The device showed an MR behaviour similar to that observed in spin valves. This peak in the MR occurred when F layers in the device was in the anti-parallel configuration, and was observable at $I \sim I_c$ and below the onset of superconductivity. The effect varied with temperature (in the T_c transition temperature range) and bias current.

The chapter provided evidence that the magnetization of the F layers was sensed by carriers in the YBCO spacer. This effect was strongly suggestive of spin transport in YBCO in the presence of superconductivity.

Chapter 9

Conclusions

9.1 Summary

This thesis examined both active and passive means of controlling superconductivity in various devices and multilayers which comprise manganite/cuprate heterostructures. This is in line with recent interests in such heterostructures due to their potential for the application of superconductivity.

9.1.1 Materials and Fabrication

The materials issues, such as the deoxygenation of YBCO and epitaxial film quality, associated with the effective combination of Lanthanum manganites with YBCO using PLD were studied. We have proven the feasibility of using 'eclipse' PLD as a method for depositing good quality multilayers of ultrathin repeats, with homogenous and well-calibrated sub-layers. The multilayers were superconducting to an YBCO sublayer thickness 3nm, and magnetic when the manganite layer is at least 4nm thick.

We fabricated, using photolithography and other cleanroom techniques, spin injection devices with widths comparable to the transfer lengths associated with the material. These devices were fabricated with ramp junctions to allow for the study of effects caused by spin polarized current injected into the YBCO a-b plane.

9.1.2 Spin Injection from LC(0.3)MO into YBCO

Spin injection effects in superconductors have proven to be difficult to isolate due to various other causes of I_c suppression such as localized heating, external field and current summation effects. Using a 3-terminal geometry, we have shown that the I_c suppression effects observed are due mainly to heating and current summation effects. Interfacial studies indicated that such small-scale ramp junctions fabricated by ex-situ means were ineffective for spin-polarized current injection, which is very susceptible to spin scattering. Current behaviour at the junction is complicated and requires further examination

9.1.3 Proximity effects in manganite/cuprate heterostructures

Proximity effects were observed in these oxide F/S multilayers, as the T_c suppression was greater in various F/S compared to N/S systems. However, unexpectedly, magnetic properties such as magnetic moment and exchange interaction did not have a major influence on the T_c suppression.

Above T_c, we observed that structural effects were responsible for the decrease of multilayer T_{Curie} with decreasing manganite thickness. Coupling effects between manganite layers were also evident as the magnetization of the multilayers decreased with increasing YBCO spacer layer thickness. We observed that the T_c showed a manganite spacer thickness dependence up to $\sim$20nm. This is the critical thickness below which the coupling between YBCO layers directly affects the multilayer superconducting properties.

9.1.4 Investigation of spin-valve type behaviour in trilayers

We fabricated the first oxide trilayer heterostructure, comprising LSMO(15nm)/ YBCO(10nm)/ LCMO(15nm), which employed the parallel and anti-parallel configuration of the F layers to change the device properties, hence resembling a pseudo spin valve. Within the limits of our measurements, there were no observable change in the I_c or T_c in the two different F orientations.

However, using a current-in-plane geometry, at $I>I_c$ and superconducting transition temperatures, where the superconducting order parameter is weakest, the trilayer behaved like a pseudo spin valve. A magnetoresistance peak, which was observed when in the AP state, varied inversely with bias current and temperature. This effect was suggestive of spin transport present in YBCO in its transition state between normal metal and superconductor. One possibility is that the spin information, which may be carried by quasiparticles present when $T>0$, can be transferred across the YBCO layer if the spacer if thinner than the spin diffusion length. This theory requires further study using a current perpendicular to plane geometry.

9.2 Further work

The future of devices incorporating perovskite oxide heterostructures would benefit greatly from detailed interfacial characterization of these heterostructures. In particular, issues of interest are the possible chemical effects at the interfaces, and the nature of spin scattering and current transport across such interfaces.

Cuprate/Manganite interfaces

At present, the chemical compatibility [81] and epitaxial quality of manganite/cuprate (by TEM and XRD [1, 64, 116] have been studied by various groups. However, as ferromagnetic manganites have been widely used as a means to inject spin polarized currents due to their fully polarized spin conduction bands [98], it is neccessary for the improved understanding of transport mechanisms at the interfaces.

Interdiffusion of ions at the cuprate/manganite interfaces can be examined using composition analysis techniques, for example: a simple method of using secondary ion-mass spectroscopy for the detection of ion species, during the slow dry-etching of oxide F/S bilayers would give valuable information with respect to the sharpness of the interfaces and hence the mobility of individual ion species across the interfaces. Interfacial resistance can be measured using the cross-junction geometry as illustrated in Figure 6.17.

Spin transport across these interfaces can be studied with CPP measurements by incorporating the samples into F/N/F spin valve systems and evaluating comparing them to the Valet and Fert GMR model [117], as suggested by Baxter et al [118]. In their study, spin relaxation near Nb/Cu interfaces were tested by sandwiching the structure in the middle of the Cu layer in an FeMn/Py/Cu/Py exchange-biased spin valve. As the Cu layer should be thick enough that the magnetic layers are decoupled, this 'insert' should not affect the magnetic order of the

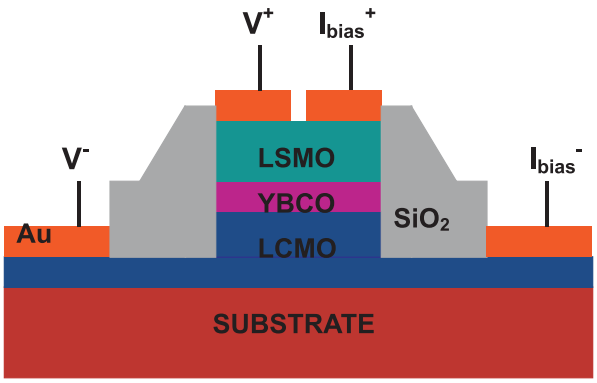

Figure 9.1 Cross-section profile of the trilayer device used for CPP measurements.

spin valve. The antiferromagnetic FeMn layer was used to pin the magnetization of the adjacent Py layer while the other Py layer is 'free'. The AΔR=AR(AP)-AR(P) (where A is the area of the interface) of the layers were measured. The AΔR values obtained experimentally were then directly compared with those calculated using the Valet and Fert theory for CPP-GMR effect assuming the both the absence of spin relaxation in the multilayers, as well as the spin-relaxation due to a finite spin-diffusion length in a thin alloy region at each interface.

This method for measuring spin-direction memory loss at interfaces can be adapted for cuprate/manganite systems in AF/F/S(N)/F structures, such as [LC(0.55)MO/ LC(0.3)MO/ YBCO/ LC(0.3)MO] structures. Such interfacial studies with respect to processing conditions allows for the optimization of such interfaces.

In order to investigate spin transport further in the LSMO/YBCO/LC(0.3)MO trilayer, this CPP geometry, as schematically illustrated in Figure 9.1, can be employed. Using the CPP configuration, there is no shunting of the current through YBCO. The transport process can also be more effectively modelled, using the Valet and Fert model.

To isolate spin induced non-equilibrium effects, the use of ferromagnetic manganites with $T_{Curie} < T_c$ in the F/S system would be useful. At $T<T_c$, current can be injected into the same device from a normal/paramagnetic metal and from a ferromagnetic layer. All other conditions, apart from the device temperature, would remain the same. The difference in the spin polarization of the injected current in this device would be much larger than that between the zero and remanent polarization as used in our experiments. Multilayers with $T_{Curie}<T_c$ are also interesting for investigating the coexistence of ferromagnetism with superconductivity, ie. a comparison of F/S versus N/S systems.

Proximity effects

Ferromagnetic manganites with lower T_{Curie} would also be useful for the investigation of proximity effects in F/S multilayers, as discussed in Section 7.2.2. As shown in Figure 9.2, a re-entrant normal state in [YBCO/LC(0.33)M0] multilayers were observed at the onset of saturation mag-

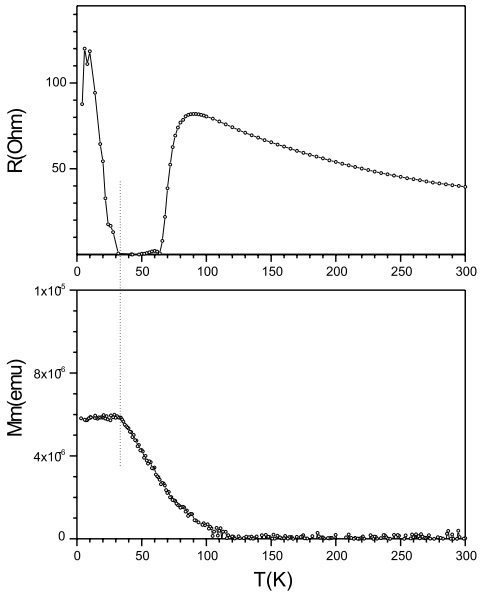

Figure 9.2 Resistance (upper panel) and magnetic moment (lower panel) of a $[YBCO_{7.5nm}/LC(0.33)MO_{5nm}]_{t=20}$ superlattice as a function of temperature indicating the reentrant normal state at 30K [64].

netization. This behaviour has not been reproduced but further evidence would reveal the nature of coupling between the alternating F and S layers, and F/S coexistence, relevant to the use of ferromagnetism to control superconductivity. Along these lines, there is increasing research recently in investigating the proximity effects in cuprate/manganite heterostructures which have not been as extensively studied as the metallic systems (as summarized in Table B.1).

Thus, although thin film technology has allowed for various types of manganite/cuprate heterostructures to be fabricated. Research, both experimental and theoretical, into the physics of the combination of the these two classes of perovskites is still primitive.

Appendix A

Overview of spin injection experiments

Table A.1 Summary of investigations of spin injection into high-temperature superconductors. List of abbreviation used: chemical formulas such as DBCO − $DyBa_2Cu_3O_7$, LAO − $LaAlO_3$, LCO − La_2CuO_4, LNO − $LaNiO_3$ and YSZ − Yttrium-stablized Zirconia, 3T and 4T represents 3-terminal and 4-terminal devices respectively, λ_s represents spin diffusion length.

Authors	Materials and Dimensions	Control	Geometry	Gain (G)	Comments
Vas'ko (1997) [55]	$LSMO_{40nm}$/ $LCO_{2u.c.}$/ $DBCO_{60nm}$	DBCO/ Au	4T bottom, I_{LSMO} parallel to I_{DBCO}	G increased from T = 60K to T = 50K, G remained the same below 40K, No T dependence	I offset was a measure of the amount of injected I from F into S
Koller (1997) [119]	$YBCO_{200nm}$/ Au_{50nm}/ $Permalloy_{100nm}$	YBCO/ Au	3T top		
Stroud (1998) [51]	$LSMO_{100nm}$/ STO_{5-40nm}/ $YBCO_100nm$	nil	3T bottom	G ∼ 35, No T dependence	
Dong (1998) [52]	$NSMO_200nm$/ LAO_{0-56nm}/ $YBCO_{100nm}$	LNO_{200nm}/ LAO/ $YBCO_{100nm}$/	3T inline, width of track 20-250μm	5 at 74K, G increases with decreasing T, G is 10-30 times higher than in control devices, G < 1 for devices with barrier > 20nm, G(control) ∼ 0.01-0.1	
Yeh (1999) [120]	$LCMO_{100nm}$/ $YSZ_{1.3nm}$/ $YBCO_{100nm}$, $LSMO_{100nm}$/STO_{2nm}/ $YBCO_{100nm}$, $LSMO_{100nm}$/ STO_{10nm}/ $YBCO_{100nm}$	LNO_{100nm}/ STO_{2nm}/ $YBCO_{100nm}$	4T	G ∼ 1, decreases with decreasing T	A shadow mask was used to fabricated device during deposition, in-situ deposition
Lee (1999) [50]	$YBCO_{50nm}$/ Au_{15nm}/ Co	$YBCO_{50nm}$/ Au_{50nm}	3T	G ∼ 5-10 × > control sample	

Authors	Materials and Dimensions	Control	Geometry	Gain (G)	Comments
Mikheenko (2000) [54]	$LCMO_{100nm}$/ STO_{2nm}/ $YBCO_{150nm}$, $LSMO_{100nm}$/ $YBCO_{150nm}$	LNO_{100nm}/ STO_{2nm}/ $YBCO_{150nm}$	N.A. Measurement of sample moment, m, decaying with time, I injection at t=4min	Δm increased with longer I injection pulse	16mT was applied and removed to magnetise samples just before measurements
Raychaudhuri (2000) [121]	$LCMO_{100nm}$/ $DBCO_{100nm}$	NIL	3T side	G $\sim$ 0	I_c was measured between narrowest part of DBCO track, which is far from the ferromagnetic layers to rule out proximity effects.
Gim (2001) [27]	LSMO/ STO_{2nm}/ YBCO, LCMO/ STO_{10nm}/ YBCO	LNO/ STO_{2nm}/ YBCO	3T and 4T	G = 0	T_c was width dependent, and decreased with thermal cycling
Wei (2002) [41]	YBCO/YSZ/LC(0.3)MO	scanning tunnelling spectroscopy		c-axis $\lambda_s \sim$ 20nm @ 4.2K	
Ireland (2003) [56]	STO 12°/12° bicrystal/ $LCMO_{100nm}$/ STO_{1-3nm}/ $YBCO_{100nm}$	Injection into grain boundary junction, ie. region of weakest superconducting order parameter	3T		Current suppression effects in the YBCO due to heating and magnetic field from the injected current

Appendix B

Proximity effect studies of metallic F/S multilayers

Table B.1 A survey of the F/S metallic systems used for proximity effect studies.

Authors	Materials	Results
Hauser (1964) [57]	Pb / X where X is Fe, Ni, Gd or Cr	1^{st} evidence of proximity effects
Wong (1986) [66]	V / Fe	Found that T_c decreased sharply for increasing Fe thickness. For some V thicknesses, the T_c increased again
Koorevaar (1994) [122]	V / Fe	No evidence of π coupling
Strunk (1994) [123]	V / Fe	• Deposition method: MBE. • Observed step-like behaviour of T_c as a function of Gd thickness.
Jiang (1995) [70]	Nd / Gd	• Deposition method: Sputtering. • Oscillatory T_c behaviour in multilayers. • Concluded that results show the first evidence of π phase difference in S/F multilayers.

Authors	Materials	Results
Muhge (1996, 1997) [71, 124]	Fe/Nb/Fe	• Deposited by sputtering. • Only one S layer but observed oscillatory T_c dependence similar to results obtained by Jiang et al. • Conclusion: effect is due to strong modification of properties of the magnetically 'dead' Fe layer at the interface at onset of ferromagnetic order.
Muhge (1998) [68]	Nb/Fe bilayers	• Deposited by MBE. • 'Dead' layer reduced to 5 angstroms. • Results show step-like behaviour
Verbanck (1998) [69]	Fe/Nb multilayers by MBE	Step-like T_c behaviour with F thickness. Results very similar to Muhge 1998.
Aarts (1997) [65]	$V/V_{1-x}Fe_x$ multilayers.	• Penetration depth of Cooper pairs in F found to be inversely proportional to the effective magnetic moment of Fe. • Increase in exchange splitting of conduction band of F layer leads to a decrease in the S/F transparency at the interface for Cooper pairs.

Authors	Materials	Results
Lazar (2000) [125]	Pb/Fe, V/Fe	
Tagirov (2002) [75]	Fe/V/Fe trilayers deposited by RF sputtering	• T_c mimina at certain Fe thicknesses. • Re-entrant superconductivity at larger thicknesses.

Appendix C

Review of oxide F/S heterostructures

Table C.1 Survey of multilayer oxide heterostructures

Authors	Materials and Dimensions	Materials Properties	Conclusion
Habermeier (2001) [64]	YBCO/ LCMO, YBCO/$SrRuO_3$		Re-entrant normal state at 30K, at the onset of saturation magnetization.
Prieto (2001) [72]	$LCMO_{6u.c.}/YBCO_{3-10u.c.}$	Samples were superconducting when $d_{YBCO} >$ 4u.c.	
Sefrioui (2002) [126]	$LCMO_{15u.c.}/YBCO_{1-12u.c.}$, $PBCO_{5u.c.}$/ $YBCO_{1-8u.c.}$	T_{Curie} = 150K, M_s = 100 emu/cm^3	Rate of T_c suppression in LCMO/YBCO systems > PBCO/YBCO. Growth of YBCO to 3u.c. in LCMO/YBCO systems with sharp interface w/ little structural disorder.
Przyslupski (2002-2003) [73, 127, 105]	$(Nd_{0.67}Sr_{0.3}MnO_3)_{10u.c.}$/ $YBCO_{2-6u.c.}$, $(Nd_{0.81}Sr_{0.19}MnO_3)_{13u.c.}$/ $YBCO_{2-6u.c.}$	T_{Curie} = 200K and 100K respectively	
Sefrioui (2003) [1]	$LCMO_{1-100u.c.}/YBCO_{5u.c.}$, $LCMO_{15u.c.}$/ $YBCO_{1-12u.c.}$	T_{Curie} = 200K, M_s = 400 emu/cm^3	T_c close to bulk YBCO for samples of thicknesses > 5u.c.
Holden (2004) [74]		YBCO/LC(0.3)MO, YBCO/$SrRuO_3$, YBCO/LNO	$d_{crit}\sim$20nm in YBCO/LC(0.3)MO and YBCO/$SrRuO_3$ SL, suppression is higher than in YBCO/LNO SL
Przyslupski (2004) [96] [116]	$[YBCO_{1-16u.c.}/LS(0.33)MO_{16u.c.}]_{t=16}$		Evidence of an AF interlayer at the LS(0.33)MO/YBCO interface. This formation is the result of hole-charge exchange. Multilayers show $T_{cd}<T_c$.

Appendix D

Error propagation

Errors, due to noise, are associated with data extraction from measurements, and, where significant, are represented by error bars in the plots.

Error propagation, in this thesis, was calculated as follows, where ϵ represents the estimated error in the data.

1. The error propagation in I_c calculation, as shown in Figure 6.15 is given by,

$$\begin{aligned} I_c &= \frac{I_c^+ - I_c^-}{2} \\ &= \frac{(I_c^+ \pm \epsilon^+) - (I_c^- \pm \epsilon^-)}{2} \\ &= I_c \pm \frac{(|\epsilon^+| + |\epsilon^-|)}{2} \end{aligned} \tag{D.1}$$

2. Using the above error calculation for I_c, the error propagation in normalized I_c as illustrated in Figure 6.16 can be summarized by the following equations.
   If ϵ^b is the error as calculated for the I_c at a particular value of I_{inj}, I_c^b, and ϵ^0 is the error as calculated for I_c at $I_{inj} = 0$, I_c^0.

   The relative error for the I_c^b is $\frac{\epsilon^b}{I_c^b}$ and is represented by ϵ_r^b

   Hence,

$$\begin{aligned} NormalizedI_c &= \frac{I_c^b \pm \epsilon^b}{I_c^0 \pm \epsilon^0} \\ &= \frac{I_c^b}{I_c^0} \pm (|\epsilon_r^b| + |\epsilon_r^0|) \end{aligned} \tag{D.2}$$

3. The error bars associated with %MR in Figures 8.18 and 8.16 represents the range of possible %MR values which can be obtained taking into account the level of noise in the measurements.

   The error, ϵ_{MR}, was an estimation of the noise associated with the MR measurements. As MR $= \frac{R(AP)-R(P)}{R(P)}$ see section 2.10, the maximum MR was calculated by using:

$$MR = \frac{(R(AP) + |\epsilon_{MR}|) - (R(P) - |\epsilon_{MR}|)}{R(P) - |\epsilon_{MR}|} \tag{D.3}$$

Whilst the minimum MR was calculated by:

$$MR = \frac{(R(AP) - |\epsilon_{MR}|) - (R(P) + |\epsilon_{MR}|)}{R(P) + |\epsilon_{MR}|} \tag{D.4}$$

Bibliography

[1] Z. Sefrioui, D. Arias, V. Pena, J. E. Villegas, M. Varela, P. Prieto, C. Leon, J. L. Martinez, and J. Santamaria, Physical Review B **67**, 214511 (2003).

[2] J. Y. Gu, C. Y. You, J. S. Jiang, J. Pearson, Y. B. Bazaliy, and S. D. Bader, Physical Review Letters **89**, 267001 (2002).

[3] D. Grundler, Physics World **April**, 39 (2002).

[4] M. Oestreich, Physics World **August**, 23 (2001).

[5] M. Johnson and R. H. Silsbee, Phys. Rev.Letters **55**, 1790 (1985).

[6] V. La Bella, D. Bullock, Z. Ding, C. Emery, A. Venkatsen, W. Oliver, G. Salamo, P. Thibado, and M. Mortazavi, Science **292**, 1518 (2001).

[7] C. Poole, ed., *Handbook of Superconductivity* (Academic Press, 2000), 1st ed.

[8] H. Frohlich, Phys. Rev. **79**, 845 (1950).

[9] L. Cooper, Phys. Rev. **104**, 1189 (1956).

[10] W. Meissner and R. Ochsenfeld, Naturwissenschaften **21**, 787 (1933).

[11] M. Tinkham, *Introduction to Superconductivity* (McGraw-Hill, 1996), 2nd ed.

[12] D. Jiles, *Introduction to magnetism and magnetic materials* (Chapman and Hall, London, 1998), 2nd ed.

[13] M. Ziese and S. Sena, J. Phys: Condens. Matter **10**, 2727 (1997).

[14] M. Baibich, J. Broto, A. Fert, F. Nguyen Van Dau, F. Petroff, P. Etienner, G. Creuzet, A. Friederich, and J. Chazelas, Phys. Rev.Letters **61**, 2472 (1988).

[15] S. Parkin, Phys. Rev.Letters **71**, 1641 (1993).

[16] S. Parkin, N. More, and K. Roche, Phys. Rev.Letters **64**, 2304 (1990).

[17] J. Mattson, C. Sowers, A. Berger, and S. D. Bader, Phys. Rev.Letters **68**, 3252 (1992).

[18] D. Kang, Ph.D. thesis, University of Cambridge (1998).

[19] J. D. Cava R.J., Santoro A., Physical Review B **35** (1987).

[20] M. Bijlsma, Ph.D. thesis, University of Twente (1996).

[21] H. Scheel, MRS bulletin XIX **9**, 26 (1994).

[22] S. J. Rothman, J. L. Routbort, U. Welp, and J. E. Baker, Physical Review B **44**, 2326 (1991).

[23] P. W. Anderson and H. Suhl, Phys. Rev. **116**, 898 (1959).

[24] C. E. Gough, M. S. Colclough, E. M. Forgan, R. G. Jordan, M. Keene, C. M. Muirhead, A. I. M. Rae, N. Thomas, J. S. Abell, and S. Sutton, Nature **326**, 855 (1987).

[25] C. Poole, H. Farach, and R. Creswich, *Superconductivity* (Academic Press Inc., London, 1995), 1st ed.

[26] C. Tsuei and J. Kirtley, Reviews of modern physics **72**, 969 (2000).

[27] Y. Gim, A. W. Kleinsasser, and J. B. Barner, Journal of Applied Physics **90**, 4063 (2001).

[28] S. Jin, T. Tiefel, M. McCormack, R. Fastnacht, R. Ramesh, and L. Chen, Science **264**, 413 (1994).

[29] R. Pauthenet and V. C., J. Phys. **31** (1970).

[30] C. Zener, Phys. Rev. **82** (1951).

[31] J. Goodenough, Phys. Rev. **100**, 564 (1955).

[32] M. A. Dagotto E., Hotto T., Tech. Rep. (2001).

[33] M. Tinkham and J. Clarke, Phys. Rev.Letters **28**, 1366 (1972).

[34] R. Moseley, Ph.D. thesis, University of Cambridge (2000).

[35] W. Parker, Phys. Rev. B **12**, 3667 (1975).

[36] N. V. Dynes R.C. and G. J.P., Phys. Rev. Lett. **41**, 1509 (1978).

[37] C. W. Schneider, R. Moerman, F. J. G. Roesthuis, R. G. Wichern, G. J. Gerritsma, and H. Rogalla, Ieee Transactions on Applied Superconductivity **7**, 2730 (1997).

[38] W. Eisenmenger, *Nonequilibrium Superconductivity, Phonons and Kapitza Boundaries* (Plenum, New York, 1981).

[39] G. Prinz, Physics Today **April**, 58 (1995).

[40] M. Johnson, Journal of Superconductivity **14**, 273 (2001).

[41] J. Y. T. Wei, Journal of Superconductivity **15**, 67 (2002).

[42] M. DeJong and C. Beenakker, Phys. Rev.Letters **74**, 1657 (1995).

[43] R. J. Soulen, J. Byers, M. S. Osofsky, B. Nadgorny, T. Ambrose, S. Cheng, P. R. Broussard, C. Tanaka, J. Nowak, J. Moodera, et al., Science **282**, 85 (1998).

[44] C. W. Schneider, R. Moerman, D. Fuchs, R. Schneider, G. J. Gerritsma, and H. Rogalla, Ieee Transactions on Applied Superconductivity **9**, 3648 (1999).

[45] W. Pickett, Rev. Mod. Phys. **61** (1989).

[46] Q. Yang, P. Holody, S. F. Lee, L. L. Henry, R. Loloee, P. A. Schroeder, W. P. Pratt, and J. Bass, Physical Review Letters **72**, 3274 (1994).

[47] M. Johnson, Phys. Rev. Lett. **70** (1993).

[48] A. S. Yeong, G. Aeppli, N. Mathur, and M. Blamire, Journal of Applied Physics **87**, 6743 (2000).

[49] M. Rubinstein, P. Lubitz, W. E. Carlos, P. R. Broussard, D. B. Chrisey, J. Horwitz, and J. J. Krebs, Physical Review B **47**, 15350 (1993).

[50] K. Lee, W. Wang, I. Iguchi, B. Friedman, T. Ishibashi, and K. Sato, Applied Physics Letters **75**, 1149 (1999).

[51] R. M. Stroud, J. Kim, C. R. Eddy, D. B. Chrisey, J. S. Horwitz, D. Koller, M. S. Osofsky, R. J. Soulen, and R. C. Y. Auyeung, Journal of Applied Physics **83**, 7189 (1998).

[52] Z. W. Dong, R. Ramesh, T. Venkatesan, M. Johnson, Z. Y. Chen, S. P. Pai, V. Talyansky, R. P. Sharma, R. Shreekala, C. J. Lobb, et al., Applied Physics Letters **71**, 1718 (1997).

[53] N. C. Yeh, J. Y. T. Wei, C. C. Fu, and R. P. Vasquez, Physica B **284**, 507 (2000).

[54] P. Mikheenko, R. Chakalov, C. Severac, F. Wellhofer, M. Colclough, C. Muirhead, and K. Kawano, Physica C **341**, 2711 (2000).

[55] V. Vas'ko, P. Larkin, K. Kraus, D. Nikolaev, C. Grupp, A. Nordman, and Goldman, Physical Review Letters **78**, 1134 (1997).

[56] J. Ireland, R. Chakalov, M. S. Colclough, and C. M. Muirhead, Applied Physics Letters **83**, 725 (2003).

[57] J. Hauser, H. Theuerer, and W. N.R., Phys. Rev. **142** (1966).

[58] H. U. Habermeier and G. Cristiani, Ieee Transactions on Applied Superconductivity **13**, 2842 (2003).

[59] H. U. Habermeier and G. Cristiani, Journal of Superconductivity **15**, 425 (2002).

[60] L. Bauernfeind, W. Widder, and H. F. Braun, Physica C **254**, 151 (1995).

[61] C. Bernhard, J. L. Tallon, C. Niedermayer, T. Blasius, A. Golnik, E. Brucher, R. K. Kremer, D. R. Noakes, C. E. Stronach, and E. J. Ansaldo, Physical Review B **59**, 14099 (1999).

[62] C. W. Chu, Physica C-Superconductivity and Its Applications **341**, 25 (2000).

[63] B. Matthias, H. Suhl, and E. Corenzwitz, Phys. Rev.Letters **1**, 444 (1958).

[64] H. U. Habermeier, G. Cristiani, R. K. Kremer, O. Lebedev, and G. van Tendeloo, Physica C **364**, 298 (2001).

[65] J. Aarts, J. M. E. Geers, E. Bruck, A. A. Golubov, and R. Coehoorn, Physical Review B **56**, 2779 (1997).

[66] H. Wong, B. Jin, H. Yang, J. Ketterson, and H. J.E., Journal of Low Temperature Physics **63** (1986).

[67] Z. Radovic, M. Ledvij, L. Dobrosavljevicgrujic, A. I. Buzdin, and J. R. Clem, Physical Review B **44**, 759 (1991).

[68] T. Muhge, K. Theis-Brohl, K. Westerholt, H. Zabel, N. N. Garif'yanov, Y. V. Goryunov, I. A. Garifullin, and G. G. Khaliullin, Physical Review B **57**, 5071 (1998).

[69] G. Verbanck, C. D. Potter, V. Metlushko, R. Schad, V. V. Moshchalkov, and Y. Bruynseraede, Physical Review B **57**, 6029 (1998).

[70] J. S. Jiang, D. Davidovic, D. H. Reich, and C. L. Chien, Phys. Rev.Letters **74**, 314 (1995).

[71] T. Muhge, N. N. Garifyanov, Y. V. Goryunov, G. G. Khaliullin, L. R. Tagirov, K. Westerholt, I. A. Garifullin, and H. Zabel, Physical Review Letters **77**, 1857 (1996).

[72] P. Prieto, P. Vivas, G. Campillo, E. Baca, L. F. Castro, M. Varela, C. Ballesteros, J. E. Villegas, D. Arias, C. Leon, et al., Journal of Applied Physics **89**, 8026 (2001).

[73] P. Przyslupski, I. Komissarov, E. Dynowska, M. Sawicki, J. Wosik, and A. Szewczyk, Ieee Transactions on Applied Superconductivity **13**, 2853 (2003).

[74] T. Holden, H. Habermeier, G. Cristiani, A. Golnik, A. Boris, A. Pimenov, J. Humlicek, O. Lebedev, G. Van Tendeloo, B. Keimer, et al., Physical Review B **69**, 064505 (2004).

[75] L. R. Tagirov, Physica C **307**, 145 (1998).

[76] T. Muhge, K. Westerholt, H. Zabel, N. N. Garifyanov, Y. V. Goryunov, I. A. Garifullin, and G. G. Khaliullin, Physical Review B **55**, 8945 (1997).

[77] D. B. Chrisey and H. G.K., *Pulsed Laser Deposition of thin films* (1994).

[78] S. R.E. and B. Z.H., in *Physics and Materials Science of High Temperature Superconductors, II,*, edited by K. R. (Kluwer Academic Publishers, Netherlands, 1992), pp. 443–469.

[79] S. Campbell, *The Science and Engineering of Microelectronic Fabrication.* (Oxford University Press, New York, 1996), 1st ed.

[80] M. Vickers, M. Kappers, T. Smeeton, E. Thrush, J. Barnard, and C. Humphreys, Journal of Applied Physics **94**, 1565 (2003).

[81] O. Toshiyuki, K. Masahiro, K. Yoko, K. Yuuzoo, H. Masanobu, and S. Yutaka, Japanese Journal of Applied Physics **29**, L607 (1990).

[82] A. M. Goldman, V. Vas'ko, P. Kraus, K. Nikolaev, and V. A. Larkin, Journal of Magnetism and Magnetic Materials **200**, 69 (1999).

[83] G. Jakob, V. V. Moshchalkov, and Y. Bruynseraede, Applied Physics Letters **66**, 2564 (1995).

[84] M. Jo, N. Mathur, J. Evetts, M. G. Blamire, M. Bibes, and J. Fontcuberta, Applied Physics Letters **75**, 3689 (1999).

[85] P. Schiffer, A. Ramirez, W. Bao, and S. Cheong, Phys. Rev.Letters **75**, 3336 (1994).

[86] U. Schoop, M. Schonecke, S. Thienhaus, S. Schymon, L. Alff, and R. Gross, Physica C **351**, 200 (2001).

[87] D. H. A. Blank and H. Rogalla, Journal of Materials Research **12**, 2952 (1997).

[88] D. K. Chin and T. Vanduzer, Applied Physics Letters **58**, 753 (1991).

[89] C. Stolzel, M. Siegel, G. Adrian, C. Krimmer, J. Sollner, W. Wilkens, G. Schulz, and H. Adrian, Applied Physics Letters **63**, 2970 (1993).

[90] M. I. Faley, U. Poppe, H. Soltner, C. L. Jia, M. Siegel, and K. Urban, Applied Physics Letters **63**, 2138 (1993).

[91] J. B. Barner, B. D. Hunt, M. C. Foote, W. T. Pike, and R. P. Vasquez, Physica C **207**, 381 (1993).

[92] B. D. Hunt, M. C. Foote, and L. J. Bajuk, Applied Physics Letters **59**, 982 (1991).

[93] C. L. Jia, B. Kabius, K. Urban, K. Herrman, G. J. Cui, J. Schubert, W. Zander, A. I. Braginski, and C. Heiden, Physica C **175**, 545 (1991).

[94] C. Horstmann, P. Leinenbach, A. Engelhardt, R. Gerber, J. L. Jia, R. Dittmann, U. Memmert, U. Hartmann, and A. I. Braginski, Physica C **302**, 176 (1998).

[95] H. Yi, Ph.D. thesis, Chalmers University of Technology (1996).

[96] P. Przyslupski, I. Komissarov, W. Paszkowicz, P. Dluzewski, R. Minikayev, and M. Sawicki, Physical Review B **69**, 134428 (2004).

[97] G. Lian, Z. Wang, J. Gao, Y. Zhou, J. Kang, M. Li, and G. Xiong, Solid State Communications **108**, 123 (1998).

[98] J. H. Park, E. Vescovo, H. J. Kim, C. Kwon, R. Ramesh, and T. Venkatesan, Nature **392**, 794 (1998).

[99] Z. Trajanovic, S. Choopun, R. P. Sharma, and T. Venkatesan, Applied Physics Letters **70**, 3461 (1997).

[100] J. Mira, J. Rivas, L. Hueso, F. Rivadulla, M. Quintela, M. Rodriguez, and C. Ramos, Phys. Rev.B **65**, 024418 (2002).

[101] A. Haghiri-Gosnet and J. Renard, J. Phys.D: Appl. Phys. **36**, R127 (2003).

[102] M. Lopez-Quintela, L. Hueso, J. Rivas, and F. Rivadulla, Nanotechnology **14**, 212 (2003).

[103] M. Varela, Z. Sefrioui, D. Arias, M. Navacerrada, M. Lucia, M. Lopez de la Torre, C. Leon, G. Loos, F. Sanchez-Quesada, and J. Santamaria, Phys. Rev.Letters **83**, 3936 (1999).

[104] M. Salamon and M. Jaime, Reviews of modern physics **73**, 583 (2001).

[105] P. Przyslupski, I. Komissarov, P. Dluzewski, J. Pelka, E. Dynowska, and M. Sawicki, Physica C-Superconductivity and Its Applications **387**, 40 (2003).

[106] C. Bell, E. J. Tarte, G. Burnell, C. W. Leung, D. J. Kang, and M. G. Blamire, Physical Review B **68**, art. no. (2003).

[107] M. Hubener, D. A. Tikhonov, K. Garifullin, K. Westerholt, and H. Zabel, J. Phys.:Condens. Matter **14**, 8687 (2002).

[108] V. N. Krivoruchko, Zhurnal Eksperimentalnoi I Teoreticheskoi Fiziki **109**, 649 (1996).

[109] R. Kinsey, G. Burnell, and M. G. Blamire, Ieee Transactions on Applied Superconductivity **11**, 904 (2001).

[110] A. Rusanov, M. Hesselberth, S. Habraken, and J. Aarts (2004).

[111] M. Allsworth, R. Chakalov, M. Colclough, P. Mikheenko, and C. Muirhead, Applied Physics Letters **80**, 4196 (2002).

[112] S. P. Pai, S. Wanchoo, S. Purandare, T. Banerjee, P. Apte, A. Narsale, and R. Pinto, Pre-print, Cond-mat/0109388 (2001).

[113] J. Y. T. Wei, N. C. Yeh, R. P. Vasquez, and A. Gupta, Journal of Applied Physics **83**, 7366 (1998).

[114] T. E.Y. and P. D.G., Solid State Physics **56**, 113 (2001).

[115] S. Maekawa, S. Takahashi, and H. Imamura, Materials Science and Engineering B-Solid State Materials for Advanced Technology **84**, 44 (2001).

[116] P. Przyslupski, I. Komissarov, W. Paszkowicz, P. Dluzewski, R. Minikayev, and M. Sawicki, Journal of Applied Physics **95**, 2906 (2004).

[117] T. Valet and A. Fert, Phys. Rev.B **48**, 48 (1993).

[118] D. Baxter, S. Steenwyk, J. Bass, and W. P. Pratt, Journal of Applied Physics **85**, 4545 (1999).

[119] D. Koller, M. S. Osofsky, D. B. Chrisey, J. S. Horwitz, R. J. Soulen, R. M. Stroud, C. R. Eddy, J. Kim, R. C. Y. Auyeung, J. M. Byers, et al., Journal of Applied Physics **83**, 6774 (1998).

[120] N. C. Yeh, R. P. Vasquez, C. C. Fu, A. V. Samoilov, Y. Li, and K. Vakili, Physical Review B **60**, 10522 (1999).

[121] P. Raychaudhuri, S. Sarkar, P. Mal, A. Bhangale, and R. Rinto, J. Phys.:Condens. Matter **12**, 9933 (2000).

[122] P. Koorevaar, Y. Suzuki, R. Coehoorn, and J. Aarts, Physical Review B **49**, 441 (1994).

[123] C. Strunk, C. Surgers, U. Paschen, and H. Vonlohneysen, Physical Review B **49**, 4053 (1994).

[124] T. Muhge, Y. V. Goryunov, K. Theis-Brohl, K. Westerholt, H. Zabel, and I. A. Garifullin, Applied Magnetic Resonance **14**, 567 (1998).

[125] L. Lazar, K. Westerholt, H. Zabel, L. R. Tagirov, Y. V. Goryunov, N. N. Garif'yanov, and I. A. Garifullin, Physical Review B **61**, 3711 (2000).

[126] Z. Sefrioui, M. Varela, V. Pena, D. Arias, C. Leon, J. Santamaria, J. E. Villegas, J. L. Martinez, W. Saldarriaga, and P. Prieto, Applied Physics Letters **81**, 4568 (2002).

[127] I. Komissarov, E. Dynowska, M. Sawicki, A. Szewczyk, and P. Przyslupski, Physica Status Solidi a-Applied Research **196**, 66 (2003).